

Searches for New Physics at the Compact Muon  
Solenoid Experiment and Precision Timing Calorimetry

Thesis by  
Cristián H. Peña

In Partial Fulfillment of the Requirements for the  
degree of  
Doctor of Philosophy

**Caltech**

CALIFORNIA INSTITUTE OF TECHNOLOGY  
Pasadena, California

2016  
Defended October 2016

© 2016

Cristián H. Peña  
ORCID: [Author ORCID]

All rights reserved

Choose one from  
the choices in the  
source code!! And  
delete this todo  
when you're done  
that. :-)

## ACKNOWLEDGEMENTS

To the two times Copa America Champions!!!

## ABSTRACT

[This abstract must provide a succinct and informative condensation of your work. Candidates are welcome to prepare a lengthier abstract for inclusion in the dissertation, and provide a shorter one in the CaltechTHESIS record.]

## TABLE OF CONTENTS

Acknowledgements . . . . .	iii
Abstract . . . . .	iv
Table of Contents . . . . .	v
List of Illustrations . . . . .	viii
List of Tables . . . . .	xxii
<b>I Preliminaries, Supersymmetry, and Dark Matter</b>	<b>1</b>
Chapter I: Introduction . . . . .	2
Chapter II: The Standard Model in a Nutshell . . . . .	3
Chapter III: Supersymmetry and Naturalness . . . . .	4
Chapter IV: Dark Matter and Weakly Interacting Particles . . . . .	5
<b>II The Large Hadron Collides and The Compact Muon Solenoid Experiment</b>	<b>6</b>
Chapter V: The Large Hadron Collider . . . . .	7
5.1 The Large Hadron Collider . . . . .	7
Chapter VI: The Compact Muon Solenoid Experiment . . . . .	12
6.1 Detector System . . . . .	12
6.2 The Compact Muon Solenoid Detector . . . . .	12
6.3 Physics Object Reconstruction . . . . .	12
6.4 Physics Object Reconstruction . . . . .	12
<b>III Searches for New Physics with the Compact Muon Solenoid Experiment</b>	<b>13</b>
Chapter VII: Searches for Dark Matter at the LHC with 8 TeV pp collisions . .	14
7.1 Introduction . . . . .	14
7.2 Data set and simulated samples . . . . .	16
7.3 Event selection . . . . .	17
7.4 Analysis Strategy . . . . .	19
7.5 Background estimation . . . . .	21
7.6 Systematic uncertainties . . . . .	29
7.7 Results and interpretation . . . . .	33
7.8 Summary . . . . .	41
Acknowledgments . . . . .	43
7.9 Background estimation and observed yield . . . . .	45
Chapter VIII: Searches for Anomalous Higgs Boson Production . . . . .	47

8.1	Introduction	47
8.2	Summary of the 8 TeV Results	48
8.3	Object Selection	51
8.4	Event Selection and Analysis Strategy	52
8.5	Background Estimation	54
8.6	Nos-resonant Background Functional Form Selection: AIC Criterion and Bias Tests	56
8.7	Systematic Uncertainties	62
8.8	Results and Interpretations	64
8.9	Summary	66
<b>IV Precision Timing Calorimetry</b>		<b>76</b>
Chapter IX: Introduction		77
9.1	EM Calorimeter Preliminaries	79
Chapter X: LYSO-based Calorimeters		88
10.1	Introduction	88
10.2	Experimental Setup	89
10.3	Event Selection and Data Analysis	90
10.4	Timing in LYSO-based Calorimeters	92
10.5	Results Discussion and Summary	98
10.6	Acknowledgements	101
Chapter XI: High-Granularity MCP-BASED Calorimeters		102
11.1	Introduction	102
11.2	Experimental Setup	104
11.3	Event Selection and Pulse Reconstruction	105
11.4	Electromagnetic Shower Position Reconstruction and Resolution	106
11.5	Electromagnetic Shower Time Resolution	108
11.6	Summary	111
11.7	Acknowledgements	112
Chapter XII: Silicon-Based Sampling Calorimeters		115
12.1	Introduction	115
12.2	General Properties of Silicon Timing and Bench Test Studies	115
12.3	Test-beam Setup and Experimental Apparatus	117
12.4	Test Beam Measurements and Results	117
12.5	Discussion	123
12.6	Conclusion	125
Chapter XIII: CMS High-Granularity Calorimeter Timing Layer		126
13.1	Introduction	126
13.2	General Properties of Silicon Timing and Bench Test Studies	126
13.3	Test-beam Setup and Experimental Apparatus	127
13.4	Test Beam Measurement, Data Analysis, and Results	128
13.5	Conclusions	135

<b>V Summary and Conclusions</b>	<b>138</b>
13.6 Conclusion . . . . .	139
Bibliography . . . . .	140
Appendix A: Search for Massive Resonances Decaying into Two Photons . .	152
Appendix B: Phenomenology of Anamalous Higgs Production in SuperSymmetric models . . . . .	153

## LIST OF ILLUSTRATIONS

<i>Number</i>	<i>Page</i>
5.1 The CERN accelerator complex. . . . .	8
5.2 The CERN Large Hadron Collider schematic layout. . . . .	9
5.3 An schematic cross sectional view of the LHC dipole magnet. . . . .	10
5.4 An 3D visualization of a LHC dipole magnet. . . . .	10
5.5 Intregated luminosity received by the CMS experiment during the LHC operation. . . . .	11
7.1 Feynman diagrams for the pair production of DM particles corresponding to an effective field theory using a vector or axial-vector operator (left), and a scalar operator (right). . . . .	16
7.2 $R^2 - \Delta\phi(J_1, J_2)$ distribution for the QCD background in the $0\mu$ box. . . . .	22
7.3 (a) $R^2$ and (b) $M_R - R^2$ razor distributions for the QCD background in the $0\mu$ box. . . . .	23
7.4 Comparison of observed yields in the $1\mu$ control region and the data-driven background estimate derived from on the $2\mu$ control region data in the four $M_R$ categories: VL (top left), L (top right), H (bottom left), and VH (bottom right). The bottom panel in each plot shows the ratio between the two distributions. The observed bin-by-bin deviation from unity is interpreted as an estimate of the systematic uncertainty associated to the background estimation methodology for the $0\mu$ search region. The dark and light bands represent the statistical and the total uncertainties in the estimates, respectively. The horizontal bars indicate the variable bin widths. . . . .	25
7.5 Comparison of the observed yield and the prediction from simulation as a function of $R^2$ in the $2\mu b$ control region. The uncertainties in the data and the simulated sample are represented by the vertical bars and the shaded bands, respectively. The horizontal bars indicate the variable bin widths. . . . .	26

7.6 Comparison of the observed yield in the zero b-tag control region and the background estimates in the four $M_R$ categories: VL (top left), L (top right), H (bottom left), and VH (bottom right). The contribution of individual background processes is shown by the filled histograms. The bottom panels show the ratio between the observed yields and the total background estimate. For reference, the distributions from two benchmark signal models are also shown, corresponding to the pair production of DM particles of mass 1 GeV in the EFT approach with vector coupling to u or d quarks. The horizontal bars indicate the variable bin widths. . . . .	27
7.7 Comparison of the observed yield and the prediction from simulation in the $Z(\mu\mu)b$ control sample (left) and of the observed yield in the $1\mu b$ control sample and the background estimates from the $2\mu b$ and $Z(\mu\mu)b$ control samples (right), shown as a function of $R^2$ . The bottom panel of each figure shows the ratio between the data and the estimates. The shaded bands represent the statistical uncertainty in the left plot, and the total uncertainty in the right plot. The horizontal bars indicate the variable bin widths. . . . .	29
7.8 Comparison of observed event yields and background estimates as a function of $R^2$ , for the one (left) and two (right) b-tag search regions. The shaded bands represent the total uncertainty in the estimate. The horizontal bars indicate the variable bin widths. . . . .	29
7.9 Total (estimated using the cross-check analysis) and JES systematic uncertainties. The green band corresponds to the systematic uncertainty associated with the background prediction method, while the red band corresponds to the JES systematic only. Panels (a) and (b) show the VL and L $M_R$ categories, respectively. Panels (c) and (d) show the H and VH $M_R$ categories, respectively. . . . .	31
7.10 Total (estimated using the cross-check analysis) and ISR systematic uncertainties. The green band corresponds to the systematic uncertainty associated with the background prediction method, while the red band corresponds to the ISR systematic only. Panels (a) and (b) show the VL and L $M_R$ categories, respectively. Panels (c) and (d) show the H and VH $M_R$ categories, respectively. . . . .	32

7.11	PDF systematic uncertainty for a vector mediated EFT signal model with DM mass = 700 GeV. The blue band corresponds to the systematic error associated with PDF uncertainty. Panels (a) and (b) show the VL and L $M_R$ categories, respectively. Panels (c) and (d) show the H and VH $M_R$ categories, respectively. . . . .	33
7.12	JES systematic uncertainty for a vector mediated EFT signal model with DM mass = 700 GeV. The blue band corresponds to the systematic error associated with JES uncertainty. Panels (a) and (b) show the VL and L $M_R$ categories, respectively. Panels (c) and (d) show the H and VH $M_R$ categories, respectively. . . . .	34
7.13	ISR systematic uncertainty for a vector mediated EFT signal model with DM mass = 700 GeV. The blue band corresponds to the systematic error associated with ISR uncertainty. Panels (a) and (b) show the VL and L $M_R$ categories, respectively. Panels (c) and (d) show the H and VH $M_R$ categories, respectively. . . . .	35
7.14	Lower limit at 90% CL on the cutoff scale $\Lambda$ as a function of the DM mass $M_\chi$ in the case of axial-vector (left) and vector (right) currents. The validity of the EFT is quantified by $R_\Lambda = 80\%$ contours, corresponding to different values of the effective coupling $g_{\text{eff}}$ . For completeness, regions forbidden by the EFT validity condition $\Lambda > 2M_\chi/g_{\text{eff}}$ are shown for two choices of the effective coupling: $g_{\text{eff}} = 1$ (light gray) and $g_{\text{eff}} = 4\pi$ (dark gray). . . . .	37
7.15	Upper limit at 90% CL on the DM-nucleon scattering cross section $\sigma_{N\chi}$ as a function of the DM mass $M_\chi$ in the case of spin-dependent axial-vector (left) and spin-independent vector (right) currents. A selection of representative direct detection experimental bounds are also shown. . . . .	40
7.16	Lower limit at 90% CL on the cutoff scale $\Lambda$ as a function of the DM mass $M_\chi$ in the case of axial-vector (left) and vector (right) currents. A selection of direct detection experimental bounds are also shown. . . . .	40

7.17	Lower limit at 90% CL on the cutoff scale $\Lambda$ for the scalar operator $\hat{O}_S$ as a function of the DM mass $M_\chi$ . The validity of the EFT is quantified by $R_\Lambda = 80\%$ (left) and $R_\Lambda = 25\%$ (right) contours, corresponding to different values of the effective coupling $g_{\text{eff}}$ . For completeness, regions forbidden by the EFT validity condition $\Lambda > 2M_\chi/g_{\text{eff}}$ are shown for two choices of the effective coupling: $g_{\text{eff}} = 1$ (light gray) and $g_{\text{eff}} = 4\pi$ (dark gray). . . . .	42
8.1	Diagram illustrating the SUSY benchmark simplified model of bottom squark decays to a Higgs boson, a b-jet, and the LSP. . . . .	48
8.2	Summary of the results in the HighRes category for the 8 TeV version of the analysis. . . . .	49
8.3	Summary of the results in the HighRes category for the 8 TeV version of the analysis. . . . .	49
8.4	Summary of the results in the HighRes category for the 8 TeV version of the analysis. . . . .	50
8.5	Summary of the results in the HighRes category for the 8 TeV version of the analysis. . . . .	50
8.6	Summary of the results in the HighRes category for the 8 TeV version of the analysis. . . . .	50
8.7	Diagram illustrating the event categorization used in the analysis. . .	53
8.8	Distribution of events in the $M_R$ and $R^2$ plane for the HighPt and $H(\gamma\gamma)$ -H/Z(bb) category for sbottom pair production with $m_{\tilde{b}} = 300$ GeV and $m_\chi = 1$ GeV. The signal expectation is shown in the color scale and the bin numbers show where each bin is located in the $M_R$ and $R^2$ plane. . . . .	55
8.9	Distribution of events in the $M_R$ and $R^2$ plane for the HighRes and LowRes categories for sbottom pair production with $m_{\tilde{b}} = 300$ GeV and $m_\chi = 1$ GeV. The signal expectation is shown in the color scale and the bin numbers show where each bin is located in the $M_R$ and $R^2$ plane. . . . .	55
8.10	sideband fits for the search region: HighPt, $M_R > 600$ GeV, $R^2 > 0.025$ . . . . .	57
8.11	sideband fits for the search region: HighRes, $150 < M_R < 250$ GeV, $R^2 > 0$ . . . . .	58
8.12	Sideband fits for the search region: LowRes, $150 < M_R < 250$ GeV, $R^2 > 0.175$ . . . . .	58

8.13	Sideband fits for the search region: $H(\gamma\gamma)$ - $H/Z(bb)$ , $M_R > 150$ GeV, $R^2 > 0$ . . . . .	61
8.14	Examples of the bias distribution for bin0 (HighPt, $M_R > 600$ , $R^2 > 0.025$ ). Left: $f_1$ (assumed parent function) = poly3, $f_2$ (tested function) = singleExp; right: $f_1$ = poly3, $f_2$ = poly3. From the left plot we can see that singleExp does not pass the bias test since it has large bias to fit poly3. . . . .	63
8.15	The diphoton mass distribution for various search region bins in the HighPt category are shown along with the background-only fit (left) and the signal plus background fit (right). The red curve represents the background prediction; the green curve represents the signal; and the blue curve represents the sum of the signal and background. The definition of the search bin is labeled above each pair of plots. . . . .	65
8.16	The diphoton mass distribution for various search region bins in the HighPt category are shown along with the background-only fit (left) and the signal plus background fit (right). The red curve represents the background prediction; the green curve represents the signal; and the blue curve represents the sum of the signal and background. The definition of the bin is labeled above each pair of plots. . . . .	66
8.17	The diphoton mass distribution for various search region bins in the HighPt category are shown along with the background-only fit (left) and the signal plus background fit (right). The red curve represents the background prediction; the green curve represents the signal; and the blue curve represents the sum of the signal and background. The definition of the bin is labeled above each pair of plots. . . . .	67
8.18	The diphoton mass distribution for various search region bins in the $H(\gamma\gamma)$ - $H/Z(bb)$ category are shown along with the background-only fit (left) and the signal plus background fit (right). The red curve represents the background prediction; the green curve represents the signal; and the blue curve represents the sum of the signal and background. The definition of the bin is labeled above each pair of plots.	67

8.19 The diphoton mass distribution for the search region bin 9 are shown along with the background-only fit (left) and the signal plus background fit (right). The top row shows the HighRes category, while the bottom row shows the LowRes category. The red curve represents the background prediction; the green curve represents the signal; and the blue curve represents the sum of the signal and background. The definition of the bin is labeled above each pair of plots.	68
8.20 The diphoton mass distribution for the search region bin 10 are shown along with the background-only fit (left) and the signal plus background fit (right). The top row shows the HighRes category, while the bottom row shows the LowRes category. The red curve represents the background prediction; the green curve represents the signal; and the blue curve represents the sum of the signal and background. The definition of the bin is labeled above each pair of plots.	69
8.21 The diphoton mass distribution for the search region bin 11 are shown along with the background-only fit (left) and the signal plus background fit (right). The top row shows the HighRes category, while the bottom row shows the LowRes category. The red curve represents the background prediction; the green curve represents the signal; and the blue curve represents the sum of the signal and background. The definition of the bin is labeled above each pair of plots.	70
8.22 The diphoton mass distribution for the search region bin 12 are shown along with the background-only fit (left) and the signal plus background fit (right). The top row shows the HighRes category, while the bottom row shows the LowRes category. The red curve represents the background prediction; the green curve represents the signal; and the blue curve represents the sum of the signal and background. The definition of the bin is labeled above each pair of plots.	71

8.23 The diphoton mass distribution for the search region bin 13 are shown along with the background-only fit (left) and the signal plus background fit (right). The top row shows the HighRes category, while the bottom row shows the LowRes category. The red curve represents the background prediction; the green curve represents the signal; and the blue curve represents the sum of the signal and background. The definition of the bin is labeled above each pair of plots.	72
8.24 The observed significance in units of standard deviations is plotted for each search bin. The significance is computed using the profile likelihood, where the sign reflects whether an excess (positive sign) or deficit (negative sign) is observed. The categories that the bins belong to are labeled at the bottom. The yellow and green bands represent the $1\sigma$ and $2\sigma$ regions, respectively. . . . .	74
8.25 The observed 95% confidence level (C.L.) upper limits on the production cross section for sbottom pair production decaying to a bottom quark, a Higgs boson, and the LSP are shown. The solid and dotted black contours represent the observed exclusion region and its $1\sigma$ bands, while the analogous blue contours represent the expected exclusion region and its $1\sigma$ bands. . . . .	74
8.26 The observed significance scan for sbottom pair production decaying to a bottom quark, a Higgs boson, and the LSP is shown. . . . .	75
9.1 Cross section as a function of the incoming photon energy in lead. . . . .	80
9.2 Fractional energy loss per radiation length in lead as a function of the electron/positron energy. . . . .	81
9.3 Graphical definition of the critical energy ( $E_c$ ). The intersection of the solid lines is the definition used in this thesis. The intersection between the solid (ionization) and dashed line is alternative definition. . . . .	82
9.4 Electron critical energy ( $E_c$ ) for the chemical elements. Experimental data is shown for gases (red circles) and solids (magenta crosses). Fits are shown for gases (dashed red line) and solids (solid magenta line) . . . . .	83

9.5 Shower profile in the longitudinal direction for a 30 GeV electron in iron from an EGS4 simulation. The solid line histogram shows the fractional energy per radiation length, and the solid line curve is a fit to the distribution using a gamma function. The number of electrons (solid circles) and photons (hollowed squares) with energies larger than 1.5 MeV and crossing planes at $X_0/2$ intervals (scale on the right) is also shown. The number of photons has been scaled down to have the same area as the number of electrons distribution. . . . .	84
9.6 Shower profile in the longitudinal direction for electrons in copper. The different curves and points represent different electron energies ranging from 1 GeV-1 TeV. . . . .	85
9.7 Energy deposited per unit length in the transverse direction for 10 GeV electrons in copper. The shower has been sample in three different places; at $2X_0$ (red circles), $6X_0$ (black dots), and $15X_0$ (blue crosses). . . . .	86
10.1 Timing measurement schematic breakdown using a monolithic, large scintillating crystal. The incident particle impinges on the crystal face from the left. The characteristic time intervals are discussed in the text. . . . .	89
10.2 The basic schematic diagram of the experimental setup for a typical TOF measurement is shown to illustrate the basic detector elements. One photodetector is used as a time reference and the second measures energy and time simultaneously. . . . .	90
10.3 Sample pulses as digitized by the DRS4 board. On the left a pulse is shown from the reference Hamamatsu R3809 MCP-PMT, and on the right is a pulse from the Hamamatsu R3809 MCP-PMT optically coupled to a $(1.7 \text{ cm})^3$ LYSO crystal cube recorded using 8 GeV electron beam. . . . .	91
10.4 Sample fits used to assign timestamps to digitized MCP-PMT pulses. On the left is a pulse from the reference Hamamatsu R3809 MCP-PMT, and on the right is a pulse from the Hamamatsu R3809 MCP-PMT optically coupled to a $(1.7 \text{ cm})^3$ LYSO crystal recorded during an 8 GeV electron run. . . . .	91
10.5 A schematic diagram of the experimental setup for the TOF measurement using the LYSO sampling calorimeter is shown on the left, along with a picture of the experimental setup shown on the right. . . . .	93
10.6 TOF distributions for the LYSO cube sampling calorimeter for 4 GeV (top left), 8 GeV (top right), 16 GeV (bottom left), 32 GeV (bottom right) electron beam energy. . . . .	94

10.7	The shashlik configuration based upon interleaved W and LYSO layers. Twenty-eight LYSO crystal plates and twenty-seven W plates comprise the module. Four WLS fibers are used to read out the scintillation light from the tiles. . . . .	95
10.8	A schematic diagram of the experimental setup for the TOF measurement using the LYSO-tungsten shashlik calorimeter with fiber signal extraction, along with a photograph of the experimental setup. . . . .	95
10.9	(a) Pulse shapes digitized by the DRS4 board and averaged over several hundred events obtained from the LYSO-tungsten shashlik calorimeter with light extracted using DSB1 (blue) and Y11 (red) WLS fibers. (b) DSB1(blue) shashlik average light pulse shape compared with the averaged pulse shape obtained from direct optical coupling of the photodetector to one edge of a LYSO tile in the shashlik calorimeter. (green) . . . . .	96
10.10	(Left) Histogram of the pulse integral which is proportional to the total collected charge is shown for events recorded using the LYSO cube sampling calorimeter for a 32 GeV electron beam. (Right) Histogram of the pulse integral for events recorded using the LYSO-tungsten shashlik calorimeter using DSB1 fibers, for a 32 GeV electron beam. The background is included due to a misconfiguration of the Cherenkov counter. . . . .	97
10.11	TOF distributions for the LYSO-tungsten shashlik calorimeter using DSB1 fibers for electron beams with varying beam energies. . . . .	97
10.12	A schematic diagram of the experimental setup for the TOF measurement using the LYSO-tungsten shashlik calorimeter with signal extraction from the edges of two LYSO plates, along with a picture of the experimental setup. . . . .	98
10.13	A photograph of the two exposed LYSO layers in the shashlik cell. The scintillation light signal is extracted by optically coupling the edges of these two exposed LYSO layers to MCP-PMT photodetectors. . . . .	98
10.14	TOF distributions for the LYSO-tungsten shashlik calorimeter with signal extracted from the edges of two LYSO layers. . . . .	99
10.15	. . . . .	99

10.16	Timing resolution measurement as a function of the electron beam energy for (left) the LYSO cube sampling calorimeter (middle) the LYSO-tungsten shashlik calorimeter read-out with DSB1 fibers (right) the LYSO-tungsten shashlik calorimeter read-out directly by optically coupling to the edges of two LYSO layers. In all cases we fit the data with a function of $1/\sqrt{E}$ and a constant term. . . . .	99
10.17	Comparison of time resolutions obtained with the $(1.7 \text{ cm})^3$ LYSO cube (blue), and the LYSO-tungsten shashlik calorimeter with light extracted using DSB1 fibers (red). The x-axis in this figure displays the amplitude of the signal, corrected for the attenuation factors. . . . .	100
11.1	The experimental setup inside of the dark box is shown. The beam direction is from the bottom of the photograph to the top. The detector elements shown in the order from upstream to downstream of the beam are: the tungsten absorber, the Photonis XP85011 MCP-PMT located on the motorized stage, and the Photek 240 MCP-PMT used as a time reference detector. The DRS4 waveform digitizers are also shown on the lower right side. . . . .	104
11.2	The external view of the Photonis XP85011 MCP-PMT is shown on the left, and the schematic diagram is shown on the right. The red square indicates the pixels used for the experiment and data analysis. . . . .	105
11.3	Example of a digitized signal from a single Photonis pixel (left) and Photek (right) MCP-PMT following a high-energy electron shower, via DRS4. . . . .	106
11.4	The mean charge measured for each pixel for one example run is shown. During this run, the Photonis MCP-PMT was held in the same location. Based on the distribution of the mean charge among the pixels, we can infer that the beam center is located in the upper half of the center pixel. Pixel 44 is not shown as it was found to be not operational. . . . .	107
11.5	The distribution of reconstructed shower positions is shown for three runs with the beam centered near the top, center, and bottom of the central pixel. . . . .	108
11.6	The distributions of reconstructed shower position in the y axis is shown for the three runs corresponding to the distributions shown in Figure 11.5. The measured beam displacements are compared to the known displacements as recorded by the motorized stage. . . . .	109

11.7	The distributions of the measured $x$ (left) and $y$ (right) coordinates are shown along with the fit to the resolution model. The position resolution of the EM shower as measured by the MCP-PMT detector is determined from the fit to the resolution model. . . . .	110
11.8	The time distributions obtained using the highest energy pixel (left) and the energy weighted algorithm (right) are shown for one example run. The distributions are fitted with Gaussian models, and the width parameter of the Gaussian is displayed on the plot. . . . .	111
11.9	Time resolution found for each run. The time-stamp obtained using the energy weighting method yields time resolutions consistently below 60 ps. The time resolution measured using the single pixel with the largest signal is significantly worse. . . . .	112
11.10	The correlation between the time measurement and the measured integrated charge is shown on the left for one example pixel. The same correlation after performing the time measurement correction is shown on the right. . . . .	113
11.11	The time resolution of the electromagnetic shower for various runs is shown after performing the time measurement correction based on the measured integrated charge. . . . .	114
11.12	The time resolution is plotted as a function of the number of pixels included in the energy-weighted algorithm for one example run. . . .	114
12.1	The measured capacitance as a function of the applied bias voltage. .	116
12.2	The electric diagram for the silicon diode connections (left). External view of the box with silicon diode, and the bias voltage connection is shown below it (right). . . . .	116
12.3	A schematic diagram of the test-beam setup is shown. The $t_0$ and $t_1$ are defined in Section 12.4. . . . .	118
12.4	Test beam setup. . . . .	119
12.5	Examples of the signal pulse waveform for the silicon sensor (left) and the Photek MCP-PMT (right) digitized by CAEN V1742 digitizer board. The bias voltage applied to the silicon pad sensor is 500 V.	119
12.6	The distribution of charge integrated in the silicon sensor is shown for data events with no beam and random trigger. . . . .	120

12.7	The distribution of charge integrated in the silicon sensor is shown for a beam of 120 GeV protons (left) and 8 GeV electrons (right) without any absorber upstream of the silicon sensor. These conditions mimic the response of the silicon sensor to a minimum-ionizing particle. All triggered events were used in these distributions. . . . .	121
12.8	Left: An example of the distribution of integrated charge in the silicon sensor for 32 GeV electrons and 6 $X_0$ absorber shown in units of $Q_{MIP}$ . Right: The integrated charge in the silicon sensor expressed in units of $Q_{MIP}$ is shown for the same 6 $X_0$ absorber as a function of the electron beam energy. The uncertainty bands show the RMS of the measured charge distribution. The red line is the best fit to a linear function. . . . .	122
12.9	The dependence of $\Delta t$ on the integrated charge in the silicon sensor is shown on the left. The red curve represents the fit to the profile plot of the two dimensional distribution, and is used to correct $\Delta t$ for this effect. On the right, we show the corresponding two dimensional distribution after performing the correction. A 16 GeV electron beam is used, and the silicon sensor is placed after 6 $X_0$ of tungsten absorber.	123
12.10	Left: The distribution of $\Delta t$ between the silicon sensor and the Photek MCP-PMT. A 32 GeV electron beam is used, and the silicon sensor is placed after 6 $X_0$ of tungsten absorber. Right: The measured time resolution between the silicon sensor and the Photek MCP-PMT reference is shown as a function of the electron beam energy. The silicon sensor is placed after 6 $X_0$ of tungsten absorber. . . . .	124
12.11	On the left, the integrated charge in the silicon sensor expressed in units of $Q_{MIP}$ is shown as a function of the absorber ( $W$ ) thickness measured in units of radiation lengths ( $X_0$ ). The electron beam energy was 8 GeV. The uncertainty bands show the RMS of the measured charge distribution. On the right, the time resolution between the silicon sensor and the Photek MCP-PMT reference is shown as a function of the absorber thickness. . . . .	124
12.12	The time resolution between the silicon sensor and the Photek MCP-PMT reference is shown as a function of bias voltage applied on the silicon sensor. The electron beam energy was 16 GeV, and the silicon sensor is placed after 6 $X_0$ of tungsten absorber. . . . .	125

13.1	An HGC sensor schematic geometry with 7 pixels (left), and a s CAD schematic of the entire sensor (right) are shown. . . . .	127
13.2	The implemented HGC timing layer is shown. 25 pixels with full analog electronics were implemented. The silicon sensor is at the back of the PCB. . . . .	127
13.3	A schematic diagram of the test-beam setup is shown. The $t_0$ and $t_1$ are defined in Section 12.4. . . . .	128
13.4	HGC timing layer test beam setup. . . . .	129
13.5	Examples of the signal pulse waveform for one the pixels of the HGC timing layer (left) and the Photek MCP-PMT (right) digitized by CAEN V1742 digitizer board. The bias voltage applied to the HGC silicon sensor is $-300$ V. . . . .	129
13.6	Examples of the timestamps extraction for a pulse waveform in one the pixels of the HGC timing layer (left) and the Photek 240 MCP-PMT (right) digitized by CAEN V1742 digitizer board. The timestamp on the HGC pixel is extracted by intersecting the linear fit (solid red line) with the horizontal line corresponding to 45% of the pulse maximum. The timestamp for the Photek 240 is the mean parameter of the Gaussian fit (solid blue line). . . . .	130
13.7	Examples of the shower transverse profile sampled by the HGC layer for a 32 GeV (left) and 16 GeV (right) electron beam. There is $6X_0$ of tungsten right upstream of the HGC layer. . . . .	131
13.8	TOF distributions for (left) the pixel with the highest and (right) the the pixel with the second highest charge in the HGC layer using a 32 GeV electron beam and $6X_0$ of tungsten. The TOF resolutions are estimated by the standard deviation parameter of the Gaussian fit (red solid curve) to the TOF distribution. . . . .	132
13.9	TOF distributions of the HGC layer using a 32 GeV electron beam and $6X_0$ of tungsten, where the pixels are combined with (left) the default algorithm and (right) the mpv of the charge distribution as the weight. The TOF resolutions are estimated by the standard deviation parameter of the Gaussian fit (red solid curve) to the TOF distribution .	132
13.10	HGC layer TOF resolution as a function of the number of pixels combined. The distance between the absorber and the HGC layer was varied to sample the shower at different location. . . . .	133

13.11	R <sub>7</sub> distribution for different separations between the HGC layer and the 6X <sub>0</sub> of tungsten. . . . .	133
13.12	HGC layer TOF resolution as a function of the beam energy using 6X <sub>0</sub> of tungsten. The functional form $A/\sqrt{E} + B$ was fitted to the data points (red solid curve). . . . .	134
13.13	TOF distributions for (left) the Photonis MCP-PMT and (right) the final two-layer combination using a 32 GeV electron beam and 6X <sub>0</sub> of tungsten. The TOF resolutions are estimated by the standard deviation parameter of the Gaussian fit (red solid curve) to the TOF distribution . . . . .	135
13.14	TOF distributions after a 50 ps Gaussian smearing for (left) the pixel with the highest and (right) the pixel with the second highest charge in the HGC layer using a 32 GeV electron beam and 6X <sub>0</sub> of tungsten. The TOF resolutions are estimated by the standard deviation parameter of the Gaussian fit (red solid curve) to the TOF distribution. . . . .	136
13.15	TOF distributions after a 50 ps Gaussian smearing for (left) the HGC layer and (right) the final two-layer combination using a 32 GeV electron beam and 6X <sub>0</sub> of tungsten. The TOF resolutions are estimated by the standard deviation parameter of the Gaussian fit (red solid curve) to the TOF distribution. . . . .	136
13.16	HGC layer TOF resolution after a 50 ps Gaussian smearing as a function of the number of pixels combined. . . . .	137
13.17	TOF distributions as a function of the beam energy after a 50 ps Gaussian smearing for (left) the HGC layer and (right) the final two-layer combination using 6X <sub>0</sub> of tungsten. The functional form $A/\sqrt{E} + B$ was fitted to the data points (red solid curve). . . . .	137

## LIST OF TABLES

<i>Number</i>	<i>Page</i>
7.1 Measured trigger efficiency for different $M_R$ regions. The selection $R^2 > 0.35$ is applied. The uncertainty shown represents the statistical uncertainty in the measured efficiency. . . . .	17
7.2 Observed yield in each in events with $0\mu$ and no b-tagged jets for each $M_R$ category. The number overlapping events between the razor and monojet seaches is also presented. . . . .	20
7.3 Analysis regions for events with zero identified b-tagged jets. The definition of these regions is based on the muon multiplicity, the output of the CSV b-tagging algorithm, and the value of $M_R$ . For all the regions, $R^2 > 0.5$ is required. . . . .	21
7.4 Analysis regions for events with identified b-tagged jets. The definition of these regions is based on the muon multiplicity, the output of the CSV b-tagging algorithm, and the value of $M_R$ . For all the regions, $R^2 > 0.5$ is required. . . . .	21
7.5 Comparison of the observed yield in the $1\mu$ control region in each $M_R$ category and the corresponding data-driven background estimate obtained by extrapolating from the $2\mu$ control region. The uncertainty in the estimates takes into account both the statistical and systematic components. The contribution of each individual background process is also shown, as estimated from simulated samples, as well as the total MC predicted yield. . . . .	24
7.6 Comparison of the observed yield for the $2\mu$ control region in each $M_R$ category and the corresponding prediction from background simulation. The quoted uncertainty in the prediction reflects only the size of the simulated sample. The contribution of each individual background process is also shown, as estimated from simulated samples. . . . .	24
7.7 Observed yield and predicted background from simulated samples in the $2\mu b$ control region. The quoted uncertainty in the prediction only reflects the size of the simulated sample. The contribution of each individual background process is also shown, as estimated from simulated samples. . . . .	25

7.8 Comparison of the observed yields for for the zero b-tag search region in each $M_R$ category and the corresponding background estimates. The uncertainty in the background estimate takes into account both the statistical and systematic components. The contribution of each individual background process is also shown, as estimated from simulated samples, as well as the total MC predicted yield. . . . .	26
7.9 Comparison of the observed yields in the $Z(\mu\mu)b$ and $1\mu b$ samples, the corresponding predictions from background simulation, and (for $1\mu b$ only) the cross-check background estimate. The contribution of each individual background process is also shown, as estimated from simulated samples. . . . .	28
7.10 Comparison of the observed yield for events in the one and two b-tag search regions and the corresponding background estimates. The uncertainty in the estimates takes into account both the statistical and systematic components. The contribution of each individual background process is also shown, as estimated from simulated samples, as well as the total MC predicted yield. . . . .	30
7.11 Systematic uncertainties associated with the description of the DM signal. The values indicated represent the typical size. The dependence of these systematic uncertainties on the $R^2$ and $M_R$ values is taken into account in the determination of the results. . . . .	36
7.12 The 90% CL limits on DM production in the case of axial-vector couplings. Here, $\sigma_{UL}^u$ and $\sigma_{UL}^d$ are the observed upper limits on the production cross section for u and d quarks, respectively; $\Lambda_{LL}$ is the observed cutoff energy scale lower limit; and $\sigma_{N\chi}$ is the observed DM-nucleon scattering cross section upper limit. . . . .	39
7.13 The 90% CL limits on DM production in the case of vector couplings. Here, $\sigma_{UL}^u$ and $\sigma_{UL}^d$ are the observed upper limits on the production cross section for u and d quarks, respectively; $\Lambda_{LL}$ is the observed cutoff energy scale lower limit; and $\sigma_{N\chi}$ is the observed DM-nucleon scattering cross section upper limit. . . . .	39
7.14 The 90% CL limits on DM production in the case of scalar couplings. Here, $\sigma_{UL}^{obs}$ is the observed upper limit on the production cross section, $\Lambda_{LL}^{obs}$ and $\Lambda_{LL}^{exp}$ are the observed and expected cutoff energy scale lower limit, respectively. . . . .	41

7.15	Background estimates and observed yield for each $R^2$ bin in the VL $M_R$ category. . . . .	45
7.16	Background estimates and observed yield for each $R^2$ bin in the L $M_R$ category. . . . .	45
7.17	Background estimates and observed yield for each $R^2$ bin in the H $M_R$ category. . . . .	46
7.18	Background estimates and observed yield for each $R^2$ bin in the VH $M_R$ category. . . . .	46
7.19	Background estimates and observed yield for each bin in the $0\mu b$ signal region. . . . .	46
7.20	Background estimates and observed yield for each bin in the $0\mu bb$ signal region. . . . .	46
8.1	A summary of the search region bins in each category is presented. The functional form used to model the non-resonant background is also listed. An exponential function of the form $e^{-ax}$ is denoted as “singleExp”; a modified exponential function of the form $e^{-ax^b}$ is denoted as “modExp”; and an N’th order Bernstein polynomial is denoted by “polyN”. . . . .	54
8.2	The predicted yields for the standard model Higgs background processes are shown for an integrated luminosity corresponding to $15.2 \text{ fb}^{-1}$ for each search region considered in this analysis. The contributions from each standard model Higgs process is shown separately, and the total is shown on the rightmost column along with its full uncertainty.	59
8.3	Full list of p.d.f (function) used in the AIC test. . . . .	60
8.4	AIC results summary for the search region: HighPt, $M_R > 600 \text{ GeV}$ , $R^2 > 0.025$ . . . . .	60
8.5	AIC results summary for the search region: HighRes, $150 < M_R < 250 \text{ GeV}$ , $R^2 > 0$ . . . . .	60
8.6	AIC results summary for the search region: LowRes, LowRes, $150 < M_R < 250 \text{ GeV}$ , $R^2 > 0.175$ . . . . .	61
8.7	AIC results summary for the search region: H( $\gamma\gamma$ )-H/Z(bb), $M_R > 150 \text{ GeV}$ , $R^2 > 0$ . . . . .	61

8.8 Examples of the bias estimate for different function pairs passing the AIC test for bin0 (HighPt, $M_R > 600$ , $R^2 > 0.025$ ). Functions in the first column are the assumed parent functions ( $f_1$ ), while functions in the first row are the ones being tested ( $f_2$ ). In the first row, the numbers in brackets are the AIC weights. . . . .	63
8.9 List of the selected background functions for different search regions. . . . .	64
8.10 Summary of systematic uncertainties and their size. . . . .	64
8.11 The non-resonant background yields, SM Higgs background yields, best fit signal yields, and observed local significance are shown for the signal plus background fit in each search region bin. The uncertainties include both statistical and systematic components. The non-resonant background yields shown correspond to the yield within the window between 122 GeV and 129 GeV and is intended to better reflect the background under the signal peak. The observed significance for the bins in HighRes and LowRes categories are identical because they are the result of a simultaneous fit. The significance is computed using the profile likelihood, where the sign reflects whether an excess (positive sign) or deficit (negative sign) is observed. . . . .	73
9.1 Tabulated values for $L_{\text{rad}}$ and $L'_{\text{rad}}$ from Y. S Tsai. . . . .	81

# **Part I**

## **Preliminaries, Supersymmetry, and Dark Matter**

*Chap ter 1*

## INTRODUCTION

*Chapter 2***THE STANDARD MODEL IN A NUTSHELL**

*Chapter 3***SUPERSYMMETRY AND NATURALNESS**

*Chapter 4***DARK MATTER AND WEAKLY INTERACTING PARTICLES****Introduction****Cosmological Preliminaries****Observational Evidence for Dark Matter Existance****Supersymmetry****Simplified Models****Effective Field Theories at the LHC**

## **Part II**

# **The Large Hadron Collides and The Compact Muon Solenoid Experiment**

## C h a p t e r 5

# THE LARGE HADRON COLLIDER

### **5.1 The Large Hadron Collider**

The CERN Large Hadron Collider (LHC) is a two-ring superconducting accelerator and collider with 27 km of circumference, which is located in the tunnel constructed for the CERN Large Electron-Positron Collider (LEP). The tunnel lies between 45 m and 170 m below the surface on an inclind plane (1.41% slope) towards Lake Lèman and spans between the French and Swiss border close to Geneva. The layout of the tunnel is such that contains 8 arc sections that spans most of the circumference and 8 straight sections where the experimental halls are located.

The LHC is a particle-particle collider – in its most common configuration it collides protons – with a designed center-of-mass energy of 14 TeV. In order to achieve such high energies, the LHC uses the existing CERN facilities to gradually increase the energy of the protons. Everything starts with a bottle of compressed hydrogen gas, then, hydrogen atoms are fed into the source chamber of the linear accelerator, where an electric field strips off their electrons. The resulting protons are then injected into the linear accelaretor, Linac 2, which is the first step in the accelerator chain and boosts the protons energy up to 50 MeV. The accelerated proton beam is then divided into 4 (to increase its intensity) and enters the second stage of acceleration, this occurs in the Proton Synchrotron Booster (PSB), where protons are now accelerated to 1.4 GeV. Subsequently, the proton beam is recombined and sent to the Proton Synchrotron (PS), which increases the energy to 25 GeV, followed by the Super Proton Synchrotron (SPS), which brings the beam energy to 450 GeV.

Finally, the proton beam is transferred to the two beam pipes of the LHC. The beams circulate in opposite directions. The LHC filling time is 4 minutes and 20 seconds, but it takes around 20 minutes for the protons to reach their maximum energy. Figure 5.1 shows the CERN accelerator complex just described. At this point, the two beams are brought to collide at the four interaction points (IP) in the straight sections where the LHC's experiments are located. There are two main purpose experiments located in diametrical opposite locations, the ATLAS experiment is located at point 1 and the CMS experiment is located at point 1. There are also two specialized experiments; the LHCb experiment, which studies B-hadron physics, and

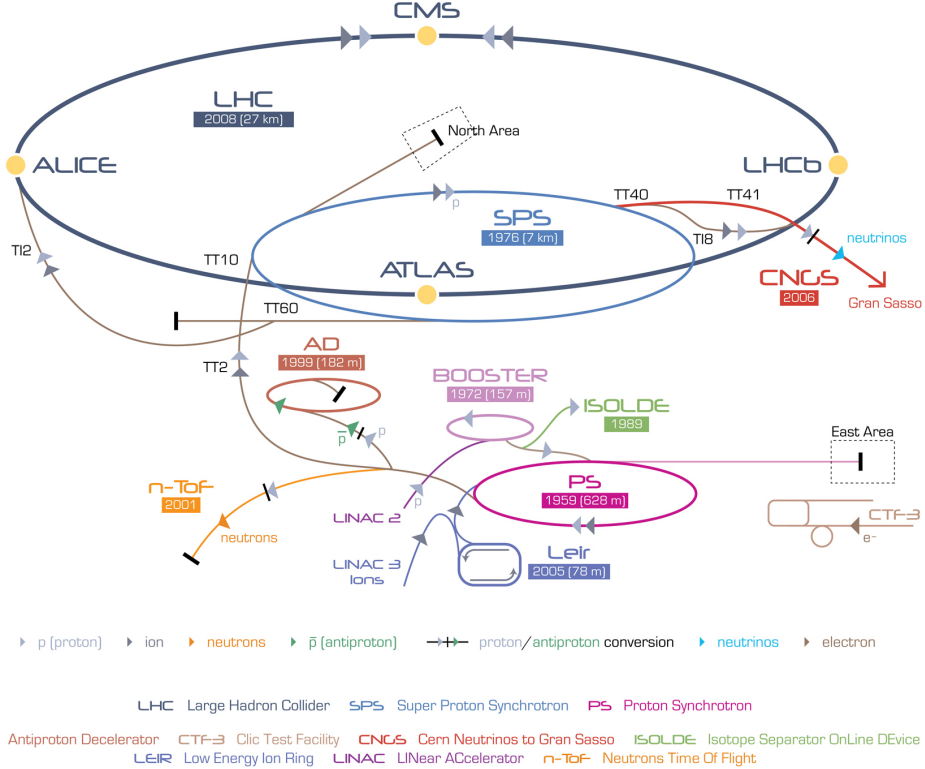


Figure 5.1: The CERN accelerator complex.

the ALICE experiment, which specializes in studying heavy ion collisions (another type of collision possible at the LHC). Figure 5.2 shows an schematic layout of the LHC. Due to the small diameter of the tunnel in the arcs (3.7 m), which complicates the installation of two separate proton rings, the LHC uses a twin-bore magnet design, proposed in 1971 by John Blewett at the Brookhaven National Laboratory (BNL) [JBlewett] as a cost-saving alternative.

Since the usage of superconducting magnets at the Intersecting Storage Rings at CERN, particle colliders have used them as the default technology for their operation. However, the main difference is that the LHC's superconducting magnets operate at a temperature lower (below 2 K) than the standard superconducting magnets in other particle colliders (4-5 K). The LHC ring accommodates 1,232 NbTi main dipole magnets, cooled down to 1.9 K by using superfluid helium; they operate at fields above 8 T. The twin-bore design allows for a common nonmagnetic collar and iron yoke, as well as common cryogenic system. The core of the dipole magnet system is enclosed by a cylindrical alloyed low-carbon steel vacuum vessel with an outer diameter of 914 mm and a wall thickness of 12 mm. Figures 5.3 and 5.4 show a cross sectional view and a 3-dimensional visualization of the main dipole magnet

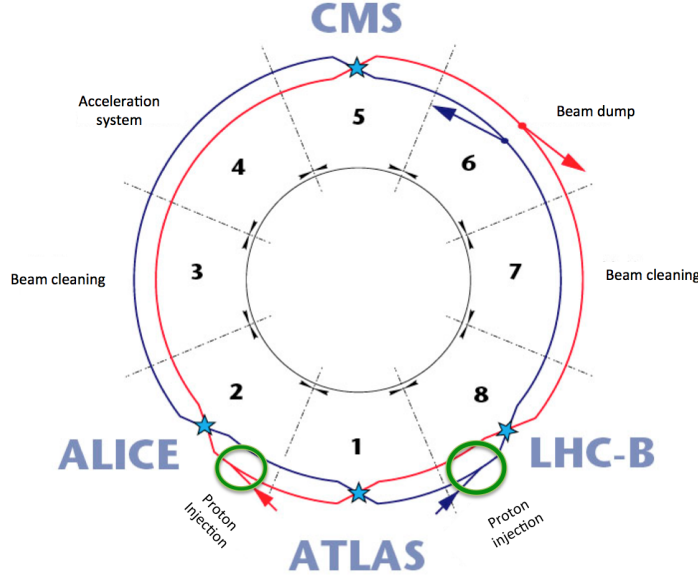


Figure 5.2: The CERN Large Hadron Collider schematic layout.

system, respectively.

The goal of the LHC program is to reveal the nature of new physics. The high-energy collision (14 TeV) are a key ingredient to probe new physics, since new physics could just be present at that energy scale. However, it is by no means the only ingredient; new physics will likely have smaller cross sections than that of the known SM processes and therefore a large number of proton-proton collision is needed. The number of events for a particular physics process  $N_{exp}$  generated in the LHC is the product of the experimental cross section  $\sigma_{exp}$  and the integrated luminosity, i.e.

$$N_{exp} = \sigma_{exp} \int \mathcal{L}(t) dt. \quad (5.1)$$

Where  $\mathcal{L}(t)$  is the instantaneous luminosity, which depends on the LHC beam parameters and can be written as [LHCbeamParam ]:

$$\mathcal{L}(t) = \frac{N_b^2 n_b f_{rev} \gamma_r}{4\pi \epsilon_n \beta^*}, \quad (5.2)$$

where  $N_b$  is the number of particles per bunch,  $n_b$  is the number of bunches per beam,  $f_{rev}$  is the revolution frequency,  $\gamma_r$  is the relativistic factor,  $\epsilon_n$  is the normalized transverse beam emittance,  $\beta^*$  is the transverse size of the beam at the IP, and

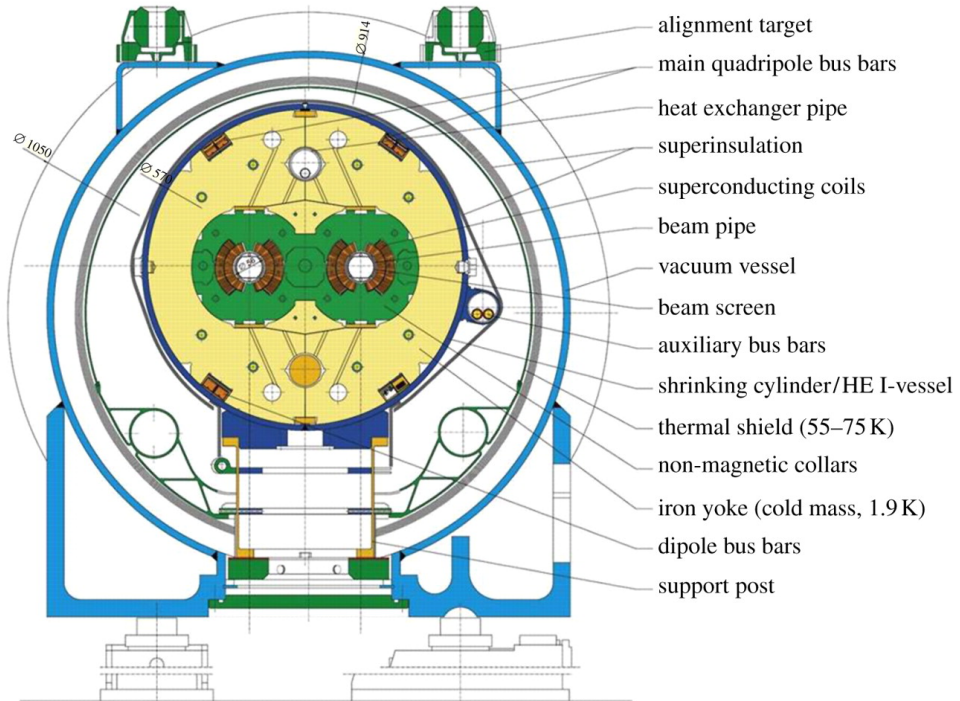


Figure 5.3: An schematic cross sectional view of the LHC dipole magnet.

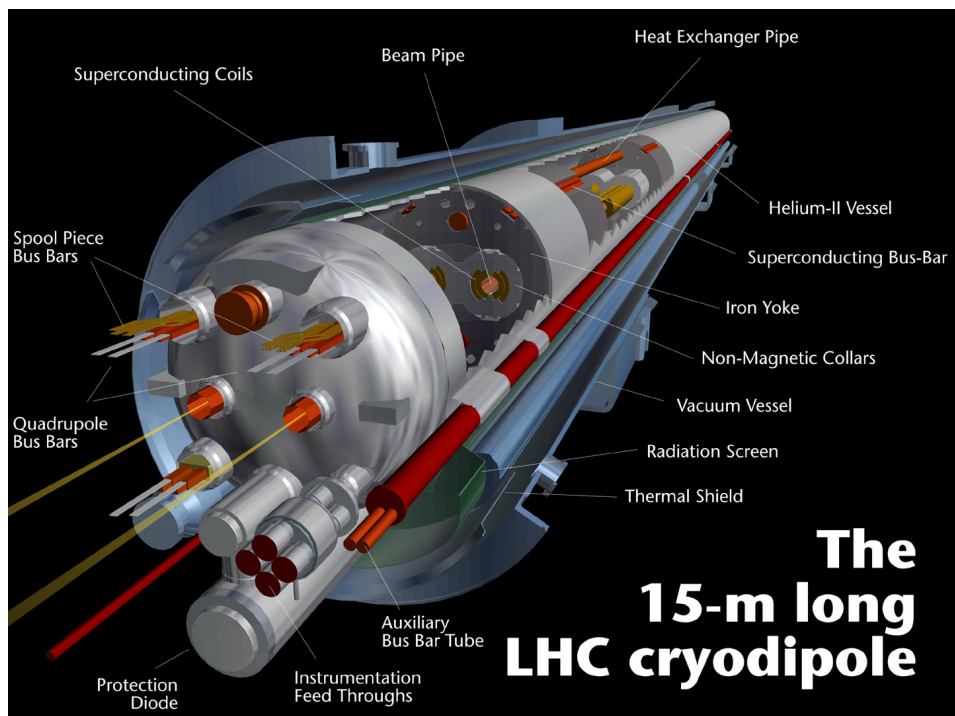


Figure 5.4: An 3D visualization of a LHC dipole magnet.

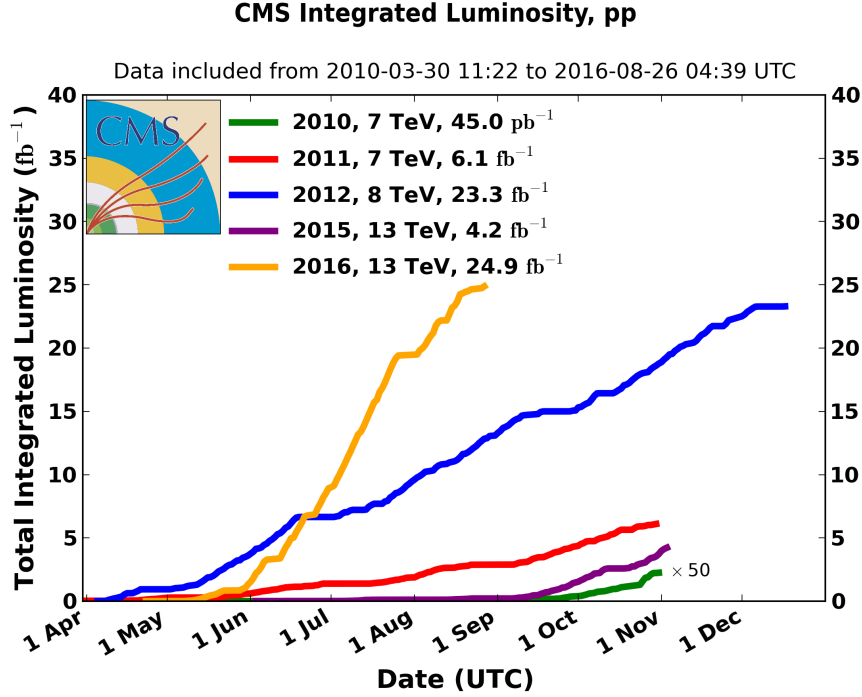


Figure 5.5: Intregated luminosity received by the CMS experiment during the LHC operation.

$F$  is the geometric luminosity reduction factor due to the crossing angle at the IP:

$$F = \left( 1 + \left( \frac{\theta_c \sigma_z}{2\sigma^*} \right) \right)^{-1/2} \quad (5.3)$$

In the last expression,  $\theta_c$  is the full crossing angle at the IP,  $\sigma_z$  is the rms bunch length, and  $\sigma^*$  is the transverse rms beam size at the IP. The designed peak luminosity to be delivered the ATLAS and CMS is  $\mathcal{L}(t) = 10^{34} \text{ cm}^{-2} \text{ s}^{-1}$ . Figure 5.5 shows the integrated luminosity received by the CMS experiment from 2007 to 2016.

*C h a p t e r ~ 6***THE COMPACT MUON SOLENOID EXPERIMENT****6.1 Detector System****6.2 The Compact Muon Solenoid Detector****The Tracker System****The Electromagnetic Calorimeter****The Hadronic Calorimeter****The Superconducting Solenoid****The Muon Chambers****6.3 Physics Object Reconstruction****6.4 Physics Object Reconstruction****Muon Identification****Electron and Photon Identification****Jet Identification****Missing Energy Reconstruction**

## **Part III**

# **Searches for New Physics with the Compact Muon Solenoid Experiment**

## C h a p t e r ~ 7

# SEARCHES FOR DARK MATTER AT THE LHC WITH 8 TEV PP COLLISIONS

## 7.1 Introduction

The existence of dark matter (DM) in the universe, originally proposed [134] to reconcile observations of the Coma galaxy cluster with the prediction from the virial theorem, is commonly accepted as the explanation of many experimental phenomena in astrophysics and cosmology, such as galaxy rotation curves [89, 119], large structure formation [132, 48, 128], and the observed spectrum [125, 37, 126, 15] of the cosmic microwave background [35]. A global fit to cosmological data in the  $\Lambda$ CDM model (also known as the standard model of cosmology) [49] suggests that approximately 85% of the mass of the universe is attributable to DM [15]. To accommodate these observations and the dynamics of colliding galaxy clusters [61], it has been hypothesized that DM is made mostly of weakly interacting massive particles (WIMPs), sufficiently massive to be in nonrelativistic motion following their decoupling from the hot particle plasma in the early stages of the expansion of the universe.

While the standard model (SM) of particle physics does not include a viable DM candidate, several models of physics beyond the SM, e.g., supersymmetry (SUSY) [112, 84, 129, 131, 74] with  $R$ -parity conservation, can accommodate the existence of WIMPs. In these models, pairs of DM particles can be produced in proton-proton (pp) collisions at the CERN LHC. Dark matter particles would not leave a detectable signal in a particle detector. When produced in association with high-energy quarks or gluons, they could provide event topologies with jets and a transverse momentum ( $p_T$ ) imbalance ( $\vec{p}_T^{\text{miss}}$ ). The magnitude of  $\vec{p}_T^{\text{miss}}$  is referred to as missing transverse energy ( $E_T^{\text{miss}}$ ). The ATLAS and CMS collaborations have reported searches for events with one high- $p_T$  jet and large  $E_T^{\text{miss}}$  [14, 56], which are sensitive to such topologies. In this paper, we refer to these studies as monojet searches. Complementary studies of events with high- $p_T$  photons [95, 13];  $W$ ,  $Z$ , or Higgs bosons [8, 9, 11, 10];  $b$  jets [6] and top quarks [6, 91, 123]; and leptons [12, 96] have also been performed.

This paper describes a search for dark matter particles  $\chi$  in events with at least

two jets of comparable transverse momenta and sizable  $E_T^{\text{miss}}$ . The search is based on the razor variables  $M_R$  and  $R^2$  [114, 53]. Given a dijet event, these variables are computed from the two jet momenta  $\vec{p}^{j_1}$  and  $\vec{p}^{j_2}$ , according to the following definition:

$$\begin{aligned} M_R &= \sqrt{(|\vec{p}^{j_1}| + |\vec{p}^{j_2}|)^2 - (p_z^{j_1} + p_z^{j_2})^2}, \\ R &= \frac{M_T^R}{M_R}, \end{aligned} \quad (7.1)$$

with

$$M_T^R = \sqrt{\frac{E_T^{\text{miss}}(p_T^{j_1} + p_T^{j_2}) - \vec{p}_T^{\text{miss}} \cdot (\vec{p}_T^{j_1} + \vec{p}_T^{j_2})}{2}}. \quad (7.2)$$

In the context of SUSY,  $M_R$  provides an estimate of the underlying mass scale of the event, and quantity  $M_T^R$  is a transverse observable that includes information about the topology of the event. The variable  $R^2$  is designed to reduce QCD multijet background; it is correlated with the angle between the two jets, where co-linear jets have large  $R^2$  while back-to-back jets have small  $R^2$ . These variables have been used to study the production of non-interacting particles in cascade decays of heavier partners, such as squarks and gluinos in SUSY models with  $R$ -parity conservation [59, 121]. The sensitivity of these variables to direct DM production was suggested in Ref. [80], where it was pointed out that the dijet event topology provides good discrimination against background processes, with a looser event selection than that applied in the monojet searches. Sensitivity to DM production is most enhanced for large values of  $R^2$ , while categorizing events based on the value of  $M_R$  improves signal to background discrimination and yields significantly improved search sensitivity to a broader and more inclusive class of DM models. The resulting sensitivity is expected to be comparable to that of monojet searches [80, 108]. This strategy also offers the possibility to search for DM particles that couple preferentially to b quarks [18], as proposed to accommodate the observed excess of photons with energies between 1 and 4 GeV in the gamma ray spectrum of the galactic center data collected by the Fermi-LAT gamma-ray space telescope [88]. The results are interpreted using an effective field theory approach and the Feynman diagrams for DM pair production are shown in Fig. 7.1.

Unlike the SUSY razor searches [121, 53], which focus on events with large values of  $M_R$ , this study also considers events with small values of  $M_R$ , using  $R^2$  to

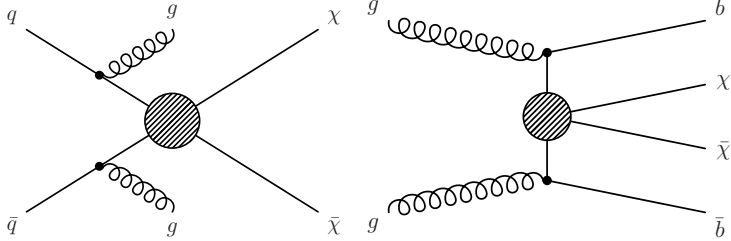


Figure 7.1: Feynman diagrams for the pair production of DM particles corresponding to an effective field theory using a vector or axial-vector operator (left), and a scalar operator (right).

discriminate between signal and background, in a kinematic region ( $R^2 > 0.5$ ) excluded by the baseline selection of Refs. [121, 53].

A data sample corresponding to an integrated luminosity of  $18.8 \text{ fb}^{-1}$  of pp collisions at a center-of-mass energy of 8 TeV was collected by the CMS experiment with a trigger based on a loose selection on  $M_R$  and  $R^2$ . This and other special triggers were operated in 2012 to record events at a rate higher than the CMS computing system could process during data taking. The events from these triggers were stored on tape and their reconstruction was delayed until 2013, to profit from the larger availability of processing resources during the LHC shutdown. These data, referred to as “parked data” [64], enabled the exploration of events with small  $M_R$  values, thereby enhancing the sensitivity to direct DM production.

This paper is organized as follows: the CMS detector is briefly described in Section ???. Section 7.2 describes the data and simulated samples of events used in the analysis. Sections 7.3 and 7.4 discuss the event selections and categorization, respectively. The estimation of the background is described in Section 8.5. The systematic uncertainties are discussed in Section 7.6, while Section 7.7 presents the results and the implications for several models of DM production. A summary is given in Section 7.8.

## 7.2 Data set and simulated samples

The analysis is performed on events with two jets reconstructed at L1 in the central part of the detector ( $|\eta| < 3.0$ ). The L1 jet triggers are based on the sums of transverse energy in regions  $\Delta\eta \times \Delta\phi$  approximately  $1.05 \times 1.05$  in size [51] (where  $\phi$  is the azimuthal angle in the plane transverse to the LHC beams.). At the HLT, energy deposits in ECAL and HCAL are clustered into jets and the razor variables  $R^2$  and  $M_R$  are computed. In the HLT, jets are defined using the FASTJET [46] implementa-

tion of the anti- $k_T$  [47] algorithm, with a distance parameter equal to 0.5. Events with at least two jets with  $p_T > 64\text{ GeV}$  are considered. Events are selected with  $R^2 > 0.09$  and  $R^2 \times M_R > 45\text{ GeV}$ . This selection rejects the majority of the background, which tends to have low  $R^2$  and low  $M_R$  values, while keeping the events in the signal-sensitive regions of the ( $M_R$ ,  $R^2$ ) plane. The trigger efficiency, measured using a pre-scaled trigger with very loose thresholds, is shown in Table 7.1. The requirements described above correspond to the least stringent event selection, given the constraints on the maximum acceptable rate.

Table 7.1: Measured trigger efficiency for different  $M_R$  regions. The selection  $R^2 > 0.35$  is applied. The uncertainty shown represents the statistical uncertainty in the measured efficiency.

$M_R$ region (GeV)	200–300	300–400	400–3500
Trigger efficiency (%)	$91.1 \pm ^{1.5}_{1.7}$	$90.7 \pm ^{2.3}_{2.9}$	$94.4 \pm ^{2.4}_{3.6}$

Monte Carlo (MC) simulated signal and background samples are generated with the leading order matrix element generator **MADGRAPH v5.1.3** [24, 25] and the CTEQ6L parton distribution function set [110]. The generation includes the PYTHIA 6.4.26 [124] Z2\* tune, which is derived from Z1 tune [75] based on the CTEQ5L set. Parton shower and hadronization effects are included by matching the generated events to PYTHIA, using the MLM matching algorithm [87]. The events are processed with a GEANT4 [17] description of the CMS apparatus to include detector effects. The simulation samples for SM background processes are scaled to the integrated luminosity of the data sample ( $18.8\text{ fb}^{-1}$ ), using calculations of the inclusive production cross sections at the next-to-next-to-leading order (NNLO) in the perturbative QCD expansion [83, 82, 69]. The signal processes corresponding to pair production of DM particles are simulated with up to two additional partons with  $p_T > 80\text{ GeV}$ .

### 7.3 Event selection

Events are selected with at least one reconstructed interaction vertex within  $|z| < 24\text{ cm}$ . If more than one vertex is found, the one with the highest sum of the associated track momenta squared is used as the interaction point for event reconstruction. Events containing calorimeter noise, or large missing transverse momentum due to beam halo and instrumental effects (such as jets near non-functioning channels in the ECAL) are removed from the analysis [50].

A particle-flow (PF) algorithm [65, 62] is used to reconstruct and identify individual

particles with an optimized combination of information from the various elements of the CMS detector. The energy of photons is directly obtained from the ECAL measurement, corrected for zero-suppression effects. The energy of electrons is determined from a combination of the electron momentum at the primary interaction vertex as measured by the tracker, the energy of the corresponding ECAL cluster, and the energy sum of all bremsstrahlung photons (or emissions) spatially compatible with originating from the electron track. The energy of muons is obtained from the curvature of the associated track. The energy of charged hadrons is determined from a combination of their momentum measured in the tracker and the matching ECAL and HCAL energy deposits, corrected for zero-suppression effects and for the response function of the calorimeters to hadronic showers. Finally, the energy of neutral hadrons is obtained from the corresponding corrected ECAL and HCAL energies. Contamination of the energy determinations from other pp collisions is mitigated by discarding the charged PF candidates incompatible with originating from the main vertex. Additional energy from neutral particles is subtracted on average when computing lepton (electron or muon) isolation and jet energy. This contribution is estimated as the per-event energy deposit per unit area, in the cone  $\Delta R = \sqrt{(\Delta\eta)^2 + (\Delta\phi)^2} = 0.3$ , times the considered jet size or isolation cone area.

Electrons (muons) are required to have  $p_T > 15$  GeV and  $|\eta| < 2.5$  (2.4). In order to reduce the background from hadrons misidentified as leptons, additional requirements based on the quality of track reconstruction and isolation are applied. Lepton isolation is defined as the scalar  $p_T$  sum of all PF candidates other than the lepton itself, within a cone of size  $\Delta R = 0.3$ , and normalized to the lepton  $p_T$ . A candidate is identified as a lepton if the isolation variable is found to be smaller than 15%. For electrons [93], a characteristic of the shower shape of the energy deposit in the ECAL (the shower width in the  $\eta$  direction) is used to further reduce the contamination from hadrons. PF candidates with  $p_T > 10$  GeV that are not consistent with muons and satisfy the same isolation requirements as those used for electrons are also identified to increase the lepton selection efficiency as well as to identify single-prong tau decays.

Jets are formed by clustering the PF candidates, using the anti- $k_T$  algorithm with distance parameter 0.5. Jet momentum is determined as the vectorial sum of all particle momenta in the jet, and is found from simulation to be within 5% to 10% of the generated hadron level jet momentum over the whole  $p_T$  spectrum and detector acceptance. Jet energy corrections are derived from simulation, and are confirmed

with in situ measurements of the energy balance in dijet and photon+jet events. Additional selection criteria are applied to each event to remove spurious jet-like features originating from isolated noise patterns in certain HCAL regions. We select events containing at least two jets with  $p_T > 80 \text{ GeV}$  and  $|\eta| < 2.4$ , for which the corresponding L1 and HLT requirements are maximally efficient. The combined secondary vertex (CSV) b-tagging algorithm [109, 52] is used to identify jets originating from b quarks. The loose and tight working points of the CSV algorithm, with 85% (10%) and 50% (0.1%) identification efficiency (misidentification probability) respectively, are used to assign the selected events to categories based on the number of b-tagged jets, as described below.

In order to compute the razor variables inclusively, the event is forced into a two-jet topology, by forming two *megajets* [59] out of all the reconstructed jets with  $p_T > 40 \text{ GeV}$  and  $|\eta| < 2.4$ . All possible assignments of jets to the megajets are considered, with the requirement that a megajet consist of at least one jet. The sum of the four-momenta of the jets assigned to a megajet defines the megajet four-momentum. When more than two jets are reconstructed, more than one megajet assignment is possible. We select the assignment that minimizes the sum of the invariant masses of the two megajets. In order to reduce the contamination from multijet production, events are rejected if the angle between the two selected megajets in the transverse plane  $|\Delta\phi(j_1, j_2)|$  is larger than 2.5 radians. The momenta of the two megajets are used to compute the razor variables, according to Eq. (7.1, 7.2). Events are required to have  $M_R > 200 \text{ GeV}$  and  $R^2 > 0.5$ .

#### 7.4 Analysis Strategy

To enhance the DM signal and suppress background contributions from the  $W + \text{jets}$  and  $t\bar{t}$  processes, we veto events with selected electrons, muons, or isolated charged PF candidates. We define three different search regions based on the number of b-tagged jets. The zero b-tag search region contains events where no jets were identified with the CSV loose b-tagging criterion; the one b-tag search region contains events where exactly one jet passed the CSV tight criterion; and the two b-tag search region contains events where two or more jets passed the CSV tight criterion. Events in the zero b-tag search region are further classified into four categories based on the value of  $M_R$ , to enhance signal to background discrimination for a broad class of DM models: (i) *very low*  $M_R$  (VL), defined by  $200 < M_R \leq 300 \text{ GeV}$ ; (ii) *low*  $M_R$  (L), with  $300 < M_R \leq 400 \text{ GeV}$ ; (iii) *high*  $M_R$  (H), with  $400 < M_R \leq 600 \text{ GeV}$ ; and (iv) *very high*  $M_R$  (VH), including events with  $M_R > 600 \text{ GeV}$ . Be-

Table 7.2: Observed yield in each in events with  $0\mu$  and no b-tagged jets for each  $M_R$  category. The number overlapping events between the razor and monojet seaches is also presented.

$M_R$ category	Observed	Monojet & Razor
VL	11623	0
L	3785	3
H	1559	57
VH	261	92

cause of the limited size of the data sample, no further categorization based on  $M_R$  is made for the one and two b-tag search regions. Within each category, the search is performed in bins of the  $R^2$  variable, with the binning chosen such that the expected background yield in each bin is larger than one event, as estimated from Monte Carlo simulation. In the H and VH categories, 3% and 35% respectively of the selected events were also selected in the monojet search [57], which used data from the same running period. The overlap in the L and VL categories is negligible, while the overlapping events in the H and VH categories were shown not to have an impact on the final sensitivity. Consequently, the results from this analysis and from the monojet analysis are largely statistically independent. Table 7.2 shows the events selected by this analysis and the overlapping events with the monojet search.

The main backgrounds in the zero b-tag search region are from the  $W(\ell\nu)+\text{jets}$  and  $Z(\nu\bar{\nu})+\text{jets}$  processes, while the dominant background in the one and two b-tag search regions is the  $t\bar{t}$  process. To estimate the contribution of these backgrounds in the search regions, we use a data-driven method that extrapolates from appropriately selected control regions to the search region, assisted by Monte Carlo simulation. A detailed description of the background estimation method is discussed in Section 8.5.

To estimate the  $W(\ell\nu)+\text{jets}$  and  $Z(\nu\bar{\nu})+\text{jets}$  background in the zero b-tag search region, we define the  $1\mu$  control region by selecting events using identical requirements to those used in the search region, with the exception of additionally requiring one selected muon. Events in this control region are extrapolated to the search region in order to estimate the background. In addition, we define the  $2\mu$  control region, enhanced in the  $Z+\text{jets}$  process, by requiring two selected muons with invariant mass between 80 GeV and 100 GeV. The  $2\mu$  control region is used to perform a cross-check prediction for the  $1\mu$  control region, and the systematic

Table 7.3: Analysis regions for events with zero identified b-tagged jets. The definition of these regions is based on the muon multiplicity, the output of the CSV b-tagging algorithm, and the value of  $M_R$ . For all the regions,  $R^2 > 0.5$  is required.

analysis region	purpose	b-tagging selection	$M_R$ category
$0\mu$	signal search region		$200 < M_R \leq 300$ GeV (VL)
$1\mu$	$W(\ell\nu)$ control region	no CSV loose jet	$300 < M_R \leq 400$ GeV (L) $400 < M_R \leq 600$ GeV (H)
$2\mu$	$Z(\ell\ell)$ control region		$M_R > 600$ GeV (VH)

Table 7.4: Analysis regions for events with identified b-tagged jets. The definition of these regions is based on the muon multiplicity, the output of the CSV b-tagging algorithm, and the value of  $M_R$ . For all the regions,  $R^2 > 0.5$  is required.

analysis region	purpose	b-tagging selection	$M_R$ category
$0\mu bb$		$\geq 2$ CSV tight jets	
$0\mu b$	signal serach region	$= 1$ CSV tight jet	
$1\mu b$	$t\bar{t}$ control region		
$2\mu b$	$t\bar{t}$ control region	$\geq 1$ CSV tight jets	$M_R > 200$ GeV
$Z(\mu\mu)b$	$Z(\ell\ell)$ control region	$\geq 1$ CSV loose jets	

uncertainties in background prediction are estimated based on this comparison.

To estimate the  $t\bar{t}$  background in the one and two b-tag search regions, we define the  $1\mu b$  and  $2\mu b$  control regions, by requiring at least one jet satisfying the CSV tight b-tagging criterion along with one and two selected muons respectively. Both of these control regions are dominated by the  $t\bar{t}$  process. The  $t\bar{t}$  background prediction is estimated by extrapolating from the  $2\mu b$  control region, while the  $1\mu b$  control region is used as a cross-check to estimate systematic uncertainties. Finally, we define the  $Z(\mu\mu)b$  control region by requiring two muons with invariant mass between 80 GeV and 100 GeV. This is used to estimate the  $Z(\nu\bar{\nu})+j$ ets background in the one and two b-tag search regions.

The definitions of the search and control regions, and their use in this analysis are summarized in Tables 7.3 and 7.4.

## 7.5 Background estimation

The largest background contribution to the zero b-tag search region is from events in which a W or Z boson is produced, in association with jets, decaying to final states with one or more neutrinos. These background processes are referred to as  $W(\ell\nu)+j$ ets and  $Z(\nu\bar{\nu})+j$ ets events. Additional backgrounds arise from events

involving the production of top quark pairs, and from events in which a Z boson decays to a pair of charged leptons. These processes are referred to as  $t\bar{t}$  and  $Z(\ell\ell)+\text{jets}$ , respectively. Using simulated samples, the contribution from other SM processes, such as diboson and single top production, is found to be negligible.

The main background in the one and two b-tag search regions comes from  $t\bar{t}$  events. The use of the tight working point of the CSV algorithm reduces the  $Z(\nu\bar{\nu})+\text{jets}$  and  $W(\ell\nu)+\text{jets}$  contribution as shown in Table 7.8. Multijet production, which is the most abundant source of events with jets and unbalanced  $p_T$ , contributes to the search region primarily due to instrumental mismeasurement of the energy of jets. As a result the  $E_T^{\text{miss}}$  direction tends to be highly aligned in the azimuthal coordinate with the razor megajets. The requirement on the razor variables and  $|\Delta\phi(j_1, j_2)|$  reduces the multijet background to a negligible level, which is confirmed by checking data control regions with looser cuts on the razor variables. Figure 7.2 shows the 2-dimensional  $R^2$ - $|\Delta\phi(j_1, j_2)|$  distribution, where it is observed that for  $R^2 > 0.5$  and  $|\Delta\phi(j_1, j_2)| < 2.5$ , the multijet contribution is indeed negligible. Other relevant distributions for the multijet background are shown in Figure 7.3.

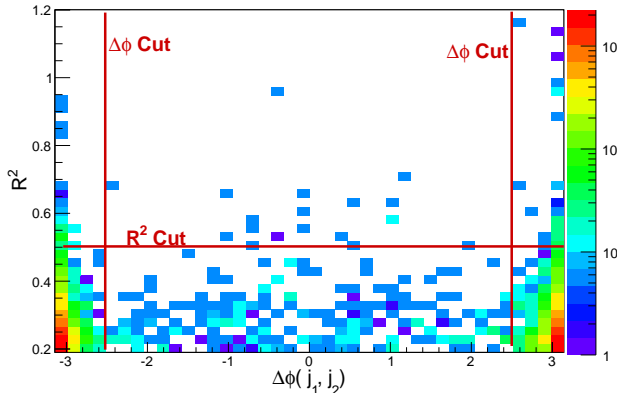


Figure 7.2:  $R^2$ - $\Delta\phi(J_1, J_2)$  distribution for the QCD background in the  $0\mu$  box.

### Background estimation for the zero b-tag search region

To predict the background from  $W(\ell\nu)+\text{jets}$  and  $Z(\nu\bar{\nu})+\text{jets}$  in the zero b-tag search region, we use a data-driven method that extrapolates the observed data yields in the  $1\mu$  control region to the search region. Similarly, the observed yield in the  $2\mu$  control region allows the estimation of the contribution from  $Z(\ell\ell)+\text{jets}$  background process. Each  $M_R$  category is binned in  $R^2$ .

The background expected from  $W$  and  $Z$  boson production, in each  $R^2$  bin and in

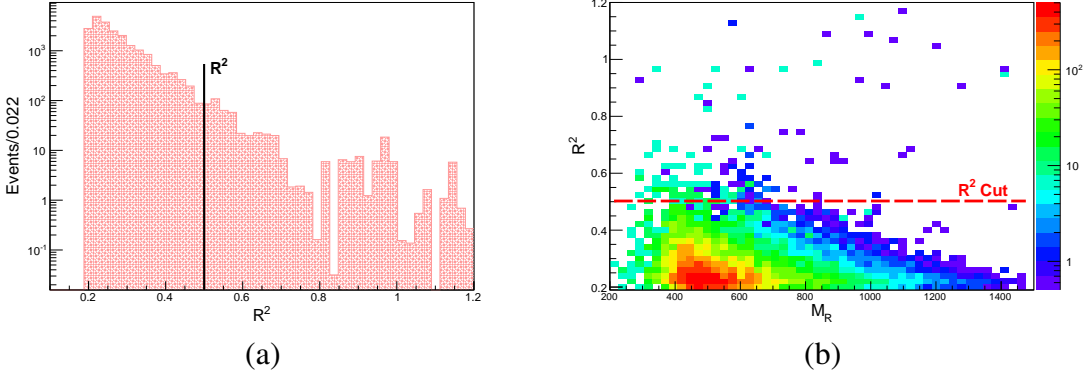


Figure 7.3: (a)  $R^2$  and (b)  $M_R$ - $R^2$  razor distributions for the QCD background in the  $0\mu$  box.

each  $M_R$  category of the  $0\mu$  sample, is computed as

$$n_i^{0\mu} = \left( n_i^{1\mu} - N_i^{\bar{t}\bar{t},1\mu} - N_i^{Z(\ell\ell)+\text{jets},1\mu} \right) \frac{N_i^{W(\ell\nu)+\text{jets},0\mu} + N_i^{Z(\nu\bar{\nu})+\text{jets},0\mu}}{N_i^{W(\ell\nu)+\text{jets},1\mu}} + \left( n_i^{2\mu} - N_i^{\bar{t}\bar{t},2\mu} \right) \frac{N_i^{Z(\ell\ell)+\text{jets},0\mu}}{N_i^{Z(\ell\ell)+\text{jets},2\mu}}, \quad (7.3)$$

where  $n_i^{k\mu}$  labels the data yield in bin  $i$  for the sample with  $k$  muons, and  $N_i^{X,k\mu}$  indicates the corresponding yield for process  $X$ , derived from simulations. This background estimation method relies on the assumption that the kinematic properties of events in which  $W$  and  $Z$  bosons are produced are similar.

To estimate the accuracy of the background estimation method, we perform a cross-check by predicting the background in the  $1\mu$  control region using the observed data yield in the  $2\mu$  control region. The Monte Carlo simulation is used to perform this extrapolation analogous to the calculation in Equation 7.3. The small contribution from the  $t\bar{t}$  background process is also estimated using the simulated samples. In Tables 7.5 and 7.6, the observed yields in the  $1\mu$  and  $2\mu$  control regions respectively are compared to the estimate derived from data. In Tables 7.5-7.10, the contribution of each process as predicted directly by simulated samples are also given.

Figure 7.4 shows the comparison of the  $R^2$  distributions between the observed yield and the data-driven background estimate in the  $1\mu$  control region. The observed bin-by-bin difference is propagated as a systematic uncertainty in the data-driven background method, and accounts for the statistical uncertainty in the event yield in the  $2\mu$  control region data as well as potential differences in the modeling of the recoil spectra between  $W+\text{jets}$  and  $Z+\text{jets}$  processes. Some bins exhibit relatively large uncertainties primarily due to statistical fluctuations in the  $2\mu$  control region from which the background is prediction estimated. Though the uncertainties are

Table 7.5: Comparison of the observed yield in the  $1\mu$  control region in each  $M_R$  category and the corresponding data-driven background estimate obtained by extrapolating from the  $2\mu$  control region. The uncertainty in the estimates takes into account both the statistical and systematic components. The contribution of each individual background process is also shown, as estimated from simulated samples, as well as the total MC predicted yield.

$M_R$ category	$Z(\nu\bar{\nu})+\text{jets}$	$W(\ell\nu)+\text{jets}$	$Z(\ell\ell)+\text{jets}$	$t\bar{t}$	MC predicted	Estimated	Observed
VL	$0.7 \pm 0.3$	$4558 \pm 32$	$133 \pm 3$	$799 \pm 9$	$5491 \pm 33$	$5288 \pm 511$	5926
L	$0.5 \pm 0.3$	$1805 \pm 17$	$44 \pm 2$	$213 \pm 4$	$2063 \pm 18$	$1840 \pm 233$	2110
H	$0.1 \pm 0.1$	$915 \pm 11$	$16 \pm 1$	$66 \pm 2$	$997 \pm 11$	$629 \pm 240$	923
VH	<0.1	$183 \pm 5$	$2.6 \pm 0.2$	$8.5 \pm 0.8$	$194 \pm 5$	$166 \pm 93$	143

Table 7.6: Comparison of the observed yield for the  $2\mu$  control region in each  $M_R$  category and the corresponding prediction from background simulation. The quoted uncertainty in the prediction reflects only the size of the simulated sample. The contribution of each individual background process is also shown, as estimated from simulated samples.

$M_R$ category	$Z(\nu\bar{\nu})+\text{jets}$	$W(\ell\nu)+\text{jets}$	$Z(\ell\ell)+\text{jets}$	$t\bar{t}$	MC predicted	Observed
VL	<0.1	<0.1	$214 \pm 4$	$1.9 \pm 0.3$	$215 \pm 4$	207
L	<0.1	$0.4 \pm 0.3$	$88 \pm 2$	$0.5 \pm 0.2$	$89 \pm 2$	78
H	<0.1	$0.1 \pm 0.1$	$48 \pm 1$	$0.1 \pm 0.1$	$48 \pm 1$	30
VH	<0.1	<0.1	$10 \pm 1$	$0.1 \pm 0.1$	$10 \pm 1$	7

rather large in fractional terms, sensitivity to DM signal models is still obtained, because of the enhanced signal to background ratio for the bins at large values of  $M_R$  and  $R^2$ .

The  $t\bar{t}$  background is estimated using an analogous data-driven method, where we derive corrections to the Monte Carlo simulation prediction scaled to the  $t\bar{t}$  production cross-section computed to NNLO accuracy [83, 82, 69] using data in the  $2\mu b$  control region for each bin in  $R^2$ . The correction is then applied to the simulation prediction for the  $t\bar{t}$  background contribution to the zero b-tag search region. This correction factor reflects potential mismodeling of the recoil spectrum predicted by the Monte Carlo simulation. The contribution of each background process to the  $2\mu b$  sample, predicted from simulated samples, is given in Table 7.7. The fraction of  $t\bar{t}$  events in the  $2\mu b$  control sample is  $\approx 95\%$ . Figure 7.5 shows the comparison of the observed yield and the prediction from simulation, as a function of  $R^2$ . We observe no significant deviations between the observed data and the simulation prediction. The uncertainty derived from the data-to-simulation correction factor is propagated to the systematic uncertainty of the  $t\bar{t}$  prediction in the zero b-tag search region.

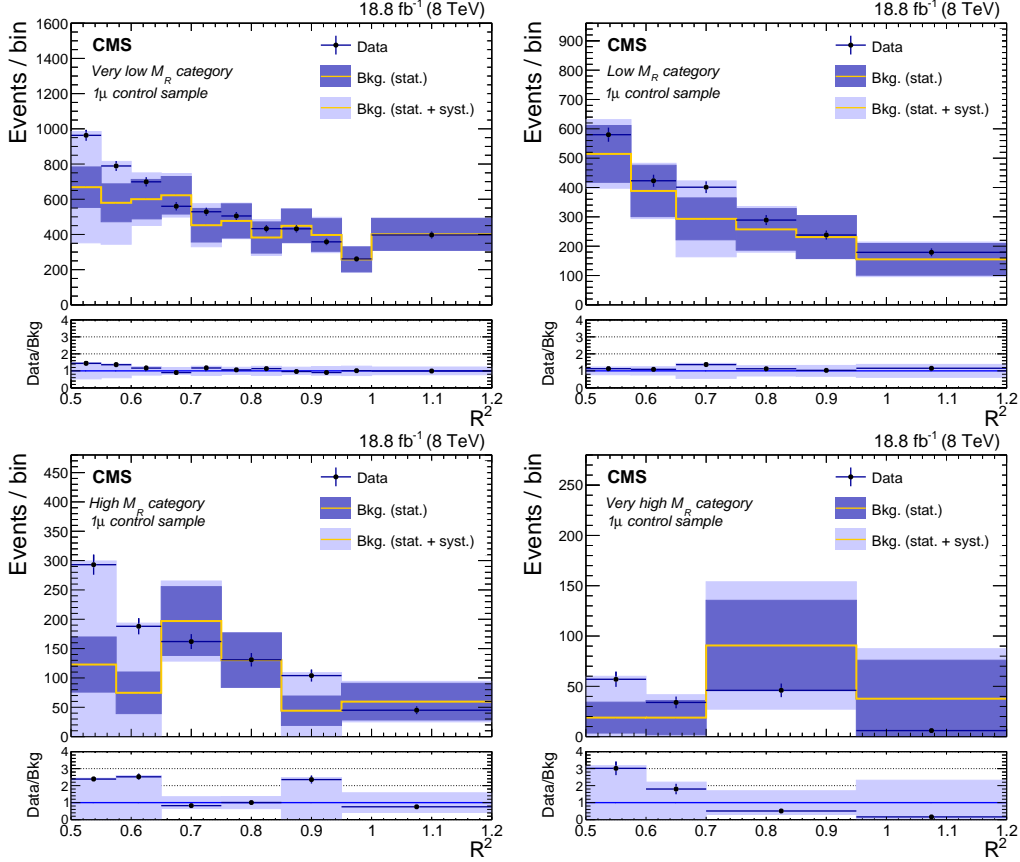


Figure 7.4: Comparison of observed yields in the  $1\mu$  control region and the data-driven background estimate derived from the  $2\mu$  control region data in the four  $M_R$  categories: VL (top left), L (top right), H (bottom left), and VH (bottom right). The bottom panel in each plot shows the ratio between the two distributions. The observed bin-by-bin deviation from unity is interpreted as an estimate of the systematic uncertainty associated to the background estimation methodology for the  $0\mu$  search region. The dark and light bands represent the statistical and the total uncertainties in the estimates, respectively. The horizontal bars indicate the variable bin widths.

Table 7.7: Observed yield and predicted background from simulated samples in the  $2\mu b$  control region. The quoted uncertainty in the prediction only reflects the size of the simulated sample. The contribution of each individual background process is also shown, as estimated from simulated samples.

Sample	$Z(\nu\bar{\nu})+\text{jets}$	$W(\ell\nu)+\text{jets}$	$Z(\ell\ell)+\text{jets}$	$t\bar{t}$	MC predicted	Observed
$2\mu b$	<0.1	$0.1 \pm 0.1$	$2.2 \pm 0.3$	$58 \pm 2$	$60 \pm 2$	60

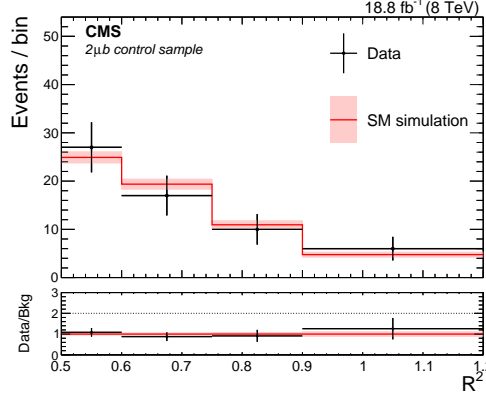


Figure 7.5: Comparison of the observed yield and the prediction from simulation as a function of  $R^2$  in the  $2\mu b$  control region. The uncertainties in the data and the simulated sample are represented by the vertical bars and the shaded bands, respectively. The horizontal bars indicate the variable bin widths.

Table 7.8: Comparison of the observed yields for the zero b-tag search region in each  $M_R$  category and the corresponding background estimates. The uncertainty in the background estimate takes into account both the statistical and systematic components. The contribution of each individual background process is also shown, as estimated from simulated samples, as well as the total MC predicted yield.

$M_R$ category	$Z(v\bar{v}) + \text{jets}$	$W(\ell\nu) + \text{jets}$	$Z(\ell\ell) + \text{jets}$	$t\bar{t}$	MC predicted	Estimated	Observed
VL	$6231 \pm 37$	$4820 \pm 33$	$49 \pm 2$	$555 \pm 7$	$11655 \pm 50$	$12770 \pm 900$	11623
L	$2416 \pm 19$	$1513 \pm 16$	$11 \pm 1$	$104 \pm 3$	$4044 \pm 25$	$4170 \pm 270$	3785
H	$1127 \pm 7$	$625 \pm 9$	$2.9 \pm 0.3$	$24 \pm 1$	$1779 \pm 12$	$1650 \pm 690$	1559
VH	$229 \pm 2$	$103 \pm 3$	$0.2 \pm 0.1$	$3.1 \pm 0.5$	$335 \pm 3$	$240 \pm 160$	261

The result of the background estimation in the zero b-tag search region is given in Table 7.8, where it is compared to the observed yields in data. The uncertainty in the background estimates takes into account both the statistical and systematic components. The comparison of the data-driven background estimates and the observations for each  $M_R$  category is shown in Fig. 7.6, as a function of  $R^2$ . The expected event distribution is shown for two signal benchmark models, corresponding to the pair production of DM particles of mass 1 GeV in the effective field theory (EFT) approach with vector coupling to u or d quarks. Details on the signal benchmark models are given in Section 7.7.

### Background estimation for the $0\mu b$ and $0\mu bb$ samples

A similar data-driven technique is used to determine the expected background for the one and two b-tag search regions. The background from  $t\bar{t}$  events for each  $R^2$

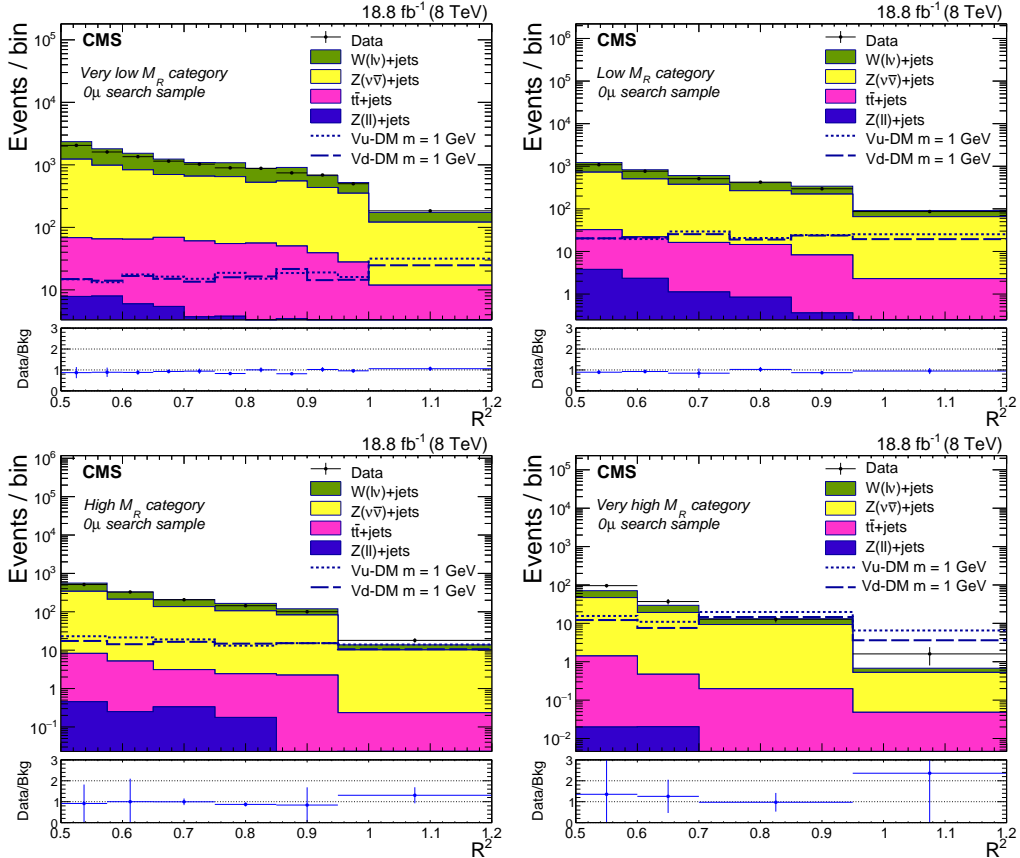


Figure 7.6: Comparison of the observed yield in the zero b-tag control region and the background estimates in the four  $M_R$  categories: VL (top left), L (top right), H (bottom left), and VH (bottom right). The contribution of individual background processes is shown by the filled histograms. The bottom panels show the ratio between the observed yields and the total background estimate. For reference, the distributions from two benchmark signal models are also shown, corresponding to the pair production of DM particles of mass 1 GeV in the EFT approach with vector coupling to u or d quarks. The horizontal bars indicate the variable bin widths.

Table 7.9: Comparison of the observed yields in the  $Z(\mu\mu)b$  and  $1\mu b$  samples, the corresponding predictions from background simulation, and (for  $1\mu b$  only) the cross-check background estimate. The contribution of each individual background process is also shown, as estimated from simulated samples.

Sample	$Z(v\bar{v})+{\rm jets}$	$W(\ell\nu)+{\rm jets}$	$Z(\ell\ell)+{\rm jets}$	$t\bar{t}$	MC predicted	Estimated	Observed
$Z(\mu\mu)b$	<0.1	<0.1	$134 \pm 3$	$17 \pm 1$	$151 \pm 3$	—	175
$1\mu b$	$0.2 \pm 0.1$	$279 \pm 7$	$11 \pm 1$	$3038 \pm 17$	$3328 \pm 18$	$3410 \pm 540$	2920

bin in the one b-tag search region,  $n(t\bar{t})_i^{0\mu b}$ , is computed as:

$$n(t\bar{t})_i^{0\mu b} = (n(t\bar{t})_i^{2\mu b} - N_i^{Z(\ell\ell)+{\rm jets}, 2\mu b} - N_i^{W(\ell\nu)+{\rm jets}, 2\mu b}) \frac{N(t\bar{t})_i^{0\mu b}}{N(t\bar{t})_i^{2\mu b}} \quad (7.4)$$

where  $n(t\bar{t})_i^{2\mu b}$  is the observed yield in the  $i$ th  $R^2$  bin in the  $2\mu b$  control region, while  $N(t\bar{t})_i^{0\mu b}$  and  $N(t\bar{t})_i^{2\mu b}$  are the  $t\bar{t}$  yields in the  $i$ th  $R^2$  bin predicted by the simulation for the one b-tag search region and the  $2\mu b$  control region respectively. Similarly, the  $t\bar{t}$  background in the two b-tag search region is derived from Eq. (7.4), replacing  $N(t\bar{t})_i^{0\mu b}$  with  $N(t\bar{t})_i^{0\mu bb}$ , the  $t\bar{t}$  background yield in the  $i$ th bin of the two b-tag search region predicted by the simulation. The data yield in the  $2\mu b$  control region is corrected to account for the small contamination from  $Z+{\rm jets}$  and  $W+{\rm jets}$ , predicted with the simulated yields  $N_i^{Z(\ell\ell)+{\rm jets}, 2\mu b}$  and  $N_i^{W(\ell\nu)+{\rm jets}, 2\mu b}$ , respectively.

The background contribution from  $W(\ell\nu)+{\rm jets}$  and  $Z(v\bar{v})+{\rm jets}$  events is predicted using the  $Z(\mu\mu)b$  control region, and summarized in Table 7.9. The  $Z+{\rm jets}$  purity of this control region is  $\approx 89\%$ . The observed yield in the  $Z(\mu\mu)b$  control region is shown in the left plot of Fig. 7.7, as a function of  $R^2$ , along with the Monte Carlo simulation prediction. The uncertainty on the simulation prediction accounts only for the statistical uncertainty of the simulated sample. This contribution, scaled by the ratio of the predicted  $V+{\rm jets}$  background in the search regions to that in the control region, obtained from simulation, provides an estimate for each  $R^2$  bin.

We perform a cross-check of the method on the  $1\mu b$  control region by predicting the background from the  $2\mu b$  control region data. The data and prediction are compared on the right of Fig. 7.7, where we observe reasonable agreement. The difference between the prediction and the observed data in this cross-check region is propagated as a systematic uncertainty of the method.

The estimated background in the one and two b-tag search regions is given in Table 7.10 and shown in Fig. 7.8, where it is compared to the observed yields in data.

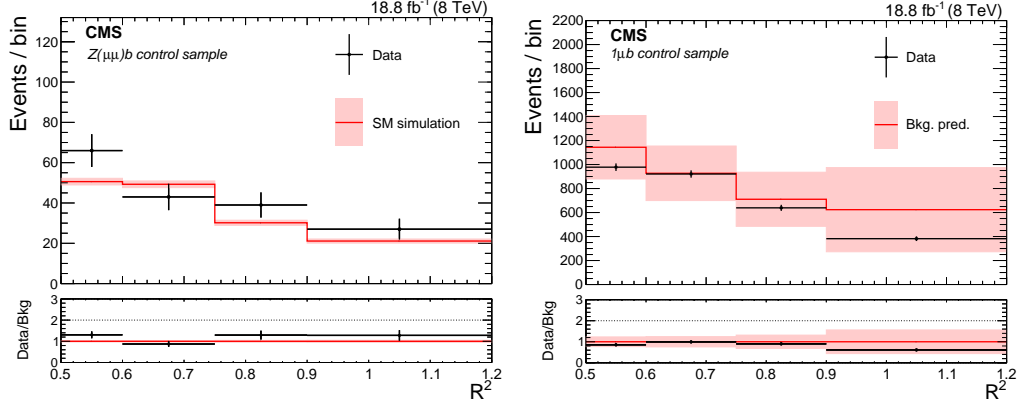


Figure 7.7: Comparison of the observed yield and the prediction from simulation in the  $Z(\mu\mu)b$  control sample (left) and of the observed yield in the  $1\mu b$  control sample and the background estimates from the  $2\mu b$  and  $Z(\mu\mu)b$  control samples (right), shown as a function of  $R^2$ . The bottom panel of each figure shows the ratio between the data and the estimates. The shaded bands represent the statistical uncertainty in the left plot, and the total uncertainty in the right plot. The horizontal bars indicate the variable bin widths.

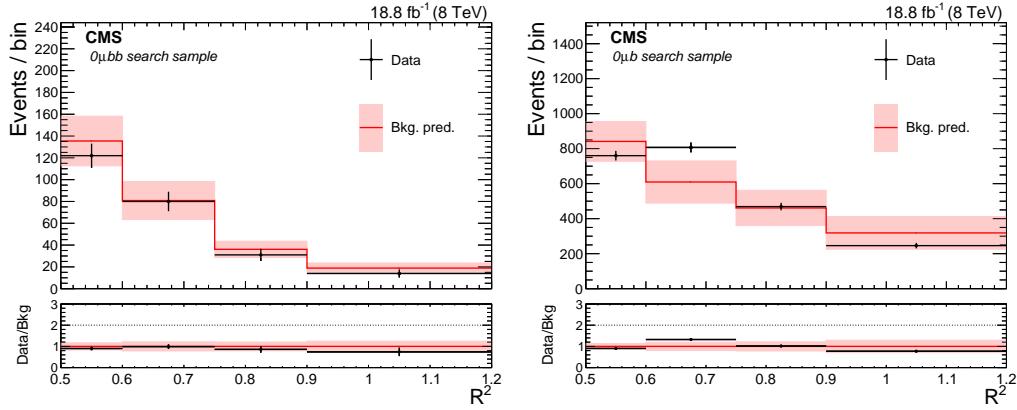


Figure 7.8: Comparison of observed event yields and background estimates as a function of  $R^2$ , for the one (left) and two (right) b-tag search regions. The shaded bands represent the total uncertainty in the estimate. The horizontal bars indicate the variable bin widths.

The uncertainty in the estimates take into account both the statistical and systematic components.

## 7.6 Systematic uncertainties

For each  $R^2$  bin in each  $M_R$  category, the difference between the observed and estimated yields in the crosscheck analysis (see Section 8.5) is taken as the estimate of the uncertainty associated with the method. The uncertainty is found to be typically

Table 7.10: Comparison of the observed yield for events in the one and two b-tag search regions and the corresponding background estimates. The uncertainty in the estimates takes into account both the statistical and systematic components. The contribution of each individual background process is also shown, as estimated from simulated samples, as well as the total MC predicted yield.

Sample	$Z(\nu\bar{\nu})+\text{jets}$	$W(\ell\nu)+\text{jets}$	$Z(\ell\ell)+\text{jets}$	$t\bar{t}$	MC predicted	Estimated	Observed
$0\mu\text{bb}$	$44 \pm 3$	$14 \pm 2$	$0.2 \pm 0.1$	$204 \pm 4$	$262 \pm 5$	$271 \pm 37$	247
$0\mu\text{b}$	$417 \pm 8$	$216 \pm 7$	$2.4 \pm 0.4$	$1480 \pm 12$	$2115 \pm 16$	$2230 \pm 280$	2282

$\approx 20\text{--}40\%$ , depending on the considered bin in the ( $M_R$ ,  $R^2$ ) plane. Other sources of systematic uncertainties such as the modeling of the jet energy scale correction, and the initial-state radiation in the event are found to be negligible compared to the systematic from the cross-check. Figures 7.9 and 7.10 show the individual systematic uncertainties just mentioned and the systematic uncertainty from the cross-check.

The largest systematic uncertainty arises from the crosscheck analysis. This uncertainty is affected by statistical fluctuations from the limited number of selected events in the  $2\mu$  control region. This uncertainty covers the differences in the modeling of the recoil spectra between  $W+\text{jets}$  and  $Z+\text{jets}$  processes as well as the cross section uncertainties.

For the  $0\mu$  analysis, differences between the kinematic properties of  $W+\text{jets}$  and  $Z+\text{jets}$  events are additional sources of systematic uncertainty. These differences arise from the choice of the PDF set, jet energy scale corrections, b tagging efficiency corrections, and trigger efficiency. These effects largely cancel when taking the ratio of the two processes, and the resulting uncertainty is found to be smaller than one fifth of the total uncertainty. The quoted uncertainty is an upper estimate of the total systematic uncertainty.

For the  $0\mu\text{b}$  and  $0\mu\text{bb}$  samples, both the signal and control samples are dominated by  $t\bar{t}$  events. The cancellation of the systematic uncertainties is even stronger in this case, since it does not involve different processes, and different PDFs. The remaining uncertainty is dominated by the contribution arising from the small size of the control sample.

Systematic uncertainties in the signal simulation originate from the choice of the PDF set, the jet energy scale correction, the modeling of the initial-state radiation in the event generator, and the uncertainty in the integrated luminosity. The luminosity uncertainty changes the signal normalization while the other uncertainties also modify the signal shape. These effects are taken into account by propagat-

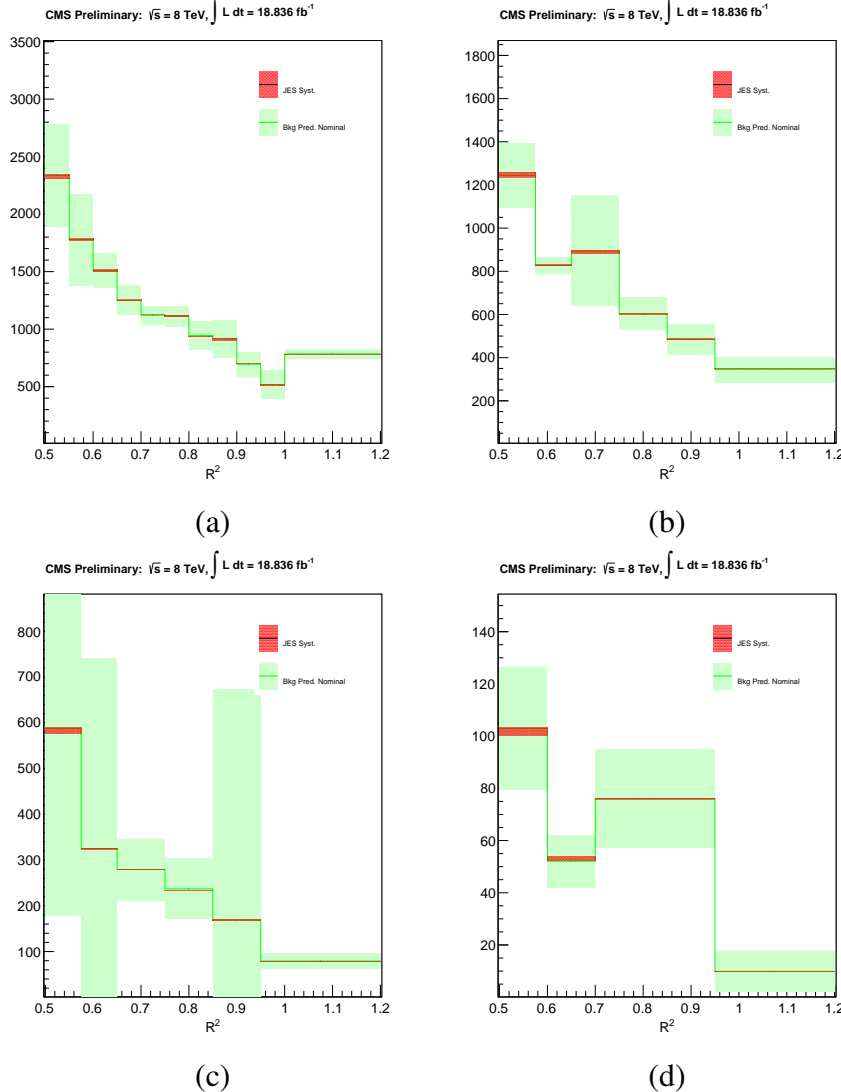


Figure 7.9: Total (estimated using the cross-check analysis) and JES systematic uncertainties. The green band corresponds to the systematic uncertainty associated with the background prediction method, while the red band corresponds to the JES systematic only. Panels (a) and (b) show the VL and L  $M_R$  categories, respectively. Panels (c) and (d) show the H and VH  $M_R$  categories, respectively.

ing these uncertainties into the  $M_R$  category and the  $R^2$  bin. Figures 7.11, 7.12, and 7.13 show the PDF, jet energy scale, and the initial-state radiation systematic uncertainties for a vector-mediated EFT signal model with DM mass of 700 GeV, respectively. These uncertainties are considered to be fully correlated across  $M_R$  categories and  $R^2$  bins. Typical values for the individual contributions are given in Table 7.11. The total uncertainty in the signal yield is obtained by propagating the individual effects into the  $M_R$  and  $R^2$  variables and comparing the bin-by-bin

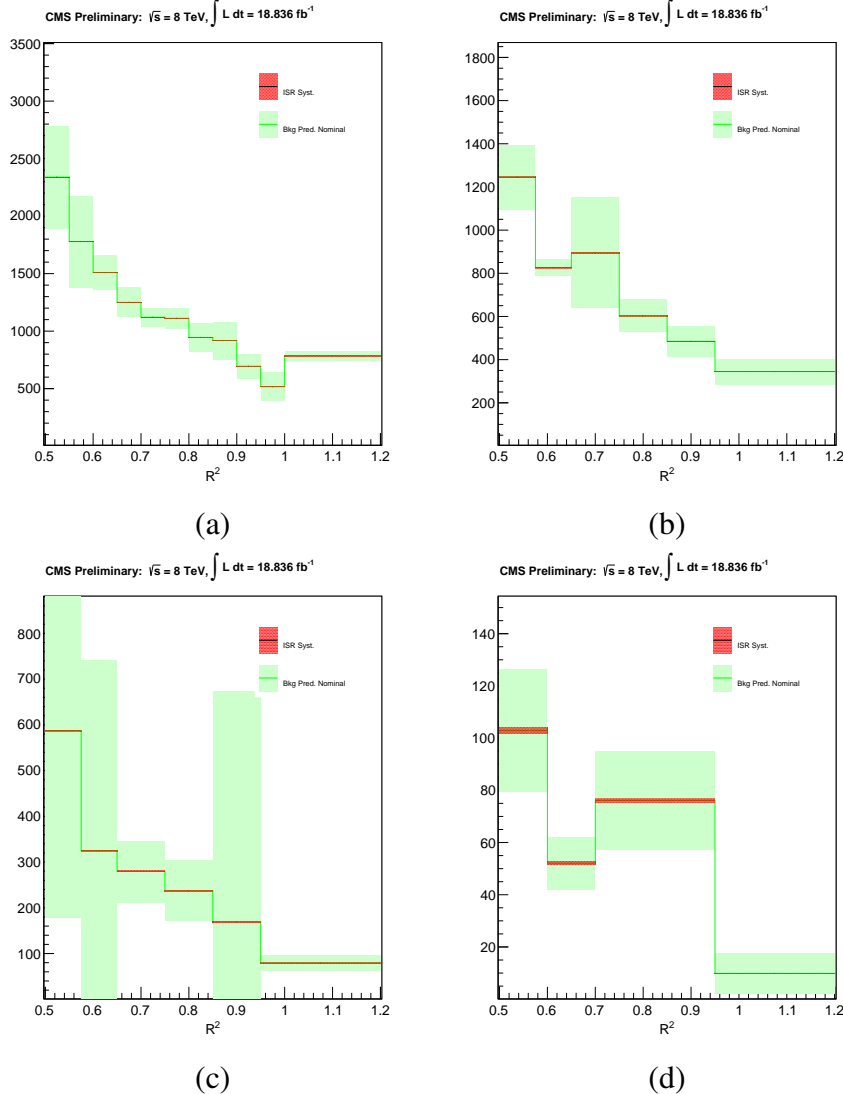


Figure 7.10: Total (estimated using the cross-check analysis) and ISR systematic uncertainties. The green band corresponds to the systematic uncertainty associated with the background prediction method, while the red band corresponds to the ISR systematic only. Panels (a) and (b) show the VL and L  $M_R$  categories, respectively. Panels (c) and (d) show the H and VH  $M_R$  categories, respectively.

variations with respect to the central value of the prediction based on simulation. In the particular case of the uncertainties due to the choice of the PDF set we have followed the PDF4LHC [40, 23, 39] prescription, using the CTEQ-6.6[106] and MRST-2006-NNLO [103] PDF sets.

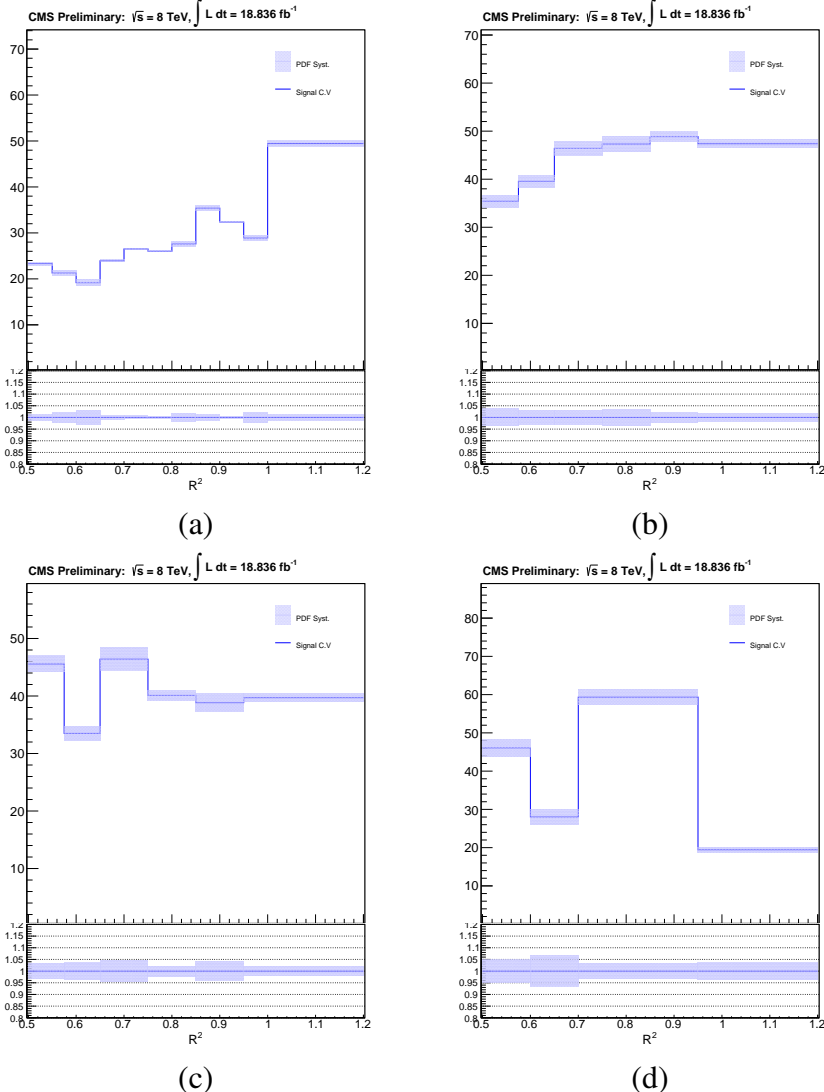


Figure 7.11: PDF systematic uncertainty for a vector mediated EFT signal model with DM mass = 700 GeV. The blue band corresponds to the systematic error associated with PDF uncertainty. Panels (a) and (b) show the VL and L  $M_R$  categories, respectively. Panels (c) and (d) show the H and VH  $M_R$  categories, respectively.

## 7.7 Results and interpretation

In Figs. 7.6 and 7.8 the estimated backgrounds are compared to the observed yield in each  $M_R$  region, for events without and with b-tagged jets, respectively. The background estimates agree with the observed yields, within the uncertainties. This result is interpreted in terms of exclusion limits for several models of DM production.

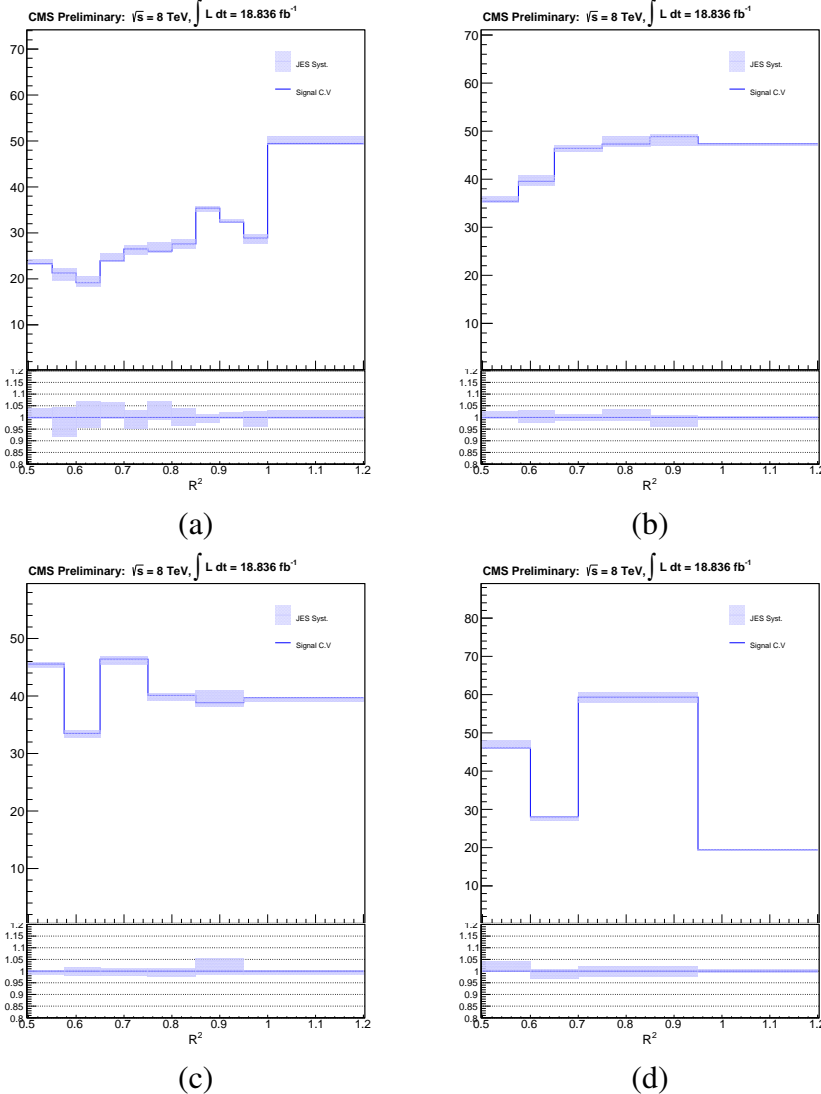


Figure 7.12: JES systematic uncertainty for a vector mediated EFT signal model with DM mass = 700 GeV. The blue band corresponds to the systematic error associated with JES uncertainty. Panels (a) and (b) show the VL and L  $M_R$  categories, respectively. Panels (c) and (d) show the H and VH  $M_R$  categories, respectively.

### Limits on dark matter production from the $0\mu$ sample

The result is interpreted in the context of a low-energy effective field theory, in which the production of DM particles is mediated by six or seven dimension operators [36, 34]. This choice allows the results be compared with those of previous analyses [14, 56], and shows that a similar sensitivity is achieved.

Operators of dimension six and seven are generated assuming the existence of a heavy particle, mediating the interaction between the DM and SM fields. To de-

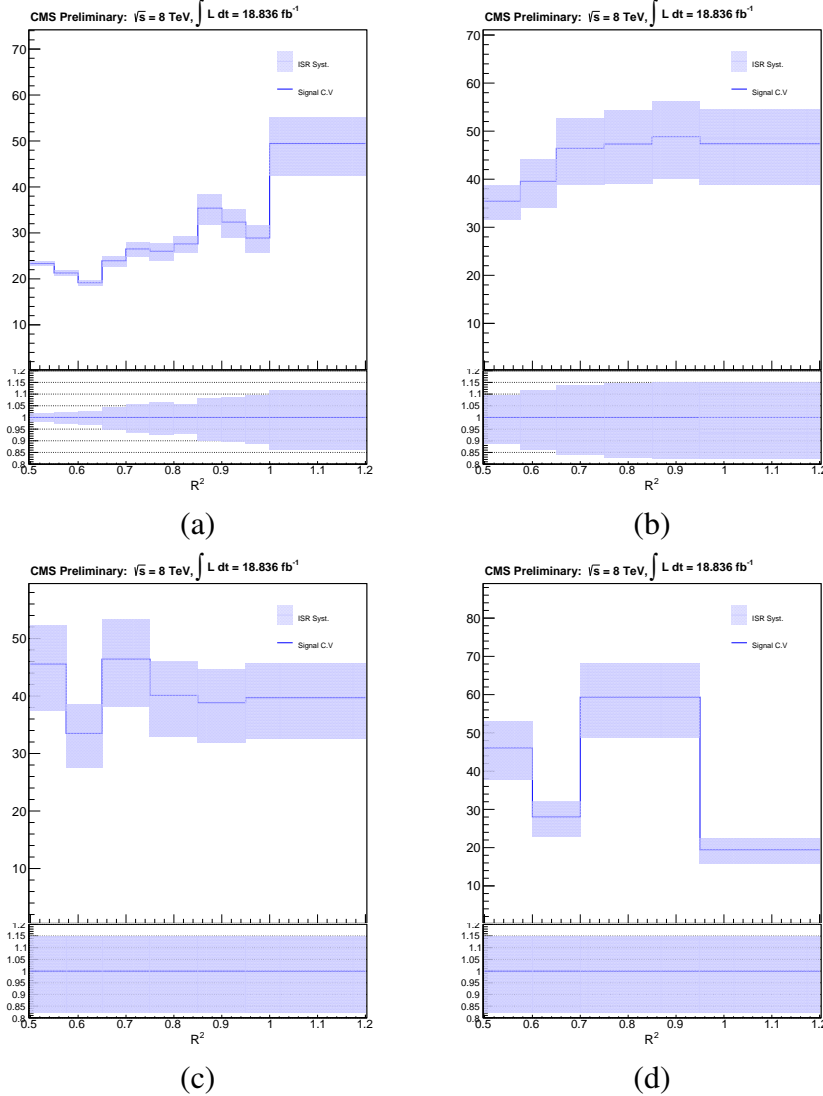


Figure 7.13: ISR systematic uncertainty for a vector mediated EFT signal model with DM mass = 700 GeV. The blue band corresponds to the systematic error associated with ISR uncertainty. Panels (a) and (b) show the VL and L  $M_R$  categories, respectively. Panels (c) and (d) show the H and VH  $M_R$  categories, respectively.

scribe DM production as a local interaction, the propagator of the heavy mediator is expanded through an operator product expansion. The nature of the mediator determines the nature of the effective interaction. Two benchmark scenarios are considered in this study, axial-vector (AV), and vector (V) interactions [79], described by the following operators:

$$\hat{O}_{AV} = \frac{1}{\Lambda^2} (\bar{\chi} \gamma^\mu \gamma_5 \chi) (\bar{q} \gamma_\mu \gamma_5 q) ; \quad \hat{O}_V = \frac{1}{\Lambda^2} (\bar{\chi} \gamma^\mu \chi) (\bar{q} \gamma_\mu q) . \quad (7.5)$$

Here  $\gamma_\mu$  and  $\gamma_5$  are the Dirac matrices,  $\chi$  is the DM field, and  $q$  is an SM quark

Table 7.11: Systematic uncertainties associated with the description of the DM signal. The values indicated represent the typical size. The dependence of these systematic uncertainties on the  $R^2$  and  $M_R$  values is taken into account in the determination of the results.

Effect	Uncertainty
Jet energy scale	3–6%
Luminosity	2.6%
Parton distribution functions	3–6%
Initial-state radiation	8–15%

field. The DM particle is assumed to be a Dirac fermion where both operators will contribute in the low-energy theory, while in the case of a Majorana DM particle the vector coupling  $\hat{O}_V$  will vanish in the low-energy theory. Below the cutoff energy scale  $\Lambda$ , DM production is described as a contact interaction between two quarks and two DM particles. In the case of  $s$ -channel production through a heavy mediator, the energy scale  $\Lambda$  is identified with  $M/g_{\text{eff}}$ , where  $M$  is the mediator mass and  $g_{\text{eff}} = \sqrt{g_q g_\chi}$  is an effective coupling, determined by the coupling of the mediator to quark and DM fields,  $g_q$  and  $g_\chi$ , respectively.

The results in Tables 7.15-7.18 in the Appendix are used to obtain an upper limit at 90% confidence level (CL) on the DM production cross section,  $\sigma_{\text{UL}}^i$  (where the superscript denotes the coupling to an up or down quark). The limits are obtained using the LHC CL<sub>s</sub> procedure [33, 67] and a global likelihood determined by combining the likelihoods of the different search categories. Each systematic uncertainty (see Section 7.6) is incorporated in the likelihood with a dedicated nuisance parameter, whose value is not known a priori but rather must be estimated from the data.

Subsequently, the cross section ( $\sigma_{\text{UL}}^i$ ) limit is translated into a lower limit  $\Lambda_{\text{LL}}$  on the cutoff scale, through the relation:

$$\Lambda_{\text{LL}} = \Lambda_{\text{GEN}} \left( \frac{\sigma_{\text{GEN}}}{\sigma_{\text{UL}}} \right)^{\frac{1}{4}}. \quad (7.6)$$

Here  $\Lambda_{\text{GEN}}$  and  $\sigma_{\text{GEN}}$  are the cutoff energy scale and cross section of the simulated sample, respectively. The derived values of  $\Lambda_{\text{LL}}$  as a function of the DM mass, shown in Fig. 7.14, are comparable to those derived for the CMS monojet search [57]. The exclusion limits on  $\Lambda$  weaken at large DM masses since the cross section for DM production is reduced. The analysis has been repeated removing the events also selected by the monojet search. The reduction in background yields due

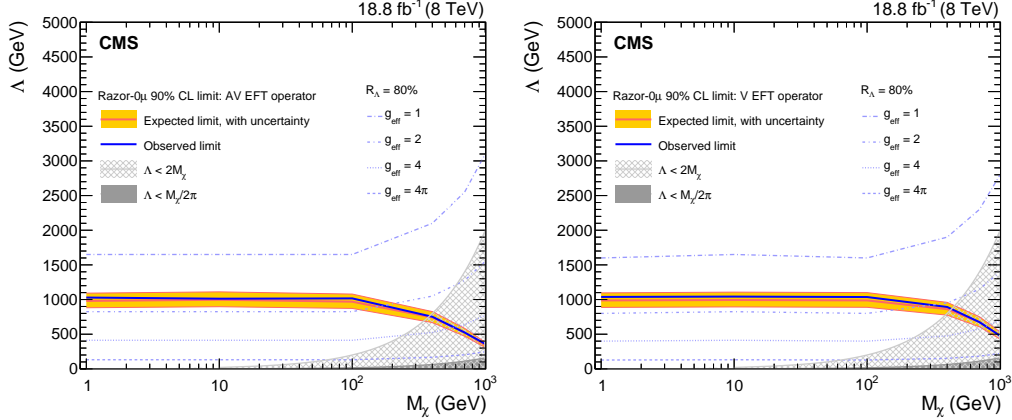


Figure 7.14: Lower limit at 90% CL on the cutoff scale  $\Lambda$  as a function of the DM mass  $M_\chi$  in the case of axial-vector (left) and vector (right) currents. The validity of the EFT is quantified by  $R_\Lambda = 80\%$  contours, corresponding to different values of the effective coupling  $g_{\text{eff}}$ . For completeness, regions forbidden by the EFT validity condition  $\Lambda > 2M_\chi/g_{\text{eff}}$  are shown for two choices of the effective coupling:  $g_{\text{eff}} = 1$  (light gray) and  $g_{\text{eff}} = 4\pi$  (dark gray).

to this additional requirement compensates for the reduction in signal efficiency, resulting in a negligible difference in the exclusion limit on  $\Lambda$ .

The EFT framework provides a benchmark scenario to compare the sensitivity of this analysis with that of previous searches for similar signatures. However, the validity of an EFT approach is limited at the LHC because a fraction of events under study are generated at a  $\sqrt{s}$  comparable to the cutoff scale  $\Lambda$  [85, 34, 81, 41]. For theories to be perturbative,  $g_{\text{eff}}$  is typically required to be smaller than  $4\pi$ , and this condition is unlikely to be satisfied for the entire region of phase space probed by the collider searches. In addition, the range of values for the couplings being probed within the EFT may be unrealistically large. Following the study presented in Refs. [42, 43, 44], we quantify this effect through two EFT validity measures. The first is a minimal kinematic constraint on  $\Lambda$  obtained by requiring  $Q_{\text{tr}} < g_{\text{eff}}\Lambda$  and  $Q_{\text{tr}} > 2M_\chi$ , where  $Q_{\text{tr}}$  is the momentum transferred from the mediator to the DM particle pair, which yields  $\Lambda > 2M_\chi/g_{\text{eff}}$ . The second is more stringent and uses the quantity:

$$R_\Lambda = \frac{\int dR^2 \int dM_R \frac{d^2\sigma}{dR^2 dM_R} \Big|_{Q_{\text{tr}} < g_{\text{eff}}\Lambda}}{\int dR^2 \int dM_R \frac{d^2\sigma}{dR^2 dM_R}}. \quad (7.7)$$

Values of  $R_\Lambda$  close to unity indicate a regime in which the assumptions of the EFT

approximation hold, while a deviation from unity quantifies the fraction of events for which the EFT approximation is still valid. We consider the case of  $s$ -channel production, and we compute  $R_\Lambda$  as a function of the effective coupling  $g_{\text{eff}}$  in the range  $0 < g_{\text{eff}} \leq 4\pi$ . The contours corresponding to  $R_\Lambda = 80\%$  for different values of  $g_{\text{eff}}$  are shown in Fig. 7.14. For values of  $g_{\text{eff}} \gtrsim 2$ , the limit set by the analysis lies above the  $R_\Lambda = 80\%$  contour.

The exclusion limits on  $\Lambda$  for the axial-vector and vector operators are transformed into upper limits on the spin-dependent ( $\sigma_{N\chi}^{\text{SD}}$ ) [27, 105, 77, 76, 26, 32, 31] and spin-independent ( $\sigma_{N\chi}^{\text{SI}}$ ) [76, 77, 71, 120, 70, 78, 30, 29] DM-nucleon scattering cross section, respectively; using the following expressions [79]:

$$\sigma_{N\chi}^{\text{SD}} = 0.33 \frac{\mu^2}{\pi \Lambda_{\text{LL}}^4}, \quad (7.8)$$

$$\sigma_{N\chi}^{\text{SI}} = 9 \frac{\mu^2}{\pi \Lambda_{\text{LL}}^4}, \quad (7.9)$$

where

$$\mu = \frac{M_\chi M_p}{M_\chi + M_p}, \quad (7.10)$$

with  $M_p$  and  $M_\chi$  indicating the proton and DM masses, respectively. The numerical values of the derived limits are given in Tables 7.12 and 7.13. The bound on  $\sigma_{N\chi}$  as a function of  $M_\chi$  is shown in Fig. 7.15 for spin-dependent and spin-independent DM-nucleon scattering. A summary of the observed limits for the axial-vector and vector operators can be found in Tables 7.12 and 7.13 respectively. It is observed that the spin-independent bounds obtained by direct detection experiments are more stringent than those obtained by the present result for masses above  $\simeq 5$  GeV. Such an effect is expected since the spin-independent DM-nucleus cross section is enhanced by the coherent scattering of DM off nucleons in the case of spin-independent operators. We note that the present result is more sensitive for small DM mass because the recoil energy in direct detection experiments is lower in this region and therefore more difficult to detect. In the case of spin-dependent DM-nucleus scattering, the present results are more stringent than those obtained by direct detection experiments because the DM-nucleus cross section does not benefit from the coherent enhancement. A summary of the observed limits for the axial-vector and vector operators can be found in Tables 7.12 and 7.13 respectively.

In order to compare our results with those from direct detection experiments, the experimental bounds in [76, 77, 71, 120, 70, 78, 27, 105, 77, 76] are translated

Table 7.12: The 90% CL limits on DM production in the case of axial-vector couplings. Here,  $\sigma_{\text{UL}}^u$  and  $\sigma_{\text{UL}}^d$  are the observed upper limits on the production cross section for u and d quarks, respectively;  $\Lambda_{\text{LL}}$  is the observed cutoff energy scale lower limit; and  $\sigma_{N\chi}$  is the observed DM-nucleon scattering cross section upper limit.

$M_\chi$ (GeV)	$\sigma_{\text{UL}}^u$ (pb)	$\sigma_{\text{UL}}^d$ (pb)	$\Lambda_{\text{LL}}$ (GeV)	$\sigma_{N\chi}$ ( $\text{cm}^2$ )
1	0.39	0.45	1029	$8.5 \times 10^{-42}$
10	0.43	0.45	1012	$2.9 \times 10^{-41}$
100	0.30	0.37	1017	$3.3 \times 10^{-41}$
400	0.25	0.26	752	$1.1 \times 10^{-40}$
700	0.21	0.26	524	$4.7 \times 10^{-40}$
1000	0.17	0.22	360	$2.1 \times 10^{-39}$

Table 7.13: The 90% CL limits on DM production in the case of vector couplings. Here,  $\sigma_{\text{UL}}^u$  and  $\sigma_{\text{UL}}^d$  are the observed upper limits on the production cross section for u and d quarks, respectively;  $\Lambda_{\text{LL}}$  is the observed cutoff energy scale lower limit; and  $\sigma_{N\chi}$  is the observed DM-nucleon scattering cross section upper limit.

$M_\chi$ (GeV)	$\sigma_{\text{UL}}^u$ (pb)	$\sigma_{\text{UL}}^d$ (pb)	$\Lambda_{\text{LL}}$ (GeV)	$\sigma_{N\chi}$ ( $\text{cm}^2$ )
1	0.41	0.38	1038	$2.3 \times 10^{-40}$
10	0.36	0.45	1043	$6.9 \times 10^{-40}$
100	0.33	0.44	1036	$8.3 \times 10^{-40}$
400	0.23	0.35	893	$1.5 \times 10^{-39}$
700	0.22	0.27	674	$4.7 \times 10^{-39}$
1000	0.22	0.27	477	$1.8 \times 10^{-38}$

into bounds on  $\Lambda$ . This comparison is shown in Fig. 7.16. This translation is well defined since the momentum transfer in most direct detection experiments is low compared to the values of  $\Lambda$  being probed, and thus the EFT approximations in question are mostly valid.

### Limits on dark matter production from the $0\mu b$ and $0\mu bb$ samples

The results from the  $0\mu b$  and  $0\mu bb$  samples are interpreted in an EFT scenario, following a methodology similar to that of Section 7.7. In this case, a heavy scalar mediator is considered [102], generating an operator:

$$\hat{O}_S = \frac{M_q}{\Lambda^3} \bar{\chi} \chi \bar{q} q. \quad (7.11)$$

The dependence on the mass, induced by the scalar nature of the mediator, implies a stronger coupling to third-generation quarks, enhancing the sensitivity of the  $0\mu b$  and  $0\mu bb$  samples to this scenario. Unlike the case of V and AV operators, the

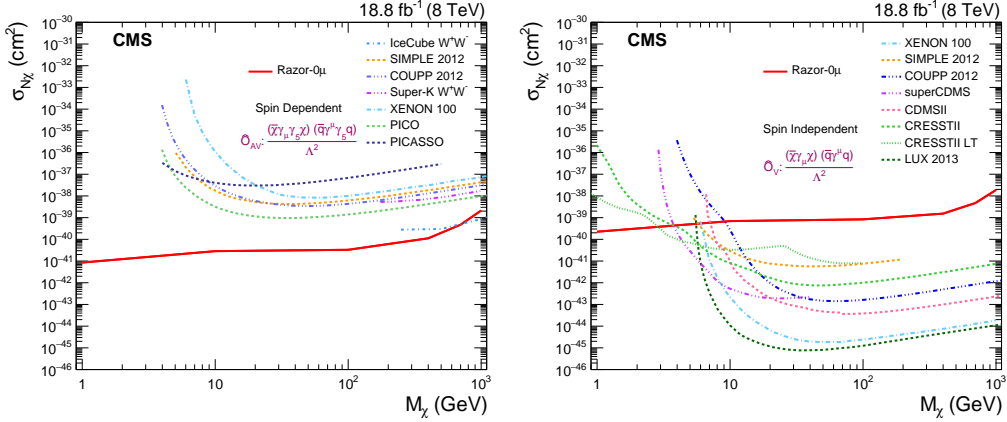


Figure 7.15: Upper limit at 90% CL on the DM-nucleon scattering cross section  $\sigma_{N\chi}$  as a function of the DM mass  $M_\chi$  in the case of spin-dependent axial-vector (left) and spin-independent vector (right) currents. A selection of representative direct detection experimental bounds are also shown.

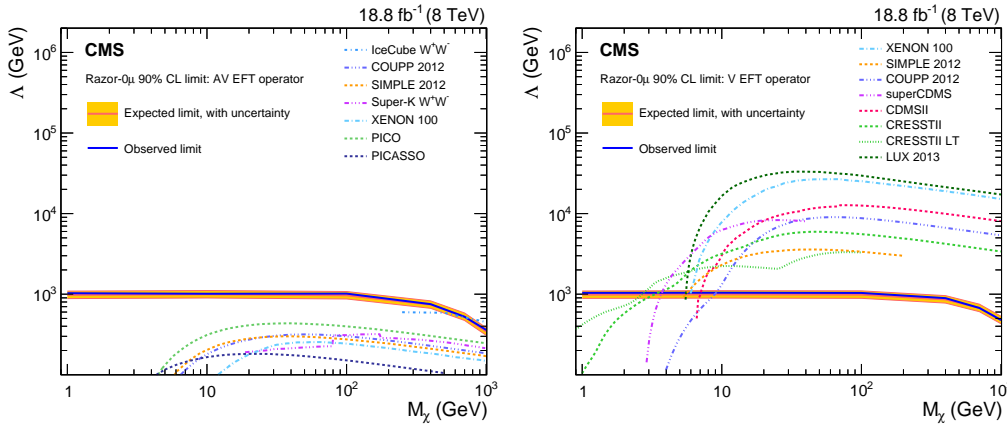


Figure 7.16: Lower limit at 90% CL on the cutoff scale  $\Lambda$  as a function of the DM mass  $M_\chi$  in the case of axial-vector (left) and vector (right) currents. A selection of direct detection experimental bounds are also shown.

Table 7.14: The 90% CL limits on DM production in the case of scalar couplings. Here,  $\sigma_{\text{UL}}^{\text{obs}}$  is the observed upper limit on the production cross section,  $\Lambda_{\text{LL}}^{\text{obs}}$  and  $\Lambda_{\text{LL}}^{\text{exp}}$  are the observed and expected cutoff energy scale lower limit, respectively.

$M_\chi$ (GeV)	$\sigma_{\text{UL}}^{\text{obs}}$ (pb)	$\Lambda_{\text{LL}}^{\text{obs}}$ (GeV)	$\Lambda_{\text{LL}}^{\text{exp}}$ (GeV)
0.1	5.4	43.0	48.2
1	3.8	45.3	49.9
10	6.3	43.2	48.4
100	0.8	53.7	55.1
200	0.7	47.2	48.3
300	2.8	32.5	35.8
400	2.8	28.3	30.8
1000	1.7	13.2	13.8

production cross section for this process is proportional to  $1/\Lambda^6$ . The value of  $\Lambda_{\text{LL}}$  is then derived as

$$\Lambda_{\text{LL}} = \Lambda_{\text{GEN}} \left( \frac{\sigma_{\text{GEN}}}{\sigma_{\text{UL}}} \right)^{\frac{1}{6}}. \quad (7.12)$$

Given the results of Table 7.10 we proceed to set limits at 90% CL on the cutoff scale (see Table 7.14) using the LHC CL<sub>s</sub> procedure. To quantify the validity of the EFT we follow the discussion in Section 7.7, considering an interaction mediated by an *s*-channel produced particle. The operator of Eq. (7.11) is suppressed by an additional factor  $m_b/\Lambda$  with respect to the operators in Eq. (7.5). As a result, for a given value of the coupling  $g_{\text{eff}}$ , smaller values of  $\Lambda$  are probed in this case. The observed limit stays below the contours derived for  $R_\Lambda = 80\%$ , even when the coupling is fixed to the largest value considered,  $g_{\text{eff}} = 4\pi$ , as shown in the left plot of Fig. 7.17. For the same choice of coupling, the derived limit on  $\Lambda$  would correspond to  $R_\Lambda \approx 25\%$ , as shown in the right plot of Fig. 7.17. Only for  $g_{\text{eff}} > 4\pi$  does the observed limit correspond to values of  $R_\Lambda > 80\%$ . This requirement implies a UV completion of the EFT beyond the perturbative regime. For this reason, this result is not interpreted in terms of an exclusion limit on  $\sigma_{N\chi}$ .

## 7.8 Summary

A search for dark matter has been performed studying proton-proton collisions collected with the CMS detector at the LHC at a center-of-mass energy of 8 TeV. The data correspond to an integrated luminosity of  $18.8 \text{ fb}^{-1}$ , collected with a dedicated high-rate trigger in 2012, made possible by the creation of parked data, and processed during the LHC shutdown in 2013.

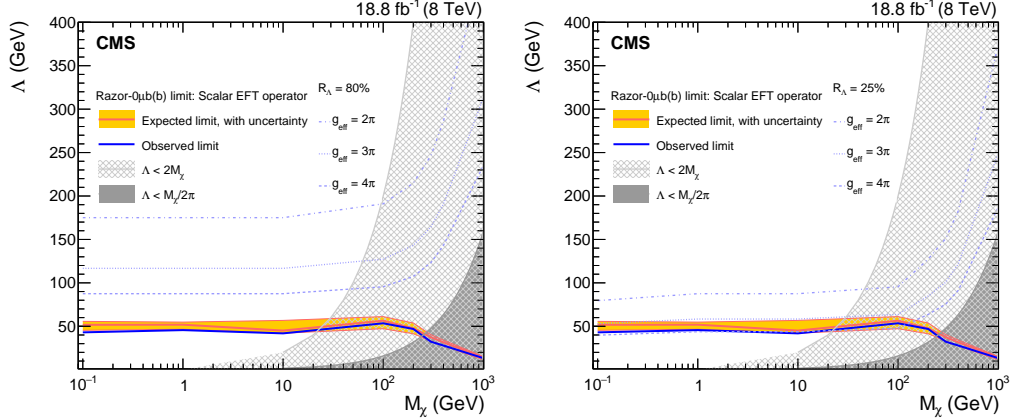


Figure 7.17: Lower limit at 90% CL on the cutoff scale  $\Lambda$  for the scalar operator  $\hat{O}_S$  as a function of the DM mass  $M_\chi$ . The validity of the EFT is quantified by  $R_\Lambda = 80\%$  (left) and  $R_\Lambda = 25\%$  (right) contours, corresponding to different values of the effective coupling  $g_{\text{eff}}$ . For completeness, regions forbidden by the EFT validity condition  $\Lambda > 2M_\chi/g_{\text{eff}}$  are shown for two choices of the effective coupling:  $g_{\text{eff}} = 1$  (light gray) and  $g_{\text{eff}} = 4\pi$  (dark gray).

Events with at least two jets are analyzed by studying the distribution in the ( $M_R$ ,  $R^2$ ) plane, in an event topology complementary to that of monojet searches. Events with one or two muons are used in conjunction with simulated samples, to predict the expected background from standard model processes, mainly  $Z+jets$  and  $W+jets$ . The analysis is performed on events both with and without b-tagged jets, originating from the hadronization of a bottom quark, where in the latter case the dominant background comes from  $t\bar{t}$ .

No significant excess is observed. The results are presented as exclusion limits on dark matter production at 90% confidence level for models based on effective operators and for different assumptions on the interaction between the dark matter particles and the colliding partons. Dark matter production at the LHC is excluded for a mediator mass scale  $\Lambda$  below 1 TeV in the case of a vector or axial vector operator. While the sensitivity achieved is similar to those of previously published searches, this analysis complements those results since the use of razor variables provides more inclusive selection criteria and since the exploitation of parked data allows events with small values of  $M_R$  to be included.

## ACKNOWLEDGMENTS

We congratulate our colleagues in the CERN accelerator departments for the excellent performance of the LHC and thank the technical and administrative staffs at CERN and at other CMS institutes for their contributions to the success of the CMS effort. In addition, we gratefully acknowledge the computing centers and personnel of the Worldwide LHC Computing Grid for delivering so effectively the computing infrastructure essential to our analyses. Finally, we acknowledge the enduring support for the construction and operation of the LHC and the CMS detector provided by the following funding agencies: the Austrian Federal Ministry of Science, Research and Economy and the Austrian Science Fund; the Belgian Fonds de la Recherche Scientifique, and Fonds voor Wetenschappelijk Onderzoek; the Brazilian Funding Agencies (CNPq, CAPES, FAPERJ, and FAPESP); the Bulgarian Ministry of Education and Science; CERN; the Chinese Academy of Sciences, Ministry of Science and Technology, and National Natural Science Foundation of China; the Colombian Funding Agency (COLCIENCIAS); the Croatian Ministry of Science, Education and Sport, and the Croatian Science Foundation; the Research Promotion Foundation, Cyprus; the Ministry of Education and Research, Estonian Research Council via IUT23-4 and IUT23-6 and European Regional Development Fund, Estonia; the Academy of Finland, Finnish Ministry of Education and Culture, and Helsinki Institute of Physics; the Institut National de Physique Nucléaire et de Physique des Particules / CNRS, and Commissariat à l'Énergie Atomique et aux Énergies Alternatives / CEA, France; the Bundesministerium für Bildung und Forschung, Deutsche Forschungsgemeinschaft, and Helmholtz-Gemeinschaft Deutscher Forschungszentren, Germany; the General Secretariat for Research and Technology, Greece; the National Scientific Research Foundation, and National Innovation Office, Hungary; the Department of Atomic Energy and the Department of Science and Technology, India; the Institute for Studies in Theoretical Physics and Mathematics, Iran; the Science Foundation, Ireland; the Istituto Nazionale di Fisica Nucleare, Italy; the Ministry of Science, ICT and Future Planning, and National Research Foundation (NRF), Republic of Korea; the Lithuanian Academy of Sciences; the Ministry of Education, and University of Malaya (Malaysia); the Mexican Funding Agencies (CINVESTAV, CONACYT, SEP, and UASLP-FAI); the Ministry of Business, Innovation and Employment, New Zealand; the Pakistan Atomic Energy Commission; the Ministry of Science and Higher Education and the National Sci-

ence Center, Poland; the Fundação para a Ciência e a Tecnologia, Portugal; JINR, Dubna; the Ministry of Education and Science of the Russian Federation, the Federal Agency of Atomic Energy of the Russian Federation, Russian Academy of Sciences, and the Russian Foundation for Basic Research; the Ministry of Education, Science and Technological Development of Serbia; the Secretaría de Estado de Investigación, Desarrollo e Innovación and Programa Consolider-Ingenio 2010, Spain; the Swiss Funding Agencies (ETH Board, ETH Zurich, PSI, SNF, UniZH, Canton Zurich, and SER); the Ministry of Science and Technology, Taipei; the Thailand Center of Excellence in Physics, the Institute for the Promotion of Teaching Science and Technology of Thailand, Special Task Force for Activating Research and the National Science and Technology Development Agency of Thailand; the Scientific and Technical Research Council of Turkey, and Turkish Atomic Energy Authority; the National Academy of Sciences of Ukraine, and State Fund for Fundamental Researches, Ukraine; the Science and Technology Facilities Council, UK; the US Department of Energy, and the US National Science Foundation.

Individuals have received support from the Marie-Curie programme and the European Research Council and EPLANET (European Union); the Leventis Foundation; the A. P. Sloan Foundation; the Alexander von Humboldt Foundation; the Belgian Federal Science Policy Office; the Fonds pour la Formation à la Recherche dans l'Industrie et dans l'Agriculture (FRIA-Belgium); the Agentschap voor Innovatie door Wetenschap en Technologie (IWT-Belgium); the Ministry of Education, Youth and Sports (MEYS) of the Czech Republic; the Council of Science and Industrial Research, India; the HOMING PLUS programme of the Foundation for Polish Science, cofinanced from European Union, Regional Development Fund; the OPUS programme of the National Science Center (Poland); the Compagnia di San Paolo (Torino); MIUR project 20108T4XTM (Italy); the Thalis and Aristeia programmes cofinanced by EU-ESF and the Greek NSRF; the National Priorities Research Program by Qatar National Research Fund; the Rachadapisek Sompot Fund for Postdoctoral Fellowship, Chulalongkorn University (Thailand); the Chulalongkorn Academic into Its 2nd Century Project Advancement Project (Thailand); and the Welch Foundation, contract C-1845; and the Weston Havens Foundation (USA).

## Appendix

### 7.9 Background estimation and observed yield

In this section, we provide the background estimate and the observed yield for each bin of the ( $M_R$ ,  $R^2$ ) plane.

Tables 7.15-7.18 show the expected and observed yields in each  $R^2$  bin of each  $M_R$  category for the  $0\mu$  sample. Tables 7.19 and 7.20 show the corresponding values for the  $0\mu b$  and the  $0\mu bb$  samples, respectively.

Table 7.15: Background estimates and observed yield for each  $R^2$  bin in the VL  $M_R$  category.

$R^2$ range	0.5–0.55	0.55–0.6	0.6–0.65	0.65–0.7
Observed	2049	1607	1352	1147
Estimated	$2350 \pm 720$	$1810 \pm 450$	$1530 \pm 180$	$1240 \pm 110$
$R^2$ range	0.7–0.75	0.75–0.8	0.8–0.85	0.85–0.9
Observed	1026	896	880	744
Estimated	$1090 \pm 140$	$1081 \pm 76$	$876 \pm 97$	$909 \pm 63$
$R^2$ range	0.9–0.95	0.95–1.0	1.0–2.5	
Observed	688	499	735	
Estimated	$674 \pm 67$	$521 \pm 43$	$694 \pm 62$	

Table 7.16: Background estimates and observed yield for each  $R^2$  bin in the L  $M_R$  category.

$R^2$ range	0.5–0.575	0.575–0.65	0.65–0.75
Observed	1088	765	682
Estimated	$1220 \pm 120$	$828 \pm 65$	$810 \pm 210$
$R^2$ range	0.75–0.85	0.85–0.95	0.95–2.5
Observed	565	395	290
Estimated	$551 \pm 59$	$454 \pm 32$	$304 \pm 43$

Table 7.17: Background estimates and observed yield for each  $R^2$  bin in the H  $M_R$  category.

$R^2$ range	0.5–0.575	0.575–0.65	0.65–0.75
Observed	513	328	279
Estimated	$560 \pm 550$	$330^{+360}_{-330}$	$275 \pm 41$
$R^2$ range	0.75–0.85	0.85–0.95	0.95–2.5
Observed	203	151	85
Estimated	$242 \pm 18$	$171^{+173}_{-171}$	$74 \pm 17$

Table 7.18: Background estimates and observed yield for each  $R^2$  bin in the VH  $M_R$  category.

$R^2$ range	0.5–0.6	0.6–0.7	0.7–0.95	0.95–2.5
Observed	117	58	75	11
Estimated	$100^{+150}_{-100}$	$59 \pm 36$	$75 \pm 30$	$9 \pm 7$

Table 7.19: Background estimates and observed yield for each bin in the  $0\mu b$  signal region.

$R^2$ range	0.5–0.6	0.6–0.75	0.75–0.9	0.9–2.5
Observed	760	807	469	246
Estimated	$850 \pm 170$	$620 \pm 120$	$470 \pm 110$	$320 \pm 160$

Table 7.20: Background estimates and observed yield for each bin in the  $0\mu bb$  signal region.

$R^2$ range	0.5–0.6	0.6–0.75	0.75–0.9	0.9–2.5
Observed	122	80	31	14
Estimated	$135 \pm 30$	$81 \pm 18$	$36 \pm 8$	$19 \pm 9$

## C h a p t e r ~ 8

# SEARCHES FOR ANOMALOUS HIGGS BOSON PRODUCTION

### 8.1 Introduction

The discovery of the standard model (SM) Higgs boson at the LHC [7, 55] presents a unique opportunity to search for physics beyond the SM (BSM) using the Higgs boson as a search tool. Given the small value of the Higgs production cross section in the standard model, any BSM scenario predicting new mechanisms for Higgs boson production can be investigated with dedicated searches, using the known Higgs mass to suppress SM background processes.

This Chapter presents a search of this kind in pp collisions at 13 TeV using data from the CMS detector at the CERN LHC. Events with two photons consistent with a Higgs candidate are selected and categorized according to the  $p_T$  of the Higgs candidate, the presence of additional Higgs to  $b\bar{b}$  or Z to  $b\bar{b}$  candidates, and the estimated resolution of the diphoton pair. Motivated by supersymmetric (SUSY) scenarios, we use the razor variables [53, 114]  $M_R$  and  $R^2$ —extensively discussed and illustrated in Chapter ??—to define search regions that may contain additional events above the SM prediction if a BSM Higgs production mechanism is present. The contribution in the search regions from the non-resonant QCD background is distinguished from a potential BSM Higgs signal using the shape of the diphoton mass distribution. The search uses  $2.3 \text{ fb}^{-1}$  of integrated luminosity collected in 2015 and  $12.9 \text{ fb}^{-1}$  collected in 2016.

In Run 1 of the LHC, a similar CMS analysis [122] reported an excess of  $H \rightarrow \gamma\gamma$  events with  $M_R \approx 400 \text{ GeV}$  and  $R^2 > 0.05$  with a local (global) significance of  $2.9\sigma$  ( $1.6\sigma$ ). Motivated by the Run I result, we consider a SUSY simplified model in which bottom squarks are pair produced and decay to a bottom quark and the next-to-lightest supersymmetric particle (NLSP),  $\tilde{\chi}_2^0$ , with 100% branching ratio. The NLSP subsequently decays to a Higgs boson and the lightest supersymmetric particle (LSP),  $\tilde{\chi}_1^0$ , with 100% branching ratio. We assume that the mass difference between the NLSP and the LSP is 130 GeV, just above the Higgs boson mass. The relevant decay topology in the simplified model is shown in Figure 8.1. The cross section for this simplified model is assumed to be the same as the standard sbottom pair production cross section [38]. Such a signal model is observed to produce event

kinematics consistent with the excess observed in Run I data and is not ruled out by searches in other final states and decay channels. This search is interpreted using the sbottom pair production model as the benchmark, and we derive limits on the production cross section as a function of the sbottom mass and the LSP mass.

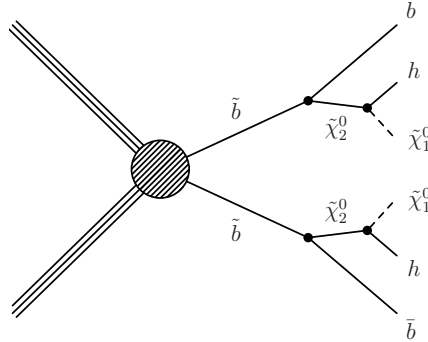


Figure 8.1: Diagram illustrating the SUSY benchmark simplified model of bottom squark decays to a Higgs boson, a b-jet, and the LSP.

## 8.2 Summary of the 8 TeV Results

The first version of the analysis to be presented in this Chapter was carried out by CMS [122] and studied in more detailed in Alex Mott’s thesis [[AlexMott](#) ]. Here, a summary of the main results is given as is relevant for the discussions to follow.

The 8 TeV analysis selects events in a very similar fashion to the one presented in this Chapter. It categorizes events based on the Higg candidate  $p_T$ , the photons energy resolution, and the invariant masses of ther possible b-jet pairs – indeed, intended to target an extra Higgs or Z boson on the event. The final results yield that most of the search bins were consisten with the SM expectations, and the results were interpreted as cross section limits on the neutralino/chargino production in the context of SUSY simplified models. The observed significances for all the search bins are shown in Figure 8.2, while the limit on the neutralino/chargino production as a function of the chargino mass is shown in Figure 8.3. Although, most of the search bins were consitent with the SM expectations, an interesting excess of events was observed in the most extreme bin – that with the highest  $M_R$  and  $R^2$  boundaries – in the High-Resolution (HighRes) event category, see Figures 8.4 and 8.5, where both photons forming the Higgs cadidate are require to have an energy resolution better than 1.5%. This excess corresponds to a  $2.9\sigma$  ( $1.6\sigma$ ) local (global) significance. Such an excess, despite the limited number of events, is interesting for mainly two reasons: first, it is located at relative high values of  $M_R$  ( $\sim 400$  GeV)

and low values of  $R^2$  (below 0.05), see 8.5 for more detail, and therefore suggest a characteristic mass scale and that they contain relative low  $E_T^{\text{miss}}$  values. second, that the diphoton invariant mass is consistent with that of the SM Higgs boson and therefore any possible model to explain such an excess should at least contain a one SM Higgs boson. The diphoton invariant mass for the events that lie in the bin with the excess are shown in 8.6. The search presented in this Chapter is largely inspired on it 8 TeV counterpart, but with significant differences when it comes to the backgrounds estimation techniques. In addition, the proposed simplified model shown in Figure 8.1 – which is studied in great detail in Chapter ?? – shows some consistency with the excess observed in the 8 TeV CMS result.

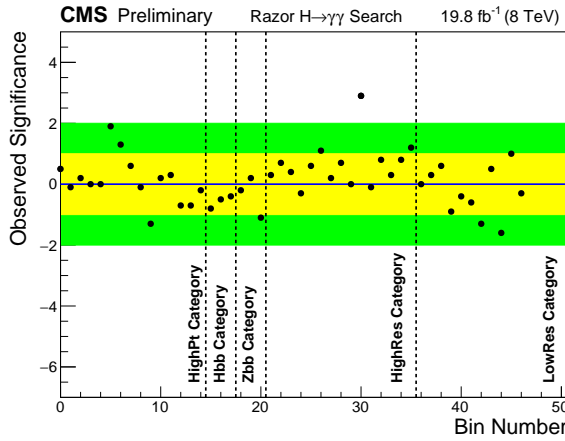


Figure 8.2: Summary of the results in the HighRes category for the 8 TeV version of the analysis.

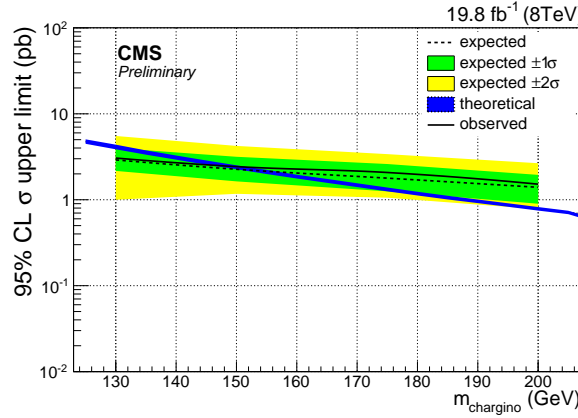


Figure 8.3: Summary of the results in the HighRes category for the 8 TeV version of the analysis.

$M_R$ region	$R^2$ region	observed events	expected background	p-value	significance ( $\sigma$ )
150 - 250	0.00 - 0.05	363	$357.6^{+5.6}_{-5.4}$ (syst.)	0.40	0.3
150 - 250	0.05 - 0.10	149	$139.4^{+5.6}_{-5.4}$ (syst.)	0.23	0.7
150 - 250	0.10 - 0.15	35	$32.5^{+3.1}_{-3.1}$ (syst.)	0.34	0.4
150 - 250	0.15 - 1.00	7	$8.0^{+1.7}_{-1.7}$ (syst.)	0.40	-0.3
250 - 400	0.00 - 0.05	218	$207.9^{+7.0}_{-7.8}$ (syst.)	0.27	0.6
250 - 400	0.05 - 0.10	20	$14.7^{+2.1}_{-2.1}$ (syst.)	0.13	1.1
250 - 400	0.10 - 1.00	3	$2.7^{+0.6}_{-0.6}$ (syst.)	0.43	0.2
400 - 1400	0.00 - 0.05	109	$101.6^{+6.0}_{-6.8}$ (syst.)	0.26	0.7
400 - 1400	0.05 - 1.00	5	$0.5^{+0.4}_{-0.2}$ (syst.)	0.002	2.9
1400 - 3000	0.00 - 1.00	0	$0.9^{+0.9}_{-0.3}$ (syst.)	0.44	-0.1

Figure 8.4: Summary of the results in the HighRes category for the 8 TeV version of the analysis.

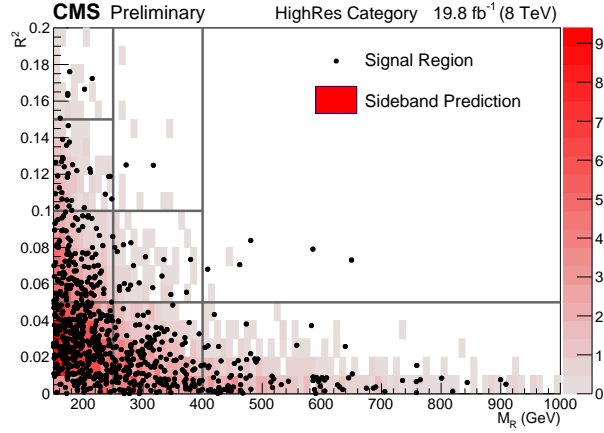


Figure 8.5: Summary of the results in the HighRes category for the 8 TeV version of the analysis.

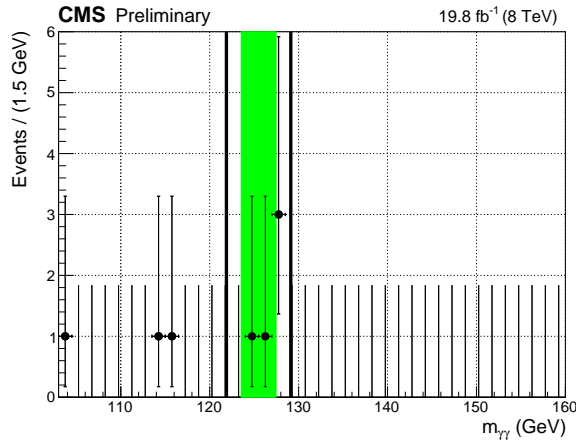


Figure 8.6: Summary of the results in the HighRes category for the 8 TeV version of the analysis.

### 8.3 Object Selection

Photon candidates with  $p_T > 25$  GeV falling in the barrel region ( $|\eta| < 1.4442$ ) are selected if they satisfy identification requirements based on the shower shape in the electromagnetic calorimeter, the hadronic to electromagnetic energy ratio, and the isolation in a cone around the photon direction [92]. To satisfy the isolation requirement, the sum of the energies of PF candidates near the photon must be smaller than a specified cut value. Isolation cuts are placed separately on energy from charged hadrons, neutral hadrons, and photons. Each isolation sum is corrected for the effect of pileup by subtracting the average energy deposited into the isolation cone estimated using a random sampling of energy density in the event. Photon objects are rejected if they match an electron candidate. The photon identification requirements correspond to a loose working point with an efficiency of about 90%.

The measured energies of the photons are corrected for clustering and local geometric effects using an energy regression trained on Monte Carlo simulation [94]. This regression gives a significant improvement to the energy resolution of the photons and provides an estimate of the uncertainty of the energy measurement. This uncertainty estimate is used in this analysis to categorize events into high and low resolution categories.

Jets are reconstructed using a global event description based on the CMS particle flow (PF) algorithm [65, 63]. Individual particles (PF candidates) are reconstructed by combining the information from the inner tracker, the calorimeters, and the muon system. Charged PF candidates associated to a vertex other than the primary one are considered pileup and are rejected. The remaining particles are clustered into jets, using the FASTJET [46] implementation of the anti- $k_T$  [47] algorithm with the distance parameter  $R = 0.4$ . Jets are required not to overlap with either of the two photons; this requirement is imposed by the condition  $\Delta R = \sqrt{(\Delta\eta)^2 + (\Delta\phi)^2} > 0.5$ . The vector sum of the reconstructed  $p_T$  of the PF particles is used to quantify the missing transverse momentum  $\vec{p}_T^{\text{miss}}$  in the event. Events with detector- and beam-related noise that can mimic event topologies with high energy and large  $E_T^{\text{miss}} = |\vec{p}_T^{\text{miss}}|$  are filtered using dedicated noise reduction algorithms [54, 58, 66].

The combined secondary vertex (CSV) tagging algorithm [109] is used to identify jets originating from the showering and hadronization of b quarks. A loose working point is used which yields a mistag rate that is approximately 10%. Jet pairs are identified as  $b\bar{b}$  candidates if the two jets satisfy the CSV requirement. Among all  $b\bar{b}$  candidates in the event (if there are any), the pair with mass closest to 125 GeV

(91.2 GeV) is chosen as a  $H \rightarrow b\bar{b}$  ( $Z \rightarrow b\bar{b}$ ) candidate. Events are not required to contain a  $b\bar{b}$  pair; the presence or absence of a  $H \rightarrow b\bar{b}$  or  $Z \rightarrow b\bar{b}$  candidate with mass in the specified range is used in the event classification procedure described in Section 8.4.

#### 8.4 Event Selection and Analysis Strategy

We select events with two photons that satisfy the identification criteria described above. If multiple photon pairs are identified, the pair with the largest scalar sum of the transverse momenta of the photons is chosen as the Higgs candidate. The Higgs candidate must additionally have leading photon  $p_T$  greater than 40 GeV, and diphoton mass between 103 GeV and 160 GeV.

In addition to the diphoton Higgs candidate, we require at least one additional jet with  $p_T > 30$  GeV and  $|\eta| < 3.0$ . The Higgs candidate and all identified jets are clustered into hemispheres according to the Razor *megajet* algorithm[60], and the razor variables [53, 114]  $M_R$  and  $R^2$  are computed as follows:

$$M_R \equiv \sqrt{(|\vec{p}^{j_1}| + |\vec{p}^{j_2}|)^2 - (p_z^{j_1} + p_z^{j_2})^2}, \quad (8.1)$$

$$R^2 \equiv \left( \frac{M_T^R}{M_R} \right)^2, \quad (8.2)$$

where  $\vec{p}$  is the momentum of a hemisphere and  $p_z$  is its longitudinal component, and  $j_1$  and  $j_2$  are used to label the two hemispheres. In the definition of  $R^2$ , the variable  $M_T^R$  is defined as:

$$M_T^R \equiv \sqrt{\frac{E_T^{\text{miss}}(p_T^{j_1} + p_T^{j_2}) - \vec{p}_T^{\text{miss}} \cdot (\vec{p}_T^{j_1} + \vec{p}_T^{j_2})}{2}}. \quad (8.3)$$

The razor variables  $M_R$  and  $R^2$  provide discrimination between SUSY signal models and standard model background processes. SUSY signals typically have large values of  $M_R$  and  $R^2$ , while the standard model background exhibits an exponentially falling spectrum in both variables.

The selected events are categorized into four mutually exclusive categories. An event is categorized as “HighPt” if the  $p_T$  of the selected Higgs candidate is larger than 110 GeV. Otherwise it is categorized as “H( $\gamma\gamma$ )-H/Z(bb)” if the event contains two b-tagged jets whose invariant mass is in the Z mass region between 76 GeV and 106 GeV, or in the Higgs mass region between 110 GeV and 140 GeV. Remaining events are categorized as “HighRes” (“LowRes”) if the mass resolution

estimate  $\sigma_M/M$  is less (greater) than 0.85%, where  $\sigma_M$  is computed as  $1/2 \times \sqrt{(\sigma_{E,\gamma 1}/E_{\gamma 1})^2 + (\sigma_{E,\gamma 2}/E_{\gamma 2})^2}$ . The “HighPt” category is intended to isolate events from SUSY signals that produce high- $p_T$  Higgs bosons. The “H( $\gamma\gamma$ )-H/Z(bb)” category is motivated by the fact that many SUSY signal models predict events with two Higgs bosons or a Higgs boson and a Z boson in the final state. Finally, the “HighRes” and “LowRes” categories are intended to capture other SUSY signals, including compressed models. The categorization procedure is illustrated in Figure 8.7.

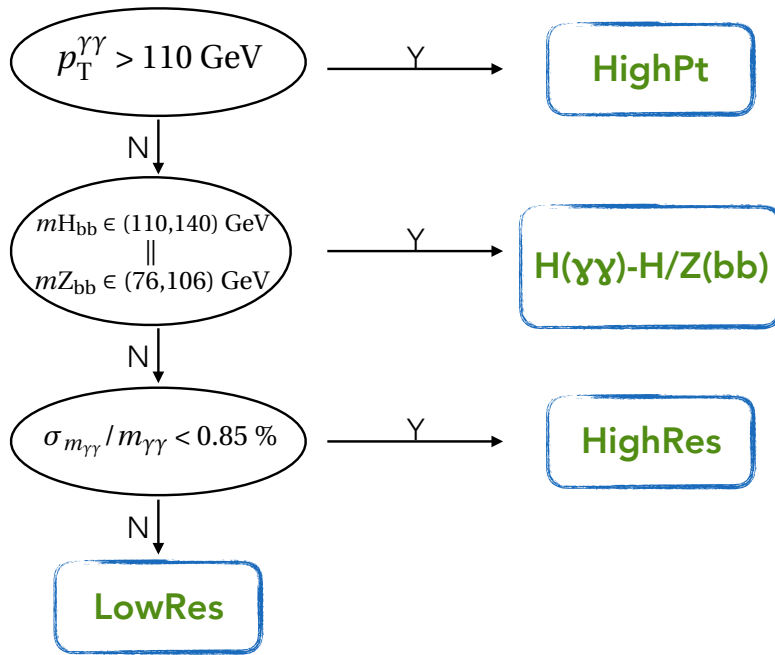


Figure 8.7: Diagram illustrating the event categorization used in the analysis.

Each event category is divided into bins by rectangular cuts on  $M_R$  and  $R^2$ . The binning is chosen via an optimization procedure that uses the sbottom pair production simplified model discussed in Section 8.1 as a benchmark model to determine the best bin boundaries. The algorithm begins with a single bin covering the entire  $M_R$ - $R^2$  plane. A division is made in either  $M_R$  or  $R^2$  at the value, which maximizes the expected statistical significance. This process is repeated on each newly created bin, and until convergence is achieved. Each bin returned by the algorithm is treated as a separate analysis search region. This procedure is not performed on the LowRes category; the binning in the LowRes category is instead taken to be the same as that in the HighRes category. The definition of the individual search regions is summarized in Table 8.1.

Table 8.1: A summary of the search region bins in each category is presented. The functional form used to model the non-resonant background is also listed. An exponential function of the form  $e^{-ax}$  is denoted as “singleExp”; a modified exponential function of the form  $e^{-ax^b}$  is denoted as “modExp”; and an N’th order Bernstein polynomial is denoted by “polyN”.

Bin Number	Category	$M_R$ Bin	$R^2$ Bin	Non-Resonant Bkg Model
0	HighPt	600 - $\infty$	0.025 - $\infty$	poly3
1	HighPt	150 - 600	0.130 - $\infty$	singleExp
2	HighPt	1250 - $\infty$	0.000 - 0.025	poly2
3	HighPt	150 - 450	0.000 - 0.130	poly2
4	HighPt	450 - 600	0.000 - 0.035	singleExp
5	HighPt	450 - 600	0.035 - 0.130	singleExp
6	HighPt	600 - 1250	0.000 - 0.015	singleExp
7	HighPt	600 - 1250	0.015 - 0.025	singleExp
8	H( $\gamma\gamma$ )-H/Z(bb)	150 - $\infty$	0.000 - $\infty$	singleExp
9	HighRes	150 - 250	0.000 - 0.175	modExp
10	HighRes	150 - 250	0.175 - $\infty$	singleExp
11	HighRes	250 - $\infty$	0.05 - $\infty$	singleExp
12	HighRes	250 - 600	0.000 - 0.05	modExp
13	HighRes	600 - $\infty$	0.000 - 0.05	singleExp
9	LowRes	150 - 250	0.000 - 0.175	modExp
10	LowRes	150 - 250	0.175 - $\infty$	singleExp
11	LowRes	250 - $\infty$	0.05 - $\infty$	modExp
12	LowRes	250 - 600	0.000 - 0.05	modExp
13	LowRes	600 - $\infty$	0.000 - 0.05	singleExp

To illustrate how events from a typical SUSY signal might be distributed in these bins, the distribution of events in the  $M_R$  and  $R^2$  plane for the sbottom pair production signal model discussed in Section 8.1 is shown in Figures 8.8 and 8.9 for the HighPt, HighRes, and LowRes categories, respectively.

## 8.5 Background Estimation

Within each search bin, we extract a potential signal by fitting to the diphoton mass spectrum. There are two types of backgrounds: a non-resonant background that is primarily due to QCD production of two photons or one photon and one jet, and a resonant background from standard model Higgs production. The non-resonant background is modeled with the functional form given in Table 8.1 for each individual search region bin, and all parameters of the function are unconstrained in the fit. The functional form model for each search region bin is selected on the basis of

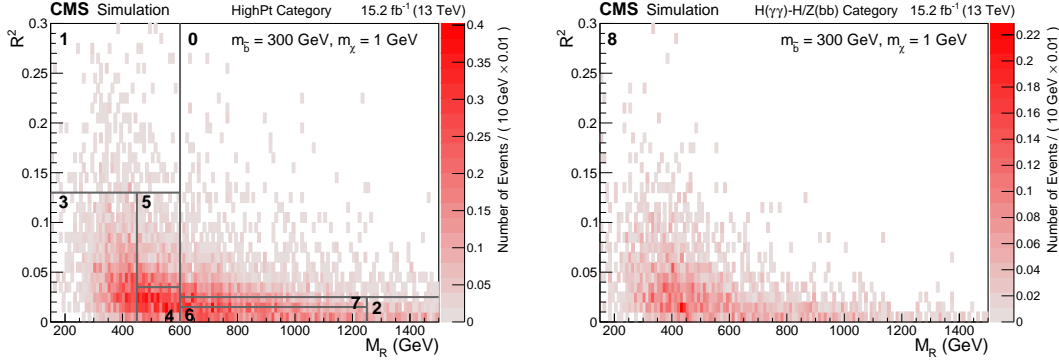


Figure 8.8: Distribution of events in the  $M_R$  and  $R^2$  plane for the HighPt and  $H(\gamma\gamma)$ - $H/Z(bb)$  category for sbottom pair production with  $m_{\tilde{b}} = 300$  GeV and  $m_\chi = 1$  GeV. The signal expectation is shown in the color scale and the bin numbers show where each bin is located in the  $M_R$  and  $R^2$  plane.

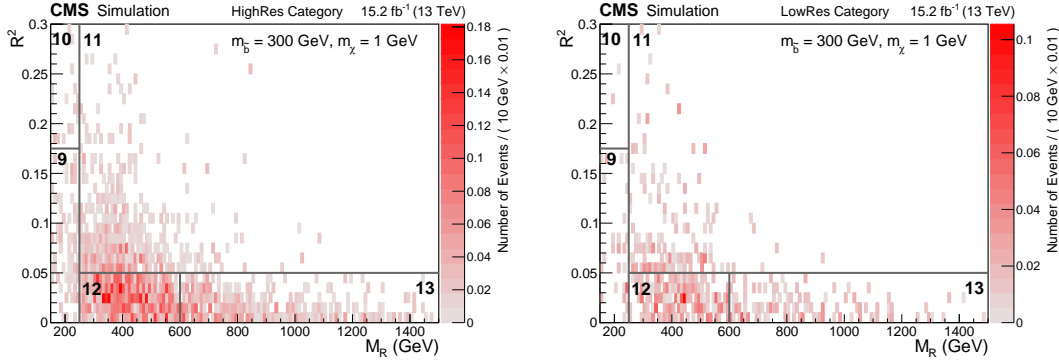


Figure 8.9: Distribution of events in the  $M_R$  and  $R^2$  plane for the HighRes and LowRes categories for sbottom pair production with  $m_{\tilde{b}} = 300$  GeV and  $m_\chi = 1$  GeV. The signal expectation is shown in the color scale and the bin numbers show where each bin is located in the  $M_R$  and  $R^2$  plane.

its Akaike Information Criterion (AIC) score [19], as well as tests of fit biases for a set of alternative models that all describe the data in the sideband well.

The standard model Higgs background and the SUSY signal are each modeled with a double-sided crystal ball function fit to the diphoton mass distribution obtained from the Monte Carlo simulation. The parameters of each double-sided crystal ball function are held constant in the signal extraction procedure, with the exception of the parameter that determines the location of the peak. This parameter is allowed to float but is restricted via a Gaussian constraint to the region around the Higgs mass. The width of the Gaussian constraint is 1%, corresponding to the systematic uncertainty on the photon energy scale.

The normalization of the standard model Higgs background in each bin is predicted from the Monte Carlo simulation, and is constrained to that value in the fit within uncertainties. Signal yields are also predicted from the Monte Carlo simulation.

Each bin in the HighRes category is fit simultaneously with the corresponding bin in the LowRes category. The relative SM Higgs and SUSY signal yields in the two categories are constrained according to the simulation prediction. The ratio of the yields in the HighRes and LowRes categories is expected to be independent of the signal model and background process.

Nuisance parameters for various theoretical and instrumental uncertainties that can affect the SM Higgs and signal normalization and are profiled to propagate systematic uncertainties. A more detailed discussion of systematic uncertainties can be found below in Section 8.7. The Monte Carlo simulation predictions for the standard model Higgs background normalization are shown in Table 8.2 for each search region bin.

## 8.6 Non-resonant Background Functional Form Selection: AIC Criterion and Bias Tests

For each signal region – i.e. every  $M_R$ - $R^2$  bin in the search – a functional form is needed to estimate the non-resonant contribution from SM QCD production. This selection process has two steps: 1) the AIC criterion, and 2) the bias test.

The AIC criterion step is used to decide what functions described reasonable well the observed data and therefore describe better the QCD background in each signal region. The AIC criterion, first introduced by Akaike in 1973 [19], is an estimate of the Kullback–Leibler divergence [KLbook] – the later is a measure of the distance between two probability density functions. Therefore the AIC criterion is a measure of the distance between the data and a particular probability density function (p.d.f.). An advantage over other goodness of fit quantities is that the AIC criterion also accounts for the fact that a function may have more free parameters and thus more flexibility to accommodate the observed data. It is useful to define the AIC score:

$$\text{AIC}_i = -2\log(\mathcal{L}) + 2k - \frac{2k(k+1)}{n-k-1}, \quad (8.4)$$

where  $i$  represents the  $i$ -th p.d.f under study,  $\mathcal{L}$  is the likelihood after the minimization process,  $k$  is the number of free parameters of the p.d.f, and  $n$  is the total number of observed events. The procedure is as follows: from a set of functions, all AIC scores are computed, then AIC score differences with respect of the minimum AIC

score ( $\Delta_i = \text{AIC}_i - \text{AIC}_{\min}$ ) are calculated. The AIC weight, which could be interpreted as the probability that the p.d.f under study is the true p.d.f from were the observed dataset was draw, is defined as

$$\omega_i = \frac{e^{-\frac{1}{2}\Delta_i}}{\sum_{j=0}^7 e^{-\frac{1}{2}\Delta_j}}. \quad (8.5)$$

Only p.d.fs with AIC weight larger than 0.1 pass the first step and are then tested for the bias test described below. Table 8.3 shows the full list of p.d.fs used in these studies. Tables 8.4, 8.5, 8.6, and 8.7 summarize four examples of the AIC results obtained for four search regions – one per each category in the analysis –, Figures 8.10, 8.11, 8.12, and 8.13 show the corresponding fits to the observed data. It is of note that the AIC fits are done only to the  $m_{\gamma\gamma} \in \{[103 - 121], [129 - 160]\}$  GeV region.

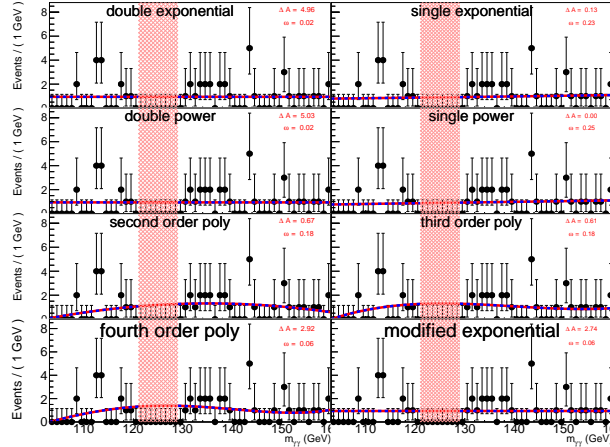


Figure 8.10: sideband fits for the search region: HighPt,  $M_R > 600$  GeV,  $R^2 > 0.025$ .

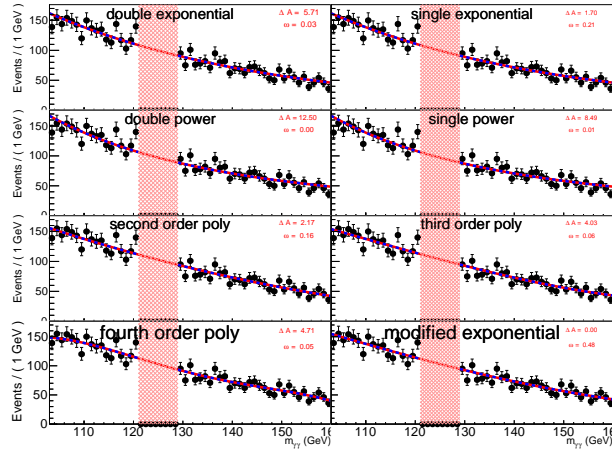


Figure 8.11: sideband fits for the search region: HighRes,  $150 < M_R < 250$  GeV,  $R^2 > 0$

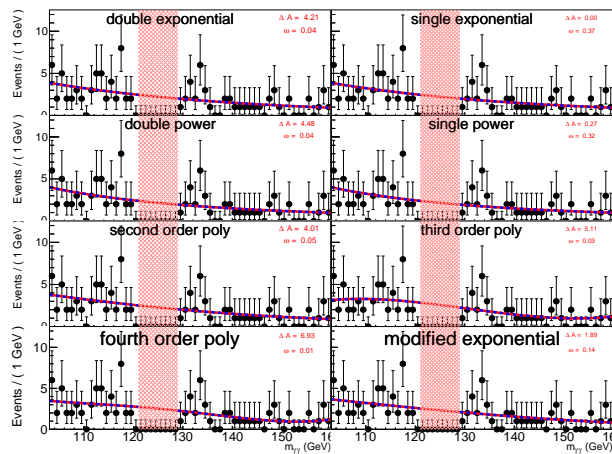


Figure 8.12: Sideband fits for the search region: LowRes,  $150 < M_R < 250$  GeV,  $R^2 > 0.175$ .

Table 8.2: The predicted yields for the standard model Higgs background processes are shown for an integrated luminosity corresponding to  $15.2 \text{ fb}^{-1}$  for each search region considered in this analysis. The contributions from each standard model Higgs process is shown separately, and the total is shown on the rightmost column along with its full uncertainty.

Bin	Category	Expected SM Higgs Yield					Total
		ggH	$t\bar{t}\text{H}$	VBF H	VH	bbH	
0	HighPt	1.09	0.49	0.17	0.25	0.01	$2.0 \pm 0.4$
1	HighPt	0.45	0.22	0.07	0.60	0.00	$1.4 \pm 0.3$
2	HighPt	1.75	0.23	0.89	0.07	0.02	$3.0 \pm 0.6$
3	HighPt	20.82	0.38	4.05	2.36	0.16	$27.7 \pm 8.0$
4	HighPt	6.30	0.20	1.77	0.45	0.06	$8.8 \pm 2.5$
5	HighPt	1.09	0.23	0.18	0.19	0.01	$1.7 \pm 0.4$
6	HighPt	7.15	0.21	2.91	0.28	0.05	$10.7 \pm 2.7$
7	HighPt	1.94	0.19	0.37	0.17	0.01	$2.7 \pm 0.8$
8	$\text{H}(\gamma\gamma)\text{-H/Z(bb)}$	0.35	0.51	0.03	0.10	0.06	$1.0 \pm 0.2$
9	HighRes	27.57	0.10	3.49	1.97	0.43	$33.5 \pm 10.4$
10	HighRes	0.26	0.06	0.04	0.20	0.01	$0.6 \pm 0.1$
11	HighRes	0.94	0.33	0.21	0.19	0.05	$1.7 \pm 0.4$
12	HighRes	16.16	0.31	3.99	0.64	0.39	$21.5 \pm 5.4$
13	HighRes	1.83	0.23	1.25	0.10	0.09	$3.5 \pm 1.0$
9	LowRes	9.55	0.039	1.18	0.72	0.14	$11.6 \pm 3.8$
10	LowRes	0.12	0.02	0.01	0.07	0.00	$0.2 \pm 0.1$
11	LowRes	0.32	0.11	0.06	0.08	0.02	$0.6 \pm 0.2$
12	LowRes	6.02	0.11	1.46	0.24	0.12	$7.9 \pm 2.3$
13	LowRes	0.82	0.09	0.46	0.04	0.03	$1.4 \pm 0.4$

Table 8.3: Full list of p.d.f (function) used in the AIC test.

function name	short name	functional form
single exponential	singleExp	$e^{-\alpha m_{\gamma\gamma}}$
double exponential	doubleExp	$f e^{-\alpha_1 m_{\gamma\gamma}} + (1-f) e^{-\alpha_2 m_{\gamma\gamma}}$
single power law	singlePow	$m_{\gamma\gamma}^{-\alpha}$
double power law	doublePow	$f m_{\gamma\gamma}^{-\alpha_1} + (1-f) m_{\gamma\gamma}^{-\alpha_2}$
modified exponential	modExp	$e^{-\alpha m_{\gamma\gamma}^\beta}$
Bernstein polynomial order 2	poly2	$p_0(1-t)^2 + p_1 2t(1-t) + p_2 t^2$
Bernstein polynomial order 3	poly3	$p_0(1-t)^3 + p_1 3t(1-t)^2 + p_2 3t^2(1-t) + p_3 t^3$
Bernstein polynomial order 4	poly4	$p_0(1-t)^4 + p_1 4t(1-t)^3 + p_2 6t^2(1-t)^2 + p_3 4t^3(1-t) + p_4 t^4$

Table 8.4: AIC results summary for the search region: HighPt,  $M_R > 600 \text{ GeV}$ ,  $R^2 > 0.025$ .

function	#P	$\Delta AIC$	$\omega$	$\omega_{max}/\omega$	status
singlePow	1	0.000	0.247	1.000	0, 3
singleExp	1	0.128	0.232	1.066	0, 3
poly3	4	0.605	0.183	1.353	0, 3
poly2	3	0.673	0.177	1.400	0, 3
modExp	2	2.738	0.063	3.932	0, 3
poly4	5	2.916	0.058	4.297	0, 3
doubleExp	3	4.958	0.021	11.929	0, 3
doublePow	3	5.031	0.020	12.371	0, 3

Table 8.5: AIC results summary for the search region: HighRes,  $150 < M_R < 250 \text{ GeV}, R^2 > 0$ .

function	#P	$\Delta AIC$	$\omega$	$\omega_{max}/\omega$	status
modExp	2	0.000	0.484	1.000	1, 2
singleExp	1	1.704	0.206	2.344	0, 3
poly2	3	2.173	0.163	2.964	0, 3
poly3	4	4.028	0.065	7.492	1, 2
poly4	5	4.714	0.046	10.560	0, 3
doubleExp	3	5.708	0.028	17.359	1, 2
singlePow	1	8.492	0.007	69.817	0, 3
doublePow	3	12.496	0.001	517.007	0, 3

Table 8.6: AIC results summary for the search region: LowRes, LowRes,  $150 < M_R < 250 \text{ GeV}$ ,  $R^2 > 0.175$

function	#P	$\Delta AIC$	$\omega$	$\omega_{max}/\omega$	status
singleExp	1	0.000	0.529	1.000	0, 3
modExp	2	1.883	0.206	2.564	1, 2
doubleExp	3	3.646	0.085	6.191	0, 3
singlePow	1	3.698	0.083	6.353	0, 3
poly2	3	4.925	0.045	11.736	0, 3
poly3	4	5.892	0.028	19.029	0, 3
poly4	5	7.657	0.012	45.992	0, 3
doublePow	3	7.703	0.011	47.065	1, 2

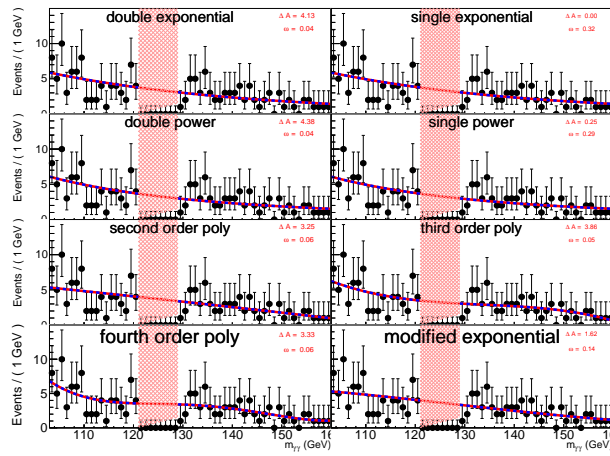


Figure 8.13: Sideband fits for the search region:  $H(\gamma\gamma)$ -H/Z(bb),  $M_R > 150 \text{ GeV}$ ,  $R^2 > 0$ .

Table 8.7: AIC results summary for the search region:  $H(\gamma\gamma)$ -H/Z(bb),  $M_R > 150 \text{ GeV}$ ,  $R^2 > 0$ .

function	#P	$\Delta AIC$	$\omega$	$\omega_{max}/\omega$	status
singleExp	1	0.000	0.323	1.000	0, 3
singlePow	1	0.247	0.285	1.131	0, 3
modExp	2	1.619	0.144	2.247	1, 2
poly2	3	3.252	0.063	5.083	0, 3
poly4	5	3.334	0.061	5.297	0, 3
poly3	4	3.858	0.047	6.881	0, 3
doubleExp	3	4.134	0.041	7.901	0, 3
doublePow	3	4.382	0.036	8.946	0, 3

The second step is the bias test, where only functions that passed the AIC test are considered. The bias test quantifies the error on the measured signal made when performing a signal-plus-background fit to the entire  $m_{\gamma\gamma}$  region in the final stage of the analysis. By requiring the selected function to have a small bias relative to any of the functions passing the AIC test, the error on the measured signal strength is reduced. In this analysis, the bias is defined relative to the fit uncertainty on the signal, i.e.

$$\delta_s = \frac{\hat{N}_s - N_s}{\sigma_{N_s}}, \quad (8.6)$$

where  $\hat{N}_s$  is the fitted signal,  $N_s$  is the actual value of the signal, and  $\sigma_{N_s}$  is the uncertainty on  $\hat{N}_s$ . The bias estimation is obtained by carrying a large number of pseudo-experiments (toys), each function passing the AIC test will be treated as the parent function from where the data was drawn, then several (10,000) toy datasets will be drawn from it containing the same amount of event as in the real dataset. For each toy dataset a known number of signal event will be injected ( $N_s$ ) and a signal-plus-background fit will be carried out and the bias will be calculated. After this procedure is done, the resulting bias distribution will be fitted with a double-sided crystal ball function, where the most probable value after the fit is taken as an estimate of the bias. Figure 8.14 shows the resulting bias distribution and fit for two different cases. The studies carried out indicate that the most stringent test occurs when the number of injected signal events is small (signal to background ratio or S/B equal to zero) and therefore the results shown here correspond to that case. Table 8.8 shows the bias estimates for one of the search regions, where you can see the relative biases for all possible function passing the AIC test. Finally, the function with the least number of free parameters and having a relative bias smaller than 30% – which yield only an additional error of 5% – is selected as the background model. The final selection for all the signal regions is shown in Table 8.9.

## 8.7 Systematic Uncertainties

The dominant systematic uncertainty is the uncertainty on the prediction of the non-resonant background shape and normalization. These are propagated by profiling the overall normalization and the shape parameters of the non-resonant background functional form.

Sub-dominant systematic uncertainties on the SM Higgs background are propagated through log-normal nuisance parameters, and take into account both theoretical and instrumental effects. The effects considered include missing higher order

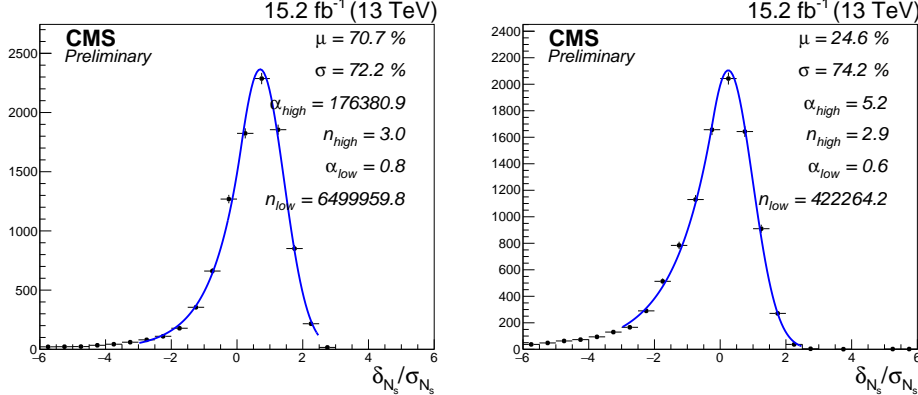


Figure 8.14: Examples of the bias distribution for bin0 (HighPt,  $M_R > 600, R^2 > 0.025$ ). Left:  $f_1$  (assumed parent function) = poly3,  $f_2$  (tested function) = singleExp; right:  $f_1$  = poly3,  $f_2$  = poly3. From the left plot we can see that singleExp does not pass the bias test since it has large bias to fit poly3.

Table 8.8: Examples of the bias estimate for different function pairs passing the AIC test for bin0 (HighPt,  $M_R > 600, R^2 > 0.025$ ). Functions in the first column are the assumed parent functions ( $f_1$ ), while functions in the first row are the ones being tested ( $f_2$ ). In the first row, the numbers in brackets are the AIC weights.

–	singlePow(0.247)	singleExp(0.232)	poly3(0.183)	poly2(0.177)
singlePow	(21.3± 1.0)%	(19.3± 1.0)%	(17.8± 1.0)%	(18.5± 1.4)%
singleExp	(22.9± 2.0)%	(18.3± 1.0)%	(7.9± 1.3)%	(18.7± 2.0)%
poly3	(69.9± 1.5)%	(70.7± 0.9)%	(24.6± 1.3)%	(33.5± 1.0)%
poly2	(60.6± 0.9)%	(62.6± 0.9)%	(15.7± 1.9)%	(17.4± 1.4)%

corrections, parton distribution functions, trigger and selection efficiencies, jet energy scale uncertainties, b-tagging efficiencies, and the uncertainty on the integrated luminosity. The typical size of these effects on the expected limit is summarized in Table 8.10.

The systematic uncertainty on the photon energy scale is implemented as a nuisance parameter that shifts the Higgs peak position, and is Gaussian constrained in the fit to lie within 1% of the nominal Higgs mass peak predicted by the Monte Carlo simulation. There is also a systematic uncertainty on the shape of the  $\sigma_M/M$  distribution, which allows for migration of SM Higgs background and signal events between the HighRes and the LowRes categories.

Table 8.9: List of the selected background functions for different search regions.

Bin	Category	LowMR	HighMR	LowRsq	HighRsq	Function	AIC weight	Max bias / $\sigma_{\text{stat}}$
0	highpt	600	10000	0.025	10.000	poly3	0.183	24.6%
1	highpt	150	600	0.130	10.000	singleExp	0.356	17.7%
2	highpt	1250	10000	0.000	0.025	singleExp	0.359	16.4%
3	highpt	150	450	0.000	0.130	–	–	–%
4	highpt	450	600	0.000	0.035	poly2	0.324	-24.2%
5	highpt	450	600	0.035	0.130	singleExp	0.348	16.1%
6	highpt	600	1250	0.000	0.015	singleExp	0.295	-3.6%
7	highpt	600	1250	0.015	0.025	singleExp	0.344	14.8%
8	hzbb	150	2000	0.00	10.000	singleExp	0.323	4.5%
9	highres	150	250	0.000	0.175	–	–	–%
10	highres	150	250	0.175	10.000	poly2	0.132	16.9%
11	highres	250	10000	0.05	10.000	singlePow	0.237	-19.1%
12	highres	250	600	0.000	0.05	singlePow	0.118	25.7%
13	highres	600	10000	0.000	0.05	singleExp	0.256	-3.4%
14	lowres	150	250	0.000	0.175	singleExp	0.529	-3.4%
15	lowres	150	250	0.175	10.000	singleExp	0.365	7.9%
16	lowres	250	10000	0.05	10.000	singleExp	0.358	-13.9%
17	lowres	250	600	0.000	0.05	–	–	–%
18	lowres	600	10000	0.000	0.05	singleExp	0.364	-9.0%

Table 8.10: Summary of systematic uncertainties and their size.

Uncertainty Source	Size
Luminosity	5.7%
PDFs and QCD Scale Variations	15-30%
Trigger and selection efficiency	3%
Jet energy scale	1-5%
Photon Energy Scale	1%
B-tagging efficiency	4%
$\sigma_M/M$ categorization	4%

## 8.8 Results and Interpretations

The fit results for all search regions using the combination of the 2015 dataset ( $2.3 \text{ fb}^{-1}$ ) and the 2016 dataset ( $12.9 \text{ fb}^{-1}$ ) are shown below. Figures 8.15, 8.16, and 8.17 show the results for the HighPt event category. The results for the H( $\gamma\gamma$ )-H/Z(bb) category are shown in Figure 8.18. Finally, the results for the HighRes and LowRes categories are shown in Figures 8.19 to 8.23.

The data yields, expected background yields, and best fit signal yields are summarized in Table 8.11 for all search region bins, together with the local statistical significance of the excess for each bin. The observed signal significance is summarized in Figure 8.24 for all statistically independent bins. The bin with the largest significance occurs in the HighPt category with  $M_R > 600 \text{ GeV}$  and  $R^2 > 0.025$ , and has a local significance of  $2.5\sigma$ . Accounting for the number of search region bins, this corresponds to a global significance of  $1.4\sigma$ .

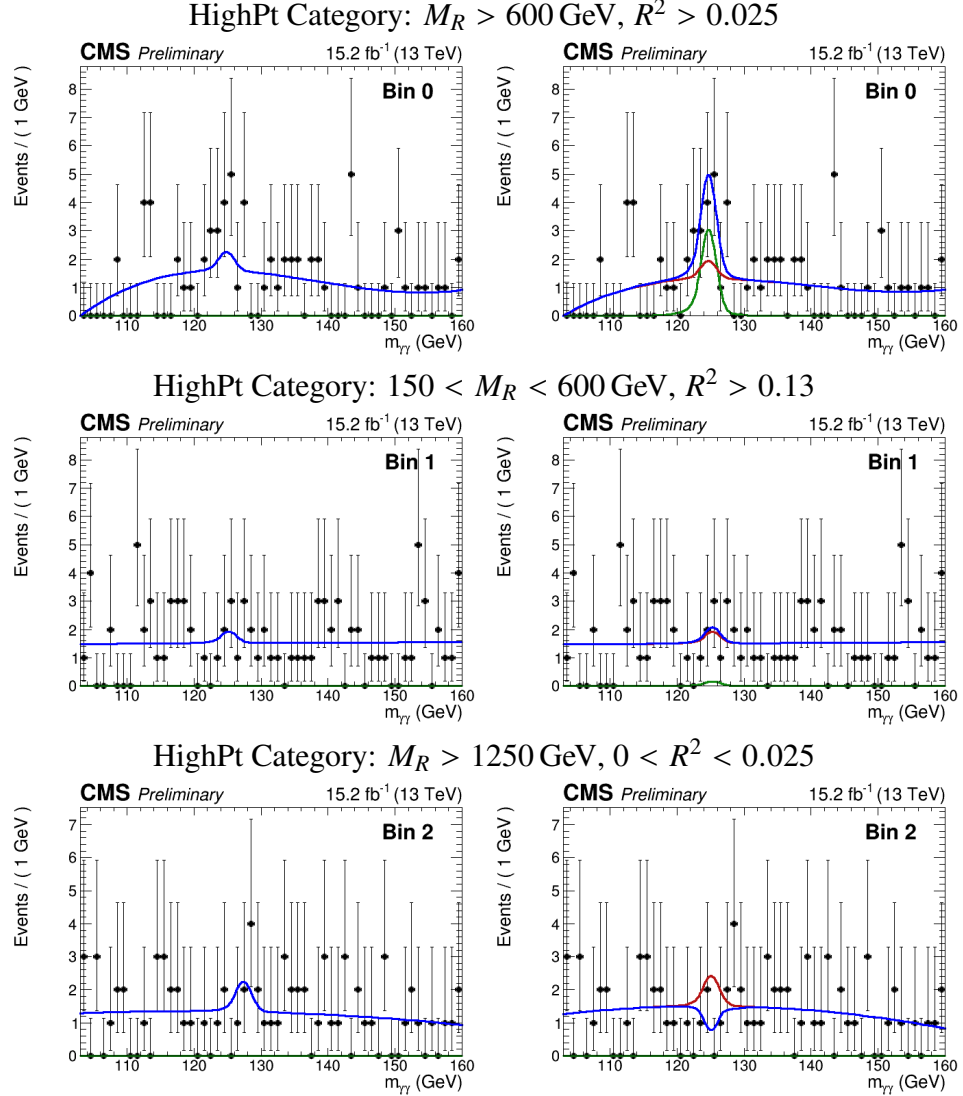


Figure 8.15: The diphoton mass distribution for various search region bins in the HighPt category are shown along with the background-only fit (left) and the signal plus background fit (right). The red curve represents the background prediction; the green curve represents the signal; and the blue curve represents the sum of the signal and background. The definition of the search bin is labeled above each pair of plots.

We interpret these results in terms of limits on the production cross-section times branching ratio for sbottom pair production with a cascade decay to a Higgs boson, a bottom quark, and the LSP. The expected and observed limits on the sbottom pair production cross section is shown in Figure 8.25 as a function of the sbottom mass and the LSP mass. The observe significance is also computed for this simplified model and shown in Figure 8.26.

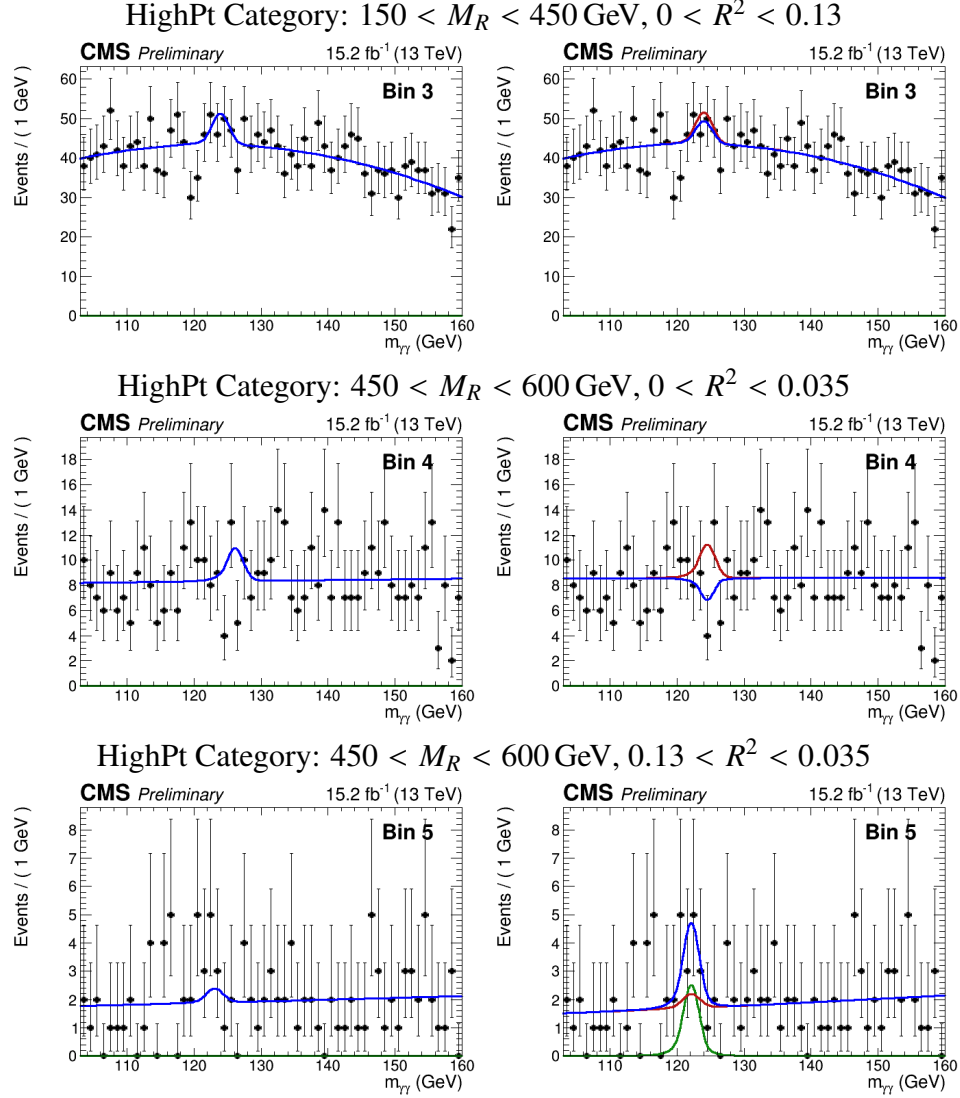


Figure 8.16: The diphoton mass distribution for various search region bins in the HighPt category are shown along with the background-only fit (left) and the signal plus background fit (right). The red curve represents the background prediction; the green curve represents the signal; and the blue curve represents the sum of the signal and background. The definition of the bin is labeled above each pair of plots.

## 8.9 Summary

A search for anomalous Higgs boson production through decays of supersymmetric particles is performed with data collected in 2015 and 2016 by the CMS experiment at the CERN LHC. Proton collisions collected at a center-of-mass energy  $\sqrt{s} = 13 \text{ TeV}$  are considered, corresponding to an integrated luminosity of about  $15.2 \text{ fb}^{-1}$  ( $2.3 \text{ fb}^{-1}$  from 2015 and  $12.9 \text{ fb}^{-1}$  from 2016). Higgs boson candidates

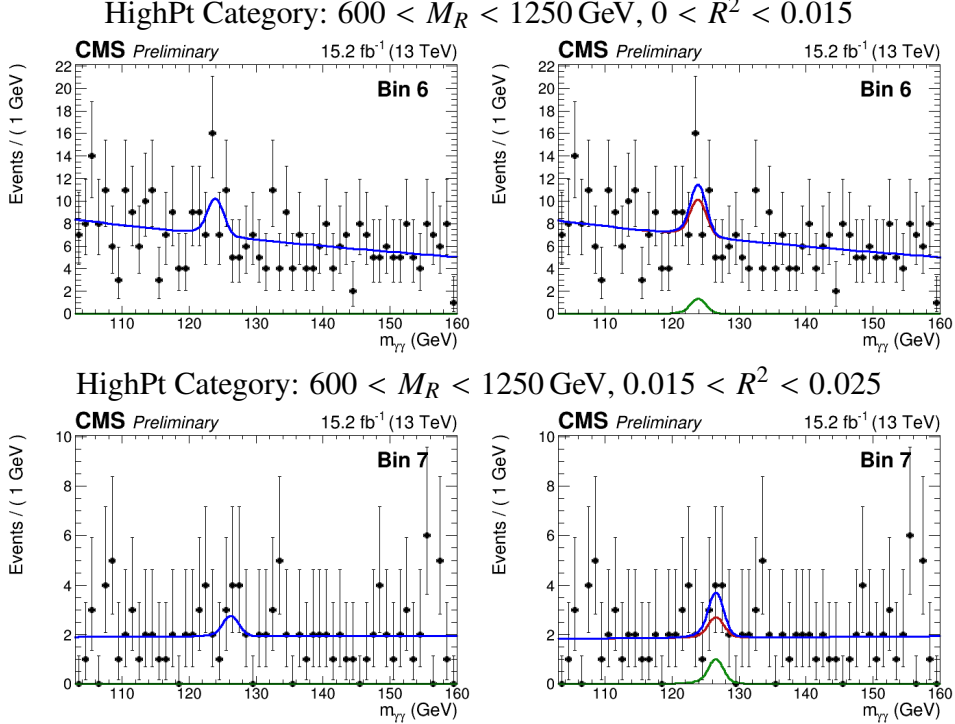


Figure 8.17: The diphoton mass distribution for various search region bins in the HighPt category are shown along with the background-only fit (left) and the signal plus background fit (right). The red curve represents the background prediction; the green curve represents the signal; and the blue curve represents the sum of the signal and background. The definition of the bin is labeled above each pair of plots.

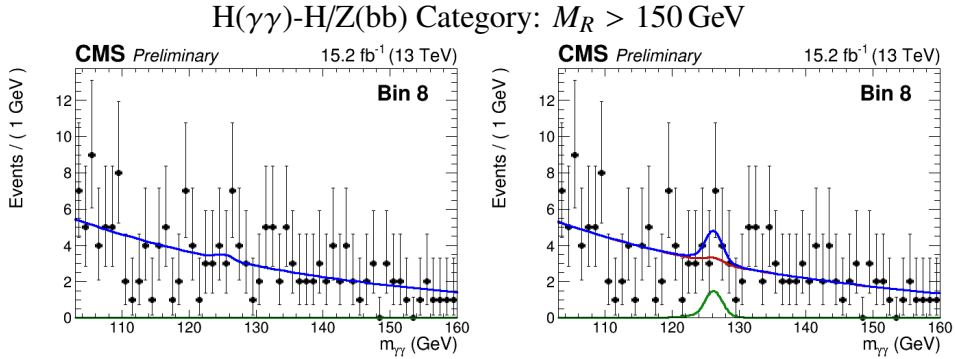


Figure 8.18: The diphoton mass distribution for various search region bins in the  $H(\gamma\gamma)$ - $H/Z(bb)$  category are shown along with the background-only fit (left) and the signal plus background fit (right). The red curve represents the background prediction; the green curve represents the signal; and the blue curve represents the sum of the signal and background. The definition of the bin is labeled above each pair of plots.

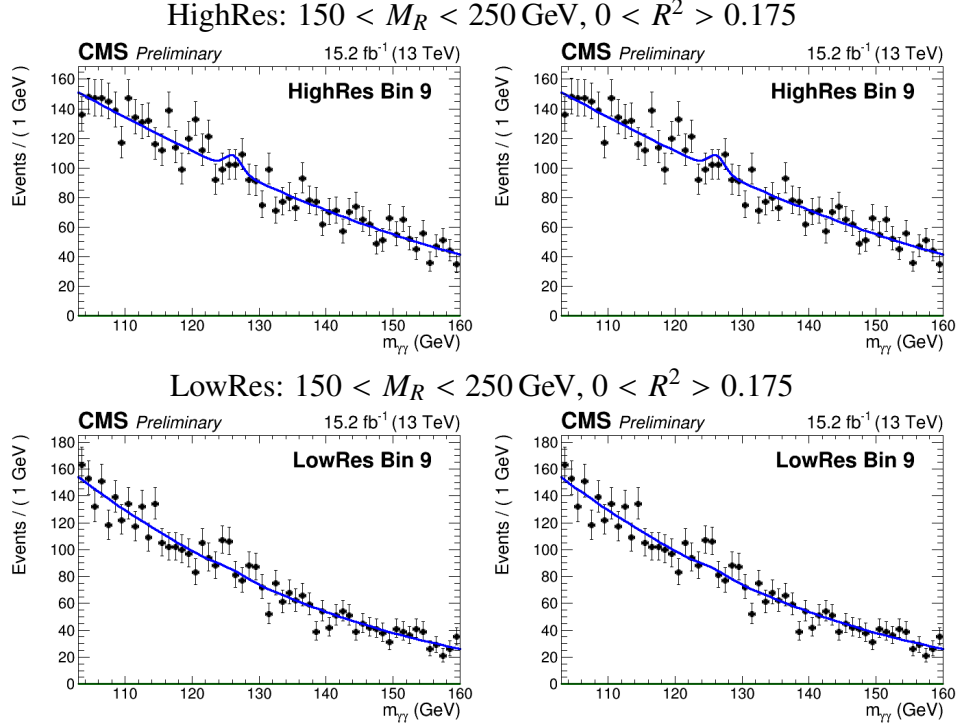


Figure 8.19: The diphoton mass distribution for the search region bin 9 are shown along with the background-only fit (left) and the signal plus background fit (right). The top row shows the HighRes category, while the bottom row shows the LowRes category. The red curve represents the background prediction; the green curve represents the signal; and the blue curve represents the sum of the signal and background. The definition of the bin is labeled above each pair of plots.

are reconstructed from pairs of photons in the central part of the detector. The razor variables  $M_R$  and  $R^2$  are used to suppress SM Higgs boson production and other SM processes. The non-resonant background is estimated through a data-driven fit to the diphoton mass distribution using a functional form model selected by a combination of the AIC score and the result of a series of bias tests. The standard model Higgs background is estimated using the Monte Carlo simulation, with systematics on instrumental and theoretical uncertainties propagated. We interpret the results in terms of production cross-section limits on sbottom pair production each decaying to a Higgs boson, a b-quark, and the LSP, and exclude sbottoms with mass below 350 GeV.

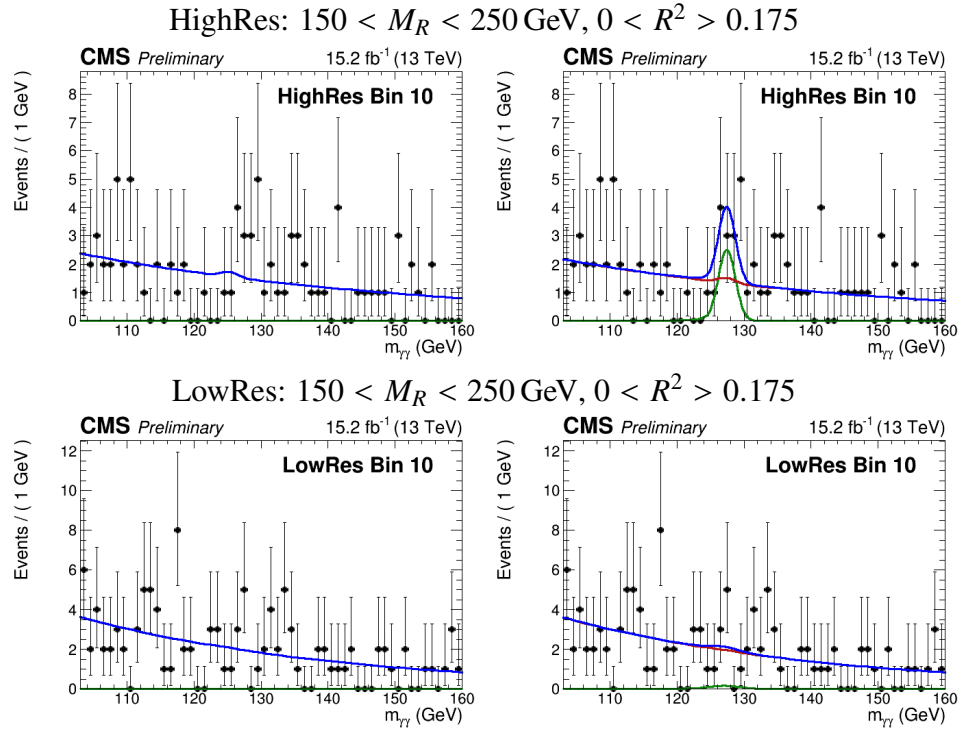


Figure 8.20: The diphoton mass distribution for the search region bin 10 are shown along with the background-only fit (left) and the signal plus background fit (right). The top row shows the HighRes category, while the bottom row shows the LowRes category. The red curve represents the background prediction; the green curve represents the signal; and the blue curve represents the sum of the signal and background. The definition of the bin is labeled above each pair of plots.

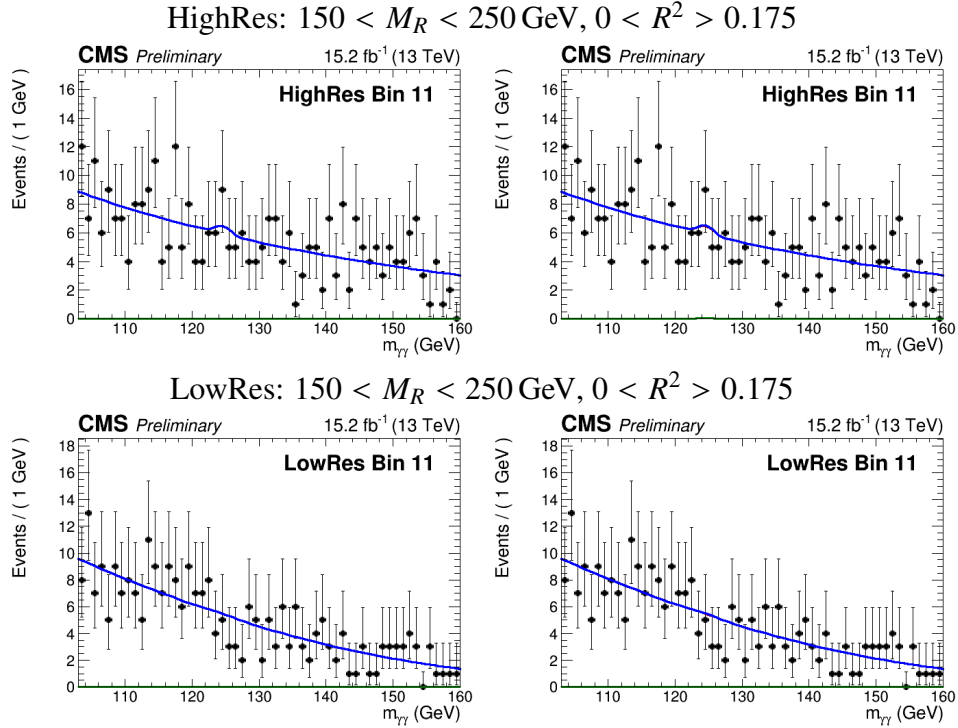


Figure 8.21: The diphoton mass distribution for the search region bin 11 are shown along with the background-only fit (left) and the signal plus background fit (right). The top row shows the HighRes category, while the bottom row shows the LowRes category. The red curve represents the background prediction; the green curve represents the signal; and the blue curve represents the sum of the signal and background. The definition of the bin is labeled above each pair of plots.

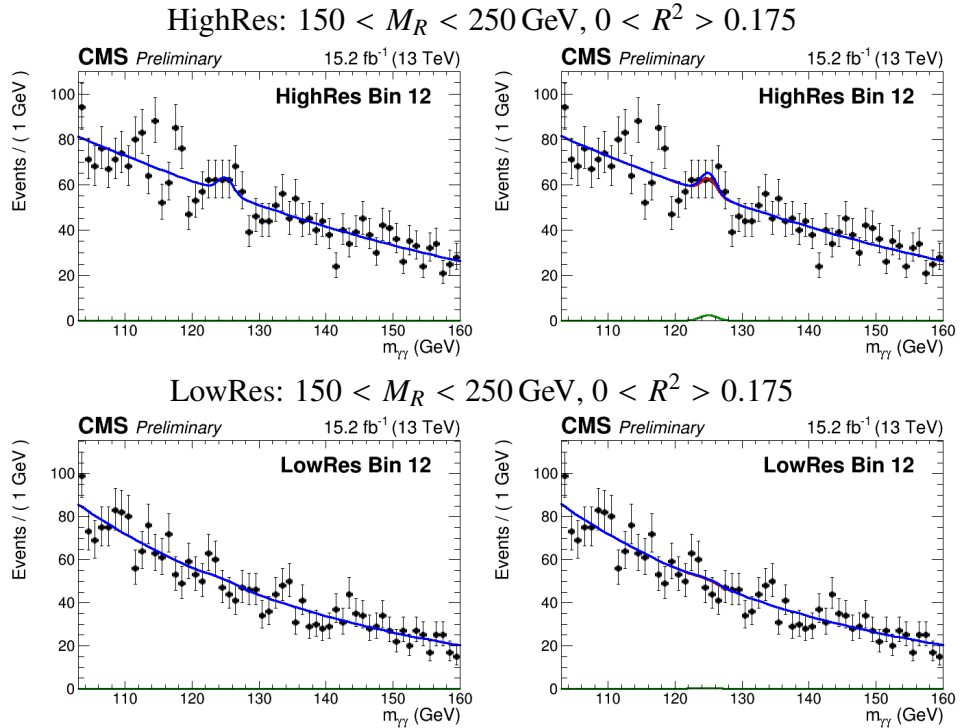


Figure 8.22: The diphoton mass distribution for the search region bin 12 are shown along with the background-only fit (left) and the signal plus background fit (right). The top row shows the HighRes category, while the bottom row shows the LowRes category. The red curve represents the background prediction; the green curve represents the signal; and the blue curve represents the sum of the signal and background. The definition of the bin is labeled above each pair of plots.

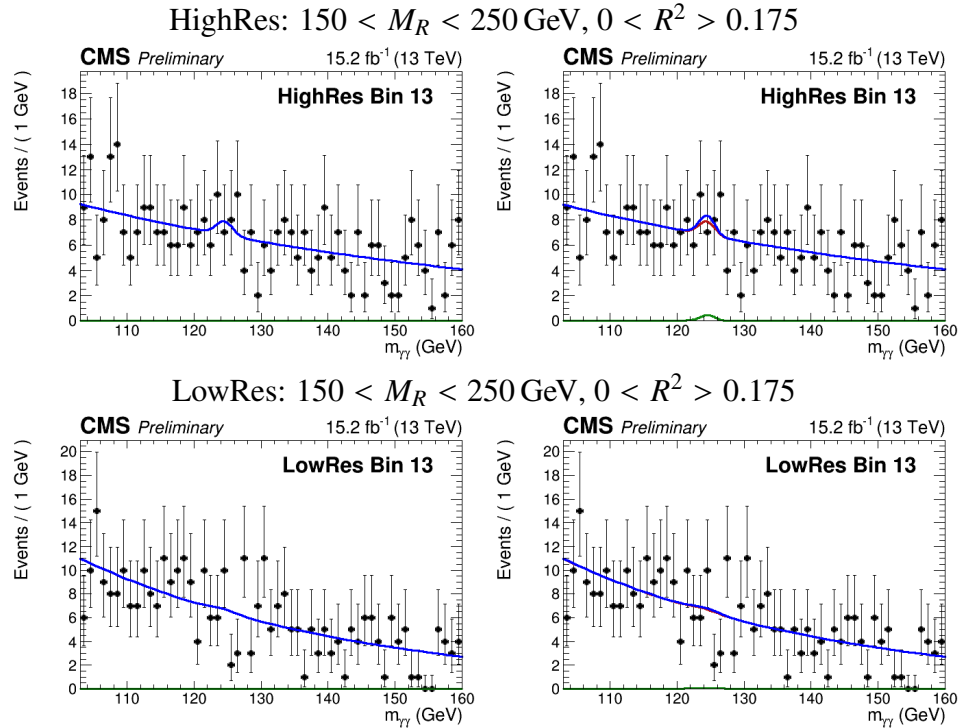


Figure 8.23: The diphoton mass distribution for the search region bin 13 are shown along with the background-only fit (left) and the signal plus background fit (right). The top row shows the HighRes category, while the bottom row shows the LowRes category. The red curve represents the background prediction; the green curve represents the signal; and the blue curve represents the sum of the signal and background. The definition of the bin is labeled above each pair of plots.

Table 8.11: The non-resonant background yields, SM Higgs background yields, best fit signal yields, and observed local significance are shown for the signal plus background fit in each search region bin. The uncertainties include both statistical and systematic components. The non-resonant background yields shown correspond to the yield within the window between 122 GeV and 129 GeV and is intended to better reflect the background under the signal peak. The observed significance for the bins in HighRes and LowRes categories are identical because they are the result of a simultaneous fit. The significance is computed using the profile likelihood, where the sign reflects whether an excess (positive sign) or deficit (negative sign) is observed.

Bin	Category	Yields				Obs. Local Significance
		Non-Resonant Bkg	Exp. SM Higgs	Fitted SM Higgs	Best Fit Signal	
0	HighPt	10.2 ± 1.4	2.0 ± 0.4	2.0 ± 0.7	9.7 ± 5.1	$2.5\sigma$
1	HighPt	10.5 ± 1.3	1.4 ± 0.3	1.4 ± 0.3	0.5 ± 3.4	$0.2\sigma$
2	HighPt	10.5 ± 1.6	3.0 ± 0.6	2.9 ± 0.9	-5.2 ± 2.5	- $1.4\sigma$
3	HighPt	304 ± 16.6	27.7 ± 8.0	27.7 ± 11.2	-7.9 ± 18.1	- $0.4\sigma$
4	HighPt	60 ± 3.0	8.8 ± 2.5	8.8 ± 3.5	-13.9 ± 6.6	- $1.6\sigma$
5	HighPt	12.1 ± 1.4	1.7 ± 0.4	1.7 ± 0.6	8.3 ± 4.7	$1.9\sigma$
6	HighPt	47.6 ± 2.6	10.7 ± 2.7	10.7 ± 3.7	4.1 ± 7.3	$0.6\sigma$
7	HighPt	13.1 ± 1.4	2.7 ± 0.8	2.7 ± 1.0	3.2 ± 4.1	$0.8\sigma$
8	H( $\gamma\gamma$ )-H/Z(bb)	21.6 ± 1.8	1.0 ± 0.2	1.0 ± 0.2	5.3 ± 4.6	$1.0\sigma$
9	HighRes	697 ± 10.6	33.5 ± 10.4	33.2 ± 12.1	0.0 ± 21.4	- $0.2\sigma$
10	HighRes	9.8 ± 1.2	0.6 ± 0.1	0.6 ± 0.1	8.2 ± 4.1	$1.7\sigma$
11	HighRes	40.7 ± 2.4	1.7 ± 0.4	1.7 ± 0.6	0.2 ± 5.5	$0.0\sigma$
12	HighRes	387 ± 14.6	21.5 ± 5.4	21.5 ± 9.1	8.1 ± 14.9	$0.5\sigma$
13	HighRes	46.8 ± 2.6	3.5 ± 1.0	3.5 ± 1.2	1.3 ± 6.0	$0.2\sigma$
9	LowRes	591 ± 9	11.6 ± 3.8	11.9 ± 5.1	0.2 ± 10.1	- $0.2\sigma$
10	LowRes	14.1 ± 1.4	0.2 ± 0.1	0.2 ± 0.1	1.1 ± 0.8	$1.7\sigma$
11	LowRes	36.6 ± 9.2	0.6 ± 0.3	0.6 ± 0.3	0.1 ± 1.8	$0.0\sigma$
12	LowRes	341 ± 7	7.9 ± 2.3	7.9 ± 3.5	2.8 ± 5.0	$0.5\sigma$
13	LowRes	44.3 ± 2.4	1.4 ± 0.4	1.4 ± 0.7	0.5 ± 2.6	$0.2\sigma$

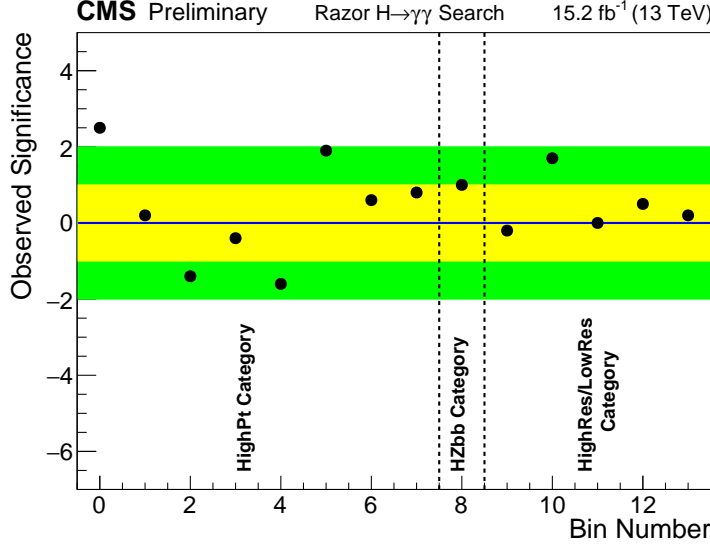


Figure 8.24: The observed significance in units of standard deviations is plotted for each search bin. The significance is computed using the profile likelihood, where the sign reflects whether an excess (positive sign) or deficit (negative sign) is observed. The categories that the bins belong to are labeled at the bottom. The yellow and green bands represent the  $1\sigma$  and  $2\sigma$  regions, respectively.

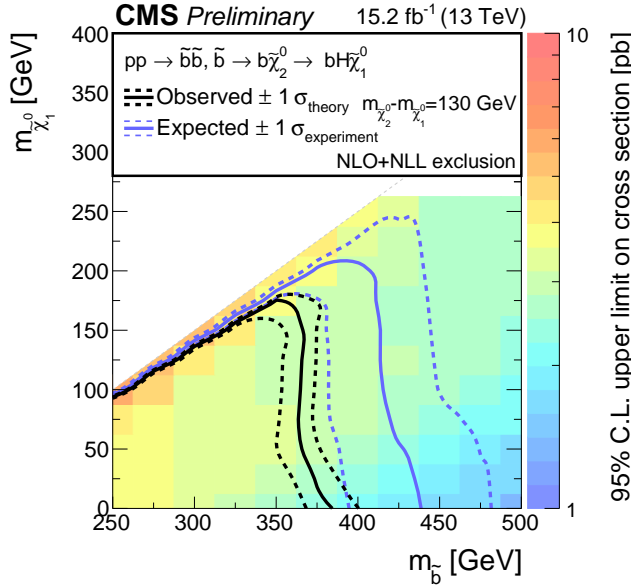


Figure 8.25: The observed 95% confidence level (C.L.) upper limits on the production cross section for sbottom pair production decaying to a bottom quark, a Higgs boson, and the LSP are shown. The solid and dotted black contours represent the observed exclusion region and its  $1\sigma$  bands, while the analogous blue contours represent the expected exclusion region and its  $1\sigma$  bands.

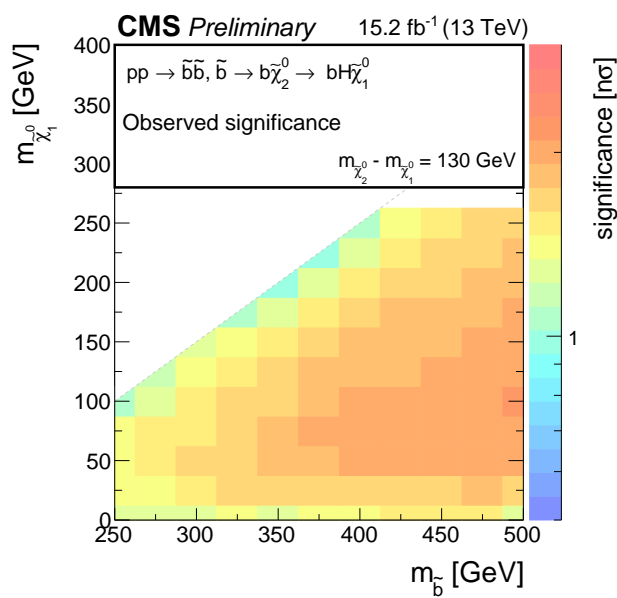


Figure 8.26: The observed significance scan for sbottom pair production decaying to a bottom quark, a Higgs boson, and the LSP is shown.

## **Part IV**

# **Precision Timing Calorimetry**

## C h a p t e r 9

### INTRODUCTION

Calorimeters are a key detector systems in high energy physics experiments ranging from neutrino to particle collider detectors. In particular, electromagnetic (EM) calorimeters are designed to fully contain the energy deposited by electrons, positrons, and photons ( $e/\gamma$ ); as well as to provide position information by means of their granular design. They are usually divided in two types: homogeneous and sampling, homogenous calorimeters are those in which their entire volume is composed of sensitive media, while sampling calorimeters are composed of alternating layers of sensitive and absorber media.

Homogeneous EM calorimeters are usually made out of dense scintillating crystals (BGO, BaF<sub>2</sub>, LYSO, PbWO<sub>4</sub>, among others) or liquid noble gases (Ar, Kr, Xe) and they provide an outstanding energy resolution for  $e/\gamma$ . For example, the CMS EM calorimeter [**cmsECAL**] is composed of PbWO<sub>4</sub> scintillating crystals coupled to avalanche photodiodes and with an energy resolution of

$$\frac{\sigma_E}{E} = \frac{2.8\% \sqrt{\text{GeV}}}{\sqrt{E}} \oplus \frac{12\% \text{ GeV}}{E} \oplus 0.3\%. \quad (9.1)$$

Sampling EM calorimeters use a sensitive medium such as scintillating crystals, liquid noble gases, and silicon, among others to measure the energy the incoming particle; while the absorber medium is a high density material such as lead or tungsten in order to require less volume to completely contain the impinging particle's energy and thus result in a compact design. An example of such an EM calorimeter is the ATLAS lead-liquid argon (LAr) sampling calorimeter with an energy resolution of

$$\frac{\sigma_E}{E} = \frac{10.1\% \sqrt{\text{GeV}}}{\sqrt{E}} \oplus \frac{0.25\% \text{ GeV}}{E} \oplus 0.17\%. \quad (9.2)$$

Particle collider experiments at the LHC such as ATLAS and CMS use EM calorimeters in the  $e/\gamma$  four-momentum and jet energy measurements, particle identification algorithms, trigger systems, and the measurement of the missing transverse energy in each proton-proton collision. Therefore, maintaining the current performance of

the EM calorimeters is critical for the current and future physics measurements of those experiments.

In order to provide the necessary datasets to perform precision measurements of the Higgs couplings, probe rare Higgs processes, study the scattering of longitudinally polarized W bosons, and search for new physics. The high luminosity upgrade of the Large Hadron Collider (HL-LHC) at CERN [99] is expected to provide instantaneous luminosities of  $5 \times 10^{34} \text{ cm}^{-2}\text{s}^{-1}$ . This enhanced data rate will increase the simultaneous interactions per bunch crossing (pileup) from an average of 20-40 to 140-200.

The large amount of pileup foreseen for the HL-LHC will increase the likelihood of confusion in the reconstruction of events of interest, due to the contamination from particles produced in different pileup interactions. The ability to discriminate between jets produced in the events of interests – especially those associated with the vector boson fusion processes – and jets produced by pileup interactions will be degraded, the missing transverse energy resolution will deteriorate, and several other physics objects performance metrics will suffer.

One way to mitigate the detrimental pileup effects, complementary to precision tracking methods, is to perform a time of arrival measurement associated with a particular layer of the calorimeter, allowing for a time assignment for both charged particles and photons. Such a measurement with a precision of about 20 to 30 ps, when unambiguously associated to the corresponding energy measurement, will significantly reduce – approximately a factor of 10 – the inclusion of pileup particles in the reconstruction of the event of interest given that the spread in collision time of pileup interactions is about 200 ps. The association of the time measurement to the energy measurement is crucial, leading to a prototype design that requires the time and energy measurements to be performed in the same sensitive medium. It is in this context that this thesis presents various prototype calorimeters equipped with precision timing capabilities and studies the current limits on their time resolution.

This part of the thesis is organized as follows: section 9.1 provides a brief and general introduction to EM calorimeters, chapter 10 is dedicated to the timing properties of LYSO crystal scintillator based calorimeters, chapter 11 discusses the possibility of a precision timing sampling calorimeter where the sensitive medium is a microchannel plate (MCP) [] chapter 12 discusses the timing capabilities of a sampling calorimeter where the sensitive medium is a 350 microns silicon sensor. finally, chapter ?? summarizes the results and possible improvements as well as

future measurements.

### 9.1 EM Calorimeter Preliminaries

Calorimeters are highly complex instruments and therefore some background is required to understand the subsequent sections in this chapter; this section is intended to provide a short overview of the most important effects – mostly different physical processes in different energy regimes – and the relevant considerations when designing a calorimeter.

#### EM Shower Development

High energy  $e/\gamma$  (with energies above 1 GeV) will develop an EM shower upon entering the calorimeter. The processes involved in the EM shower development are few and well understood. Photons lose energy mostly by photoelectric effect, Compton scattering, or pair production of electrons and positrons. The latter dominates at high energies and it is responsible for the shower development, while photoelectric effect overwhelmingly dominates at low energies (typically below 10 MeV), Figure 9.1 shows the photon cross section as a function of the incoming photon energy in lead. Electrons and positrons lose energy mainly due to two processes, ionization and radiation hereafter referred to as bremsstrahlung, see Figure 9.2. The latter dominates at high energies while the former dominates at low energies. The energy at which these two processes are equally relevant is defined as the critical energy ( $E_c$ ) [criticalE], Figure 9.3 shows a graphical representation of this definition.

Empirical functional forms for  $E_c$  can be obtained when a distinction between gaseous and liquid or solid media is made, since there are significant differences in ionization that arise mainly due to the density effect. Figure 9.4 shows the experimental data for  $E_c$  as a function of the atomic number ( $Z$ ) along with the corresponding fits, the functional forms for  $E_c$  are

$$E_c^{gas} = \frac{710 \text{ MeV}}{Z + 0.92}, \quad \text{and} \quad E_c^{solid} = \frac{610 \text{ MeV}}{Z + 1.24}. \quad (9.3)$$

EM showers are then produced when high energy photons (electron/positron) enter the calorimeter media and loses energy by pair production (bremsstrahlung), the subsequently  $e^+/e^-$  pair (high energy photon produced by radiation) loses energy by bremsstrahlung (pair production). The number of particles produced by this multiplicative process increases until a maximum is reached (shower maximum) at the certain depth inside the calorimeter. After this point the newly created parti-

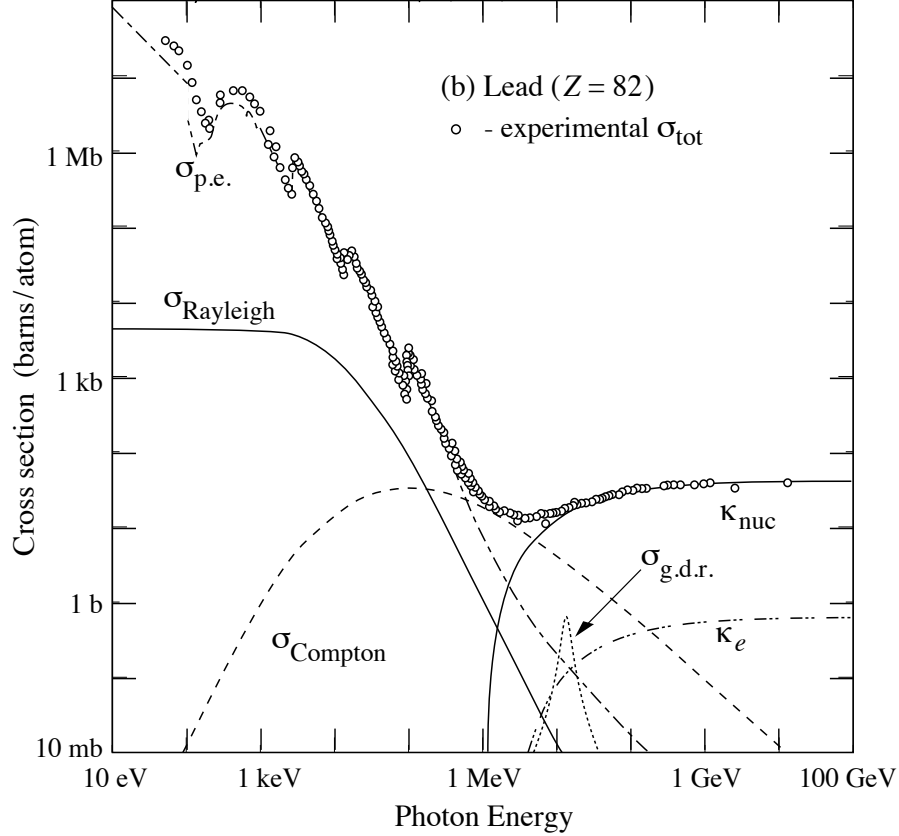


Figure 9.1: Cross section as a function of the incoming photon energy in lead.

cles have low energies and therefore other processes such as photoelectric effect, Compton scattering, and ionization start to become relevant. The shower profile in the longitudinal direction for a 30 GeV electron in iron is shown in Figure 9.5. The longitudinal shower profile is also a function of the incoming particle energy, Figure 9.5 shows this effect for electrons of different energies in copper.

Shower development is described independently of the calorimeter material by two quantities: the **radiation length** ( $X_0$ ) and the **Molière radius** ( $R_M$ ). The radiation length is the characteristic amount traversed by high energy  $e/\gamma s$  in the longitudinal direction (along the original particle's direction), it is usually measured in  $\text{gcm}^{-2}$ . The quantitative definition is (a) the mean distance over which it and electron loses  $1/e$  of its initial energy, and (b)  $7/9$  of the pair production mean free path for high energy photons.  $X_0$  has been tabulated and calculated by Y. S Tsai [], the analytical expression is the following:

$$\frac{1}{X_0} = 4\alpha r_e^2 \frac{N_A}{A} \left[ Z^2 (L_{\text{rad}} - f(Z)) + Z L'_{\text{rad}} \right], \quad (9.4)$$

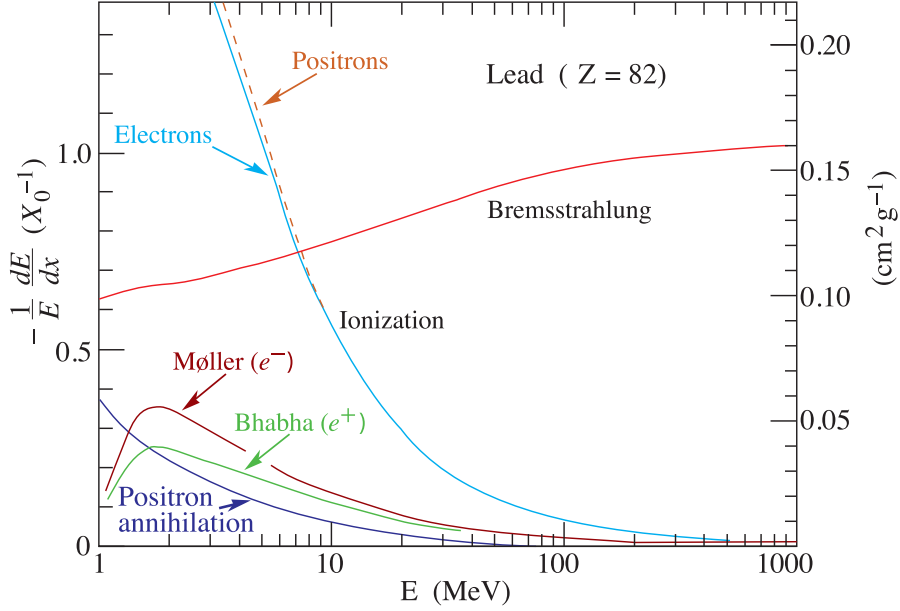


Figure 9.2: Fractional energy loss per radiation length in lead as a function of the electron/positron energy.

where  $\alpha$  is the fine structure constant,  $r_e$  is the classical electron radius,  $N_A$  is Avogadro's number,  $A$  is the atomic mass,  $Z$  is the atomic number,  $L_{\text{rad}}$  and  $L'_{\text{rad}}$  are shown in Table 9.1, and  $f(Z)$  is an infinite sum, nonetheless for chemical elements up to uranium can be expressed to the 4-decimal place accuracy by

$$f(Z) = (\alpha Z)^2 \left[ (1 + (\alpha Z)^2)^2 + 0.2020 - 0.0369(\alpha Z)^2 + 0.0083(\alpha Z)^4 - 0.0020(\alpha Z)^6 \right]. \quad (9.5)$$

Table 9.1: Tabulated values for  $L_{\text{rad}}$  and  $L'_{\text{rad}}$  from Y. S Tsai.

Element	$Z$	$L_{\text{rad}}$	$L'_{\text{rad}}$
H	1	5.31	6.144
He	2	4.79	5.621
Li	3	4.74	5.805
Be	4	4.71	5.924
Others	$> 4$	$\ln(184.15Z^{-1/3})$	$\ln(1194Z^{-2/3})$

The Molière radius is the characteristic size of the shower in the transverse direction and defined as the ratio of the radiation length and the critical energy:

$$R_M = X_0/E_c. \quad (9.6)$$

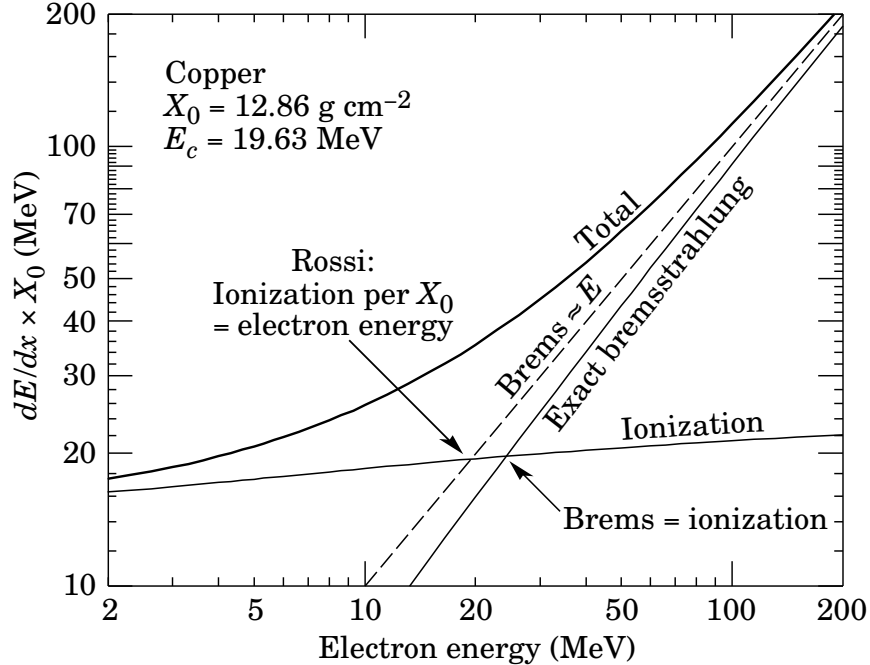


Figure 9.3: Graphical definition of the critical energy ( $E_c$ ). The intersection of the solid lines is the definition used in this thesis. The intersection between the solid (ionization) and dashed line is alternative definition.

The transverse spread of the shower is the result of high energy  $e^\pm$  moving away from the shower axis due to multiple scattering, as well as the isotropic production of low energy electrons and photons. Multiple scattering dominates the lateral evolution in the early stages while isotropic production dominates at the later stages of the shower evolution, after the shower maximum. This two components exhibit a characteristic exponential decay, see Figure 9.7, where the transverse energy density for electron showers in copper is shown.

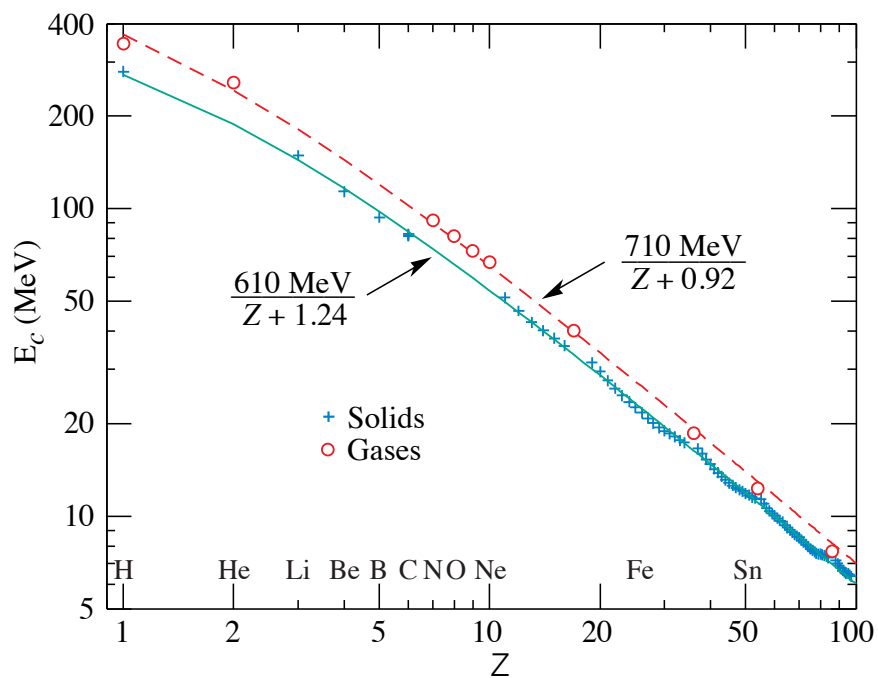


Figure 9.4: Electron critical energy ( $E_c$ ) for the chemical elements. Experimental data is shown for gases (red circles) and solids (magenta crosses). Fits are shown for gases (dashed red line) and solids (solid magenta line)

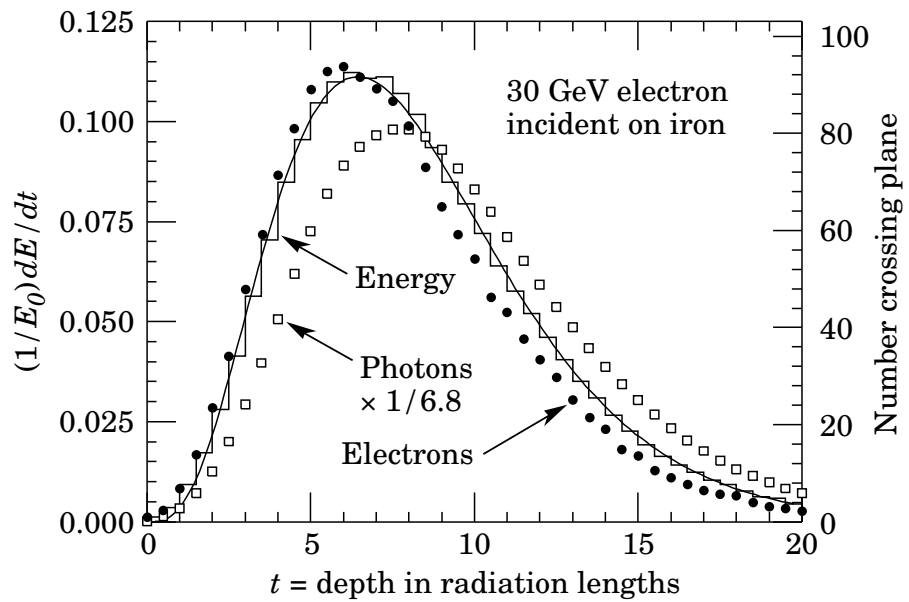


Figure 9.5: Shower profile in the longitudinal direction for a 30 GeV electron in iron from an EGS4 simulation. The solid line histogram shows the fractional energy per radiation length, and the solid line curve is a fit to the distribution using a gamma function. The number of electrons (solid circles) and photons (hollowed squares) with energies larger than 1.5 MeV and crossing planes at  $X_0/2$  intervals (scale on the right) is also shown. The number of photons has been scaled down to have the same area as the number of electrons distribution.

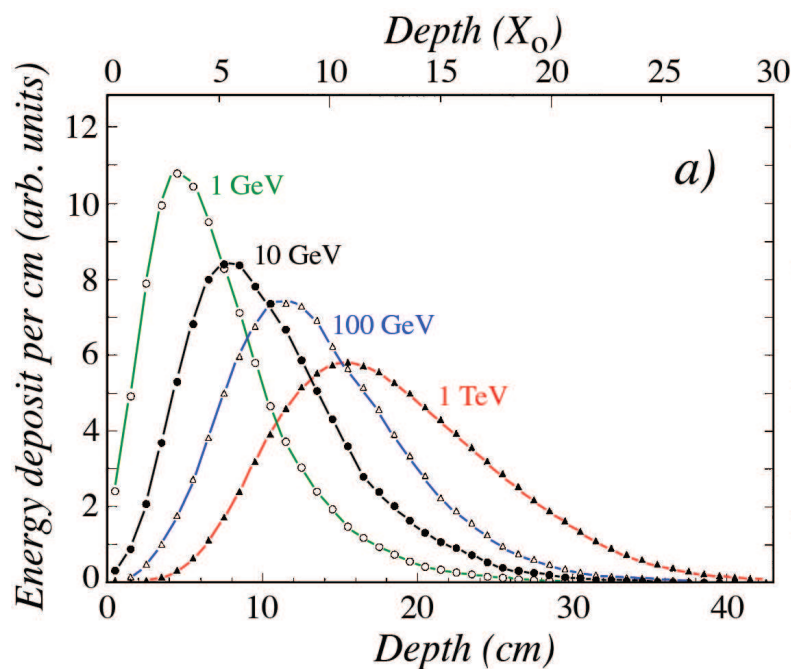


Figure 9.6: Shower profile in the longitudinal direction for electrons in copper. The different curves and points represent different electron energies ranging from 1 GeV-1 TeV.

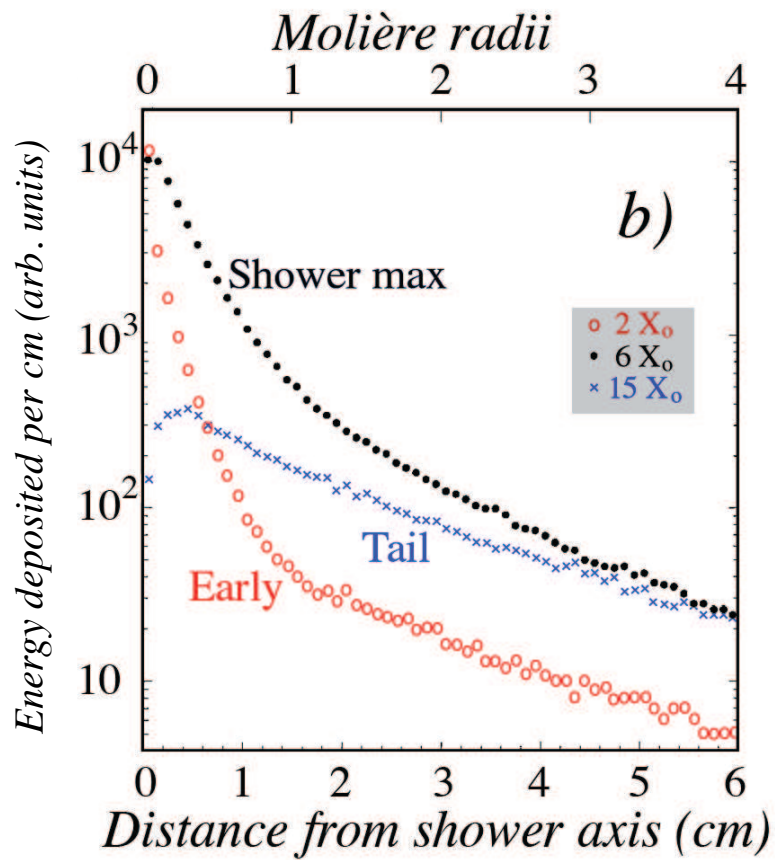


Figure 9.7: Energy deposited per unit length in the transverse direction for 10 GeV electrons in copper. The shower has been sample in three different places; at  $2X_0$  (red circles),  $6X_0$  (black dots), and  $15X_0$  (blue crosses).

**Important Calorimeter Quantities**

xyz

## Chapter 10

### LYSO-BASED CALORIMETERS

This chapter presents studies on measurements of the time of flight (TOF) using sampling calorimeters based on LYSO crystals.

#### 10.1 Introduction

Due to its very high light yield ( $\sim 30\text{K}$  photons/MeV) [101], and radiation tolerance [111, 90, 100, 73], LYSO is the active element of one of the options considered for the upgrade of the Compact Muon Solenoid (CMS) detector for the HL-LHC [68].

In Figure 10.1 presents a simplified illustration of the major time scales associated to the timing measurement using a monolithic crystal calorimeter. Upon entering the crystal the photon or electron travels at the speed of light, interacts, and begins to shower, producing scintillation light in the crystal. The time between the entry of the photon into the crystal and the first interaction is denoted by  $t_I$  and for high energy impinging particles it is the shower development time. The time associated with the conversion of the incident photon to scintillation light is denoted by  $t_S$ . The scintillation light travels from the point of interaction to the photodetector at the velocity  $c/\hat{n}$ , where  $\hat{n}$  is the effective index of refraction of the crystal [130]. The time associated with the propagation of the scintillation light to the photodetector is denoted by  $t_P$ . Once the scintillation light reaches the photodetector, the photons are converted into an electrical signal. The time associated with this process is known as the photodetector signal transit time,  $t_T$ . Finally, data acquisition (DAQ) system has a characteristic time constant  $t_D$ . Each of these time intervals will fluctuate or jitter on an event-by-event basis, contributing to the time resolution. Previous studies [115], measured the time resolution at different absorber thickness for electron beams with energies varying from 12 to 32 GeV, and showed that the time of arrival of the front of an electromagnetic shower can be determined with a precision better than 20 ps. The electronic time resolution of the DAQ system was measured to be about 6 ps. Using the same techniques, the time resolution of the MCP-PMT photodetectors used in the studies presented in this paper have been measured to be between 11 ps and 14 ps, depending on the exact device.

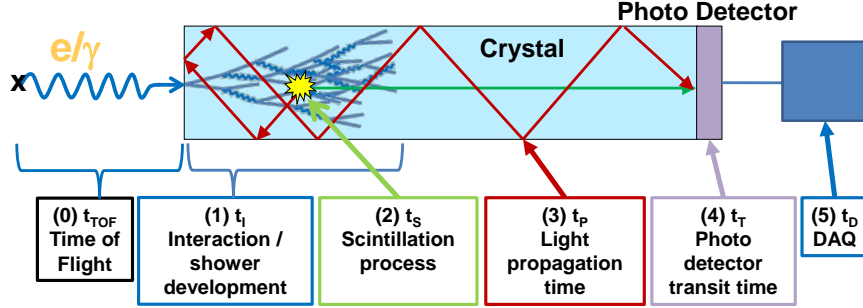


Figure 10.1: Timing measurement schematic breakdown using a monolithic, large scintillating crystal. The incident particle impinges on the crystal face from the left. The characteristic time intervals are discussed in the text.

To characterize the time resolution of an inorganic crystal scintillator calorimeter we study the contributions due to fluctuations in the shower development, scintillation process, and light propagation to the photodetector. We take advantage of the very large number of scintillation photons in a LYSO crystal which result in modest fluctuations associated with the creation and transit of each particular scintillation photon for a LYSO-based detector.

## 10.2 Experimental Setup

A schematic diagram of a typical TOF measurement setup is shown in Figure 10.2. All measurements involve a fast photodetector, typically a micro-channel-plate photomultiplier-tube (MCP-PMT), which measures the reference timestamp ( $t_0$ ), and a photodetector further downstream that detects the signal associated with the electromagnetic shower and provides a simultaneous energy and time ( $t_1$ ) measurement.

In these studies, two types of MCP-PMT photodetectors are used, one produced by Hamamatsu (model R3809-52) [1], and one produced by Photek (model PMT240) [2]. A DRS4 waveform digitizer V4 evaluation board [113] was used as the primary DAQ system, connected to a laptop via USB interface. The DRS chip contains a switched capacitor array (SCA) with 1024 cells, capable of digitizing eight analog signals with high speed (5 GSPS) and high accuracy (11.5 bit SNR). All experimental beam studies were performed at the Fermilab Test Beam Facility (FTBF), which provided proton beams from the Fermilab Main Injector accelerator at 120 GeV, and secondary electron beams of energies ranging from 4 to 32 GeV. All detector elements were placed inside of a dark box lined with copper foil, providing RF shielding. A  $2 \times 2 \text{ mm}^2$  scintillator was placed inside the box at the upstream extremity and used to trigger the DAQ readout, providing a strict constraint on the

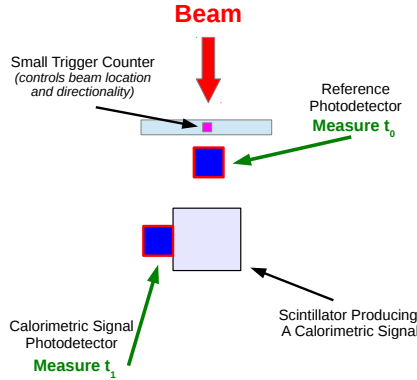


Figure 10.2: The basic schematic diagram of the experimental setup for a typical TOF measurement is shown to illustrate the basic detector elements. One photodetector is used as a time reference and the second measures energy and time simultaneously.

location and directionality of the beam particles used in the TOF studies. A differential Cherenkov counter (not shown in the schematic) provided by the FTBF facility and located upstream of our experimental hall, was used for electron identification.

### 10.3 Event Selection and Data Analysis

The primary target is to reconstruct the TOF of beam particles between different detector elements. Different time reconstruction algorithms are used for different detector elements, and all involve the assignment of a timestamp using specific features of each corresponding signal pulse. The signal pulse for the reference time detector is very sharp and symmetric around its maximum amplitude, as shown in Figure 10.3. Hence for the reference detector we determine the time position of the pulse peak by fit a Gaussian function to the peak of the pulse, using three sampling points before the pulse maximum and four sampling points after. The fitted mean parameter of the Gaussian function is assigned as the timestamp  $t_0$ . The signal pulse for the downstream time measurement is the result of scintillation light, and exhibits a fast rising edge and a significantly slower decay. Therefore, we assign the timestamp  $t_1$  using a constant fraction of the rising edge. A linear function is fit to the sampling points between 10% and 60% of the pulse maximum and the timestamp is assigned as the time at which the fitted linear function rises to 20% of the pulse maximum. Examples of fits performed to assign a time stamp from each pulse are shown in Figure 10.4. The impact from the choice of the functional forms is studied by using a set of alternative functions in the fits, and choosing the

one that results in the best time resolution. Among the functions that we tested, the difference between the best and worst performing functions was about 8 psec.

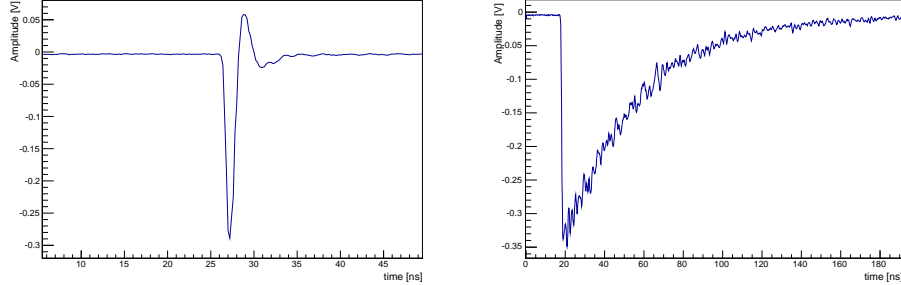


Figure 10.3: Sample pulses as digitized by the DRS4 board. On the left a pulse is shown from the reference Hamamatsu R3809 MCP-PMT, and on the right is a pulse from the Hamamatsu R3809 MCP-PMT optically coupled to a  $(1.7 \text{ cm})^3$  LYSO crystal cube recorded using 8 GeV electron beam.

Event selection and pulse cleaning procedures are used to eliminate abnormal pulses in the readout, as described in [115]. Large signals above 500 mV are rejected because they saturate the DRS4 inputs. Only pulses with amplitude larger than 20 mV are used for TOF measurements, in order to reduce the impact of noise from the DRS waveform digitizer DAQ system. Events containing more than one pulse within the 200 ns readout window are not used. Attenuators were used to extend the dynamic range of the DRS4 waveform digitizer in cases when a large fraction of signal pulses are saturated.

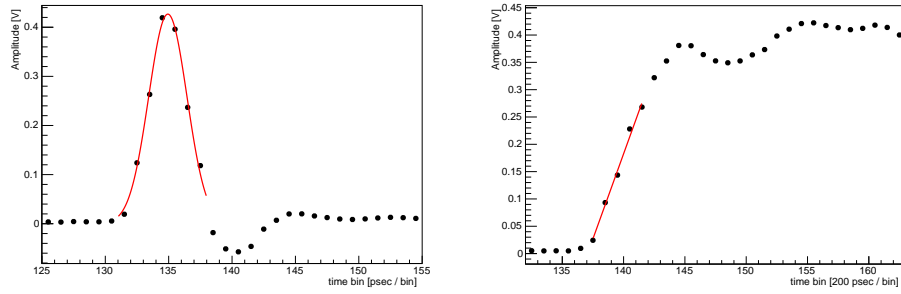


Figure 10.4: Sample fits used to assign timestamps to digitized MCP-PMT pulses. On the left is a pulse from the reference Hamamatsu R3809 MCP-PMT, and on the right is a pulse from the Hamamatsu R3809 MCP-PMT optically coupled to a  $(1.7 \text{ cm})^3$  LYSO crystal recorded during an 8 GeV electron run.

#### 10.4 Timing in LYSO-based Calorimeters

The timing measurement in LYSO-based calorimeters is driven by three main factors – other than the intrinsic transit time of the photodetector itself and the DAQ electronics : a) the shower profile fluctuations, b) the scintillation time, and c) the light propagation time. Stochastic processes during the development of an electromagnetic shower affect the time of observed signals, as both the transverse size and the depth of the shower can fluctuate event-by-event. Random processes in the scintillation mechanism and the randomization of the optical paths for the scintillation light affect both the speed of the signal formation and the time jitter. We study these effects using two independent experimental setups.

For a homogeneous crystal calorimeter we are interested in the characterization and optimization of the light propagation time, i.e. the time the scintillation light travels down the length of the crystal. Our setup uses a small LYSO cube with linear dimensions of 17mm as the active scintillation element. The size of this element reduces the effect of the light propagation time and jitter. The LYSO cube is placed behind about  $4.5 X_0$  radiation lengths of lead. Using this LYSO-based sampling calorimeter, we measure the time resolution of electrons.

We also study a shashlik calorimeter composed of alternating layers of tungsten and LYSO, in which scintillation light is extracted through wavelength shifting (WLS) fibers. In this setup, the light propagation time through the fiber is the dominant factor of the timing measurement. We study as a baseline an alternate version of this calorimeter where the light is extracted through direct optical coupling of the photodetectors at the edges of a few LYSO layers to minimize the light propagation time.

#### Timing Studies of the LYSO-based Sampling Calorimeter

We study the combined impact of the shower profile fluctuations, the scintillation mechanism in LYSO, and the light propagation time resolution using a sampling calorimeter with a  $(1.7 \text{ cm})^3$  LYSO cube as active element. The LYSO crystal is wrapped in Tyvek and attached to the Hamamatsu R3809 MCP-PMT (HAMB) with optical coupling [3]. A second Hamamatsu MCP-PMT photodetector (HAMA) is placed upstream of the calorimeter and is used to measure the reference time. A schematic diagram and a photograph of the experimental setup are shown in Figure 10.5.

To ensure that the electron beam is constrained to within a  $2 \times 2 \text{ mm}^2$  region, a

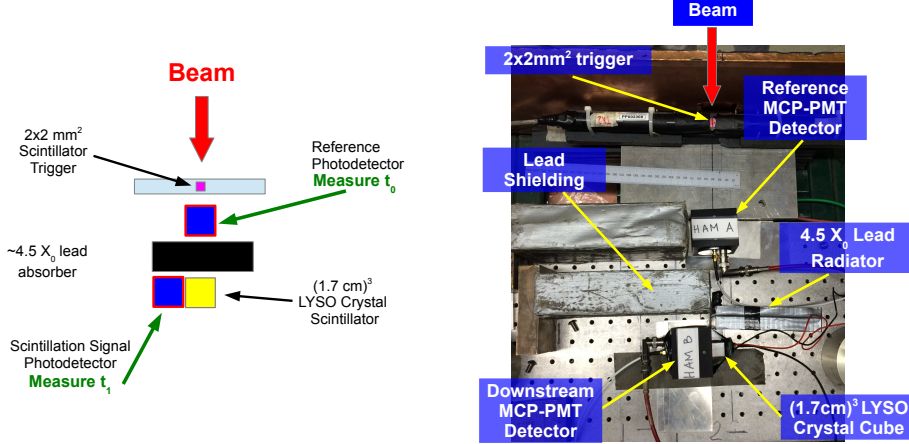


Figure 10.5: A schematic diagram of the experimental setup for the TOF measurement using the LYSO sampling calorimeter is shown on the left, along with a picture of the experimental setup shown on the right.

plastic scintillator placed upstream and approximately 2 mm by 2 mm in cross sectional area is used to trigger the DAQ readout on the DRS digitizer. Electron events are identified by requiring a signal with amplitude larger than 10 mV in a Cherenkov counter located upstream. Large lead bricks are placed upstream of the Hamamatsu R3809 MCP-PMT (HAMB), out of the path of the beam. These shield the photodetector from stray particles produced in events where an electromagnetic shower occurs upstream of the lead radiator. Such stray shower particles yield very fast signals which can significantly contaminate the scintillation signal. Using the same experimental setup without the LYSO active element in place, we find that stray shower type events yield less than 10% contamination and give a negligible effect on the scintillation signal.

The thickness of the LYSO active element is relatively small and captures only a fraction of the total energy of the electron, but yields a reasonable energy measurement as it is close to the shower maximum.

The TOF measurement is performed using the LYSO sampling calorimeter for electron beams with energies varying from 4 GeV to 32 GeV. The corresponding measured TOF distributions are shown in Figure 10.6. We achieve the best time resolution of 34 ps for electrons with beam energy of 32 GeV.

The time resolution measurement is plotted as a function of the beam energy in Figure 10.15 (left). We fit the result to the sum of a  $1/\sqrt{E}$  term and a constant term of about 11 ps. Given that we measure the contribution to the intrinsic time

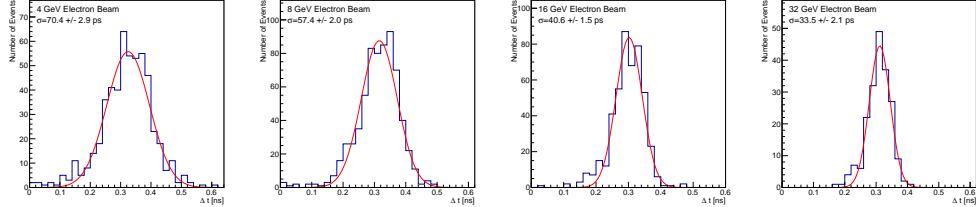


Figure 10.6: TOF distributions for the LYSO cube sampling calorimeter for 4 GeV (top left), 8 GeV (top right), 16 GeV (bottom left), 32 GeV (bottom right) electron beam energy.

resolution of the photodetector and the DAQ electronics to be about 20 ps [115], using the results from the 32 GeV electron beam, we infer that the combined contribution to the time resolution from the shower profile fluctuations, the scintillation mechanism, and the light propagation time inside the LYSO cube is about 27 ps.

### Timing Studies of the LYSO-Tungsten Shashlik Calorimeter Wavelength shifting fibers readout (WLS Y11 & DSB1)

We study the time resolution of a LYSO-tungsten Shashlik calorimeter, one of the proposed choices for the Phase 2 upgrade of the CMS endcap calorimeter system [68]. We compare the time resolution performance for two alternative light propagation schemes.

In our setup the scintillation light is collected by WLS fibers that pass through a set of four holes in the LYSO and tungsten layers. In Figure 10.7, a shashlik cell and the light extraction scheme is illustrated. A schematic diagram and a photograph showing this experimental setup are shown in Figure 10.8. Two MCP-PMTs by Hamamatsu (R3809) are used to collect the scintillation light, while a Photek 240 MCP-PMT is used as a reference time detector.

We compare the signal pulses obtained using two different types of WLS fiber in the same LYSO-tungsten shashlik calorimeter. In Figure 10.9 (a) and (b) and we show the pulse shapes averaged over a few hundred events obtained using DSB1 fibers [22] and Y11 fibers, plotted in blue and red respectively. We find that the rise time of the pulse obtained using the DSB1 fibers, about 2.4 ns, is significantly faster than the rise time of the pulse obtained using the Y11 fibers, which is about 7.1 ns. To optimize the time resolution of this type of calorimeter the DSB1 fiber provides a better choice than Y11 if only this parameter is considered. The signal rise times we observe are comparable to the measured decay times of the corresponding WLS fibers [22].

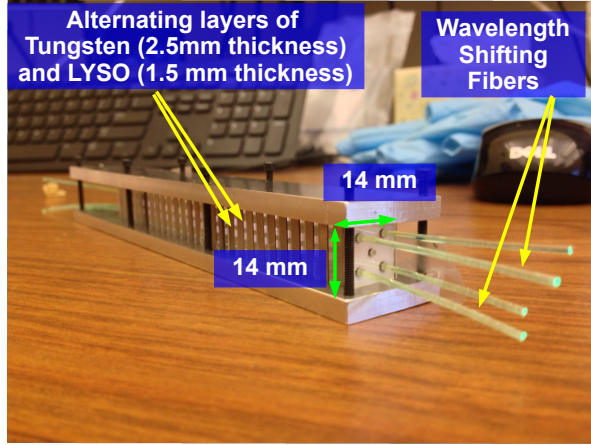


Figure 10.7: The shashlik configuration based upon interleaved W and LYSO layers. Twenty-eight LYSO crystal plates and twenty-seven W plates comprise the module. Four WLS fibers are used to read out the scintillation light from the tiles.

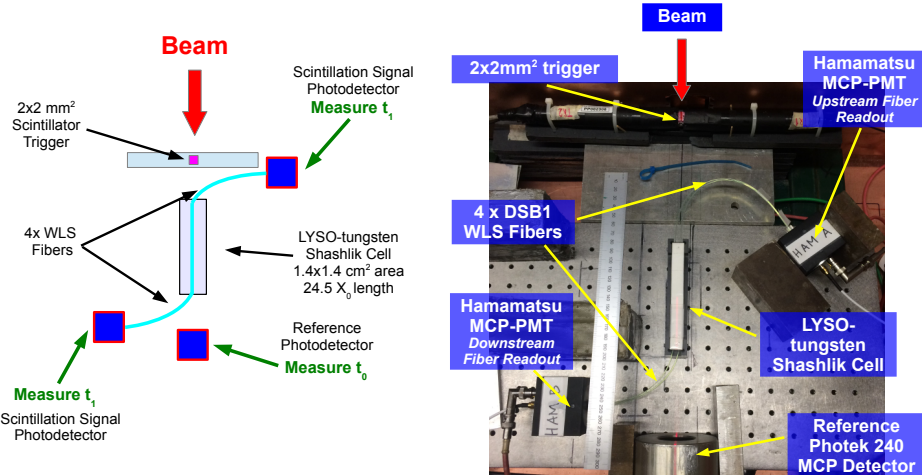


Figure 10.8: A schematic diagram of the experimental setup for the TOF measurement using the LYSO-tungsten shashlik calorimeter with fiber signal extraction, along with a photograph of the experimental setup.

Using the shashlik calorimeter cell with DSB1 fibers, we measure the time resolution for electron beams with energy varying between 4 GeV and 32 GeV. In Figure 10.10 (b) we show the distribution of the pulse integral which is proportional to the total collected charge, for the 32 GeV beam, and observe an energy resolution of about 5% while for the small LYSO cube shown in 10.10 (a), the

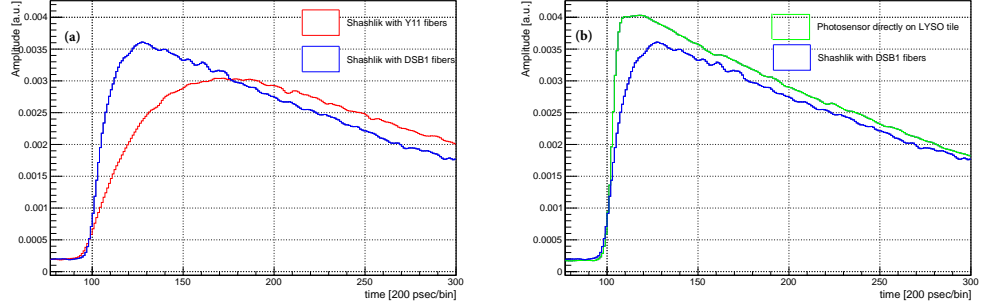


Figure 10.9: (a) Pulse shapes digitized by the DRS4 board and averaged over several hundred events obtained from the LYSO-tungsten shashlik calorimeter with light extracted using DSB1 (blue) and Y11 (red) WLS fibers. (b) DSB1(blue) shashlik average light pulse shape compared with the averaged pulse shape obtained from direct optical coupling of the photodetector to one edge of a LYSO tile in the shashlik calorimeter. (green)

energy resolution was about 20%. For this particular run in the Shashlik setup, no electron identification requirements could be made due to a misconfiguration of the upstream Cherenkov counter, so the background is visible.

TOF distributions, fitted to gaussian functions, are shown in Figure 10.11, and the  $\sigma$  parameter of the gaussian fit is plotted as a function of the beam energy in Figure 10.16. We find that the dependence of the time resolution on beam energy follows a  $1/\sqrt{E}$  functional form, indicating that the current calorimeter setup remains in the photostatistics limited regime. The best time resolution we obtain with this setup is 104 ps. As the measurements are photostatistics limited, the result can be improved in the future if the light collection efficiency is increased.

### **Directly coupled MCP-PMTs to LYSO shashlik plates**

In this setup the MCP-PMT photodetectors are directly coupled to the edges of two adjacent LYSO layers in the shashlik calorimeter and scintillation light is directly transported to the photodetector through the edges of the tile layers. A schematic diagram and corresponding picture of the experimental setup are shown in Figure 10.12. In Figure 10.13, we show a zoomed-in photograph of the exposed LYSO plates from which the scintillation light signal is extracted.

With this setup we invoke an interplay between the light propagation jitter and the limited photostatistics. By placing the photodetectors in direct contact with the edges of two LYSO layers, we minimize the distance the scintillation light travels to reach the photodetectors, and reduce the impact of light propagation jitter on the

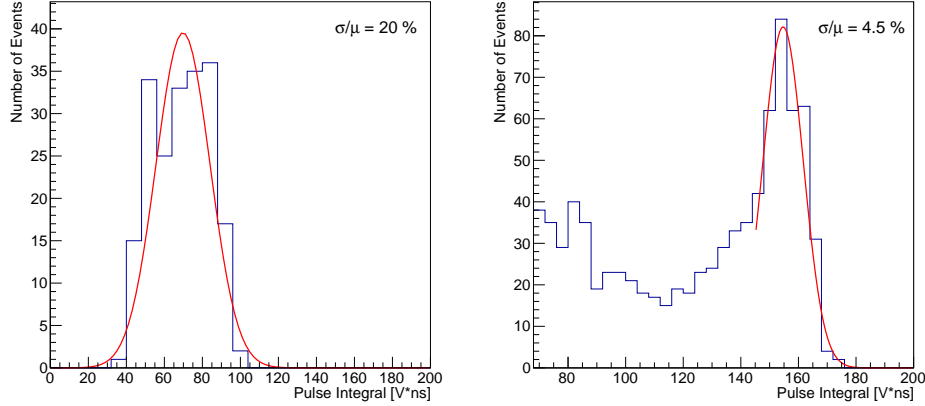


Figure 10.10: (Left) Histogram of the pulse integral which is proportional to the total collected charge is shown for events recorded using the LYSO cube sampling calorimeter for a 32 GeV electron beam. (Right) Histogram of the pulse integral for events recorded using the LYSO-tungsten shashlik calorimeter using DSB1 fibers, for a 32 GeV electron beam. The background is included due to a misconfiguration of the Cherenkov counter.

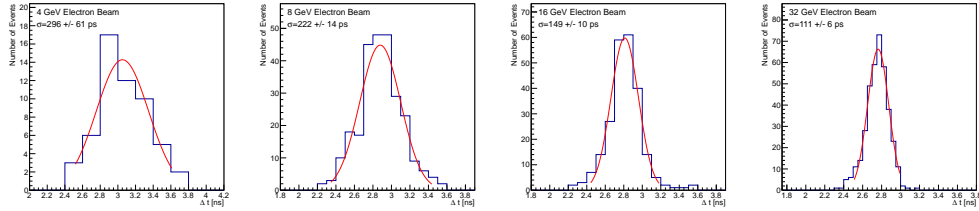


Figure 10.11: TOF distributions for the LYSO-tungsten shashlik calorimeter using DSB1 fibers for electron beams with varying beam energies.

time measurement resolution. However in this setup we have also reduced the available photostatistics, as we collect light from only a small fraction of the shashlik cell. In Figure 10.14, we show the TOF distributions for electron beams at various energies, fitted to gaussian functions. The width of the best-fit gaussian is plotted as a function of the beam energy in Figure 10.16. The best time resolution that we obtain is about 55 ps, and fitting the result to the sum of a  $1/\sqrt{E}$  term and a constant term, we find a constant term of about 30 ps.

In summary, we find that removing the impact of the wavelength shifting mechanism and minimizing the impact of optical transit does indeed improve the time resolution, but at a cost in photostatistics. Results obtained in this experiment suggest that a LYSO-tungsten shashlik calorimeter with edge readout can likely achieve

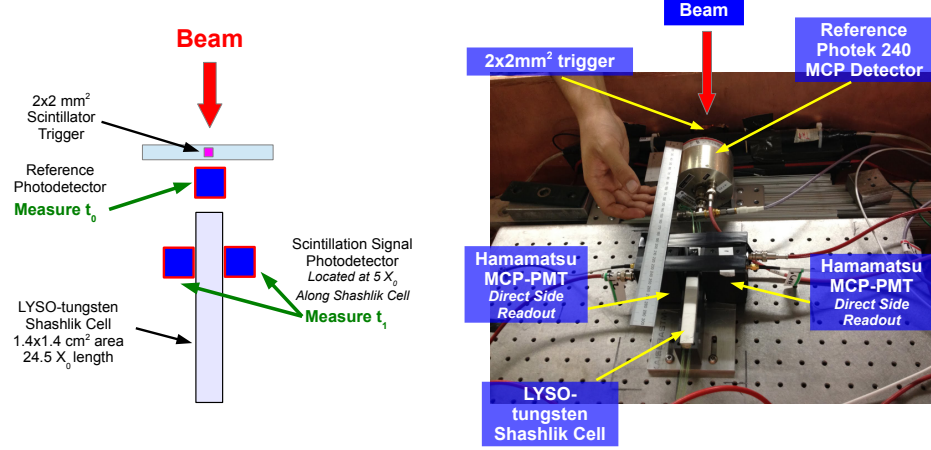


Figure 10.12: A schematic diagram of the experimental setup for the TOF measurement using the LYSO-tungsten shashlik calorimeter with signal extraction from the edges of two LYSO plates, along with a picture of the experimental setup.

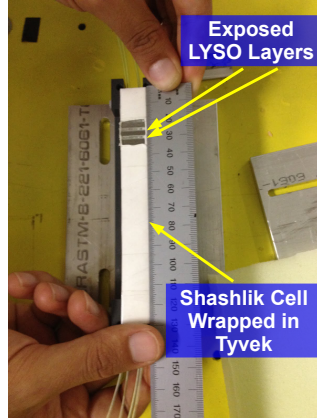


Figure 10.13: A photograph of the two exposed LYSO layers in the shashlik cell. The scintillation light signal is extracted by optically coupling the edges of these two exposed LYSO layers to MCP-PMT photodetectors.

30 ps resolution provided some improvement to the light collection efficiency is achieved.

## 10.5 Results Discussion and Summary

This section described studies characterizing the timing performance of LYSO-based calorimeters. Using a  $(1.7 \text{ cm})^3$  LYSO crystal that samples the electromagnetic showers created by electrons of various energies ranging from 4 GeV to 32 GeV at about  $4.5 X_0$ , we infer that the contribution to the time resolution from event-by-event fluctuations of the shower profile, the scintillation process, and the

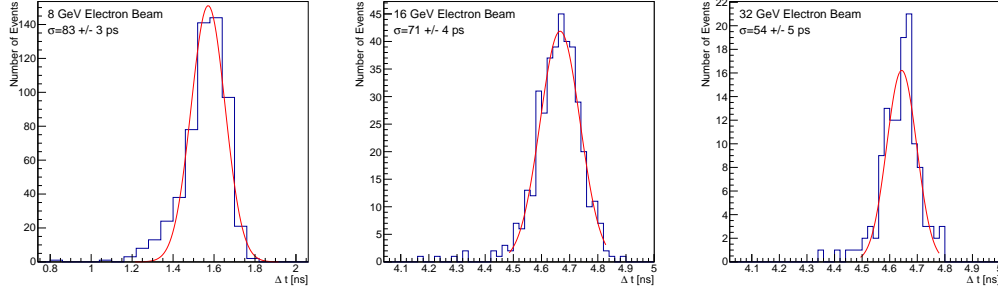


Figure 10.14: TOF distributions for the LYSO-tungsten shashlik calorimeter with signal extracted from the edges of two LYSO layers.

Figure 10.15:

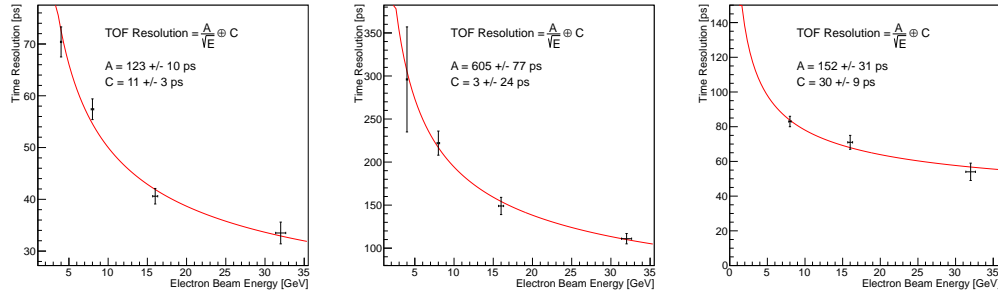


Figure 10.16: Timing resolution measurement as a function of the electron beam energy for (left) the LYSO cube sampling calorimeter (middle) the LYSO-tungsten shashlik calorimeter read-out with DSB1 fibers (right) the LYSO-tungsten shashlik calorimeter read-out directly by optically coupling to the edges of two LYSO layers. In all cases we fit the data with a function of  $1/\sqrt{E}$  and a constant term.

light propagation is less than 30 ps. Studies using different wavelength shifting fibers in a LYSO-tungsten shashlik calorimeter demonstrates that the choice of the fiber affects the timing performance. Besides the absorption and re-emission processes in the fibers, we found that another important factor influencing the timing performance is the light extraction efficiency. Using DSB1 fibers, despite being photostatistics limited, we obtained a best time resolution of about 100 ps. A future development of such a detector will be focused on increasing the light collection efficiency. In a setup where the scintillation light from the LYSO-tungsten shashlik calorimeter is extracted via the edges of two LYSO layers, thereby removing completely the wavelength shifting mechanism and long light propagation distance, we achieve a best time resolution of 55 ps. The result indicates that such a calorimeter

design can achieve the 30 ps time resolution benchmark obtained with the LYSO cube provided some improvement to the light collection efficiency.

In comparing results using different light extraction schemes, we find that at a given light yield the time resolution depends significantly on the light propagation fluctuations. As the light yield increases the dependence on the light propagation fluctuations is reduced. The effect can be seen in the summary Figure 10.17 where we show the dependence of the time resolution on the average pulse height for the shashlik cell with light extracted through the DSB1 fibers and for the sampling calorimeter with the LYSO cube. For the same average pulse height of 500 mV, the LYSO cube time resolution is about half of the shashlik using the DSB1 fibers which have also twice the rise time. As the pulse height increases the time resolution improves. Extrapolating to the regime of very large light yield, we should be able to reach asymptotically the best resolution without limitations from the light propagation fluctuations.

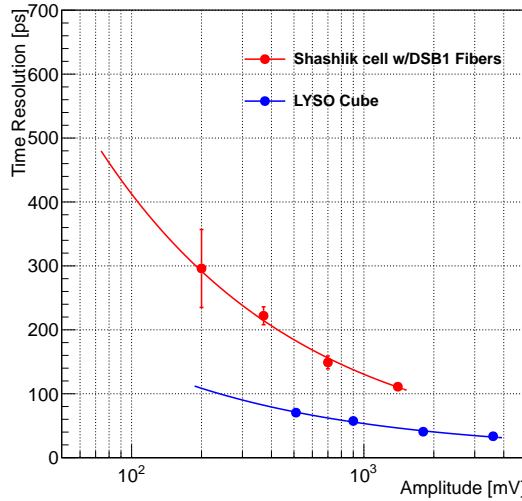


Figure 10.17: Comparison of time resolutions obtained with the  $(1.7 \text{ cm})^3$  LYSO cube (blue), and the LYSO-tungsten shashlik calorimeter with light extracted using DSB1 fibers (red). The x-axis in this figure displays the amplitude of the signal, corrected for the attenuation factors.

In summary, using a LYSO-based calorimeter and different light propagation experimental setups we obtain about 30 ps resolution time measurement for the maximum light yield achieved. As a follow-up we will investigate the time resolution in the limit of very large light yield, and attempt to improve the light collection efficiency in these types of detectors.

## 10.6 Acknowledgements

I would like to thank Erik Ramberg and Sergey Los for their help and support of this work, and Aria Soha and the FTBF test beam facility for the beam delivery and control. We thank Randy Ruchti for providing us with the DSB1 fibers used in the measurements, and Eileen Hahn for the high quality work in polishing the fibers. We would also like to thank Ewa Skup and Geoff Savage for help with operation of the Cherenkov counters, and to Todd Nobel for organizing and providing supporting equipment at FTBF.

This work is supported by funding from Fermi Research Alliance, LLC under Contract No. DE-AC02-07CH11359 with the United States Department of Energy and from California Institute of Technology High Energy Physics under Contract DE-SC0011925 with the United States Department of Energy.

## HIGH-GRANULARITY MCP-BASED CALORIMETERS

In this chapter another precision timing calorimetric prototype using MCPs as the sensitive medium is studied.

### 11.1 Introduction

The use of MCPs as the sensitive element of a shower-maximum detector or a calorimeter has been studied in the past [72, 21]. These studies demonstrated the linearity in the multiplicity of secondary shower particles that have energies that the MCP can detect. Such detectors are also a promising option for achieving time measurement precision at the level of a few tens of picoseconds [115, 117, 118, 98]. Moreover, such devices are intrinsically radiation hard and thus would tolerate the harsh radiation environment at future hadron colliders, particularly when operated without the reliance on a photocathode. In reference [118], it has been demonstrated that the intrinsic fluctuations of electromagnetic showers induce jitter on the time measurement that is less than 10 ps, removing one important potential fundamental limitation. A further advantage of MCPs is their capability for highly segmented readout, allowing for the possibility of a highly granular calorimeter with sub-millimeter spatial resolution. Such high-granularity calorimeters have been studied in the context of detector concepts for the ILC [86] and the HL-LHC upgrade of the CMS experiment [45], indicating that such calorimeters have promising potential for substantial improvement in physics reach at the TeV scale. The results in this chapter complement past results [28, 115, 117, 118] with additional studies of the position and time resolution for a calorimeter prototype with highly granular readout.

The studies in this chapter use three different MCP-PMTs:

- Photek 240: the most performant of the three devices, which provides the best time resolution, and excellent uniformity across the detector. The main parameters of the Photek 240 were reported in Ref. [115]. The pore size is  $10 \mu\text{m}$  and the distance from the photocathode to the first amplification stage is 5.3 mm. The Photek 240 has a  $41 \text{ mm}^2$  circular sensitive area, and it was operated 4.8 kV high voltage (HV). The gain at this voltage is about  $10^6$ . The

non-uniformity of the time response of the signal is limited to below 3.9 ps across the full sensitive area.

- Photonis XP85011: the anode of this MCP is composed of 64 pads, arranged as an  $8 \times 8$  matrix. The size of each pad is  $6 \times 6 \text{ mm}^2$ . The pore size is  $25 \mu\text{m}$ . The non-uniformity of the time response across the photocathode is 37 ps [115, 118]. The HV applied to the Photonis XP85011 was 2.4 kV, with a corresponding gain of  $10^6$ .
- Photonis XP85012: mostly identical to XP85011, also composed of 64 pixels arranged as an  $8 \times 8$  matrix. Additionally it can be operated in a mode with a reverse voltage applied to photocathode, which enables us to effectively turn off any signals from the photocathode. When operated in this mode, the only signals are directly from secondary shower particles [117].

This chapter reports on the studies of the high-granularity shower-maximum detector prototype that uses the Photonis XP85011 MCP as the active element. As demonstrated in reference [115], due to the fact that the input window is very thin, the signal in this device is dominated by direct detection of secondary shower particles, while Cherenkov photon signals contribute only 30% of the amplitude. The MCP is used to sample the electromagnetic shower induced by a beam of electrons impinging into a tungsten absorber layer that has a thickness of about 4 radiation lengths ( $X_0$ ). The MCP-PMT is read out with a pixelated anode, with square pixels of size  $6 \times 6 \text{ mm}^2$ . The energy of the electromagnetic showers is reconstructed using the total collected charge and the positions are reconstructed using a simple energy-weighting algorithm, described in Section 11.4. Through the use of a high-precision motorized stage, a position scan is performed during beam-tests and the position resolution of the shower-maximum detector is obtained. Finally, the precision of measuring the arrival time of electromagnetic showers with such high-granularity shower-maximum detector is investigated.

This chapter is organized as follows. Section 11.2 gives a description of the experimental setup, Section 11.3 presents the event selection and pulse reconstruction, Section 11.4 and 11.5 the presents the results on position measurements and timing resolutions, respectively.

## 11.2 Experimental Setup

The experiment was performed at the MTEST location of the FTBF using an 8 GeV beam primarily comprised of electrons. A differential Cherenkov counter, located further upstream of the MTEST location, was used to enhance the purity of electrons and to suppress pions, by requiring a signal consistent with the passage of electrons through the device. All other detectors were placed inside a dark box lined with copper foil for electromagnetic shielding. A photograph of the experimental setup within the dark box is shown in Figure 11.1. A scintillator of size 1.7 mm× 2.0 mm optically coupled to two photomultiplier tubes, one on each side, was used to trigger the data acquisition and to constrain the trajectory of the electrons. Downstream from the trigger, a tungsten absorber with a thickness of about 1 cm, equivalent to about  $4 X_0$ , was placed. The Photonis XP85011 MCP-PMT with pixelated readout was set on a high precision motorized stage and placed behind the tungsten absorber. The precision of the motorized stage is about 0.1 mm. To avoid unintended early showers due to interactions with the material of the casing and reference MCP-PMT device, the Photek 240 MCP-PMT was placed behind the Photonis XP85011 MCP-PMT. An external view of the Photonis XP85011 MCP-

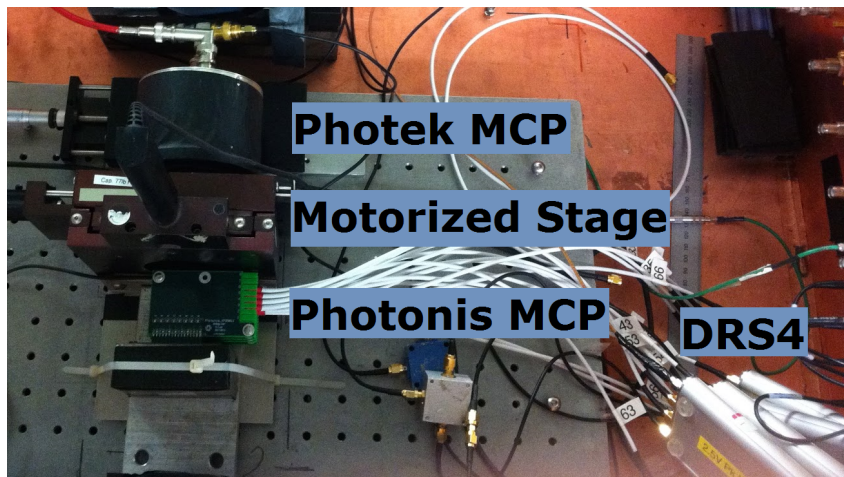


Figure 11.1: The experimental setup inside of the dark box is shown. The beam direction is from the bottom of the photograph to the top. The detector elements shown in the order from upstream to downstream of the beam are: the tungsten absorber, the Photonis XP85011 MCP-PMT located on the motorized stage, and the Photek 240 MCP-PMT used as a time reference detector. The DRS4 waveform digitizers are also shown on the lower right side.

PMT is shown on the left of Figure 11.2, and a schematic diagram is shown on the right. There are a total of 64 pixels arranged in an  $8 \times 8$  square matrix that can be

read out individually. Only the nine pixels shown within the red square are used (see Figure 11.2). During the course of the experiment it was found that the pixel labelled 44 in Figure 11.2 did not function properly and was therefore not used in the analysis of the data. Four DRS4 high speed waveform digitizers were used to

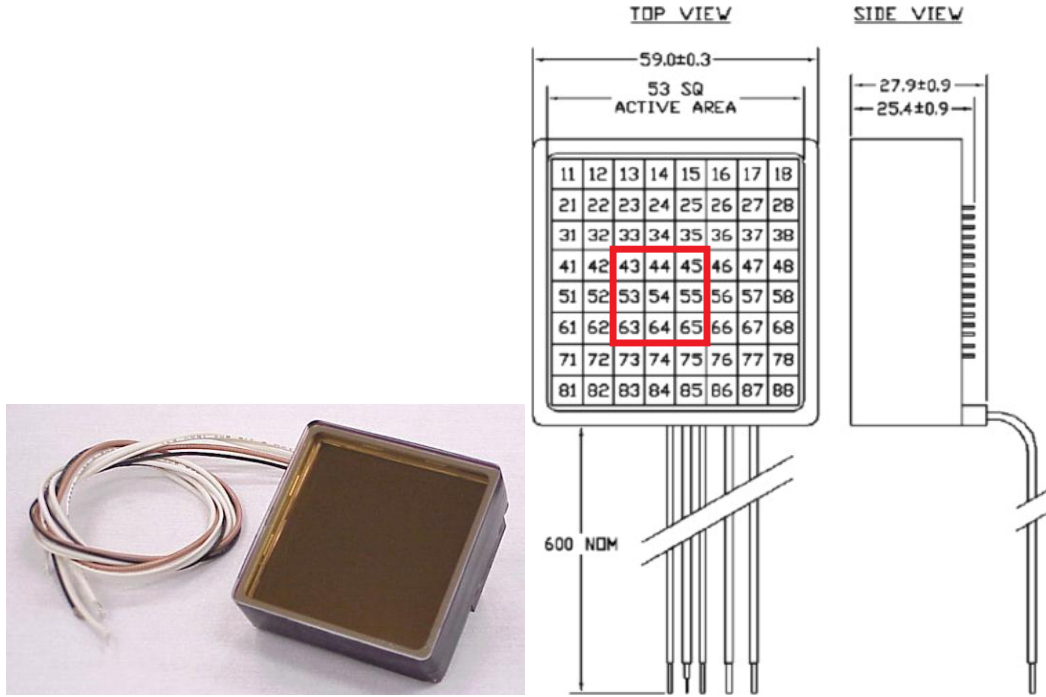


Figure 11.2: The external view of the Photonis XP85011 MCP-PMT is shown on the left, and the schematic diagram is shown on the right. The red square indicates the pixels used for the experiment and data analysis.

acquire the signals from the Photek 240 MCP-PMT, the cherenkov counter, and the eight operational channels from the Photonis XP85011 MCP-PMT. In order to allow a synchronized readout of four separate DRS4 units we split the signals from the Photek 240 MCP-PMT into four, and connected them to each of the four DRS4 units, thus achieving a “calibration” between the four different units.

### 11.3 Event Selection and Pulse Reconstruction

Reconstruction of the signal pulses and timestamps is performed using the identical methods described in Chapter 10 and other studies [28, 115, 117]. Figure 11.3 shows example pulses from one pixel channel of the Photonis XP85011 MCP-PMT and the Photek 240 MCP-PMT digitized by the DRS4.

The time resolution is measured as the standard deviation of the Gaussian fit to the TOF distribution  $t_0 - t_1$ , where  $t_0$  is the time recorded at the “start” detector, and

$t_1$  is that of the “stop” detector. To assign a time stamp for each signal pulse, we first determine the time position of the pulse peak. A Gaussian function is fitted to the pulse maximum using three points before the maximum of the pulse peak and four points after the maximum. The mean value of the Gaussian was used as the time stamp for each pulse. A Photek 240 MCP-PMT, whose time resolution was previously measured to be less than 10 ps [117] was used as a “start” signal, while pulses from individual pixels on the Photonis XP85011 MCP-PMT were used as “stop” signals. The integrated charge for each pulse is used as a proxy for the measured energy deposit in each channel, and is computed using four time samples before and after the peak of the pulse. Each time sample is approximately 0.2 ns in time. Events containing pulses above 500 mV in amplitude are rejected as they saturate the DRS4. Only pulses with amplitude larger than 20 mV are used for time measurements, to reduce the impact of the electronics noise in the DRS4. Other event selection and pulse cleaning procedures are used to eliminate abnormal pulses in the readout, as described in [115].

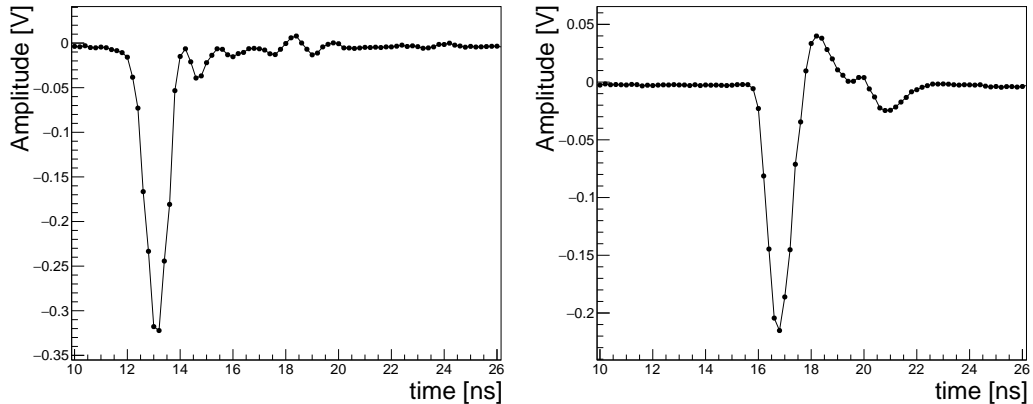


Figure 11.3: Example of a digitized signal from a single Photonis pixel (left) and Photek (right) MCP-PMT following a high-energy electron shower, via DRS4.

#### 11.4 Electromagnetic Shower Position Reconstruction and Resolution

The transverse shape of electromagnetic showers is very well known and has a characteristic width given by the Moliere radius, see Section 9.1. For tungsten, the Moliere radius is about 9 mm and therefore the shower is expected to be contained within two of the pixels in the Photonis XP85011 MCP-PMT. In Figure 11.4 shows the mean charge measured in each of the pixels for one example run where the Photonis MCP-PMT was held in a fixed location approximately centered on the beam. The electron beam has a width of about 1 cm.

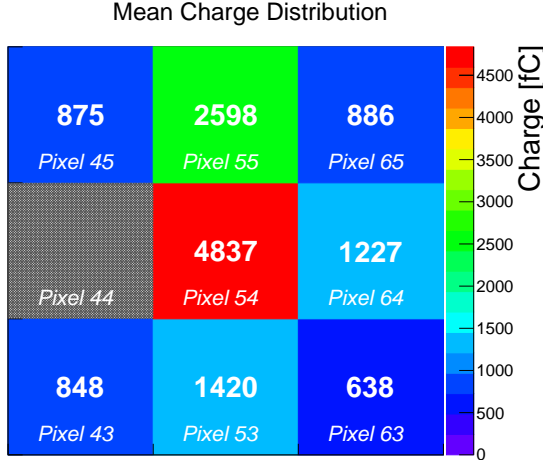


Figure 11.4: The mean charge measured for each pixel for one example run is shown. During this run, the Photonis MCP-PMT was held in the same location. Based on the distribution of the mean charge among the pixels, we can infer that the beam center is located in the upper half of the center pixel. Pixel 44 is not shown as it was found to be not operational.

Each electron impacting the shower-maximum detector will induce an electromagnetic shower, and we define such an occurrence as an event. For each event, the center of the electromagnetic shower ( $\vec{p}$ ) is reconstructed based on the the pixel positions weighted by the corresponding integrated charge as follows:

$$\vec{p} = \frac{\sum_{i \in \text{pixels}} Q_i \vec{p}_i}{\sum_{i \in \text{pixels}} Q_i}, \quad (11.1)$$

where  $i$  labels the individual pixels,  $Q_i$  is the charge collected in pixel  $i$ , and  $\vec{p}_i$  is the vector describing the  $x$  and  $y$  coordinates of the center of pixel  $i$ . The origin of the coordinate system is chosen to be at the lower left corner of the  $3 \times 3$  array of pixels.

Multiple runs were taken; scanning different beam positions relative to the Photonis MCP-PMT by moving the motorized stage. Figure 11.5 shows the distributions of the reconstructed shower positions for three example runs in which the beam was located near the top, center, and bottom of the central pixel. The distributions of the reconstructed  $y$  coordinate for the three corresponding runs are shown together in Figure 11.6. The measured beam-spot is observed to move consistent with the known movement of the motorized stage. In each run, the center of the beam-spot is determined by fitting the measured  $x$  and  $y$  coordinates with a Gaussian function. The data from all runs are combined by considering the measured  $x$  and

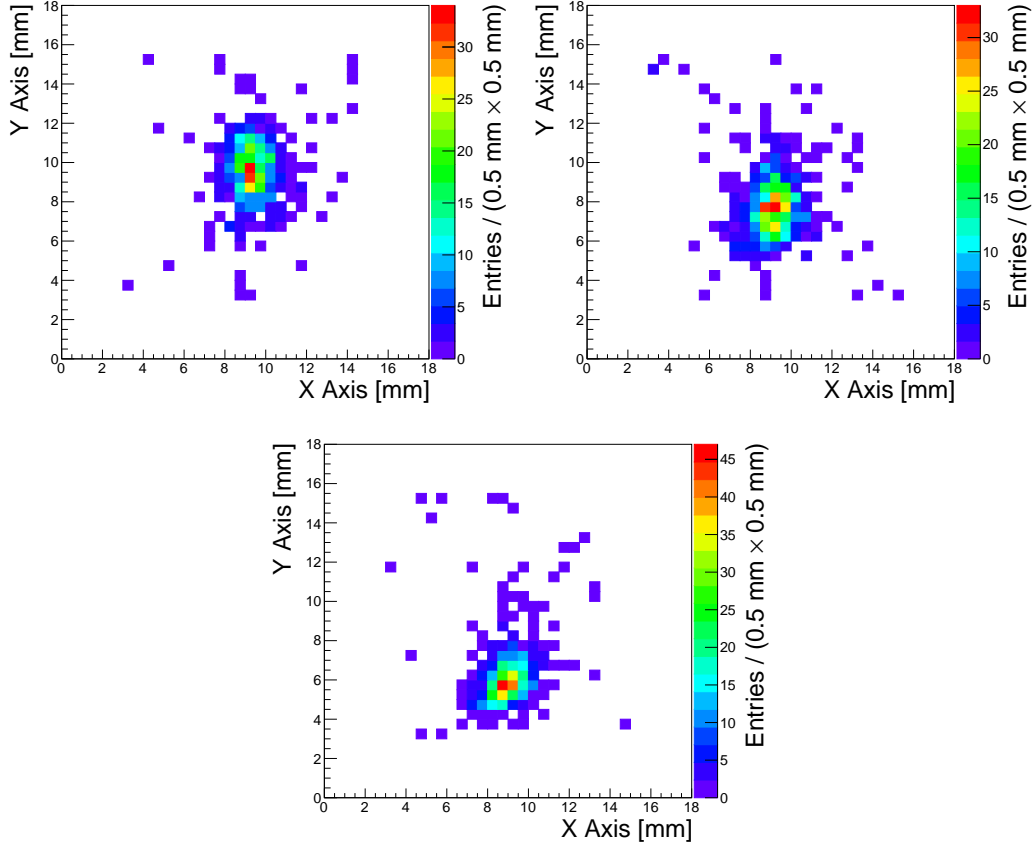


Figure 11.5: The distribution of reconstructed shower positions is shown for three runs with the beam centered near the top, center, and bottom of the central pixel.

$y$  coordinates relative to the center of the beam-spot (see Fig 11.7). We model the distribution of measured coordinates as a convolution of a flat distribution with width equal to the measured dimensions of the scintillator trigger and a Gaussian resolution function. A maximum likelihood fit is performed on the data using this model, and the position resolution of the detector is measured as the width of the Gaussian resolution function. We measure the position resolution as  $0.55 \pm 0.2$  mm in  $x$ -coordinate, and  $0.91 \pm 0.01$  mm in  $y$ -coordinates.

## 11.5 Electromagnetic Shower Time Resolution

The timestamps of the individual pixels of the Photonis MCP-PMT for each event are reconstructed as described in Section 11.3. The timestamp of the entire electromagnetic shower ( $t$ ) is estimated using the same energy weighting procedure that was used above for the shower position reconstruction, i.e.

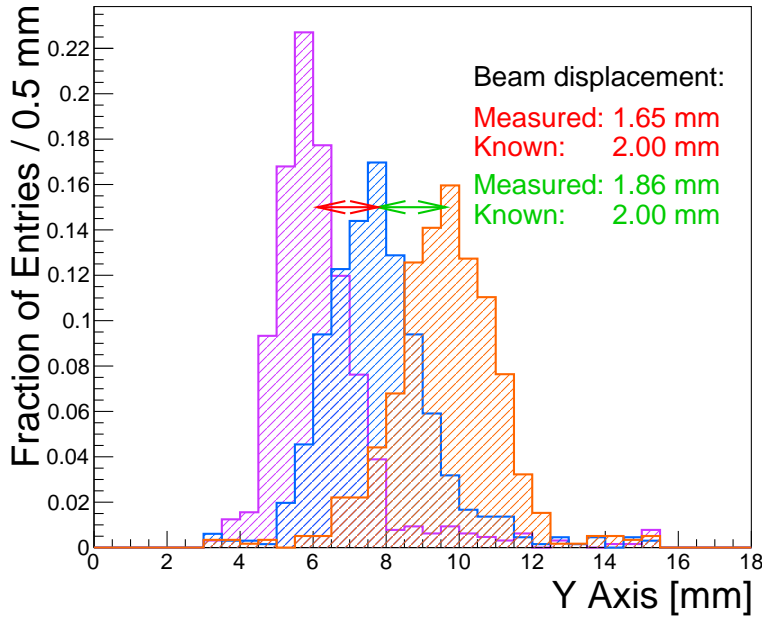


Figure 11.6: The distributions of reconstructed shower position in the  $y$  axis is shown for the three runs corresponding to the distributions shown in Figure 11.5. The measured beam displacements are compared to the known displacements as recorded by the motorized stage.

$$t = \frac{\sum_{i \in \text{pixels}} Q_i t_i}{\sum_{i \in \text{pixels}} Q_i}, \quad (11.2)$$

where  $i$  labels the individual pixels,  $Q_i$  is the charge collected in pixel  $i$ , and  $t_i$  is the reconstructed time-stamp for pixel  $i$ . Alternatively, the time resolution using the single pixel with the highest energy deposit measurement is used. Figure 11.8 shows the time distributions for these two methods of shower time reconstruction.

Figure 11.9 shows the time resolution for electromagnetic showers measured using the two methods described above. The time resolution for the pixel with the largest energy deposit is around 70 ps and 85 ps, depending on the run. Using the energy weighted algorithm improves the time resolution consistently to about 50 ps. The time measurement obtained using the Photonis MCP-PMT typically exhibit a dependence on the pulse amplitude or integrated charge. This dependence is shown on the left of Figure 11.10, and is observed to be approximately the same for all pixels. We perform a correction to the time measurement based on the measured integrated charge, and we verify that the correction does flatten the dependence of the time measurement on the integrated charge as shown on the right panel of Fig-

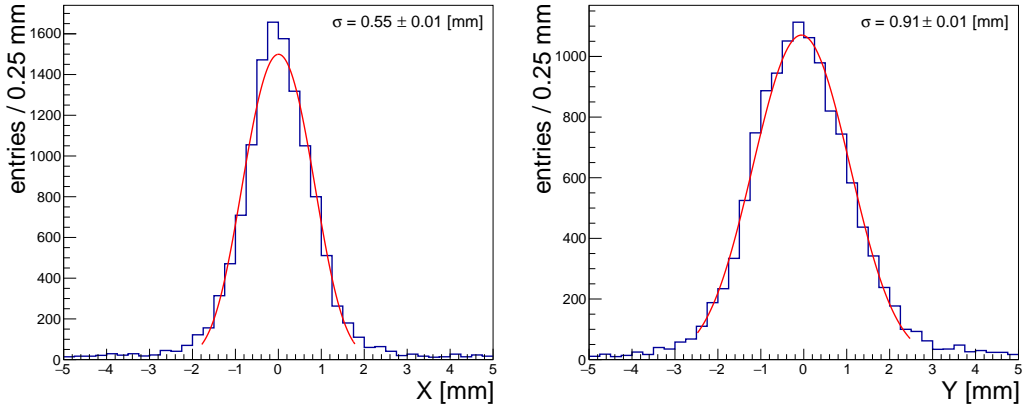


Figure 11.7: The distributions of the measured  $x$  (left) and  $y$  (right) coordinates are shown along with the fit to the resolution model. The position resolution of the EM shower as measured by the MCP-PMT detector is determined from the fit to the resolution model.

ure 11.10. After performing this time measurement correction, the time resolution measurements improve to about 35 ps and is shown in Figure 11.11. We performed two sets of correction procedures. In one set, labelled as “Self-Calibrated”, an independent correction is derived for each run and for each pixel. In the second set, labelled as “Calibrated”, a single correction is obtained for each pixel from a single run, and this correction is applied to all other runs. Figure 11.11 shows that this single correction is applicable to all other runs without loss of the precision of the measurements.

Finally, the dependence of the electromagnetic shower time resolution on of the number of pixels included in the energy-weighted algorithm is studied. Figure 11.12 shows this dependence for one example run. It is observed that the time resolution improves according to a  $1/\sqrt{N}$  scaling up to about 5–6 pixels, and then becomes flat as more pixels are included. The initial  $1/\sqrt{N}$  scaling is encouraging as it indicates that the time jitter across different pixel channels arise primarily from uncorrelated sources, and that further granularity may improve the time resolution provided that the signal is sufficiently large compared to noise. As the majority of the shower is covered by the pixels closest to the center of the shower—usually 5–6 pixels—it is not surprising that the time resolution does not further improve by adding the remainder of pixels.

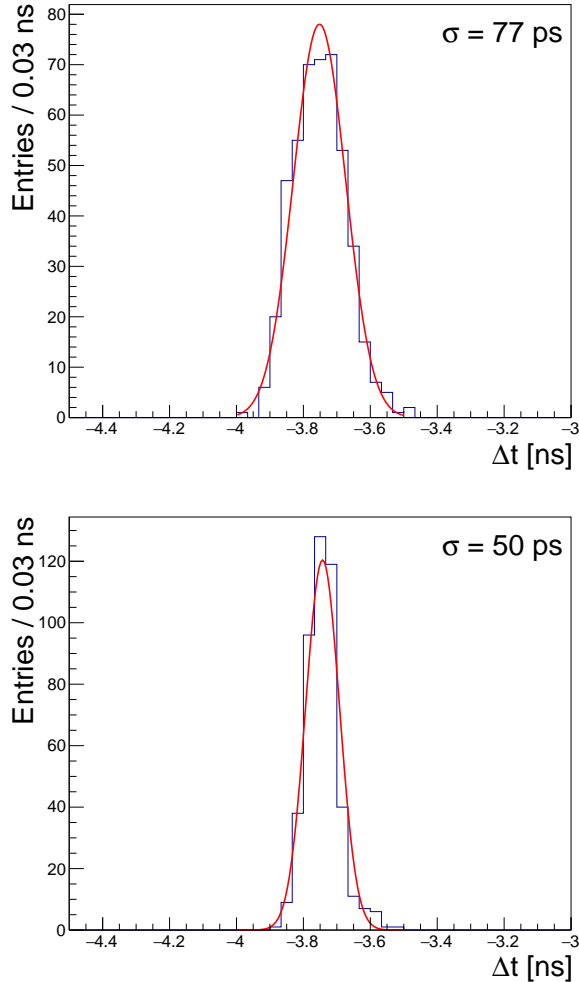


Figure 11.8: The time distributions obtained using the highest energy pixel (left) and the energy weighted algorithm (right) are shown for one example run. The distributions are fitted with Gaussian models, and the width parameter of the Gaussian is displayed on the plot.

## 11.6 Summary

Studies towards the development of future electromagnetic calorimeters capable of high precision energy and time measurements have been carried out. Such calorimeters should ultimately provide both spatial resolution below the mm level and time resolution of 20 – 30 ps, in order to mitigate the detrimental effects of pileup. A highly granular readout is required to achieve these goals.

This chapter reports the results on position and time resolution measurements of a secondary emission based calorimeter prototype that used the Photonis XP85011 MCP-PMT as the sensitive element. Using a pixelated readout of the MCP-PMT

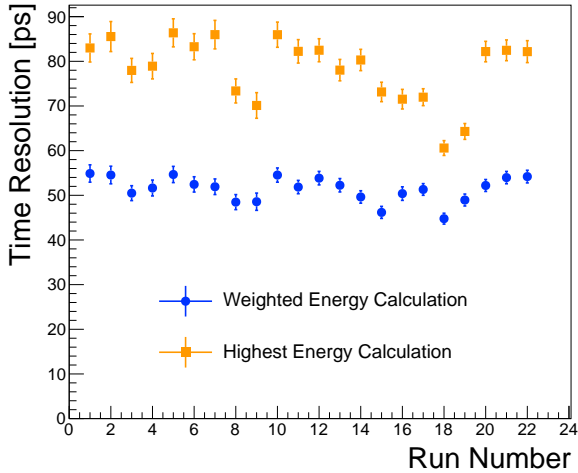


Figure 11.9: Time resolution found for each run. The time-stamp obtained using the energy weighting method yields time resolutions consistently below 60 ps. The time resolution measured using the single pixel with the largest signal is significantly worse.

a highly granular information of the shower development in the transverse plane is obtained. Combining the measurements from a  $3 \times 3$ -pixel readout a sub-millimeter position resolution is measured, which far exceeds the 6 mm size of the individual pixels. While the more granular readout degrades the signal to noise for each individual pixel, the proper combination from independent pixels preserves a good time resolution. The measured time resolution improves with the increase in the number of pixels used as  $1/\sqrt{N}$ , and when using all pixels, the time resolution is 30–40 ps. Future measurements could include larger prototypes with several layers of sensitive material, that will allow the study of the longitudinal development of the showers.

### 11.7 Acknowledgements

I like to thank Erik Ramberg for supporting this work, and Aria Soha and the FTBF test beam facility for the good beam delivery and control. Thanks to Ewa Skup and Geoff Savage for help with operation of Cherenkov counters, and to Todd Nebel for organizing and providing supporting equipment at FTBF.

This work is supported by funding from Fermi Research Alliance, LLC under Contract No. DE-AC02-07CH11359 with the United States Department of Energy, and from California Institute of Technology High Energy Physics under Contract DE-SC0011925 with the United States Department of Energy.

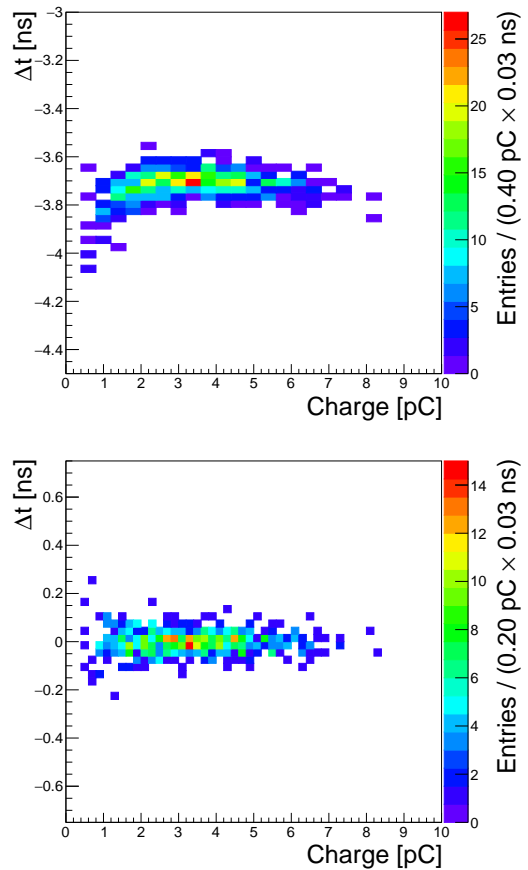


Figure 11.10: The correlation between the time measurement and the measured integrated charge is shown on the left for one example pixel. The same correlation after performing the time measurement correction is shown on the right.

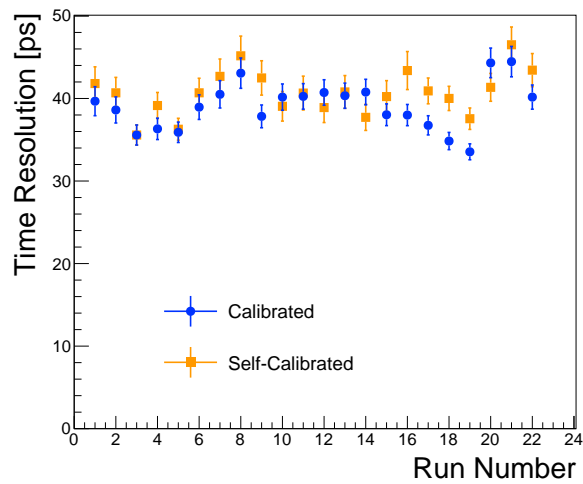


Figure 11.11: The time resolution of the electromagnetic shower for various runs is shown after performing the time measurement correction based on the measured integrated charge.

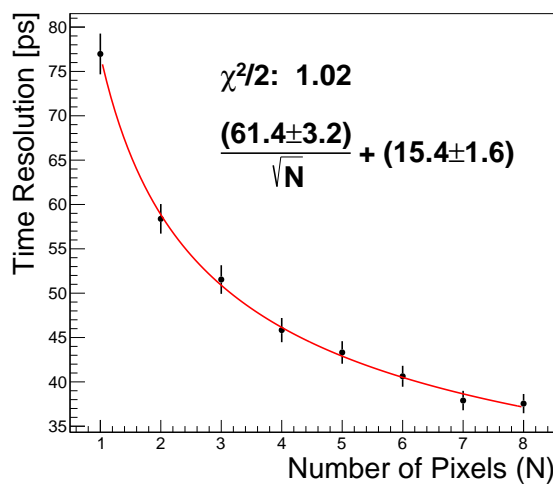


Figure 11.12: The time resolution is plotted as a function of the number of pixels included in the energy-weighted algorithm for one example run.

## SILICON-BASED SAMPLING CALORIMETERS

### 12.1 Introduction

Several alternative options to combine high resolution energy and timing measurements for calorimetry have been reported in Refs. [118, 116, 98, 133, 127] as well as those described in Chapters 10 and 11. This chapter describes the continuation of this program by using a calorimeter prototype employing a  $300\text{ }\mu\text{m}$  thick silicon pad sensor of  $6 \times 6\text{ mm}^2$  size as the sensitive element. Silicon-based calorimeters have recently become a viable choice for future colliders due to the radiation hardness of silicon, and the ability to construct highly granular detectors [16]. An important example is the forward calorimeter proposed for the CMS Phase 2 Upgrade [45]. We study the timing properties of silicon-based calorimeter using a prototype composed of tungsten absorber and a silicon sensor produced by Hamamatsu [4].

This chapter is organized as follows. General silicon timing properties and bench test results are described in Section 12.2. The test beam setup and experimental apparatus are presented in Section 13.3. The results of the test beam measurements are presented in Section 12.4. Finally, Sections 12.5 and 12.6 are devoted to discussion and conclusion, respectively.

### 12.2 General Properties of Silicon Timing and Bench Test Studies

All measurements presented in this chapter were carried out using a silicon sensor produced by Hamamatsu [4]. The thickness of the silicon sensor was measured to be  $325\text{ }\mu\text{m}$ , while its transverse size is  $6 \times 6\text{ mm}^2$ . The negative bias voltage was applied to the p-side of the silicon. The capacitance of the silicon diode is measured as a function of the bias voltage and shown in Figure 12.1. The silicon is fully depleted above about 120 V.

The electric diagram of the silicon diode connections is presented in left panel of Figure 12.2. Attention was paid to provide good filtering for the bias voltage, to reduce ground loop effects, and to minimize inductive loop for the signal readout. The timing characteristics of the signal pulses are therefore dominated primarily by properties of the silicon sensor rather than the details of the circuit. The silicon diode was placed inside a light-tight box (silicon box) of thickness 1.5 cm, which

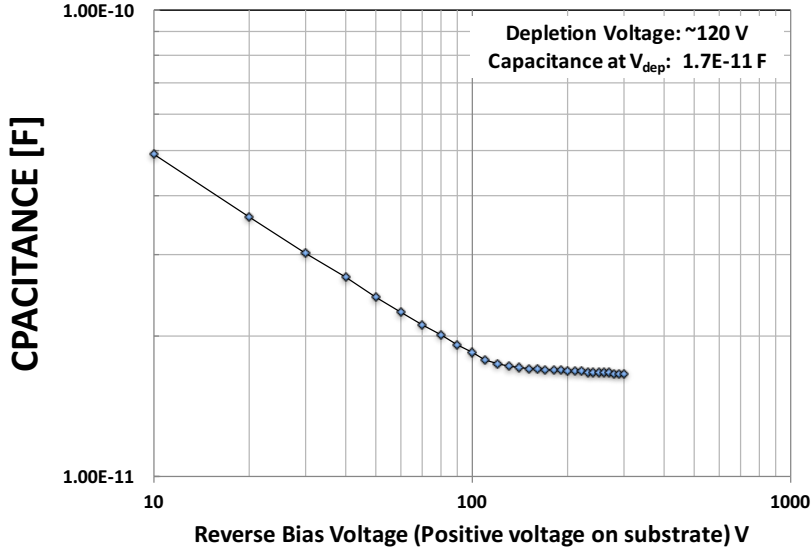


Figure 12.1: The measured capacitance as a function of the applied bias voltage.

also provides electromagnetic shielding. The box is made of 0.2 mm steel. The bias voltage was supplied to the circuitry by a cable with a balun filter, terminated with an SHV connector. The silicon diode output signal was read out through an SMA connector electrically grounded to the box. The dark current was measured at several values of the bias voltage. The maximum value of the dark current was less than 1.0 nA at -500 V, which is the largest bias voltage used in the measurements reported. The silicon box is presented in the right panel of Figure 12.2. Signals

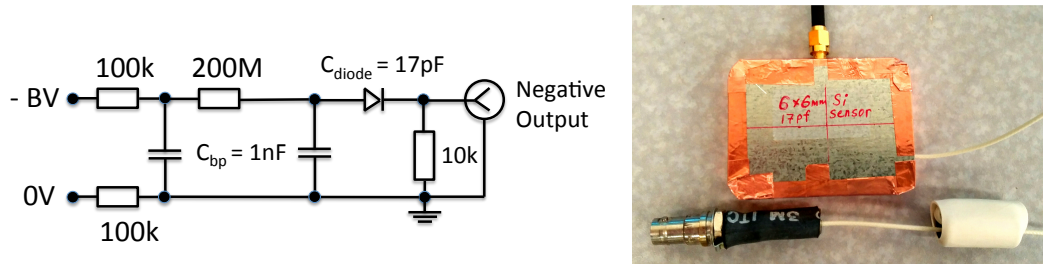


Figure 12.2: The electric diagram for the silicon diode connections (left). External view of the box with silicon diode, and the bias voltage connection is shown below it (right).

from the silicon sensor were amplified by two fast, high-bandwidth pre-amplifiers connected in series. The first amplifier is an ORTEC VT120C pre-amplifier, and the second is a Hamamatsu C5594 amplifier. The combined gain of the two amplifiers in series as a function of the input signal amplitude was measured using a pulse-

generator. Some non-linearities for typical signals produced by the silicon sensor under study were found and corrected.

### 12.3 Test-beam Setup and Experimental Apparatus

Test-beam measurements were carried out at the FTBF which provided a 120 GeV proton beam from the Fermilab Main Injector accelerator , and secondary beams composed of electrons, pions, and muons of energies ranging from 4 GeV to 32 GeV. A simple schematic diagram of the experimental setup is shown in Figure 12.3. A small plastic scintillator of transverse dimensions 1.7 mm×2 mm is used as a trigger counter to initiate the read out of the DAQ system and to select incident beam particles from a small geometric area, allowing us to center the beam particles on the silicon sensor. Next, we place a stack of tungsten absorbers of various thicknesses for measurements of the longitudinal profile of the electromagnetic shower. The silicon pad sensor is located within a metal box covered by copper foil, and is placed immediately downstream of the absorber plates. Finally, a Photek 240 MCP-PMT detector [28, 115, 118, 116] is placed furthest downstream, and serves to provide a very precise reference timestamp. Its precision was previously measured to be less than 10 ps [118]. A photograph showing the various detector components is presented in Figure 12.4. A differential Cherenkov counter is located further upstream of our experimental setup and provides additional particle identification capability. More details of the experimental setup are described in our previous studies using the same experimental facility in references [28, 115, 118, 116] as well as in Chapters 10 and 11.

The DAQ system is based on a CAEN V1742 digitizer board [5], which provides digitized waveforms sampled at 5 GS/s. The metal box containing the silicon sensor was located on a motorized X-Y moving stage allowing us to change the location of the sensor in the plane transverse to the beam at an accuracy better than 0.1 mm. A nominal bias voltage of 500 V was applied to deplete the silicon sensor in most of the studies shown below, unless noted otherwise.

### 12.4 Test Beam Measurements and Results

Measurements were performed in 2015, using the primary 120 GeV proton beam, and secondary electron beam provided for the FTBF. Secondary beams with energies ranging from 4 GeV to 32 GeV were used. Electron purity for those beams ranges between 70% at the lowest energy to about 10% at the highest energy. Stacks of tungsten plates with varying thicknesses were placed immediately upstream of

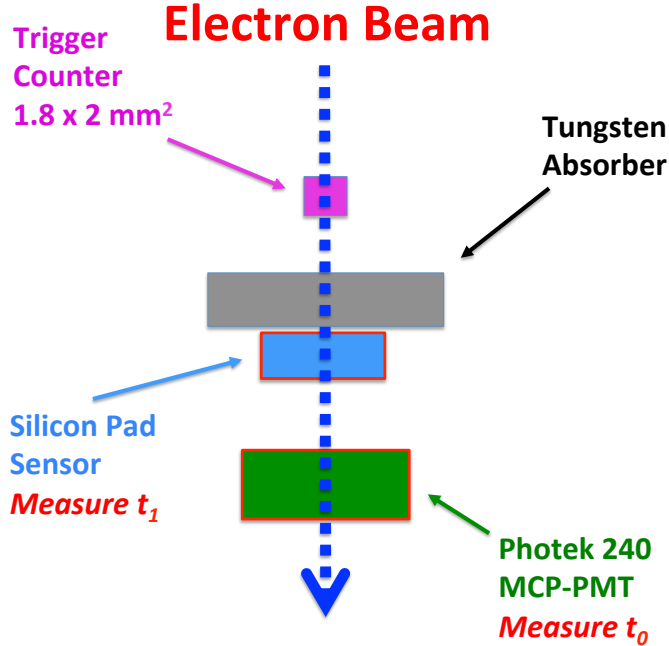


Figure 12.3: A schematic diagram of the test-beam setup is shown. The  $t_0$  and  $t_1$  are defined in Section 12.4.

the silicon device in order to measure the response along the longitudinal direction of the electromagnetic shower. The radiation length of tungsten is 3.5 mm, and the Moliere radius is 9.3 mm. The tungsten plate dimensions are sufficient to fully contain the shower in the transverse dimension. Signals from the silicon sensor and the Photek 240 MCP-PMT are read out and digitized by the CAEN V1742 digitizer, and example signal waveforms are shown in Figure 12.5. The signal pulse in the silicon sensor has a rise time of about 1.5 ns, and a full pulse width of around 7 ns. This rise time is consistent with a time constant of a silicon sensor coupled to a 50 Ohm amplifier.

The CAEN digitizer is voltage and time calibrated using the procedure described in Ref. [97]. The total collected charge for each signal pulse is computed by integrating a 10 ns window around the peak of the pulse. The time for the reference Photek MCP-PMT detector is obtained by fitting the peak region of the pulse to a Gaussian function and the mean parameter of the Gaussian is assigned as the timestamp  $t_0$ . The time for signals from the silicon sensor is obtained by performing a linear fit to the rising edge of the pulse and the time at which the pulse reaches 30% of the maximum amplitude is assigned as its timestamp  $t_1$ . The electronic time resolution of the CAEN V1742 digitizer was measured to be  $\sim 4$  ps and neglected on the timing

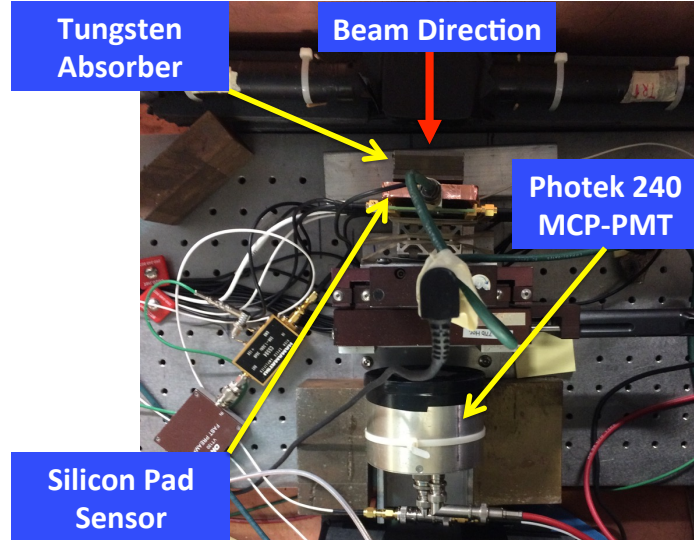


Figure 12.4: Test beam setup.

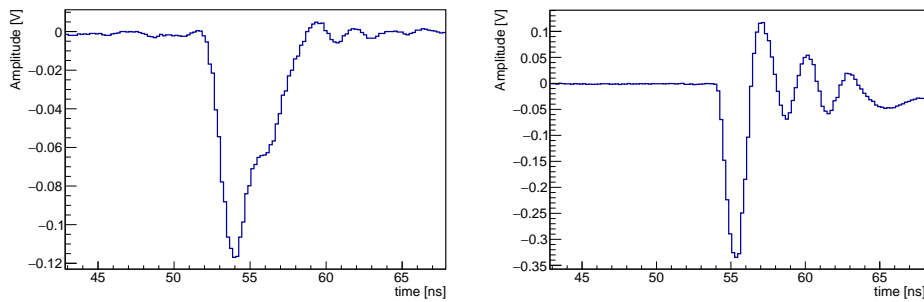


Figure 12.5: Examples of the signal pulse waveform for the silicon sensor (left) and the Photek MCP-PMT (right) digitized by CAEN V1742 digitizer board. The bias voltage applied to the silicon pad sensor is 500 V.

measurements described below.

Electrons were identified by requiring that the signal amplitude of the gas Cherenkov counter provided by the FTBF and the Photek 240 MCP-PMT detector located further downstream of the silicon sensor exceed certain thresholds because electromagnetic showers induced by electrons produce significantly larger signals, while pions produce much smaller signals. After imposing the electron identification requirements the electron purity is between 80% and 90% for all beam conditions. The purity was determined by comparing the calorimetric measurements with those from the Cherenkov detector.

Let's begin by establishing the signal characteristics of a minimum-ionizing particle

(MIP) using beams of 120 GeV protons and 8 GeV electrons with no absorbers upstream of the silicon pad sensor. To separate MIP signals from noise, separate data events with no beam and a random trigger are recorded. The charge distribution for these noise runs is presented in Figure 12.6. As expected, the charge distribution is centered at 0, and the RMS is about 2 fC. Figure 12.7 shows the silicon sensor re-

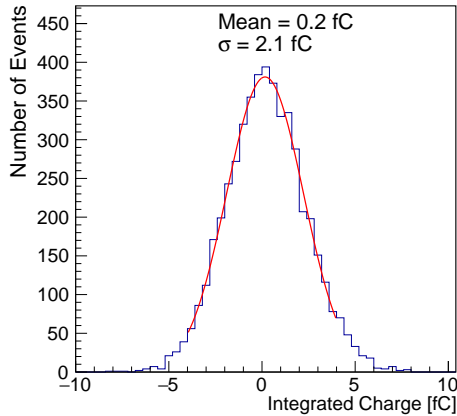


Figure 12.6: The distribution of charge integrated in the silicon sensor is shown for data events with no beam and random trigger.

sponse to 120 GeV protons and 8 GeV electrons without any absorber. We observe very similar response for these two cases, and measure a mean integrated charge of 4.5 fC and 5.0 fC for proton and electrons, respectively. The measured signals are corrected for the gain of the amplifiers used, and hence is the output charge of the silicon sensor. We expect peak charge of 28,000 and 31,000 electron-hole pairs in a 325  $\mu\text{m}$  thick silicon detector for ionizing particles with Lorentz factor  $\gamma = 120$  (protons) and 16,000 (electrons) [107], which is in a good agreement with the measured values. Having established the absolute scale of the response using single particles, the remaining studies normalize all charge measurements to the 120 GeV proton signal, which hereafter is referred to as  $Q_{\text{MIP}}$ . The response of the silicon sensor to electron beams of various energies after 6 radiation lengths ( $X_0$ ) of tungsten absorber is presented. The silicon sensor is expected to be sensitive to the number of secondary electrons produced within the electromagnetic shower, and therefore its response is expected to scale up with higher incident electron energies. Figure 12.8 shows an example of the integrated charge distribution measured in the silicon sensor after 6 radiation lengths of tungsten, for runs with 32 GeV electrons. The mean and RMS of these distributions as a function of incident electron beam energy in are shown in Figure 12.8. The plotted uncertainties represent the RMS of

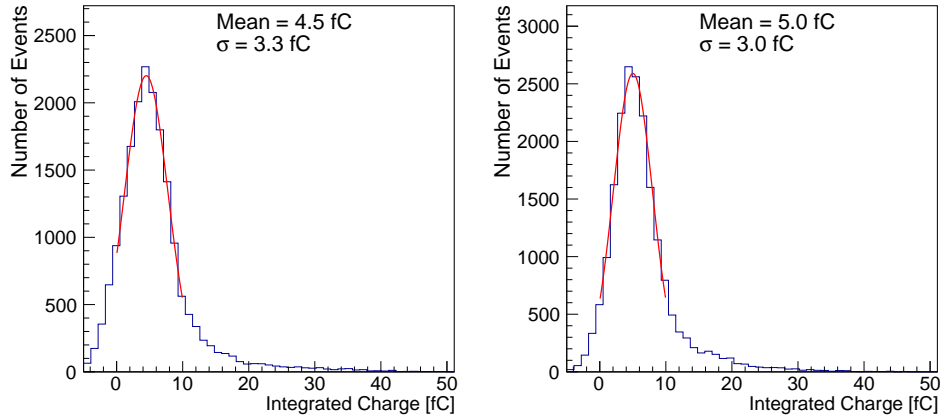


Figure 12.7: The distribution of charge integrated in the silicon sensor is shown for a beam of 120 GeV protons (left) and 8 GeV electrons (right) without any absorber upstream of the silicon sensor. These conditions mimic the response of the silicon sensor to a minimum-ionizing particle. All triggered events were used in these distributions.

the charge distribution. Since the electron beam profile and purity varies at different beam energies, we collected between 10 and 50 thousand events for each beam energy, in order to ensure sufficiently large data samples. A fairly linear dependence between the measured charge and the incident beam energy is observed, see the right panel of Figure 12.8. The measured time resolution between the silicon sensor and the Photek MCP-PMT, was obtained by measuring the standard deviation of the Gaussian fit to the TOF distribution, i.e.  $\Delta t = t_0 - t_1$ . The later exhibits a systematic dependence on the total charge measured in the silicon detector, as shown on the left panel in Figure 12.9. This dependence on the integrated charge of the amplified signal was reproduced when the output of the pulse-generator was connected to the same amplifiers as used in the measurements. Therefore a correction to  $\Delta t$  for each event using the measured charge in the silicon sensor was applied. This procedure is referred to in the following as *time correction*. The correction is obtained by fitting a second degree polynomial to the profiled distribution of the  $\Delta t$  versus total charge collected in the silicon sensor, as shown in Figure 12.9. The cross-check that the *time correction* flattens the dependence of the time measurement on the integrated charge is shown on the right panel of Figure 12.9. The *time correction* improves the time resolution measurement by 30 – 35%. All time resolution measurements in the rest of this study are performed after such a time correction. An example of a corrected  $\Delta t$  distribution for 32 GeV electrons after 6  $X_0$  is shown on the left panel of

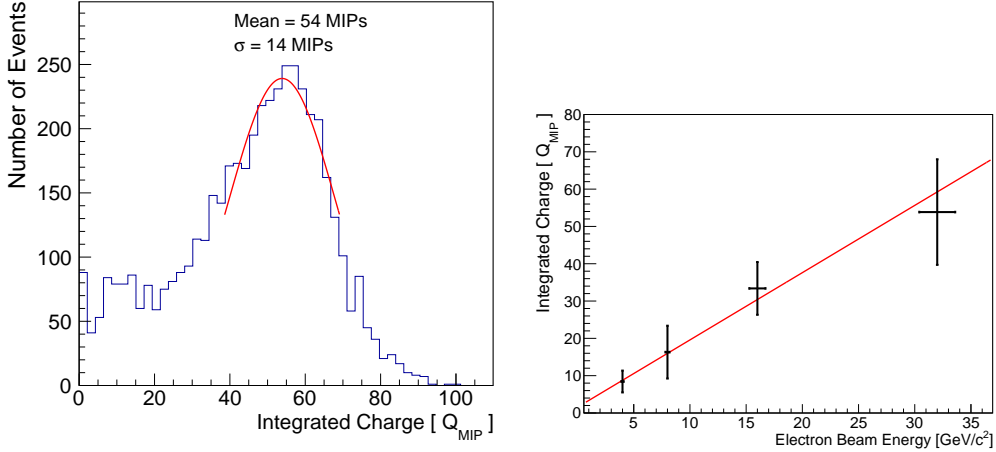


Figure 12.8: Left: An example of the distribution of integrated charge in the silicon sensor for 32 GeV electrons and 6  $X_0$  absorber shown in units of  $Q_{MIP}$ . Right: The integrated charge in the silicon sensor expressed in units of  $Q_{MIP}$  is shown for the same 6  $X_0$  absorber as a function of the electron beam energy. The uncertainty bands show the RMS of the measured charge distribution. The red line is the best fit to a linear function..

Figure 12.10. Other than the electron identification requirements, no additional selection requirements on the amplitude of the signal in the silicon sensor were made. The dependence of the measured time resolution on the beam energy is shown on the right panel of Figure 12.10. The time resolution improves as the beam energy increases, with a time resolution of 23 ps for the 32 GeV electron beam. Furthermore, the response and time resolution of the silicon sensor along the longitudinal direction of the shower development is studied. The integrated charge and the time resolution as a function of the absorber thickness is shown in Figure 12.11, for an 8 GeV electron beam. A typical longitudinal shower profile is observed, consistent with previous studies performed using a secondary emission calorimeter prototype based on MCP's [118], as well as independent studies of silicon-based calorimeter prototypes [104]. The RMS of the integrated charge distribution at each absorber thickness is relatively large, due to the small transverse size of the active element used in the experiment. It is of note that the time resolution improves as the shower develops towards its maximum in the longitudinal direction. Finally, the dependence of the time resolution as a function of the bias voltage applied to deplete the silicon sensor is also studied. The measurements are shown in Figure 12.12 for 16 GeV electrons after 6  $X_0$  of tungsten absorber. As presented in Figure 12.12, the time resolution improves as the bias voltage is increased, which is expected on the

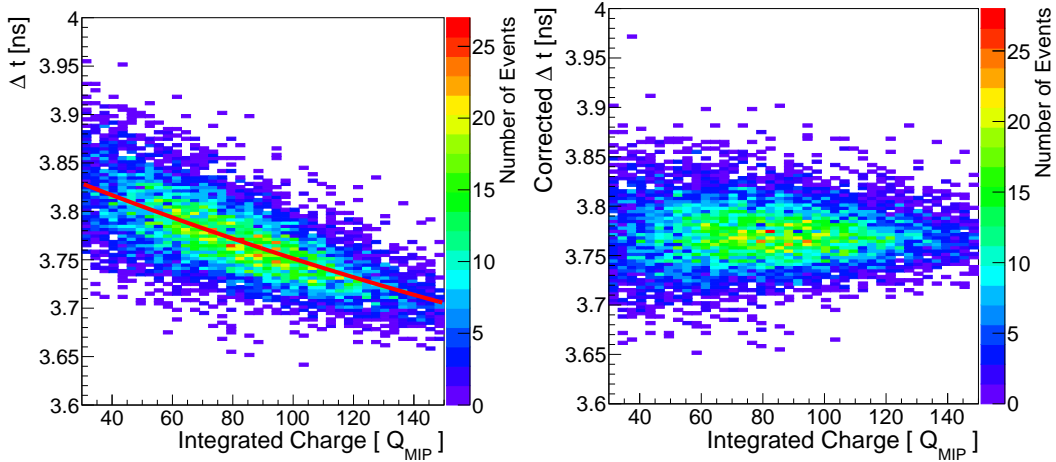


Figure 12.9: The dependence of  $\Delta t$  on the integrated charge in the silicon sensor is shown on the left. The red curve represents the fit to the profile plot of the two dimensional distribution, and is used to correct  $\Delta t$  for this effect. On the right, we show the corresponding two dimensional distribution after performing the correction. A 16 GeV electron beam is used, and the silicon sensor is placed after  $6 X_0$  of tungsten absorber.

basis of increased velocity of electrons and holes in silicon at larger bias voltage.

## 12.5 Discussion

From Figures 12.6 and 12.7, it is observed that the noise of the prototype calorimetric system is sufficiently low to extract signals from MIPs. Comparing the RMS of the noise distribution with the mean of the MIP signal, a signal-to-noise ratio around 2 to 2.5 is extracted. A rough estimate from Figure 12.7 demonstrates that the efficiency to detect 120 GeV protons and 8 GeV electrons with no absorber present is larger than 80%. The signal distributions for electromagnetic showers are normalized to the MIP response, and a linear response as a function of the beam energy is observed, as shown in Figure 12.10. The measured longitudinal shower profile in, shown in Figure 12.11, is consistent with similar past measurements.

The TOF associated with the detection of electromagnetic showers induced by electrons with energy between 20 GeV and 30 GeV can be measured with a precision better than 25 ps. Results of the measurements reported in Ref. [20] showed that a time resolution below 50 ps could be achieved for signals larger than 10 equivalent MIPs. To achieve this. Taking into account the 13 ps time resolution of the reference Photek MCP-PMT detector measured to electromagnetic showers [118] yields

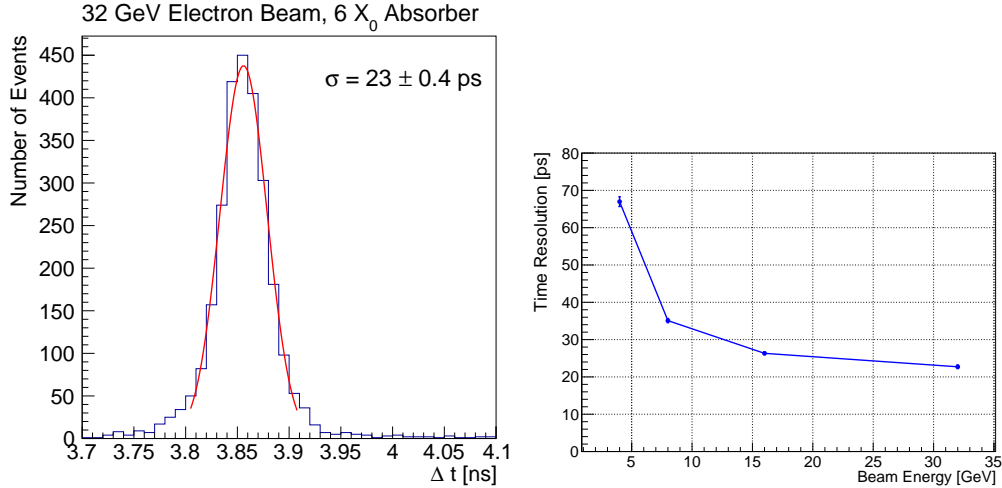


Figure 12.10: Left: The distribution of  $\Delta t$  between the silicon sensor and the Photek MCP-PMT. A 32 GeV electron beam is used, and the silicon sensor is placed after  $6 X_0$  of tungsten absorber. Right: The measured time resolution between the silicon sensor and the Photek MCP-PMT reference is shown as a function of the electron beam energy. The silicon sensor is placed after  $6 X_0$  of tungsten absorber.

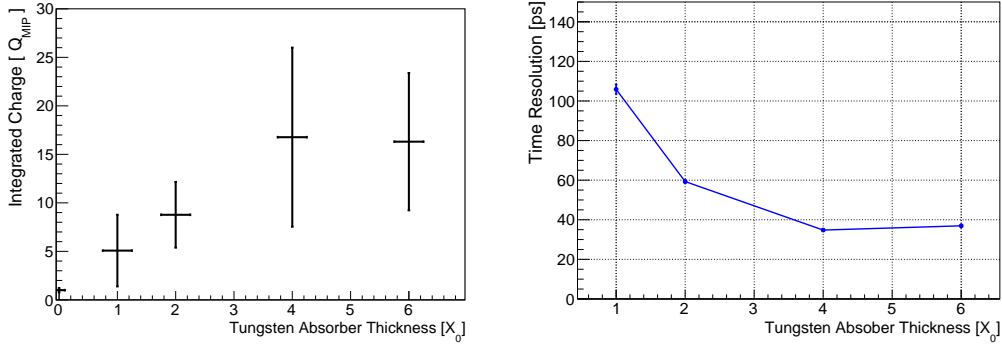


Figure 12.11: On the left, the integrated charge in the silicon sensor expressed in units of  $Q_{MIP}$  is shown as a function of the absorber ( $W$ ) thickness measured in units of radiation lengths ( $X_0$ ). The electron beam energy was 8 GeV. The uncertainty bands show the RMS of the measured charge distribution. On the right, the time resolution between the silicon sensor and the Photek MCP-PMT reference is shown as a function of the absorber thickness.

a precision close to 20 ps. Moreover, the time resolution improves with larger electron beam energy, and more generally with larger signal amplitudes. These measurements demonstrate that a calorimeter based on silicon sensors as the sensitive medium can achieve intrinsic time resolution at the 20 ps level, as long as noise is kept under control. Time jitter arising from intrinsic properties of the silicon sensor

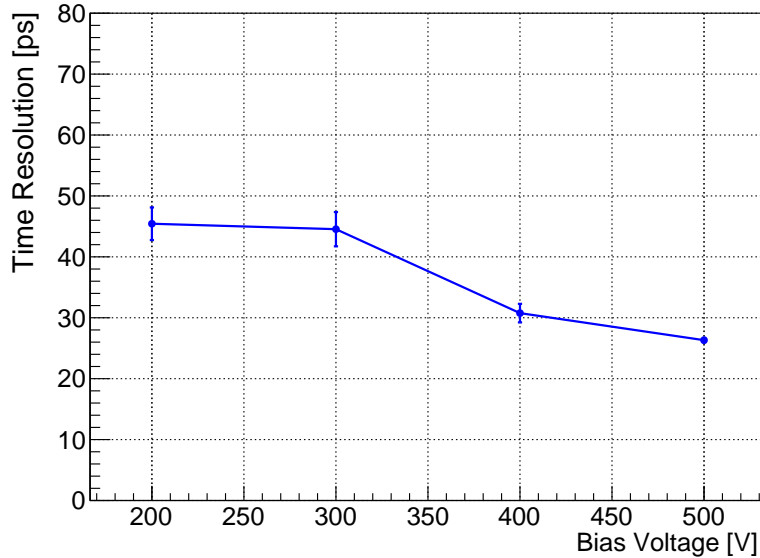


Figure 12.12: The time resolution between the silicon sensor and the Photek MCP-PMT reference is shown as a function of bias voltage applied on the silicon sensor. The electron beam energy was 16 GeV, and the silicon sensor is placed after  $6 X_0$  of tungsten absorber.

is demonstrated to be well below the 20 ps level.

## 12.6 Conclusion

The best time resolution of 23 ps for a silicon sensor was achieved with a 32 GeV beam and with the silicon sensor placed after 6 radiation lengths of tungsten absorber. Based on the calibration data for the response of the silicon sensor to MIPs, this measurement corresponds roughly to an average of 54 secondary particles registered from the electromagnetic shower. This results provide a solid ground and further encouragement to use silicon as the sensitive medium in sampling calorimeters, as is planned for example for the CMS Phase 2 upgrade [45], and explicitly demonstrates the opportunity to use silicon for timing measurements in future calorimeters. Further measurements include more realistic prototypes covering larger transverse and longitudinal regions of the electromagnetic shower and increasing the transverse granularity.

## CMS HIGH-GRANULARITY CALORIMETER TIMING LAYER

### 13.1 Introduction

Recent advances in silicon sensors in terms of radiation tolerance, highly granular designs [16], and cost per unit area offers the possibility of their use as the sensitive media in a sampling calorimeter at the HL-LHC. An important example of such a device is the forward calorimeter proposed for the CMS Phase 2 Upgrade [45], where high-granularity silicon sensors and tungsten/copper absorber layers are interleaved. As described in Chapter 12, silicon-based shower maximum detectors have extremely good precision timing capabilities – achieving a TOF resolution of 25 ps for 32 GeV electron induced shower – which could be used to reduce the detrimental effects of the high pileup environment foreseen for the HL-LHC. This chapter presents recent studies on the intrinsic timing properties of the silicon sensors to be used by the proposed CMS high-granularity calorimeter (HGC).

This chapter is organized as follows. General properties of the HGC silicon sensor are described in Section 13.2. The test beam setup and experimental apparatus are presented in Section 13.3. The results of the test beam measurements are presented in Section 13.4. Finally, Section 13.5 is devoted to discussion and conclusions.

### 13.2 General Properties of Silicon Timing and Bench Test Studies

All measurements presented in this chapter were carried out using a silicon sensor identical to that of the CMS HGC. The silicon sensor thickness is  $300\mu\text{m}$  and it is comprised of 128 hexagonal pixels with 1 cm maximal diameter. The left and right panels of Figure 13.1 show a schematic with 7 pixels and a full CAD schematic of the sensor, respectively. The silicon sensor was wire-bonded to a printed circuit board (PCB) where 25 pixels were implemented with an independent analog read-out. The PCB provided amplification for all the 25 implemented pixels and was optimized for timing measurement, this final HGC timing layer is shown in Figure 13.2. The silicon sensor was operated with a bias voltage of  $-300\text{ V}$  and the measured total current was  $170\text{ }\mu\text{A}$ .

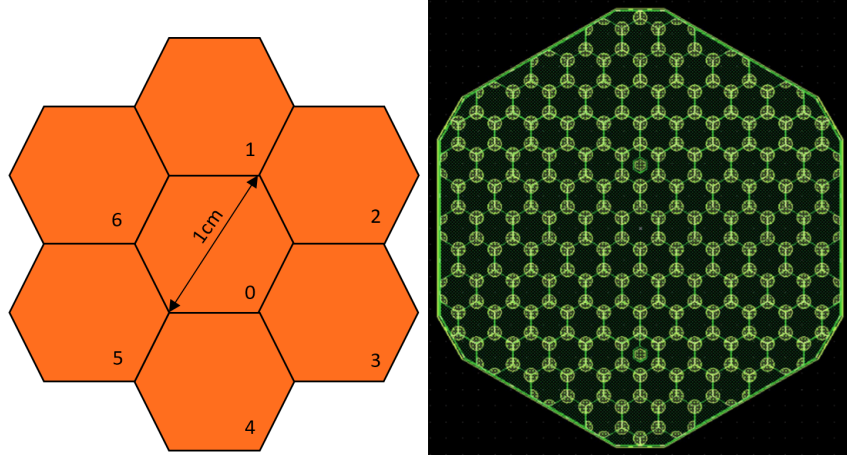


Figure 13.1: An HGC sensor schematic geometry with 7 pixels (left), and a CAD schematic of the entire sensor (right) are shown.

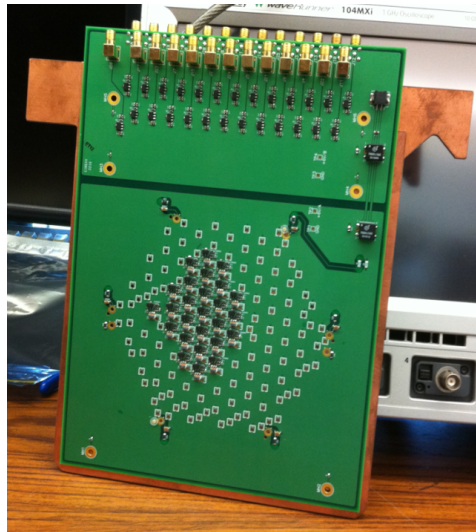


Figure 13.2: The implemented HGC timing layer is shown. 25 pixels with full analog electronics were implemented. The silicon sensor is at the back of the PCB.

### 13.3 Test-beam Setup and Experimental Apparatus

Test-beam measurements were carried out at the FTBF which provided a 120 GeV proton beam from the Fermilab Main Injector accelerator , and secondary beams composed of electrons, pions, and muons of energies ranging from 4 GeV to 32 GeV. A simple schematic diagram of the experimental setup is shown in Figure 13.3. A small plastic scintillator of transverse dimensions 1.7 mm×2 mm is used as a trigger counter to initiate the read out of the DAQ system and to select incident beam particles from a small geometric area, allowing us to center the beam particles on

the HGC timing layer. Next, we place a stack of either tungsten or lead absorbers of various thicknesses for measurements of the longitudinal profile of the electromagnetic shower. The HGC timing layer is located immediately downstream of the absorber plates. Finally, a Photek 240 MCP-PMT detector [28, 115, 118, 116] is placed furthest downstream, and serves to provide a very precise reference timestamp; Its precision has been previously measured to be less than 10 ps [118]. A photograph showing the various detector components is presented in Figure 13.4. More details of the experimental setup are described in our previous studies using the same experimental facility in references [28, 115, 118, 116] as well as in Chapters 10 and 11. The DAQ system is based on a CAEN V1742 digitizer board [5],

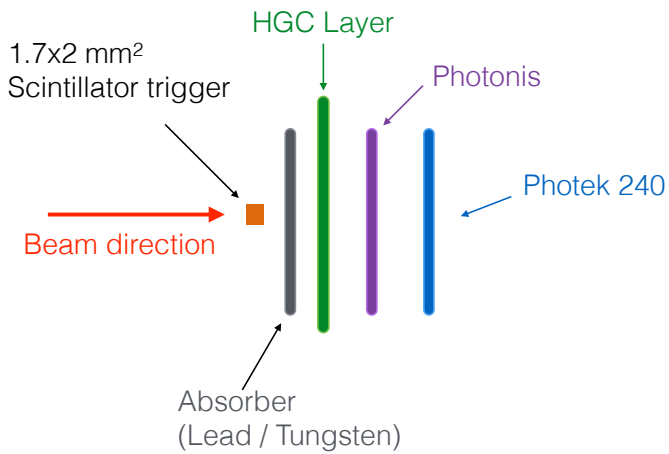


Figure 13.3: A schematic diagram of the test-beam setup is shown. The  $t_0$  and  $t_1$  are defined in Section 12.4.

which provides digitized waveforms sampled at 5 GS/s. The HGC timing layer was not electromagnetically shielded and therefore some electronic pickup noise was detected and accounted for during the offline analysis. A nominal bias voltage of  $-300$  V was applied to deplete the silicon sensor in all of the studies shown below.

### 13.4 Test Beam Measurement, Data Analysis, and Results

Measurements were performed in June 2016, using the primary 120 GeV proton beam, and secondary electron beam provided for the FTBF. Secondary beams with energies ranging from 4 GeV to 32 GeV were used. As discussed in Chapter 12, the electron purity for those beams ranges between 70% at the lowest energy to about 10% at the highest energy. Stacks of either tungsten or lead plates with varying thicknesses were placed immediately upstream of the HGC timing layer in order to measure the response along the longitudinal direction of the electromagnetic

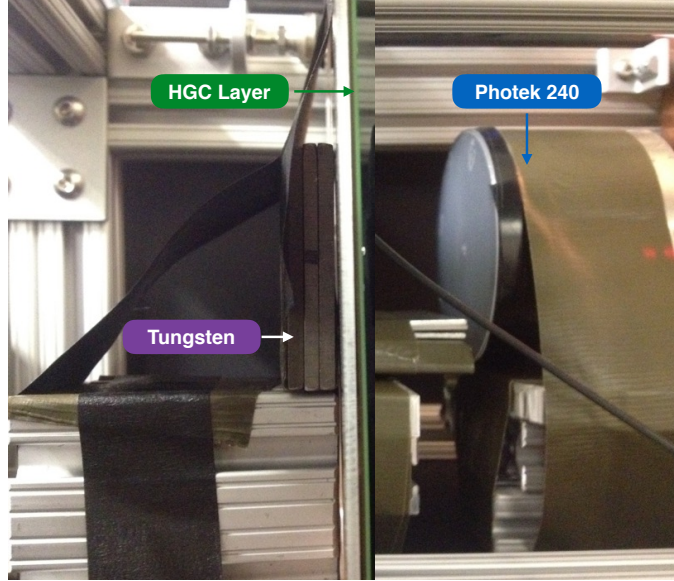


Figure 13.4: HGC timing layer test beam setup.

shower, although most of the results presented below correspond to  $6X_0$  of lead. Signals from the HGC timing layer (25 pixels were implemented and read out) and the Photek 240 MCP-PMT are read out and digitized by the CAEN V1742 digitizer; representative signal waveforms for one of the 25 silicon pixels and the Photek 240 are shown in the left and right panel of Figure 13.5, respectively. The silicon signal pulse has a rise time of about 2 ns, and a full pulse width of around 7 ns. This rise time is consistent with a time constant of a silicon sensor coupled to a 50 Ohm amplifier.

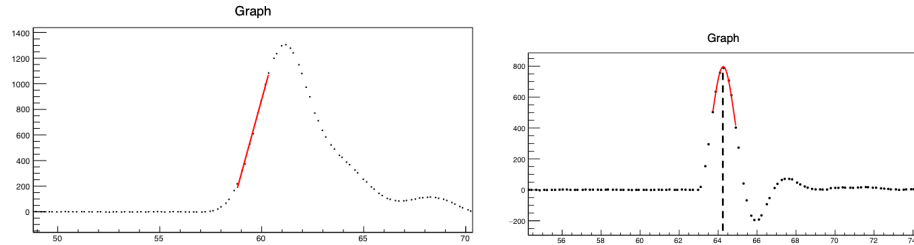


Figure 13.5: Examples of the signal pulse waveform for one the pixels of the HGC timing layer (left) and the Photek MCP-PMT (right) digitized by CAEN V1742 digitizer board. The bias voltage applied to the HGC silicon sensor is  $-300$  V.

The CAEN digitizer is voltage and time calibrated using the procedure described in Ref. [97]. The total collected charge for each signal pulse is computed by inte-

grating a 10 ns window around the peak of the pulse. The time for the reference Photek 240 MCP-PMT detector is obtained by fitting the peak region of the pulse to a Gaussian function and the mean parameter of the Gaussian is assigned as the timestamp  $t_0$ , see the right panel of Figure 13.6. The time for signals from each pixel in the HGC layer is obtained by performing a linear fit to the rising edge of the pulse and the time at which the pulse reaches 45% of the maximum amplitude is assigned as its timestamp  $t_1$ , see the left panel of Figure 13.6. The electronic time resolution of the CAEN V1742 digitizer was measured to be  $\sim 4$  ps and neglected on the timing measurements described below.

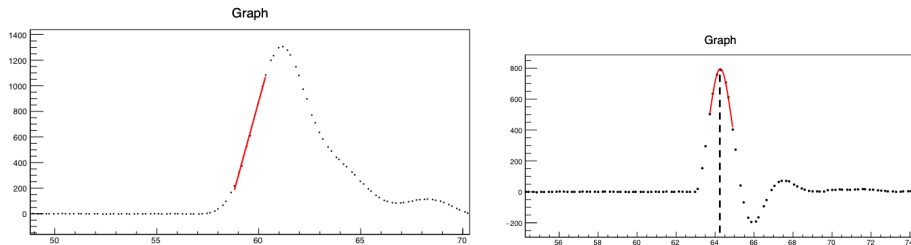


Figure 13.6: Examples of the timestamps extraction for a pulse waveform in one the pixels of the HGC timing layer (left) and the Photek 240 MCP-PMT (right) digitized by CAEN V1742 digitizer board. The timestamp on the HGC pixel is extracted by intersecting the linear fit (solid red line) with the horizontal line corresponding to 45% of the pulse maximum. The timestamp for the Photek 240 is the mean parameter of the Gaussian fit (solid blue line).

Electrons were identified by requiring that the signal amplitude of the Photek 240 MCP-PMT detector, located downstream of the HGC timing layer, exceeds certain thresholds because electromagnetic showers induced by electrons produce significantly larger signals, while pions produce much smaller signals. This procedure has been measured to provide electron purities between 80% and 90% for all beam conditions, see Chapter 12.

### Intrinsic HGC TOF resolution

Let's now examine the intrinsic timing capabilities of the HGC layer. The HGC timing layer was positioned just downstream of  $6X_0$  of lead and showering electrons were selected by requiring the signal amplitude and integrated charge in the Photek 240 MCP-PMT to be above a certain threshold. Figure 13.7 shows two examples of transverse shower profile measured by the HGC layer, where the color palette represents the integrated charge in each pixel. As observed in Figure 13.7 most of the activity is concentrated in the central and the 6 neighbouring pixels – these 7

pixel are more clearly represented in the left panel of Figure 13.1 – and therefore the studies in this chapter just include these pixels. It is of note that the central pixel could fluctuate in an event-by-event basis. The TOF for each of the considered

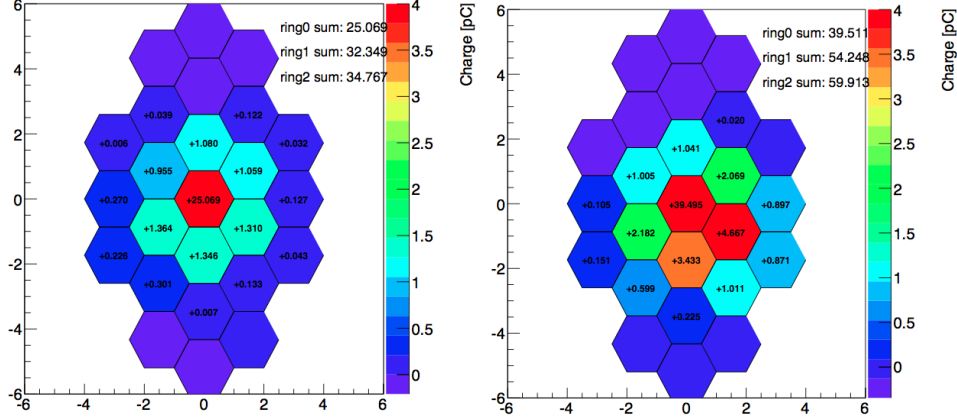


Figure 13.7: Examples of the shower transverse profile sampled by the HGC layer for a 32 GeV (left) and 16 GeV (right) electron beam. There is  $6X_0$  of tungsten right upstream of the HGC layer.

pixels in the HGC layer with respect to the Photek 240 MCP-PMT, i.e.  $\Delta t = t_1 - t_0$ , is calculated. Subsequently, the information from all the pixels is combined by weighting the individual times with the corresponding charge deposited in the following fashion:

$$\Delta t_{HGC} = \frac{\sum_{i=0}^6 \text{charge}_i \times \Delta t_i}{\sum_{i=0}^6 \text{charge}_i}, \quad (13.1)$$

where  $\Delta t_{HGC}$  is the combined HGC layer TOF,  $\text{charge}_i$  is the charge deposited in the  $i$ -th pixel, and  $\Delta t_i$  is the  $i$ -th pixel TOF. The TOF distributions for the pixels with highest and second highest charge are shown in the left and right panel of Figure 13.8, respectively. The TOF distributions of the HGC layer ( $\Delta t_{HGC}$ ) is shown in the left panel of Figure 13.9, while an alternative method for combining the HGC pixels – using the most probable value (mpv) of the deposited charge distribution in each pixel as the weight, see Eq. 13.1. These weights are constant throughout an entire run. – is shown in the right panel of Figure 13.9. It is of note that the default and the alternative (mpv) algorithms yield very similar results with an outstanding time resolution of about 15 ps for an electron beam of 32 GeV.

Comparing Figure 13.8 (left panel) and Figure 13.9, it is observed that the TOF resolution of the central pixel is already close the final time resolution of the entire

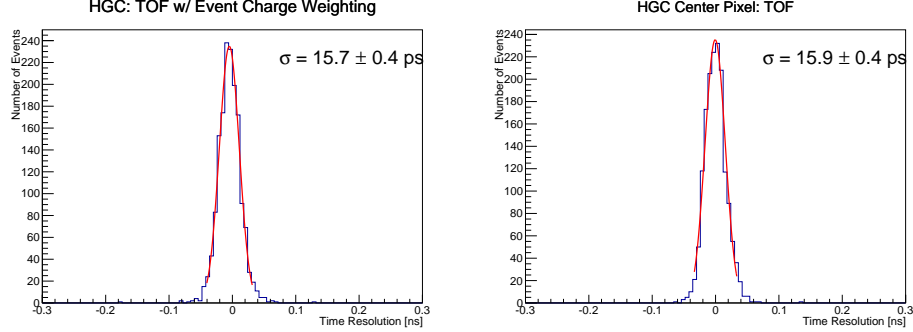


Figure 13.8: TOF distributions for (left) the pixel with the highest and (right) the pixel with the second highest charge in the HGC layer using a 32 GeV electron beam and  $6X_0$  of tungsten. The TOF resolutions are estimated by the standard deviation parameter of the Gaussian fit (red solid curve) to the TOF distribution.

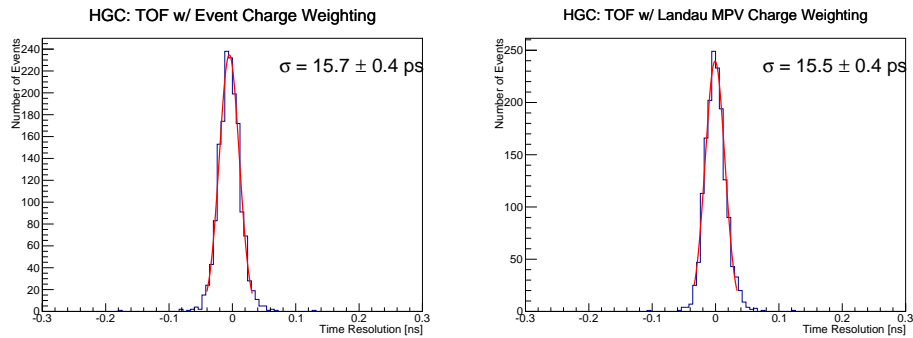


Figure 13.9: TOF distributions of the HGC layer using a 32 GeV electron beam and  $6X_0$  of tungsten, where the pixels are combined with (left) the default algorithm and (right) the mpv of the charge distribution as the weight. The TOF resolutions are estimated by the standard deviation parameter of the Gaussian fit (red solid curve) to the TOF distribution .

HGC layer. This suggests that pixels combination does not provide a significant improvement to the overall TOF resolution. Figure 13.10 shows the HGC TOF resolution as a function of the pixels combined at different separations between the tungsten absorber and the HGC layer, where it is observed that the TOF resolution is not significantly improved as a function of the added pixels for any of the separations. Despite the small improvement, it is observed that the larger the distance between the absorber and the HGC layer the larger is the relative improvement in the time resolution as more pixels are added, this is consistent with the fact that showers are more spread for the runs with more separation. Thus, it is convenient to define a quantity related to the transverse shower spread, to achieve this we use the ratio of the charge in the central pixel and the total charge in the 7 pixels as proxy

to the transverse shower profile:

$$R_7 = \frac{\text{charge}_0}{\sum_{i=0}^6 \text{charge}_i}, \quad (13.2)$$

where  $\text{charge}_i$  is the charge deposited in the  $i$ -th pixel, with the zeroth being the central pixel. The  $R_7$  distribution is shown in Figure 13.11.

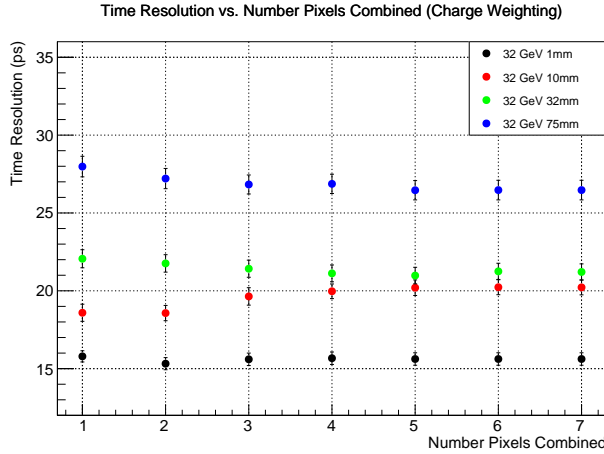


Figure 13.10: HGC layer TOF resolution as a function of the number of pixels combined. The distance between the absorber and the HGC layer was varied to sample the shower at different location.

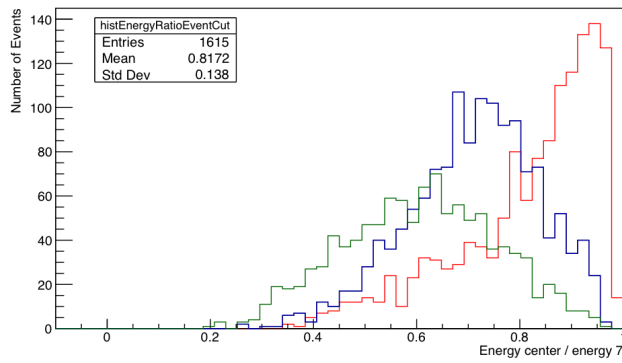


Figure 13.11:  $R_7$  distribution for different separations between the HGC layer and the  $6X_0$  of tungsten.

Finally, the dependence of the time resolution as a function of the beam energy is studied. Electron beams with energies of 8, 16, and 32 GeV were used, the separation between the absorber and the HGC layer was 1 mm. The results are summarized

in Figure 13.12, the functional form  $A/\sqrt{E} + B$  was used to fit the data points. It is observed that the functional form does not fit well the data and thus more beam energy points are needed to better constrain the floating parameters. Nevertheless, the best time resolution measured was found to be around 15 ps for a 32 GeV electron beam.

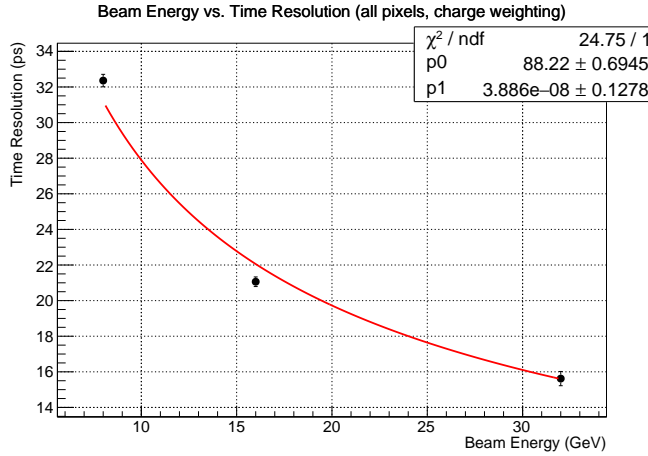


Figure 13.12: HGC layer TOF resolution as a function of the beam energy using  $6X_0$  of tungsten. The functional form  $A/\sqrt{E} + B$  was fitted to the data points (red solid curve).

### Combining Two Timing Layers

Combining the timing information of multiple HGC layers could improve the final TOF resolution of the calorimeter to em showers. The measurements presented in this chapter lack of an identical second HGC layer, but as shown in Chapter 11 the Photonis MCP-PMT located downstream of the HGC layer could be used as an additional timing measurement. To obtain the final TOF measurement (two-layer combination) the HGC layer and the Photonis MCP-PMT are combined with an equal weight. Figure 13.13 shows the TOF distribution for the Photonis MCP-PMT and the final two-layer combination in the left and right panels, respectively.

### Emulation of SKIROC2 Readout

The HGC proposed for the Phase 2 Upgrade of the CMS electromagnetic calorimeter uses a front-end electronics readout based on the *SKIROC2* chip, which has been preliminary shown to have around 50 ps jitter[45]. In order to simulate the effect of having a *SKIROC2* readout, the studies just presented above are now repeated with all the measured timestamps randomly smeared by 50 ps. Each timestamp –

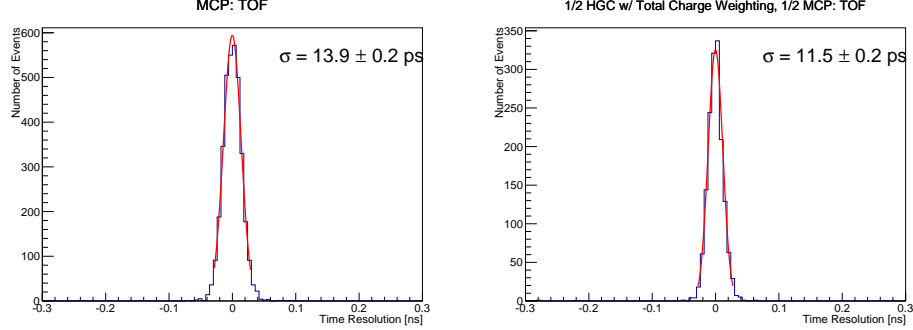


Figure 13.13: TOF distributions for (left) the Photonis MCP-PMT and (right) the final two-layer combination using a 32 GeV electron beam and  $6X_0$  of tungsten. The TOF resolutions are estimated by the standard deviation parameter of the Gaussian fit (red solid curve) to the TOF distribution .

this includes all the HGC layer pixels, the Photonis MCP-PMT, and the reference Photek 240 MCP-PMT. – is smeared by adding a random number drawn from a Gaussian p.d.f with a mean and a width of 0 and 50 ps, respectively.

Figure 13.14 shows the TOF distributions after smearing for the pixels with highest and second highest charge in the left and right panel, respectively. The  $\Delta t_{HGC}$  distribution and the two-layer combination TOF distribution are shown in the left and right panel of Figure 13.15. Here, pixels and layer are all combined with the same weight. The HGC time resolution improves from that of the central pixel only, this could be explain since the dominance of the central pixels has been diluted by the 50 ps Gaussian smearing. The HGC time resolution as a function of the number of pixels combined is shown in Figure 13.16.

Finally, the dependence of the TOF resolution is studied after the 50 ps smearing was applied. The results are summarized in Figure 13.17. It is of note that the final two-layer combination time resolution for a 32 GeV electron beam is around 30 ps and meets the requirements needed to reject pileup at the HL-LHC (30 ps is equivalent to 1 cm resolution in the collision axis).

### 13.5 Conclusions

The first timing studies on the HGC were carried out; the studies were done on a single HGC layer implemented with 25 pixels, each with an independent analog readout and then digitized by the CAEN V1742 digitizer. The HGC layer was placed right downstream of  $6X_0$  of tungsten absorber. The selected em shower events showed a transverse spread that was contained in the inner most pixels with the

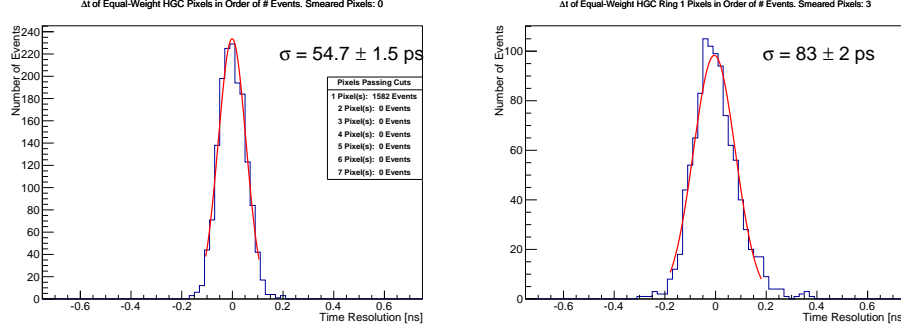


Figure 13.14: TOF distributions after a 50 ps Gaussian smearing for (left) the pixel with the highest and (right) the the pixel with the second highest charge in the HGC layer using a 32 GeV electron beam and  $6X_0$  of tungsten. The TOF resolutions are estimated by the standard deviation parameter of the Gaussian fit (red solid curve) to the TOF distribution.

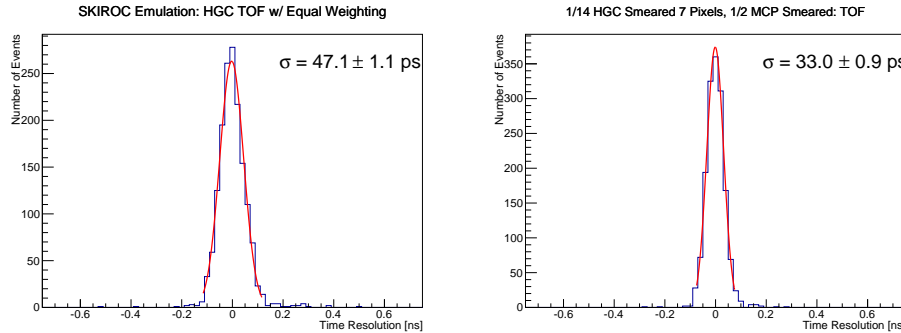


Figure 13.15: TOF distributions after a 50 ps Gaussian smearing for (left) the HGC layer and (right) the final two-layer combination using a 32 GeV electron beam and  $6X_0$  of tungsten. The TOF resolutions are estimated by the standard deviation parameter of the Gaussian fit (red solid curve) to the TOF distribution.

central pixel containig most of the energy of the shower. As expected, the total charge deposited in the 7 HGC pixels showed a linear relationship with respect to the electron beam energy. The HGC time-of-flight resolution was obtained by combining the 7 inner pixels and found to be around 15 ps, which was close to that of the central pixel alone; suggesting, that sampling the shower at place with more transverse spread could improve the timing performance, provided large signal to noise ratios in the 7 inner pixels. The combination of two timing layers was also studied, the results suggest that adding additional timing layers improves the timing performance as expected from two uncorrelated measurements. Finally, the effect of the SKIROC2 readout was studied by smearing each timestamp measurement by a Gaussian with 50 ps width. The HGC layer time resolution and the final two-

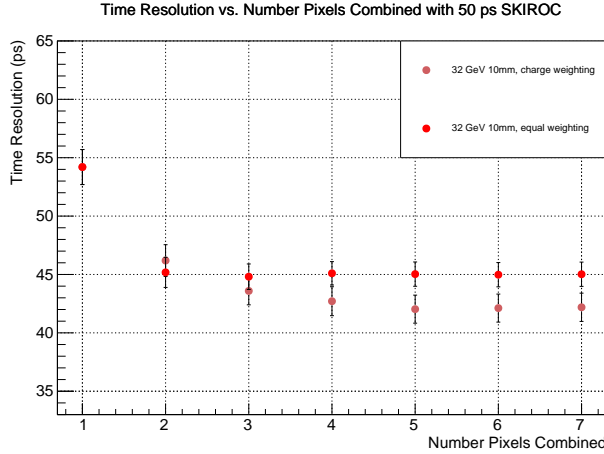


Figure 13.16: HGC layer TOF resolution after a 50 ps Gaussian smearing as a function of the number of pixels combined.

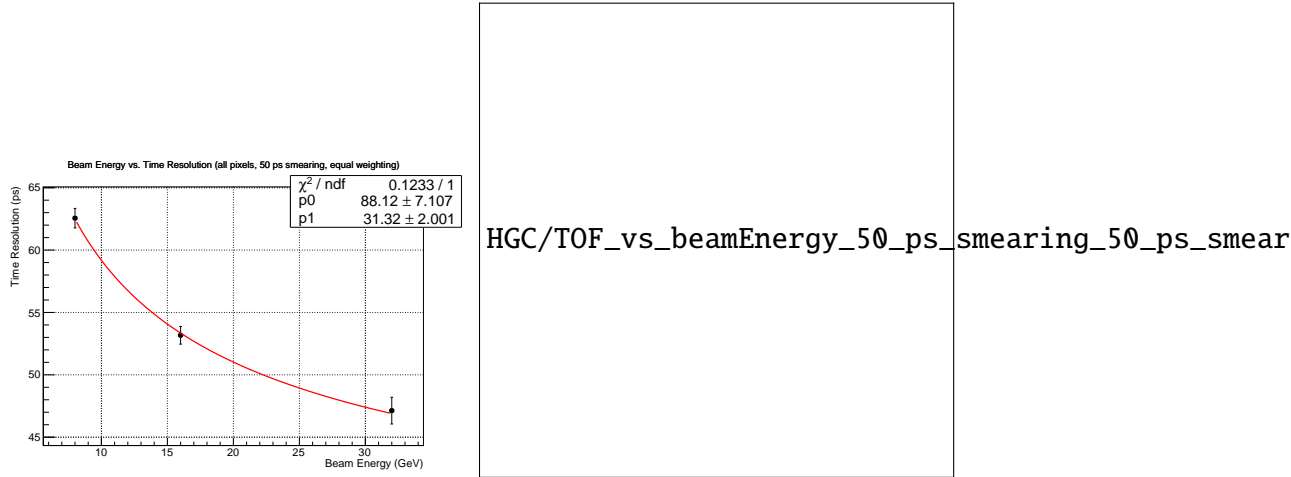


Figure 13.17: TOF distributions as a function of the beam energy after a 50 ps Gaussian smearing for (left) the HGC layer and (right) the final two-layer combination using  $6X_0$  of tungsten. The functional form  $A/\sqrt{E} + B$  was fitted to the data points (red solid curve).

layer combination were measured to be about 45 ps and 30 ps, respectively. These studies suggest that the desirable time-of-flight resolution for the proposed CMS high-granularity calorimeter are in principle well within reach.

## **Part V**

### **Summary and Conclusions**

### 13.6 Conclusion

Write your conclusion here.

[You can have chapters that were published as part of your thesis. The text style of the body should be single column, as it was submitted to the publisher, not formatted as the publisher did.]

## BIBLIOGRAPHY

- [1] In: (). <http://www.hamamatsu.com/resources/pdf/etd/R3809U-50 TPMH1067E09.pdf>.
- [2] In: (). [http://www.photek.com/pdf/datasheets/detectors/DS006\\_Photomultipliers.pdf](http://www.photek.com/pdf/datasheets/detectors/DS006_Photomultipliers.pdf).
- [3] In: (). <http://www.ellsworth.com/dow-corning-q2-3067-optical-couplant-453g-bottle>.
- [4] In: (). [https://www.hamamatsu.com/resources/pdf/ssd/e10\\_handbook\\_for\\_high\\_energy.pdf](https://www.hamamatsu.com/resources/pdf/ssd/e10_handbook_for_high_energy.pdf).
- [5] In: (). <http://www.caen.it/csite/CaenProd.jsp?parent=11&idmod=661>.
- [6] G. Aad et al. “Search for dark matter in events with heavy quarks and missing transverse momentum in pp collisions with the ATLAS detector”. In: *Eur. Phys. J. C* 75 (2015), p. 92. doi: [10.1140/epjc/s10052-015-3306-z](https://doi.org/10.1140/epjc/s10052-015-3306-z). arXiv: [1410.4031](https://arxiv.org/abs/1410.4031) [hep-ex].
- [7] Georges Aad et al. “Observation of a new particle in the search for the Standard Model Higgs boson with the ATLAS detector at the LHC”. In: *Phys. Lett. B* 716 (2012), p. 1. doi: [10.1016/j.physletb.2012.08.020](https://doi.org/10.1016/j.physletb.2012.08.020). arXiv: [1207.7214](https://arxiv.org/abs/1207.7214) [hep-ex].
- [8] Georges Aad et al. “Search for dark matter in events with a hadronically decaying W or Z boson and missing transverse momentum in pp collisions at  $\sqrt{s} = 8$  TeV with the ATLAS detector”. In: *Phys. Rev. Lett.* 112 (2014), p. 041802. doi: [10.1103/PhysRevLett.112.041802](https://doi.org/10.1103/PhysRevLett.112.041802). arXiv: [1309.4017](https://arxiv.org/abs/1309.4017) [hep-ex].
- [9] Georges Aad et al. “Search for dark matter in events with a Z boson and missing transverse momentum in pp collisions at  $\sqrt{s} = 8$  TeV with the ATLAS detector”. In: *Phys. Rev. D* 90 (2014), p. 012004. doi: [10.1103/PhysRevD.90.012004](https://doi.org/10.1103/PhysRevD.90.012004). arXiv: [1404.0051](https://arxiv.org/abs/1404.0051) [hep-ex].
- [10] Georges Aad et al. “Search for Dark Matter in Events with Missing Transverse Momentum and a Higgs Boson Decaying to Two Photons in pp Collisions at  $\sqrt{s} = 8$  TeV with the ATLAS Detector”. In: *Phys. Rev. Lett.* 115 (2015), p. 131801. doi: [10.1103/PhysRevLett.115.131801](https://doi.org/10.1103/PhysRevLett.115.131801). arXiv: [1506.01081](https://arxiv.org/abs/1506.01081) [hep-ex].
- [11] Georges Aad et al. “Search for dark matter produced in association with a Higgs boson decaying to two bottom quarks in pp collisions at  $\sqrt{s} = 8$  TeV with the ATLAS detector”. 2015.

- [12] Georges Aad et al. “Search for new particles in events with one lepton and missing transverse momentum in pp collisions at  $\sqrt{s} = 8$  TeV with the ATLAS detector”. In: *JHEP* 09 (2014), p. 037. doi: [10.1007/JHEP09\(2014\)037](https://doi.org/10.1007/JHEP09(2014)037). arXiv: [1407.7494 \[hep-ex\]](https://arxiv.org/abs/1407.7494).
- [13] Georges Aad et al. “Search for new phenomena in events with a photon and missing transverse momentum in pp collisions at  $\sqrt{s} = 8$  TeV with the ATLAS detector”. In: *Phys. Rev. D* 91 (2015). [Erratum: *Phys. Rev. D* 92 (2015) 059903], p. 012008. doi: [10.1103/PhysRevD.92.059903](https://doi.org/10.1103/PhysRevD.92.059903), [10.1103/PhysRevD.91.012008](https://doi.org/10.1103/PhysRevD.91.012008). arXiv: [1411.1559 \[hep-ex\]](https://arxiv.org/abs/1411.1559).
- [14] Georges Aad et al. “Search for new phenomena with the monojet and missing transverse momentum signature using the ATLAS detector in  $\sqrt{s} = 7$  TeV proton-proton collisions”. In: *Phys. Lett. B* 705 (2011), p. 294. doi: [10.1016/j.physletb.2011.10.006](https://doi.org/10.1016/j.physletb.2011.10.006). arXiv: [1106.5327 \[hep-ex\]](https://arxiv.org/abs/1106.5327).
- [15] P. A. R. Ade et al. “Planck 2013 results. XVI. Cosmological parameters”. In: *Astron. Astrophys.* 571 (2014), A16. doi: [10.1051/0004-6361/201321591](https://doi.org/10.1051/0004-6361/201321591). arXiv: [1303.5076 \[astro-ph.CO\]](https://arxiv.org/abs/1303.5076).
- [16] C. Adloff et al. “Tests of a particle flow algorithm with CALICE test beam data”. In: *JINST* 6 (2011), P07005. doi: [10.1088/1748-0221/6/07/P07005](https://doi.org/10.1088/1748-0221/6/07/P07005). arXiv: [1105.3417 \[physics.ins-det\]](https://arxiv.org/abs/1105.3417).
- [17] S. Agostinelli et al. “GEANT4: a simulation toolkit”. In: *Nucl. Instrum. Meth. A* 506 (2003), p. 250. doi: [10.1016/S0168-9002\(03\)01368-8](https://doi.org/10.1016/S0168-9002(03)01368-8).
- [18] Prateek Agrawal et al. “Flavored Dark Matter and the Galactic Center Gamma-Ray Excess”. In: *Phys. Rev. D* 90 (2014), p. 063512. doi: [10.1103/PhysRevD.90.063512](https://doi.org/10.1103/PhysRevD.90.063512). arXiv: [1404.1373 \[hep-ph\]](https://arxiv.org/abs/1404.1373).
- [19] H. Akaike. “A new look at the statistical model identification”. In: *IEEE Transactions on Automatic Control* 19-6 (1974), pp. 716–723. doi: [10.1109/TAC.1974.1100705](https://doi.org/10.1109/TAC.1974.1100705).
- [20] Nural Akchurin et al. “On the timing performance of thin planar silicon sensors”. In preparation, for submission to the Nucl. Instrum. Meth. A.
- [21] A. Albayrak-Yetkin et al. “Secondary Emission Calorimetry: Fast and Radiation Hard”. In: (2013). arXiv: [1307.8051 \[physics.ins-det\]](https://arxiv.org/abs/1307.8051). URL: <https://inspirehep.net/record/1245371/files/arXiv:1307.8051.pdf>.
- [22] M. Albrecht, K. Andert, P. Anselmino, et al. “Scintillators and Wavelength Shifters for the Detection of Ionizing Radiation”. In: *Proceedings of the 8th Conference on astroparticle, particle and space physics, detectors and medical physics applications* (2003), pp. 502–511. doi: [10.1142/9789812702708\\_0074](https://doi.org/10.1142/9789812702708_0074).
- [23] Sergey Alekhin et al. “The PDF4LHC Working Group Interim Report”. 2011.

- [24] Johan Alwall et al. “MadGraph5: going beyond”. In: *JHEP* 06 (2011), p. 128. doi: [10.1007/JHEP06\(2011\)128](https://doi.org/10.1007/JHEP06(2011)128). arXiv: [1106.0522](https://arxiv.org/abs/1106.0522) [hep-ph].
- [25] J. Alwall et al. “The automated computation of tree-level and next-to-leading order differential cross sections, and their matching to parton shower simulations”. In: *JHEP* 07 (2014), p. 079. doi: [10.1007/JHEP07\(2014\)079](https://doi.org/10.1007/JHEP07(2014)079). arXiv: [1405.0301](https://arxiv.org/abs/1405.0301) [hep-ph].
- [26] C. Amole et al. “Dark Matter Search Results from the PICO-2L C<sub>3</sub>F<sub>8</sub> Bubble Chamber”. In: *Phys. Rev. Lett.* 114 (2015), p. 231302. doi: [10.1103/PhysRevLett.114.231302](https://doi.org/10.1103/PhysRevLett.114.231302). arXiv: [1503.00008](https://arxiv.org/abs/1503.00008) [astro-ph.CO].
- [27] “An Indirect Search for WIMPs in the Sun using 3109.6 Days of Upward-going Muons in Super-Kamiokande”. In: *Astrophys. J.* 742 (78 2011), p. 78. doi: [doi:10.1088/0004-637X/742/2/78](https://doi.org/10.1088/0004-637X/742/2/78). arXiv: [1108.3384](https://arxiv.org/abs/1108.3384).
- [28] D. Anderson et al. “On Timing Properties of LYSO-Based Calorimeters”. In: *Nucl. Instrum. Meth. A* 794 (2015), pp. 7–14. doi: [10.1016/j.nima.2015.04.013](https://doi.org/10.1016/j.nima.2015.04.013).
- [29] G. Angloher et al. “Results on light dark matter particles with a low-threshold CRESST-II detector”. 2015.
- [30] G. Angloher et al. “Results on low mass WIMPs using an upgraded CRESST-II detector”. In: *Eur. Phys. J. C* 74 (2014), p. 3184. doi: [10.1140/epjc/s10052-014-3184-9](https://doi.org/10.1140/epjc/s10052-014-3184-9). arXiv: [1407.3146](https://arxiv.org/abs/1407.3146) [astro-ph.CO].
- [31] E. Aprile et al. “Limits on spin-dependent WIMP-nucleon cross sections from 225 live days of XENON100 data”. In: *Phys. Rev. Lett.* 111 (2013), p. 021301. doi: [10.1103/PhysRevLett.111.021301](https://doi.org/10.1103/PhysRevLett.111.021301). arXiv: [1301.6620](https://arxiv.org/abs/1301.6620) [astro-ph.CO].
- [32] S. Archambault et al. “Constraints on Low-Mass WIMP Interactions on <sup>19</sup>F from PICASSO”. In: *Phys. Lett. B* 711 (2012), p. 153. doi: [10.1016/j.physletb.2012.03.078](https://doi.org/10.1016/j.physletb.2012.03.078). arXiv: [1202.1240](https://arxiv.org/abs/1202.1240) [hep-ex].
- [33] ATLAS Collaboration. *Procedure for the LHC Higgs boson search combination in summer 2011*. Tech. rep. ATL-PHYS-PUB-2011-011. 2011. URL: <https://cds.cern.ch/record/1375842>.
- [34] Yang Bai, Patrick J. Fox, and Roni Harnik. “The Tevatron at the Frontier of Dark Matter Direct Detection”. In: *JHEP* 12 (2010), p. 048. doi: [10.1007/JHEP12\(2010\)048](https://doi.org/10.1007/JHEP12(2010)048). arXiv: [1005.3797](https://arxiv.org/abs/1005.3797) [hep-ph].
- [35] James M. Bardeen et al. “The Statistics of Peaks of Gaussian Random Fields”. In: *Astrophys. J.* 304 (1986), p. 15. doi: [10.1086/164143](https://doi.org/10.1086/164143).
- [36] Maria Beltrán et al. “Maverick dark matter at colliders”. English. In: *JHEP* 09, 37 (2010), p. 037. doi: [10.1007/JHEP09\(2010\)037](https://doi.org/10.1007/JHEP09(2010)037). arXiv: [1002.4137](https://arxiv.org/abs/1002.4137). URL: [http://dx.doi.org/10.1007/JHEP09\(2010\)037](http://dx.doi.org/10.1007/JHEP09(2010)037).

- [37] P. de Bernardis et al. “A flat Universe from high resolution maps of the cosmic microwave background radiation”. In: *Nature* 404 (2000), p. 955. doi: [10.1038/35010035](https://doi.org/10.1038/35010035). arXiv: [astro-ph/0004404](https://arxiv.org/abs/astro-ph/0004404) [astro-ph].
- [38] Christoph Borschensky et al. “Squark and gluino production cross sections in pp collisions at  $\sqrt{s} = 13, 14, 33$  and  $100$  TeV”. In: *Eur. Phys. J.* C74.12 (2014), p. 3174. doi: [10.1140/epjc/s10052-014-3174-y](https://doi.org/10.1140/epjc/s10052-014-3174-y). arXiv: [1407.5066](https://arxiv.org/abs/1407.5066) [hep-ph].
- [39] Michiel Botje et al. “The PDF4LHC Working Group Interim Recommendations”. 2011.
- [40] D Bourilkov, R C Group, and M R Whalley. “LHAPDF: PDF use from the Tevatron to the LHC”. In: *TeV4LHC Workshop - 4th meeting Batavia, Illinois, October 20-22, 2005*. 2006. arXiv: [hep-ph/0605240](https://arxiv.org/abs/hep-ph/0605240) [hep-ph].
- [41] O. Buchmueller, Matthew J. Dolan, and Christopher McCabe. “Beyond Effective Field Theory for Dark Matter Searches at the LHC”. In: *JHEP* 01 (2014), p. 025. doi: [10.1007/JHEP01\(2014\)025](https://doi.org/10.1007/JHEP01(2014)025). arXiv: [1308.6799](https://arxiv.org/abs/1308.6799) [hep-ph].
- [42] Giorgio Busoni et al. “On the Validity of the Effective Field Theory for Dark Matter Searches at the LHC”. In: *Phys. Lett. B* 728 (2014), p. 412. doi: [10.1016/j.physletb.2013.11.069](https://doi.org/10.1016/j.physletb.2013.11.069). arXiv: [1307.2253](https://arxiv.org/abs/1307.2253) [hep-ph].
- [43] Giorgio Busoni et al. “On the Validity of the Effective Field Theory for Dark Matter Searches at the LHC, Part II: Complete Analysis for the  $s$ -channel”. In: *JCAP* 06 (2014), p. 060. doi: [10.1088/1475-7516/2014/06/060](https://doi.org/10.1088/1475-7516/2014/06/060). arXiv: [1402.1275](https://arxiv.org/abs/1402.1275) [hep-ph].
- [44] Giorgio Busoni et al. “On the Validity of the Effective Field Theory for Dark Matter Searches at the LHC Part III: Analysis for the  $t$ -channel”. In: *JCAP* 09 (2014), p. 022. doi: [10.1088/1475-7516/2014/09/022](https://doi.org/10.1088/1475-7516/2014/09/022). arXiv: [1405.3101](https://arxiv.org/abs/1405.3101) [hep-ph].
- [45] J Butler et al. *Technical Proposal for the Phase-II Upgrade of the CMS Detector*. Tech. rep. CERN-LHCC-2015-010. LHCC-P-008. Geneva: CERN, June 2015. URL: <https://cds.cern.ch/record/2020886>.
- [46] Matteo Cacciari, Gavin P. Salam, and Gregory Soyez. “FastJet user manual”. In: *Eur. Phys. J. C* 72 (2012), p. 1896. doi: [10.1140/epjc/s10052-012-1896-2](https://doi.org/10.1140/epjc/s10052-012-1896-2). arXiv: [1111.6097](https://arxiv.org/abs/1111.6097) [hep-ph].
- [47] Matteo Cacciari, Gavin P. Salam, and Gregory Soyez. “The anti- $k_T$  jet clustering algorithm”. In: *JHEP* 04 (2008), p. 063. doi: [10.1088/1126-6708-2008-04-063](https://doi.org/10.1088/1126-6708-2008-04-063). arXiv: [0802.1189](https://arxiv.org/abs/0802.1189) [hep-ph].
- [48] R. G. Carlberg and H. M. P. Couchman. “Mergers and bias in a cold dark matter cosmology”. In: *Astrophys. J.* 340 (1989), p. 47. doi: [10.1086/167375](https://doi.org/10.1086/167375).

- [49] Renyue Cen. “Decaying cold dark matter model and small-scale power”. In: *Astrophys. J.* 546 (2001), pp. L77–L80. doi: [10.1086/318861](https://doi.org/10.1086/318861). arXiv: [astro-ph/0005206](https://arxiv.org/abs/astro-ph/0005206) [astro-ph].
- [50] S. Chatrchyan et al. “Performance of the CMS missing transverse momentum reconstruction in pp data at  $\sqrt{s} = 8$  TeV”. In: *JINST* 10 (2015), p. 2006. doi: [10.1088/1748-0221/10/02/P02006](https://doi.org/10.1088/1748-0221/10/02/P02006). arXiv: [1411.0511](https://arxiv.org/abs/1411.0511) [hep-ex]. URL: <http://stacks.iop.org/1748-0221/10/i=02/a=P02006>.
- [51] S. Chatrchyan et al. “The CMS experiment at the CERN LHC”. In: *JINST* 3 (2008), S08004. doi: [10.1088/1748-0221/3/08/S08004](https://doi.org/10.1088/1748-0221/3/08/S08004).
- [52] Serguei Chatrchyan et al. “Identification of b-quark jets with the CMS experiment”. In: *JINST* 8 (2013), p. 4013. doi: [10.1088/1748-0221/8/04/P04013](https://doi.org/10.1088/1748-0221/8/04/P04013). arXiv: [1211.4462](https://arxiv.org/abs/1211.4462) [hep-ex].
- [53] Serguei Chatrchyan et al. “Inclusive search for squarks and gluinos in pp collisions at  $\sqrt{s} = 7$  TeV”. In: *Phys. Rev. D* 85 (2012), p. 012004. doi: [10.1103/PhysRevD.85.012004](https://doi.org/10.1103/PhysRevD.85.012004). arXiv: [1107.1279](https://arxiv.org/abs/1107.1279) [hep-ex].
- [54] Serguei Chatrchyan et al. “Missing transverse energy performance of the CMS detector”. In: *JINST* 6 (2011), P09001. doi: [10.1088/1748-0221/6/09/P09001](https://doi.org/10.1088/1748-0221/6/09/P09001). arXiv: [1106.5048](https://arxiv.org/abs/1106.5048) [physics.ins-det].
- [55] Serguei Chatrchyan et al. “Observation of a new boson at a mass of 125 GeV with the CMS experiment at the LHC”. In: *Phys. Lett. B* 716 (2012), p. 30. doi: [10.1016/j.physletb.2012.08.021](https://doi.org/10.1016/j.physletb.2012.08.021). arXiv: [1207.7235](https://arxiv.org/abs/1207.7235) [hep-ex].
- [56] Serguei Chatrchyan et al. “Search for dark matter and large extra dimensions in monojet events in pp collisions at  $\sqrt{s} = 7$  TeV”. In: *JHEP* 09 (2012), p. 094. doi: [10.1007/JHEP09\(2012\)094](https://doi.org/10.1007/JHEP09(2012)094). arXiv: [1206.5663](https://arxiv.org/abs/1206.5663) [hep-ex].
- [57] Serguei Chatrchyan et al. “Search for dark matter, extra dimensions, and unparticles in monojet events in proton-proton collisions  $\sqrt{s} = 8$  TeV”. In: *Euro. Phys. J. C* 75 (2015), p. 235. doi: [10.1140/epjc/s10052-015-3451-4](https://doi.org/10.1140/epjc/s10052-015-3451-4). arXiv: [1408.3583](https://arxiv.org/abs/1408.3583) [hep-ex].
- [58] Serguei Chatrchyan et al. “Search for New Physics in the Multijet and Missing Transverse Momentum Final State in Proton-Proton Collisions at  $\sqrt{s} = 7$  TeV”. In: *Phys. Rev. Lett.* 109 (2012), p. 171803. doi: [10.1103/PhysRevLett.109.171803](https://doi.org/10.1103/PhysRevLett.109.171803). arXiv: [1207.1898](https://arxiv.org/abs/1207.1898) [hep-ex].
- [59] Serguei Chatrchyan et al. “Search for supersymmetry with razor variables in pp collisions at  $\sqrt{s} = 7$  TeV”. In: *Phys. Rev. D* 90 (2014), p. 112001. doi: [10.1103/PhysRevD.90.112001](https://doi.org/10.1103/PhysRevD.90.112001). arXiv: [1405.3961](https://arxiv.org/abs/1405.3961) [hep-ex].

- [60] Serguei Chatrchyan et al. “Search for supersymmetry with razor variables in pp collisions at  $\sqrt{s} = 7$  TeV”. In: *Phys. Rev. D* 90 (2014), p. 112001. doi: [10.1103/PhysRevD.90.112001](https://doi.org/10.1103/PhysRevD.90.112001). arXiv: [1405.3961](https://arxiv.org/abs/1405.3961) [hep-ex].
- [61] Douglas Clowe et al. “A direct empirical proof of the existence of dark matter”. In: *Astrophys. J.* 648 (2006), p. L109. doi: [10.1086/508162](https://doi.org/10.1086/508162). arXiv: [astro-ph/0608407](https://arxiv.org/abs/astro-ph/0608407) [astro-ph].
- [62] CMS Collaboration. *Commissioning of the Particle-flow Event Reconstruction with the first LHC collisions recorded in the CMS detector*. CMS Physics Analysis Summary CMS-PAS-PFT-10-001. 2010. URL: <https://cds.cern.ch/record/1247373>.
- [63] CMS Collaboration. *Commissioning of the particle-flow event reconstruction with the first LHC collisions recorded in the CMS detector*. CMS Physics Analysis Summary CMS-PAS-PFT-10-011. 2010. URL: <http://cdsweb.cern.ch/record/1247373>.
- [64] CMS Collaboration. *Data Parking and Data Scouting at the CMS Experiment*. CMS Physics Analysis Summary CMS-DP-2012-022. 2012. URL: <http://cdsweb.cern.ch/record/1247373>.
- [65] CMS Collaboration. *Particle-flow event reconstruction in CMS and performance for jets, taus, and  $E_T^{\text{miss}}$* . CMS Physics Analysis Summary CMS-PAS-PFT-09-001. 2009. URL: <http://cdsweb.cern.ch/record/1194487>.
- [66] CMS Collaboration. *Performance of the missing transverse energy reconstruction by the CMS experiment in  $\sqrt{s} = 8$  TeV pp data*. CMS Physics Analysis Summary CMS-PAS-JME-13-003. 2013. URL: <http://cds.cern.ch/record/1966665>.
- [67] CMS Collaboration. *Procedure for the LHC Higgs boson search combination in Summer 2011*. Tech. rep. CMS-NOTE-2011-005. 2011. URL: <https://cds.cern.ch/record/1379837>.
- [68] D Contardo and J Spalding. *CMS Phase 2 Upgrade: Preliminary Plan and Cost Estimate*. Tech. rep. CERN-RRB-2013-124. Geneva: CERN, Oct. 2013.
- [69] Michal Czakon and Alexander Mitov. “Top++: a program for the calculation of the top-pair cross-section at hadron colliders”. In: *Comp. Phys. Commun.* 185 (2014), p. 2930. doi: [10.1016/j.cpc.2014.06.021](https://doi.org/10.1016/j.cpc.2014.06.021). arXiv: [1112.5675](https://arxiv.org/abs/1112.5675) [hep-ph].
- [70] “Dark Matter Results from 100 Live Days of XENON100 Data”. In: *Phys. Rev. Lett.* 107 (13 2011), p. 131302. doi: [10.1103/PhysRevLett.107.131302](https://doi.org/10.1103/PhysRevLett.107.131302). arXiv: [1104.2549](https://arxiv.org/abs/1104.2549).
- [71] “Dark Matter Search Results from the CDMS II Experiment”. In: *Science* 86 (5 2012), p. 052001. doi: [10.1126/science.1186112](https://doi.org/10.1126/science.1186112).

- [72] A. A. Derevshchikov et al. *On possibility to make a new type of calorimeter: Radiation resistant and fast*. Tech. rep. IFVE-90-99. Protvino, Russia: IHEP, 1990. URL: <http://ccdb5fs.kek.jp/cgi-bin/img/allpdf?199010441>.
- [73] G. Dissertori, D. Luckey, Nessi-Tedaldi, et al. “Results on damage induced by high-energy protons in LYSO calorimeter crystals”. In: *NIM A* 745 (2014) 1-6. doi: [10.1016/j.nima.2014.02.003](https://doi.org/10.1016/j.nima.2014.02.003). arXiv: [1309.3872 \[physics.ins-det\]](https://arxiv.org/abs/1309.3872).
- [74] Pierre Fayet. “Supergauge Invariant Extension of the Higgs Mechanism and a Model for the Electron and its Neutrino”. In: *Nucl. Phys. B* 90 (1975), p. 104. doi: [10.1016/0550-3213\(75\)90636-7](https://doi.org/10.1016/0550-3213(75)90636-7).
- [75] Rick Field. “Early LHC Underlying Event Data - Findings and Surprises”. In: *Hadron collider physics. Proceedings, 22nd Conference, HCP 2010, Toronto, Canada, August 23-27, 2010*. arXiv: [1010.3558 \[hep-ph\]](https://arxiv.org/abs/1010.3558). URL: <http://inspirehep.net/record/873443/files/arXiv:1010.3558.pdf>.
- [76] “Final Analysis and Results of the Phase II SIMPLE Dark Matter Search”. In: *Phys. Rev. Lett.* 108 (2012), p. 201302. doi: [10.1103/PhysRevLett.108.201302](https://doi.org/10.1103/PhysRevLett.108.201302). arXiv: [1106.3014](https://arxiv.org/abs/1106.3014).
- [77] “First dark matter search results from a 4-kg CF<sub>3</sub>I bubble chamber operated in a deep underground site”. In: *Phys. Rev. D* 86 (5 2012), p. 052001. doi: [10.1103/PhysRevD.86.052001](https://doi.org/10.1103/PhysRevD.86.052001). arXiv: [1204.3094](https://arxiv.org/abs/1204.3094).
- [78] “First Results from the LUX Dark Matter Experiment at the Sanford Underground Research Facility”. In: *Phys. Rev. Lett.* 112 (9 2014), p. 091303. doi: [10.1103/PhysRevLett.112.091303](https://doi.org/10.1103/PhysRevLett.112.091303). arXiv: [1310.8214](https://arxiv.org/abs/1310.8214).
- [79] Patrick J. Fox et al. “Missing energy signatures of dark matter at the LHC”. In: *Phys. Rev. D* 85 (5 2012), p. 056011. doi: [10.1103/PhysRevD.85.056011](https://doi.org/10.1103/PhysRevD.85.056011). arXiv: [1109.4398](https://arxiv.org/abs/1109.4398). URL: <http://link.aps.org/doi/10.1103/PhysRevD.85.056011>.
- [80] Patrick J. Fox et al. “Taking a razor to dark matter parameter space at the LHC”. In: *Phys. Rev. D* 86 (2012), p. 015010. doi: [10.1103/PhysRevD.86.015010](https://doi.org/10.1103/PhysRevD.86.015010). arXiv: [1203.1662 \[hep-ph\]](https://arxiv.org/abs/1203.1662).
- [81] Alexander Friedland et al. “Probing Nonstandard Standard Model Backgrounds with LHC Monojets”. In: *Phys. Lett. B* 714 (2012), p. 267. doi: [10.1016/j.physletb.2012.06.078](https://doi.org/10.1016/j.physletb.2012.06.078). arXiv: [1111.5331 \[hep-ph\]](https://arxiv.org/abs/1111.5331).
- [82] Ryan Gavin et al. “FEWZ 2.0: A code for hadronic Z production at next-to-next-to-leading order”. 2010.
- [83] Ryan Gavin et al. “W physics at the LHC with FEWZ 2.1”. 2012.

- [84] Yu. A. Golfand and E. P. Likhtman. “Extension of the algebra of Poincare group generators and violation of p invariance”. In: *JETP Lett.* 13 (1971), p. 323.
- [85] Jessica Goodman et al. “Constraints on Dark Matter from Colliders”. In: *Phys. Rev. D* 82 (2010), p. 116010. doi: [10.1103/PhysRevD.82.116010](https://doi.org/10.1103/PhysRevD.82.116010). arXiv: [1008.1783](https://arxiv.org/abs/1008.1783) [hep-ph].
- [86] Denis Grondin and Daniel Jeans. “Next Generation CALICE Electromagnetic Calorimeter”. In: *International Linear Collider Workshop 2010 (LCWS10 & ILC10) Beijing, China, March 26-30, 2010.* 2010. arXiv: [1006.4313](https://arxiv.org/abs/1006.4313) [physics.ins-det]. URL: <http://inspirehep.net/record/859118/files/arXiv:1006.4313.pdf>.
- [87] Stefan Hoeche et al. “Matching parton showers and matrix elements”. 2006.
- [88] Dan Hooper and Lisa Goodenough. “Dark Matter Annihilation in The Galactic Center As Seen by the Fermi Gamma Ray Space Telescope”. In: *Phys. Lett. B* 697 (2011), p. 412. doi: [10.1016/j.physletb.2011.02.029](https://doi.org/10.1016/j.physletb.2011.02.029). arXiv: [1010.2752](https://arxiv.org/abs/1010.2752) [hep-ph].
- [89] H. C. van de Hulst, E. Raimond, and H. van Woerden. “Rotation and Density Distribution of the Andromeda Nebula Derived from Observations of the 21 cm line”. In: *Bull. Astr. Inst. Netherlands* 14 (1957), p. 1.
- [90] J. Chen, R. Mao, L. Zhang, and R. Zhu. “Gamma-Ray Induced Radiation Damage in Large Size LSO and LYSO Crystal Samples”. In: *IEEE Transactions on Nuclear Science* 54.4 (Aug. 2007), pp. 1319–1326. ISSN: 0018-9499. doi: [10.1109/TNS.2007.902370](https://doi.org/10.1109/TNS.2007.902370).
- [91] V. Khachatryan. “Search for Monotop Signatures in Proton-Proton Collisions at  $\sqrt{s} = 8$  TeV”. In: *Phys. Rev. Lett.* 114 (10 2015), p. 101801. doi: [10.1103/PhysRevLett.114.101801](https://doi.org/10.1103/PhysRevLett.114.101801). arXiv: [1410.1149](https://arxiv.org/abs/1410.1149). URL: <http://link.aps.org/doi/10.1103/PhysRevLett.114.101801>.
- [92] Vardan Khachatryan et al. “Observation of the diphoton decay of the Higgs boson and measurement of its properties”. In: *Eur. Phys. J. C* 74 (2014), p. 3076. doi: [10.1140/epjc/s10052-014-3076-z](https://doi.org/10.1140/epjc/s10052-014-3076-z). arXiv: [1407.0558](https://arxiv.org/abs/1407.0558) [hep-ex].
- [93] Vardan Khachatryan et al. “Performance of electron reconstruction and selection with the CMS detector in proton-proton collisions at  $\sqrt{s} = 8$  TeV”. In: *JINST* 10 (2015), P06005. doi: [10.1088/1748-0221/10/06/P06005](https://doi.org/10.1088/1748-0221/10/06/P06005). arXiv: [1502.02701](https://arxiv.org/abs/1502.02701) [physics.ins-det].
- [94] Vardan Khachatryan et al. “Performance of Photon Reconstruction and Identification with the CMS Detector in Proton-Proton Collisions at  $\sqrt{s} = 8$  TeV”. In: *JINST* 10.08 (2015), P08010. doi: [10.1088/1748-0221/10/08/P08010](https://doi.org/10.1088/1748-0221/10/08/P08010). arXiv: [1502.02702](https://arxiv.org/abs/1502.02702) [physics.ins-det].

- [95] Vardan Khachatryan et al. “Search for new phenomena in monophoton final states in proton-proton collisions at  $\sqrt{s} = 8$  TeV”. 2014.
- [96] Vardan Khachatryan et al. “Search for physics beyond the standard model in final states with a lepton and missing transverse energy in proton-proton collisions at  $\text{sqrt}(s) = 8$  TeV”. In: *Phys. Rev. D* 91 (2015), p. 092005. doi: [10.1103/PhysRevD.91.092005](https://doi.org/10.1103/PhysRevD.91.092005). arXiv: [1408.2745 \[hep-ex\]](https://arxiv.org/abs/1408.2745).
- [97] H. Kim et al. “A new time calibration method for switched-capacitor-array-based waveform samplers”. In: *Nucl. Instrum. Meth. A* 767 (2014), pp. 67–74. issn: 0168-9002. doi: <http://dx.doi.org/10.1016/j.nima.2014.08.025>. url: <http://www.sciencedirect.com/science/article/pii/S016890021400953X>.
- [98] L. Brianza, F. Cavallari, D. Del Re, S. Gelli, A. Ghezzi, C. Gotti, P. Govoni, C. Jorda Lopez, A. Martelli, B. Marzocchi, P. Meridiani, G. Organtini, R. Paramatti, L. Pernie, S. Pigazzini, S. Rahatlou, C. Rovelli, F. Santanastasio, T. Tabarelli de Fatis, N. Trevisani. “Response of microchannel plates to single particles and to electromagnetic showers”. In: *Nucl. Instrum. Meth. A* 797 (2015), pp. 216–221. issn: 0168-9002. doi: <http://dx.doi.org/10.1016/j.nima.2015.06.057>. url: <http://www.sciencedirect.com/science/article/pii/S0168900215008074>.
- [99] L. Rossi, and O. Brüning. *High Luminosity Large Hadron Collider A description for the European Strategy Preparatory Group*. Tech. rep. CERN-ATS-2012-236. Geneva: CERN, Aug. 2012.
- [100] L. Zhang, R. Mao, and R. Zhu. “Effects of neutron irradiations in various crystal samples of large size for future crystal calorimeter”. In: *Nuclear Science Symposium Conference Record (NSS/MIC), 2009 IEEE*. Oct. 2009, pp. 2041–2044. doi: [10.1109/NSSMIC.2009.5402125](https://doi.org/10.1109/NSSMIC.2009.5402125).
- [101] L. Zhang, R. Mao, F. Yang, and R. Zhu. “LSO/LYSO Crystals for Calorimeters in Future HEP Experiments”. In: *IEEE Transactions on Nuclear Science* 61.1 (Feb. 2014), pp. 483–488. issn: 0018-9499.
- [102] Tongyan Lin, Edward W. Kolb, and Lian-Tao Wang. “Probing dark matter couplings to top and bottom quarks at the LHC”. In: *Phys. Rev. D* 88 (2013), p. 063510. doi: [10.1103/PhysRevD.88.063510](https://doi.org/10.1103/PhysRevD.88.063510). arXiv: [1303.6638 \[hep-ph\]](https://arxiv.org/abs/1303.6638).
- [103] A. D. Martin et al. “Update of parton distributions at NNLO”. In: *Phys. Lett. B* 652 (2007), p. 292. doi: [10.1016/j.physletb.2007.07.040](https://doi.org/10.1016/j.physletb.2007.07.040). arXiv: [0706.0459 \[hep-ph\]](https://arxiv.org/abs/0706.0459).
- [104] Sanjib Muhuri et al. “Test and characterization of a prototype silicon-tungsten electromagnetic calorimeter”. In: *Nucl. Instrum. Meth. A* 764 (2014), pp. 24–29. issn: 0168-9002. doi: <http://dx.doi.org/10.1016/j.nima.2014.07.019>. url: <http://www.sciencedirect.com/science/article/pii/S0168900214008614>.

- [105] “Multiyear search for dark matter annihilations in the Sun with the AMANDA-II and IceCube detectors”. In: *Phys. Rev. D* 85 (4 2012), p. 042002. doi: [10.1103/PhysRevD.85.042002](https://doi.org/10.1103/PhysRevD.85.042002). arXiv: [1112.1840](https://arxiv.org/abs/1112.1840).
- [106] Pavel M. Nadolsky et al. “Implications of CTEQ global analysis for collider observables”. In: *Phys. Rev. D* 78 (2008), p. 013004. doi: [10.1103/PhysRevD.78.013004](https://doi.org/10.1103/PhysRevD.78.013004). arXiv: [0802.0007](https://arxiv.org/abs/0802.0007) [hep-ph].
- [107] K. A. Olive et al. “Review of Particle Physics”. In: *Chin. Phys. C* 38 (2014), p. 090001. doi: [10.1088/1674-1137/38/9/090001](https://doi.org/10.1088/1674-1137/38/9/090001).
- [108] Michele Papucci, Alessandro Vichi, and Kathryn M. Zurek. “Monojet versus the rest of the world I:  $t$ -channel models”. In: *JHEP* 11 (2014), p. 024. doi: [10.1007/JHEP11\(2014\)024](https://doi.org/10.1007/JHEP11(2014)024). arXiv: [1402.2285](https://arxiv.org/abs/1402.2285) [hep-ph].
- [109] *Performance of b tagging at  $\sqrt{s} = 8 \text{ TeV}$  in multijet,  $t\bar{t}$  and boosted topology events*. CMS Physics Analysis Summary CMS-PAS-BTV-13-001. 2013. URL: <http://cds.cern.ch/record/1581306>.
- [110] J. Pumplin et al. “New generation of parton distributions with uncertainties from global QCD analysis”. In: *JHEP* 07 (2002), p. 012. doi: [10.1088/1126-6708/2002/07/012](https://doi.org/10.1088/1126-6708/2002/07/012). arXiv: [hep-ph/0201195](https://arxiv.org/abs/hep-ph/0201195) [hep-ph].
- [111] R. Mao, L. Zhang, and R. Zhu. “Gamma ray induced radiation damage in PWO and LSO/LYSO crystals”. In: *Nuclear Science Symposium Conference Record (NSS/MIC), 2009 IEEE*. Oct. 2009, pp. 2045–2049. doi: [10.1109/NSSMIC.2009.5402126](https://doi.org/10.1109/NSSMIC.2009.5402126).
- [112] Pierre Ramond. “Dual theory for free fermions”. In: *Phys. Rev. D* 3 (1971), p. 2415. doi: [10.1103/PhysRevD.3.2415](https://doi.org/10.1103/PhysRevD.3.2415).
- [113] S. Ritt, R. Dinapoli, and U. Hartmann. “Application of the DRS chip for fast waveform digitizing”. In: *NIM A* 623 (2010) 486-488 () .
- [114] C. Rogan. “Kinematics for new dynamics at the LHC”. CALT-68-2790. 2010.
- [115] A. Ronzhin et al. “Development of a new fast shower maximum detector based on microchannel plates photomultipliers (MCP-PMT) as an active element”. In: *Nucl. Instrum. Meth. A* 759 (2014), pp. 65–73. ISSN: 0168-9002. doi: <http://dx.doi.org/10.1016/j.nima.2014.05.039>. URL: <http://www.sciencedirect.com/science/article/pii/S016890021400566X>.
- [116] A. Ronzhin et al. “Direct tests of micro channel plates as the active element of a new shower maximum detector”. In: *Nucl. Instrum. Meth. A* 795 (2015), pp. 52–57. ISSN: 0168-9002. doi: <http://dx.doi.org/10.1016/j.nima.2015.05.029>. URL: <http://www.sciencedirect.com/science/article/pii/S0168900215006610>.

- [117] A. Ronzhin et al. “Direct tests of micro channel plates as the active element of a new shower maximum detector”. In: *Nucl. Instrum. Meth.* A795 (2015), pp. 52–57. doi: [10.1016/j.nima.2015.05.029](https://doi.org/10.1016/j.nima.2015.05.029).
- [118] A. Ronzhin et al. “Study of the timing performance of micro-channel plate photomultiplier for use as an active layer in a shower maximum detector”. In: *Nucl. Instrum. Meth. A* 795 (2015), pp. 288–292. ISSN: 0168-9002. doi: <http://dx.doi.org/10.1016/j.nima.2015.06.006>. URL: <http://www.sciencedirect.com/science/article/pii/S0168900215007500>.
- [119] V.C. Rubin, N. Thonnard, and W.K. Ford Jr. “Rotational properties of 21 SC galaxies with a large range of luminosities and radii, from NGC 4605/R = 4 kpc to UGC 2885/R = 122 kpc”. In: *Astrophys. J.* 238 (1980), p. 471. doi: [10.1086/158003](https://doi.org/10.1086/158003).
- [120] “Search for Low-Mass Weakly Interacting Massive Particles Using Voltage-Assisted Calorimetric Ionization Detection in the SuperCDMS Experiment”. In: *Phys. Rev. Lett.* 112 (4 2014), p. 041302. doi: [10.1103/PhysRevLett.112.041302](https://doi.org/10.1103/PhysRevLett.112.041302). arXiv: [1309.3259](https://arxiv.org/abs/1309.3259).
- [121] “Search for supersymmetry using razor variables in events with b-tagged jets in pp collisions at  $\sqrt{s} = 8$  TeV”. In: *Phys. Rev. D* 91 (5 2015), p. 052018. doi: [10.1103/PhysRevD.91.052018](https://doi.org/10.1103/PhysRevD.91.052018). arXiv: [1502.00300](https://arxiv.org/abs/1502.00300). URL: <http://link.aps.org/doi/10.1103/PhysRevD.91.052018>.
- [122] *Search for SUSY with Higgs in the diphoton final state using the razor variables*. CMS Physics Analysis Summary CMS-PAS-SUS-14-017. 2014. URL: <http://cds.cern.ch/record/2047472>.
- [123] “Search for the production of dark matter in association with top-quark pairs in the single-lepton final state in proton-proton collisions at  $\sqrt{s} = 8$  TeV”. In: *JHEP* 06 (2015), p. 121. doi: [10.1007/JHEP06\(2015\)121](https://doi.org/10.1007/JHEP06(2015)121). arXiv: [1402.2285 \[hep-ph\]](https://arxiv.org/abs/1402.2285).
- [124] Torbjorn Sjöstrand, Stephen Mrenna, and Peters Skands. “PYTHIA 6.4 physics and manual”. In: *JHEP* 05 (2006), p. 026. doi: [10.1088/1126-6708/2006/05/026](https://doi.org/10.1088/1126-6708/2006/05/026). arXiv: [hep-ph/0603175 \[hep-ph\]](https://arxiv.org/abs/hep-ph/0603175).
- [125] George F. Smoot et al. “Structure in the COBE differential microwave radiometer first year maps”. In: *Astrophys. J.* 396 (1992), p. L1. doi: [10.1086/186504](https://doi.org/10.1086/186504).
- [126] D.N. Spergel et al. “Wilkinson Microwave Anisotropy Probe (WMAP) three year results: implications for cosmology”. In: *Astrophys. J. Suppl.* 170 (2007), p. 377. doi: [10.1086/513700](https://doi.org/10.1086/513700). arXiv: [astro-ph/0603449 \[astro-ph\]](https://arxiv.org/abs/astro-ph/0603449).
- [127] Maria Spiropulu. “Precision Timing Calorimetry”. CPAD Instrumentation Frontier Meeting, October 2015.

- [128] Volker Springel et al. “Simulating the joint evolution of quasars, galaxies and their large-scale distribution”. In: *Nature* 435 (2005), p. 629. doi: [10.1038/nature03597](https://doi.org/10.1038/nature03597). arXiv: [astro-ph/0504097](https://arxiv.org/abs/astro-ph/0504097) [astro-ph].
- [129] D. V. Volkov and V. P. Akulov. “Possible universal neutrino interaction”. In: *JETP Lett.* 16 (1972), p. 438.
- [130] W. W. Moses and S. E. Derenzo. “Prospects for Time-of-Flight PET using LSO Scintillator”. In: *IEEE Transactions on Nuclear Science* 46.3 (June 1999), pp. 474–478. ISSN: 0018-9499. doi: [10.1109/TNS.2007.902370](https://doi.org/10.1109/TNS.2007.902370).
- [131] J. Wess and B. Zumino. “Supergauge transformations in four-dimensions”. In: *Nucl. Phys. B* 70 (1974), p. 39. doi: [10.1016/0550-3213\(74\)90355-1](https://doi.org/10.1016/0550-3213(74)90355-1).
- [132] Simon D.M. White et al. “Clusters, filaments, and voids in a universe dominated by cold dark matter”. In: *Astrophys. J.* 313 (1987), p. 505. doi: [10.1086/164990](https://doi.org/10.1086/164990).
- [133] Si Xie. “New Developments in Secondary Emission Calorimeters”. CPAD Instrumentation Frontier Meeting, October 2015.
- [134] F. Zwicky. “On the Masses of Nebulae and of Clusters of Nebulae”. In: *Astrophys. J.* 86 (1937), p. 217. doi: [10.1086/143864](https://doi.org/10.1086/143864).

*Appendix A***SEARCH FOR MASSIVE RESONANCES DECAYING INTO  
TWO PHOTONS**

*Appendix B*

PHENOMENOLOGY OF ANAMALOUS HIGGS PRODUCTION  
IN SUPERSYMMETRIC MODELS

